Tip-enhanced nano-spectroscopy, imaging, and control: from single molecules to van der Waals materials

by

Kyoung-Duck Park

B.S., Inha University, 2008

M.E., Inha University, 2010

A thesis submitted to the
Faculty of the Graduate School of the
University of Colorado in partial fulfillment
of the requirements for the degree of
Doctor of Philosophy
Department of Physics
2017

This thesis entitled:
Tip-enhanced nano-spectroscopy, imaging, and control: from single molecules to van der Waals materials
written by Kyoung-Duck Park
has been approved for the Department of Physics

Prof. Markus B. Raschke

Prof. Xiaobo Yin

Date

The final copy of this thesis has been examined by the signatories, and we find that both the content and the form meet acceptable presentation standards of scholarly work in the above mentioned discipline.

Park, Kyoung-Duck (Ph.D., Chemical Physics [Department of Physics])

Tip-enhanced nano-spectroscopy, imaging, and control: from single molecules to van der Waals materials

Thesis directed by Prof. Markus B. Raschke

Photon-induced phenomena in molecules and other materials play a significant role in device applications as well as understanding their physical properties. While a range of device applications using organic and inorganic molecules and soft and hard materials have led striking developments in modern technologies, using bulk systems has reached the limit in their functions, performance, and regarding application range. Recently, low-dimensional systems have emerged as appealing resources for the advanced technologies based on their significantly improved functions and properties. Hence, understanding light-matter interactions at their natural length scale is of fundamental significance, in addition to the next generation device applications. This thesis demonstrates a range of new functions and behaviors of low-dimensional materials revealed and controlled by the advanced tip-enhanced near-field spectroscopy and imaging techniques exceeding the current instrumental limits.

To understand the behaviors of zero-dimensional (0D) molecular systems in interacting environments, we explore new regimes in tip-enhanced Raman spectroscopy (TERS) and scanning near-field optical microscopy (SNOM), revealing the fundamental nature of single-molecule dynamics and nanoscale spatial heterogeneity of biomolecules on the cell membranes. To gain insight into intramolecular properties and dynamic processes of single molecules, we use TERS at cryogenic temperatures. From temperature-dependent line narrowing and splitting, we investigate and quantify ultrafast vibrational dephasing, intramolecular coupling, and conformational heterogeneity. Through correlation analysis of fluctuations of individual modes, we observe rotational motion and spectral fluctuations of single-molecule. We extend single-molecule spectroscopy study into *in situ* nano-biomolecular imaging of cancer cells by developing *in-liquid* SNOM. We use a new mechanical resonance control, achieving a high-Q force sensing of the near-field probe. We reveal nanoscale correlations between surface biomolecules and intracellular organelle structures through near-field imaging of the spatial distribution of EGFRs on the membrane of A431 cancer cells. In addition, to understand modified spontaneous emission properties of single quantum dots coupled strongly with localized plasmon, we perform tip-enhanced photoluminescence (TEPL) spectroscopy of the single CdSe/ZnS quantum dots on gold film.

We probe and control nanoscale processes in van der Waals two-dimensional (2D) materials. To understand lattice and electronic structure as well as elastic and phonon scattering properties of grain boundaries (GBs) in large-area graphene, we perform TERS imaging. Through correlated analysis of multispectral TERS images with corresponding topography and near-field scattering image, we reveal bilayer structure of GBs in the form of twisted stacking. In addition, we determine the misorientation angles of the bilayer GBs from a detailed quantitative investigation of the Raman modes. In addition, we present a new hybrid nano-optomechanical tip-enhanced spectroscopy and imaging approach combining TERS, TEPL, and atomic force local strain manipulation to probe the heterogeneous PL responses at nanoscale defects and control the local bandgap in transition metal dichalcogenide (TMD) monolayer. We further extend this approach to probe and control the radiative emission of dark excitons and localized excitons. Based on nano-tip enhanced spectroscopy with $\sim 6 \times 10^5$-fold PL enhancement induced by the plasmonic Purcell effect and few-fs radiative dynamics of the optical antenna tip, we can directly probe and actively modulate the dark exciton and localized exciton emissions in time (∼ms) and space (<15 nm) at room temperature.

Lastly, to extend the range of tip-enhanced microscopy applications to nano-crystallography and nonlinear optics, we present a generalizable approach controlling the excitation polarizability for both in-plane and out-of-plane vector fields by breaking the axial symmetry of a conventional Au tip. This vector field control with the tip enables probing of nonlinear optical second harmonic generation (SHG) responses from a range of ferroic materials as well as van der Waals 2D materials. Specifically, we demonstrate SHG nano-crystallography results for MoS_2 monolayer film, ferroelectric $YMnO_3$, $BaTiO_3$-$BiFeO_3$ multiferroics, and $PbTiO_3$/$SrTiO_3$ superlattices.

Dedication

To my beloved Ji-Yeon

Acknowledgements

There are many people who deserve my warm appreciation for their contributions of one kind or another to my four-years journey through PhD studies. This thesis would not have been possible without their assistance and support, and I would like to offer my most sincere thanks.

First and foremost, I would like to thank my advisor, *Prof. Markus Raschke*, for his thoughtful mentorship, for his endless support of my work, for his wisdom in addressing a lot of issues during my study, and for his incredible enthusiasm to explore new physics. He guided me in this research throughout the entire process and helped me see the forest for the trees. He has gone far beyond general responsibilities of an advisor in every case. I will appreciate what you gave me for the rest of my research career. Many thanks also go to my thesis committee: *Profs. Minhyea Lee, Xiaobo Yin, Joe Maclennan, and Garry Rumbles.* I truly appreciate their valuable advices in my Comps III exam and PhD defense. Next, I would like to acknowledge my past and current colleagues of the Raschke group (*Ben, Bernd, Brian, Chris, Dan, Eric, Evan, Gayle, Honghua, Jiarong, Joanna, Jun, Kaiqiang, Meaghan, Molly, Omar, Peter, Ronald, Sam Berweger, Sam Johnson, Sven, Sveta, Tao, Thomas, Vasily, and Will*) for their warm friendship as well as scientific help. Some of them may not work together with me directly, but they certainly contributed in many ways to the success of our group, as a whole. I am particularly thankful to *Eric* and *Vasily*, who always provided a friendly ear for my chemistry and physics questions. Last but not least, I am very thankful to *all my family*, without whom none of this would have been possible. Many thanks, in particular, to my beautiful wife *Ji-Yeon*, who has been truly wonderful partner and mentor in all things. We will always be together in our future endeavors.

Contents

Chapter

Tables

Table

Figures

Figure

Chapter 1

Introduction

Based on our understanding in macroscopic properties of organic and inorganic molecules and soft and hard materials, a range of device applications of them have led striking developments in electronic, photonic, and biomedical technologies for the last several decades. However, using macroscopic properties of bulk systems has reached the breaking point in device performance. To achieve a breakthrough toward advanced technologies, using low-dimensional systems is desirable because the dimensional reduction in materials makes significant modifications and improvements in their functions and properties [1, 2, 3, 4].

Photon-induced phenomena in low-dimensional systems play an important role for device applications as well as characterization themselves [5, 6, 7, 8, 9, 10, 11, 12, 13]. Hence, understanding various new emerging light-matter interactions on the nanoscale in low-dimensional systems is significant. Near-field optical microscopy is an ideal method to optically access to the nanoscopic length scale of these systems [14, 15, 16]. For the past two decades, near-field microscopy has been growing technologically, from an aperture-type to a scattering-type for enhanced sensitivity [17, 18] and from an elastic scattering detection to inelastic scatterings detection for broader applications [19, 20, 21].

In this work, we perform a broad range of advanced near-field microscopy studies, such as tip-enhanced Raman spectroscopy (TERS), tip-enhanced photoluminescence (TEPL) spectroscopy, and tip-enhanced second harmonic generation (SHG) microscopy to explore unprecedented properties of low-dimensional systems.

1.1 Single molecular processes in interacting environments

Cryogenic tip-enhanced Raman spectroscopy for single molecules

Conformations, dynamics, and coupling involving single molecules determine function in catalytic, electronic, or biological systems [22, 23, 24]. Single molecules allow for the understanding of unsynchronized processes and rare events occurring at specific locations in heterogeneous systems. Although Erwin Schrödinger had envisioned in 1952 that people will never do experiments with single molecules [25], it did not take physicists long to prove his prediction was wrong due to the rapid technological development. Since the first observation of single-molecule absorption by William Moerner in 1989 [1], recent theoretical and experimental studies in chemistry have focused on understanding single molecules and their behaviors in contrast to ensembles.

Single-molecule absorption and fluorescence spectroscopies indirectly probe the effects of local perturbations [1, 26, 27, 28]. Similarly, multi-dimensional spectroscopy provides insight into intramolecular structure and dynamics on ultrafast time scales [29], yet with limited information about slower time scales, oscillator density, or real-space distribution. On the other hand, single-molecule vibrational spectroscopy with surface-enhanced Raman scattering (SERS) and TERS can directly probe molecular identities such as intramolecular dynamics and local molecular environment [2, 30, 31, 32]. However, molecules are highly mobile at room temperature, and single-molecule TERS or SERS spectra average over many adsorbate conformations [32]. Rapid spectral fluctuations that occur faster than the spectral acquisition time contribute to broadening, similar to the ensemble averaged spectra in far-field Raman spectroscopy [2, 33].

To complement these difficulties in single-molecule Raman spectroscopy at room temperature, we perform single-molecule TERS at cryogenic and variable temperatures (90-300 K). In this topic, we investigate malachite green (MG) with high spectral resolution to understand intramolecular coupling, conformational heterogeneity, and rotational and spectral diffusions.

Development of cryogen-free low-temperature tip-enhanced spectroscopy

While the high-vacuum cryogenic TERS enables us to study single-molecule dynamics, its open-cycle cryostat with liquid nitrogen (LN_2) has retained several issues. In this setup, the TERS head is rigidly mounted on the cryostat. This causes vibrational noise and mechanical drift even when the flow rate of LN_2 is set to a minimum. In addition, the sample surface is not kept clean due to multiple layers of water at high-vacuum condition. Therefore, for more detailed understanding of molecular dynamics and intramolecular coupling properties as well as better measurement and control of samples, we build a cryogen-free low-temperature tip-enhanced spectroscopy with an ultra-high-vacuum (UHV) closed cycle helium exchange gas cryostat extending the temperature range from 20 to 350 K.

Near-field imaging of cell membranes in liquid

Single-molecule detection methods have rapidly extended to advanced research in molecular biology. Recently, new types of super-resolution fluorescence microscopies have opened the door for studying biomolecular processes with diffraction-unlimited spatial resolution. For example, stimulated emission depletion (STED) increases spatial resolution by selectively deactivating fluorophores [26, 34]. The photoactivated localization microscopy (PALM) [35] and stochastic optical reconstruction microscopy (STORM) [36] overcome the diffraction barrier by using photoswitchable fluorescent probes. However, these super-resolution microscopies need to use specific fluorophores optimized for the target biomolecules and high power excitation to increase the number of photons per pixel. Further, based on their far-field sectioning methods, these microscopies are not ideal to investigate membrane proteins, even though these proteins are of particular significance as the target of over 60% of all modern medicinal drugs [37]. On the other hand, near-field scanning optical microscopy (NSOM) is an ideal super-resolution technique for cell-membrane study because it profiles surface structure and detects near-field signals only from the membrane proteins [14, 15, 16]. It thus offers correlation properties between the membrane structure and proteins, but has several technical challenges when operating it in liquid [38]. Therefore, a refined approach for optimal operation of NSOM in liquid and its biological application are highly desired for in-depth molecular biology research at the single-molecule level sensitivity.

As an extension of molecular characterization studies and instrumental development of near-field microscopy in interacting media, we demonstrate a new approach of mechanical resonance control of the near-field probe providing stable and sensitive imaging in liquid. Through high-resolution (~50 nm) near-field imaging of the spatial distribution of epidermal growth factor receptors (EGFRs) on the membrane of A431 cancer cells in liquid, we reveal nanoscale heterogeneity of surface EGFRs, as a demonstration representing a typical bioimaging application.

Tip-enhanced strong coupling in a single quantum dot

Photoluminescence (PL) is a spontaneous emission process in materials, such as semiconductors and noble metals. The PL properties such as emission rate, lifetime, and energy are strongly influenced by the interacting environments [39]. Therefore, careful environmental control gives us access to manipulate emission properties of semiconductors for a broad range of device applications. Quantum dots are promising building blocks for photonic devices because it generates high quantum yield PL due to the quantum confinement effect associated with its zero-dimensional (0D) structure [40]. In addition to the high quantum yield, this 0D nature, consisting of a few nanometers, also allows us to significantly modify PL properties by an environmental control. Therefore, understanding and controlling the environmentally modified PL properties of single quantum dots apart from the ensemble state is highly desirable.

In this topic, we further extend our tip-enhanced spectroscopy study to a single quantum dots. We place single CdSe/ZnS quantum dots at the junction of Au tip and Au substrate, and perform a TEPL spectroscopy experiment. Here, we observe not only the high PL enhancement but also the double PL peaks split by the strong coupling between exciton and plasmon.

1.2 Probing and control nanoscale processes in van der Waals materials

As described in previous topics, the investigation of single molecules allows better understanding in chemistry and biology. In addition, we envision that these 0D systems will be a fundamental unit for highly integrated nano-electronic and photonic devices in the future, as shown in examples of single-molecule transistors [41, 42]. However, we may need to wait for several decades because these 0D systems are generally not stable in ambient conditions [2, 33]. On the other hand, recently emerged layered 2-dimensional (2D) materials have several advantages in terms of manipulation compared to 0D systems, e.g., they are easy to exfoliate, stack, and cut in ambient conditions [43]. In addition, their outstanding electronic [44, 45], thermal [46], mechanical [47], and optical [48, 49] properties compared to bulk materials enable us to achieve miniature, flexible, wearable devices in the not too distant future. Therefore, we extend our tip-enhanced spectroscopy and imaging approach to probe and control the disordered states, photon energies, and couplings in 2D systems.

Probing bilayer grain boundaries in large area graphene

Van der Waals materials have been attracting much attention because they enable a broad range of application by creating a variety of heterostructures [43]. Graphene, a single-atomic sheet of sp^2-hybridized carbon, is a core element for various applications based on the observation of its ambipolar field effect [44] and the quantum hall effect [45]. Using these unique effects, graphene is already used for highly conductive and transparent electrodes [50], high speed field-effect devices [51], and optical modulators [52].

Specifically, large-area graphene sheets grown by chemical vapor deposition (CVD) have been proposed as a route to realize mass production and commercialization of near-ballistic transport electronic devices [53, 54]. So far, most large-area synthetic graphene is polycrystalline. The associated grain boundaries (GBs) [53, 55, 56, 57] have been identified as a major limitation in device applications due to their modified electronic structure and inhibition of carrier transport [58, 59]. Therefore, understanding the detailed characteristics of GBs is a prerequisite for better design of graphene sheets. Despite the greater applicability of large-area graphene sheets compared to graphene flakes, most theoretical and experimental studies of GBs have focused on the analysis of atomic defects observed in adjacent crystal faces [60], which show significant differences from larger scale deformations of GBs in large-area graphene.

In this topic, we perform < 18 nm spatial resolution TERS imaging to understand lattice and electronic structure, as well as elastic and phonon scattering properties of GBs in CVD-grown large-area graphene. Through correlated analysis of topography, near-field scattering, and multispectral TERS imaging, we reveal bilayer GBs in the form of twisted stacking at the boundary between two misoriented crystal facets. We also use a detailed quantitative analysis of phonon mode symmetries in the Raman spectra to determine the misorientation angles of the bilayer GBs.

Disordered states and local strain control of WSe_2 monolayer

While graphene is a core building block for various heterostructure applications, it is not an appealing candidate for transistors due to its zero bandgap, which inevitably causes a low on/off ratio [61]. In order to complement this issue, researchers were trying to find semiconducting van der Waals materials using the widely known scotch tape exfoliation method [62]. Transition metal dichalcogenides (TMDs) are indirect bandgap semiconductors made up of a transition metal atom (M: Mo, W, etc) and a chalcogen atom (X: S, Se, and Te) with the molecular structure of MX_2 [63]. As the TMD crystals are thinned to the monolayer (ML) limit, new properties emerge including an indirect-to-direct bandgap transition [48, 49], valley-specific circular dichroism [64], and enhanced nonlinear optical responses [65, 66]. The direct semiconducting gap, large spin-orbit coupling, and valley-selectivity provide several advantages for the use of TMDs in photodetector and other optoelectronic device applications.

A prevailing theme in TMD systems is the complex interaction between fundamental excitations inherent to the materials themselves, and extrinsic factors associated with surface morphology and the underlying substrate. In addition, the reduced dimensionality induces strong interference from impurities, defects, and disorder, creating much difficulty in isolating the intrinsic quantum properties of the material [67]. The resulting electronic properties are consequently highly inhomogeneous and sensitive to structural variations near internal and external boundaries [68, 69]. To explore these heterogeneities and how they control the optical and electronic properties, a comprehensive multimodal nanoscale imaging and spectroscopy approach is desirable.

Therefore, we present a new hybrid nano-optomechanical tip-enhanced spectroscopy and imaging approach combining TERS, TEPL, and atomic force local strain control to investigate the correlation of local structural heterogeneities with nanoscale optical properties. We study the heterogeneous PL responses at edges and twin boundaries (TBs) in WSe_2 ML microcrystals. In addition, through controlled tip-sample force we can tune the bandgap reversibly (up to 24 meV) and irreversibly (up to 48 meV) through local nanoscale strain engineering (0-1%).

Radiative control of dark excitons in WSe_2 monolayer at room temperature

We further extend this approach to probe and control the radiative emission of dark excitons at room temperature. The recent discovery of the dark exciton emission from atomically thin TMDs suggests a range of potential applications for novel quantum nano-optoelectronics. However, the approaches used for their observation are based on applying a large in-plane magnetic field (>14 T) [70] or using surface plasmon polaritons (SPP) coupling [71] which requires cryogenic temperatures. This constraint, together with the not yet demonstrated ability to control and modulate the dark exciton emission, severely limits the broader utility of these approaches to open dark excitons for applications. In this topic, we use a novel generalizable approach demonstrating excitation, modulation, and radiative control of dark exciton emission even at room temperature. Based on nano-tip enhanced spectroscopy with $\sim 6 \times 10^5$-fold photoluminescence enhancement induced by the plasmonic Purcell effect and few-fs radiative dynamics of the optical antenna-tip, we can directly probe and actively modulate the dark exciton emission in time (~ms) and space (<15 nm) at room temperature.

Radiative control of localized excitons in WSe_2 monolayer at room temperature

In addition to the bright and dark excitons, single quantum emitting states are discovered in atomically thin TMDs [72, 73]. These single exciton states are found when excitons are localized to defects or quantum dot like confined potentials [72, 73]. This new class of single quantum emitter from localized excitons (X_L) in layered 2D materials is a promising candidate for potential applications in quantum optics and information technologies. In this topic, we perform multispectral TEPL imaging on the radiative emission of localized excitons at room temperature, as an extension study of WSe_2 ML. TEPL allows us to investigate spatial local heterogeneity of X_L modes with ~10 nm spatial resolution. These X_L modes concentrate in the vicinity of the crystal edges in contrast to bright excitons which is associated with the density of structural defects. Furthermore, we control the orientation of their transition dipole moment from precise control of plasmon-exciton coupling using the nano-optical antenna-tip.

1.3 Tip-enhanced nonlinear optical nano-crystallography

One of the merits of tip-enhanced microscopy is wide versatility. Tip-enhanced microscopy can be used for not only linear elastic (Rayleigh) and inelastic (fluorescence, Raman) scattering imaging, but also nonlinear (SHG, third harmonic generation; THG, four wave mixing; FWM, etc) optical imaging. In this topic, we further extend our tip-enhanced approach to nonlinear optical nano-crystallography.

Vector field control of plasmonic antenna-tip

To extend the range of near-field microscopy application to nano-crystallography, vector field access and their polarizability control are desirable. In general, a surface normal oriented antenna-tip is used in tip-enhanced spectro-nanoscopy [19]. On the one hand, this conventional geometry of the tip is useful to selectively detect out-of-plane polarized optical responses through a strongly confined optical field. On the other hand, it typically has a weak optical confinement in other polarization angles, which reduces the detection sensitivity for the non out-of-plane optical responses. It then restricts the range of applications to the various quantum materials, especially two-dimensional (2D) samples, e.g., graphene, transition metal dichalcogenides (TMDs), and epitaxial thin films.

In this topic, we demonstrate a generalizable approach to control the excitation polarizability for both in-plane and out-of-plane vector fields and probe optical responses from samples without loss of spatial resolution. We break the axial symmetry of a conventional Au tip by engineering its tilting angle with respect to the sample surface. This active control of the broken axial symmetry increases the degrees of freedom of both in-plane and out-of-plane polarizability. In addition, this gives rise to a significantly enhanced optical field confinement with respect to both directions by creating a confined structure for free electrons and associated localized plasmon antenna effect.

Second harmonic generation nano-crystallography

The broken inversion symmetry of TMDs with the reduced dimensionality provides remarkably large nonlinear optical responses with purely in-plane polarizability, which play an important role for device applications, as well as material characterizations [65, 74, 75]. SHG microscopy provides informative knowledge on nonlinear optical responses, such as the crystalline symmetry, orientation, defect states, stacking angle, and the number of layers [65, 74, 75, 76].

Beyond layered 2D systems, ferroic materials also can be characterized with SHG spectroscopy since they are made of well-defined crystalline solid in the form of domains [77]. However, little is known about their nanoscale nonlinear optical properties and associated crystallographic properties due to the limitations in spatial resolution and polarization control of far-field SHG microscopy. Therefore, applications of tip-enhanced microscopy to nonlinear optical signals is highly desirable to investigate the detailed nano-crystallographic properties of various samples. We will discuss the development of SHG nano-crystallography and its applications to TMDs, ferroelectrics, and multiferroics in the main text.

1.4 Thesis outline

The rest of this Thesis is organized in the following manner.

In Chapter 2, I introduce fundamentals on nanoscale light confinement using noble metal nanostructures. In the first section, I introduce the Drude model to describe light-induced electron behaviors of gold, which provides a theoretical understanding for surface plasmon polariton (SPP) and the localized surface plasmon resonance (LSPR). I then describe the polarizability and the local field enhancement for single and coupled dipoles models. In the second section, I introduce general background on the invention of near-field optical microscopy and the process of its development from near-field scanning optical microscopy (NSOM) to various tip-enhanced microscopy applications.

In Chapter 3, I demonstrate several studies on single molecular processes in interacting environments. First, I demonstrate experimental observations for single-molecule dynamics at variable temperatures (90-300 K), that are measured by a home-built cryogenic TERS setup. Second, I discuss the instrumental development of a cryogen-free low-temperature tip-enhanced spectroscopy, which is built to complement limitations of the previous cryogenic TERS setup using an open-cycle cryostat. Third, I demonstrate near-field imaging results of cell membranes measured in liquid which enabled by active scanning probe mechanical resonance control, as an extension of near-field molecular characterization study into biological samples. Then, I demonstrate preliminary results on tip-enhanced strong coupling in a single quantum dot as another example of near-field microscopy study on 0D systems.

In Chapter 4, I demonstrate several studies on probing and control nanoscale processes in van der Waals materials. First, I demonstrate an experimental discovery of bilayer grain boundaries in large area graphene observed by multispectral TERS imaging. Then, I introduce a hybrid tip-enhanced nano-spectroscopy and imaging setup, not only for probing nanoscale properties, but also for control of strain and radiative emission of monolayer TMDs. For application examples, I demonstrate spatially heterogeneous disordered states, dark exciton emissions, and localized exciton emissions of WSe_2 ML at room temperature.

In Chapter 5, I introduce a new method for vector field control of plasmonic antenna tips and demonstrate tip-enhanced nonlinear optical nano-crystallography applications using the new method. In details, I demonstrate a generalizable approach to control the excitation polarizability for both in-plane and out-of-plane vector fields by breaking the axial symmetry of a conventional Au tip by engineering its tilting angle. Then, as application examples, I demonstrate SHG nano-crystallography results for MoS_2 monolayer film, ferroelectric $YMnO_3$, $BaTiO_3$-$BiFeO_3$ multiferroics, and $PbTiO_3/SrTiO_3$ superlattices.

In Chapter 6, I summarize the work performed for this thesis and discuss conclusions and outlooks drawn from this work.

Chapter 2

Nanoscale light confinement and imaging

2.1 Optical antenna using localized surface plasmon resonance

Surface plasmons are resonance oscillating state of free electrons in metal surfaces (Au, Ag, and Cu) with electromagnetic fields [78]. This surface plasmon resonance effect is widely used to confine the light on the nanoscale into two-dimensional (2D) [79], one-dimensional (1D) [80], or even zero-dimensional (0D) [81] structures by engineering the dimension and size of noble metals.

In order to understand the physical properties of surface plasmons and physical mechanism of the light confinement, we start with a simple description of the free electron (ϵ_{free}) response in metals. The complex dielectric function for free electrons in a metal is given in the Drude-Sommerfeld model [82] as

$$\epsilon_{\text{free}}(\omega) = 1 - \frac{\omega_p^2}{\omega^2 + \Gamma^2} + i\frac{\Gamma\omega_p^2}{\omega(\omega^2 + \Gamma^2)} \tag{2.1}$$

where ω and ω_p are excitation frequency and plasma frequency, and Γ is a damping constant. For gold, the real and the imaginary part of the dielectric constant with respect to the wavelength can be plotted as Fig. 2.1 [83]. While the real part of the dielectric constant is a negative value in the visible region, the positive values of the imaginary part describe the energy dissipation related to the electron motion.

In general, this Drude model gives quite accurate parameters for metals in the infrared region. However, this model should be revised in the visible region due to the surface plasmon of bound

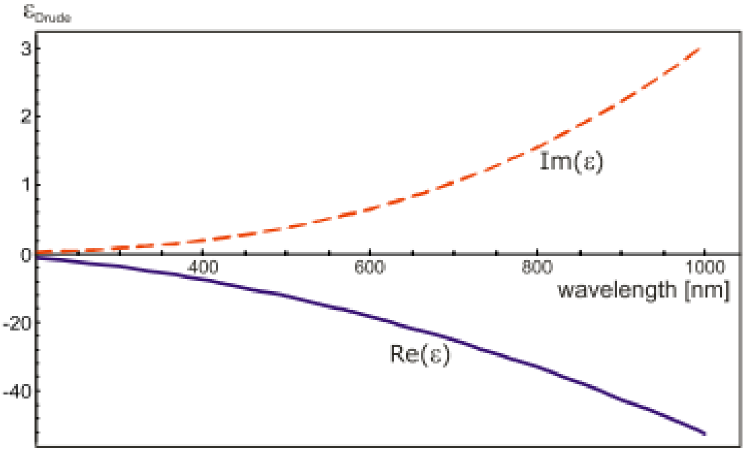

Figure 2.1: Real and imaginary parts of dielectric constant of free electrons of gold as a function of excitation wavelength [83].

electrons. The motion of bound electrons in a metal is described as [83]

$$m\frac{\mathrm{d}^2 r}{\mathrm{d}t^2} + m\gamma\frac{\mathrm{d}r}{\mathrm{d}t} + \alpha r = eE_0 \mathrm{e}^{-i\omega t} \tag{2.2}$$

where m is an effective mass of the bound electrons, r is a displacement of charge, and γ and α are the damping and restoring components of bound electrons, respectively. Using the Ansatz $r(t) = r_0\mathrm{e}^{-i\omega t}$, the complex dielectric function for bound electrons are derived as

$$\epsilon_{\text{bound}}(\omega) = 1 + \frac{\omega_p^2(\omega_0^2 - \omega^2)}{(\omega_0^2 - \omega^2) + \Gamma^2\omega^2} + i\frac{\Gamma\omega_p^2\omega}{(\omega_0^2 - \omega^2) + \Gamma^2\omega^2}. \tag{2.3}$$

For gold, the dielectric constant as a function of wavelength is plotted as shown in Fig. 2.2 [83]. From Eq. 2.3, we understand the dielectric function of bound electrons and the physical origin of the surface plasmon resonance effect. Briefly, the bound electrons show a coherent oscillation of charges at the metal surface in the visible region. Based on this, we can further understand the propagation and localization properties of plasmon polaritons, charge density oscillations on the metal surface [78, 84], by deriving a dispersion relation from Maxwell′s equation. Eq. 2.4 and 2.1 are wave vectors along the propagation direction and the surface normal direction as a function of angular frequency ω.

$$k_x^2 = \frac{\epsilon_1\epsilon_2}{\epsilon_1 + \epsilon_2}k^2 = \frac{\epsilon_1\epsilon_2}{\epsilon_1 + \epsilon_2}\frac{\omega^2}{c^2}, \tag{2.4}$$

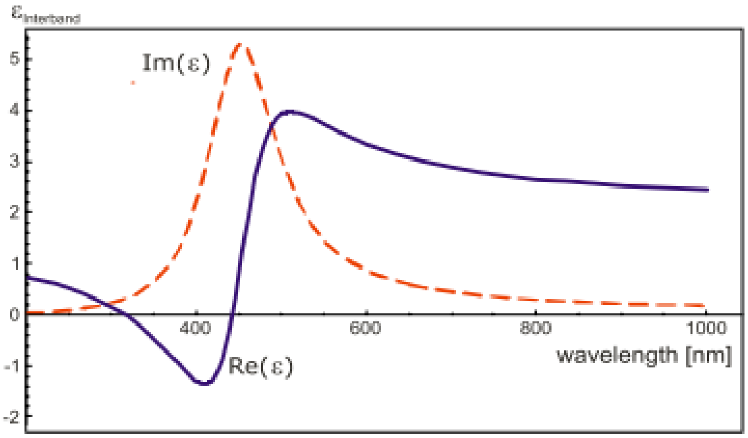

Figure 2.2: Real and imaginary parts of dielectric constant of bound electrons of gold as a function of excitation wavelength [83].

$$k_{j,z}^2 = \frac{\epsilon_j^2}{\epsilon_1 + \epsilon_2} k^2, \quad j = 1, 2, \tag{2.5}$$

where ϵ_1 and ϵ_2 are the dielectric constants of a metal and a dielectric medium, respectively. For gold and silver metal surfaces, k_x has a positive value with purely imaginary k_z term, which gives rise to propagating plasmon polaritons on the metal surface, whereas it exponentially decays into the bulk perpendicular to the surface. We can derive the plasmon polariton wavelength by considering both real and imaginary parts of the metal′s dielectric function. If we assume the dielectric medium has negligible loss, the real and imaginary parts of wave vector k_x can be derived as [83]

$$k_x' \approx \sqrt{\frac{\epsilon_1' \epsilon_2}{\epsilon_1' + \epsilon_2}} \frac{\omega}{c}, \tag{2.6}$$

$$k_x'' \approx \sqrt{\frac{\epsilon_1' \epsilon_2}{\epsilon_1' + \epsilon_2}} \frac{\epsilon_1'' \epsilon_2}{2\epsilon_1'(\epsilon_1' + \epsilon_2)} \frac{\omega}{c}. \tag{2.7}$$

Hence, the plasmon polariton wavelength is given as

$$\lambda_{SPP} = \frac{2\pi}{k_x'} \approx \sqrt{\frac{\epsilon_1' + \epsilon_2}{\epsilon_1' \epsilon_2}} \lambda, \tag{2.8}$$

where λ is an excitation wavelength [83]. Fig. 2.3a shows the dispersion relation of plasmon polaritons at the interface of air and gold. To launch a surface plasmon polariton (SPP) at the excitation

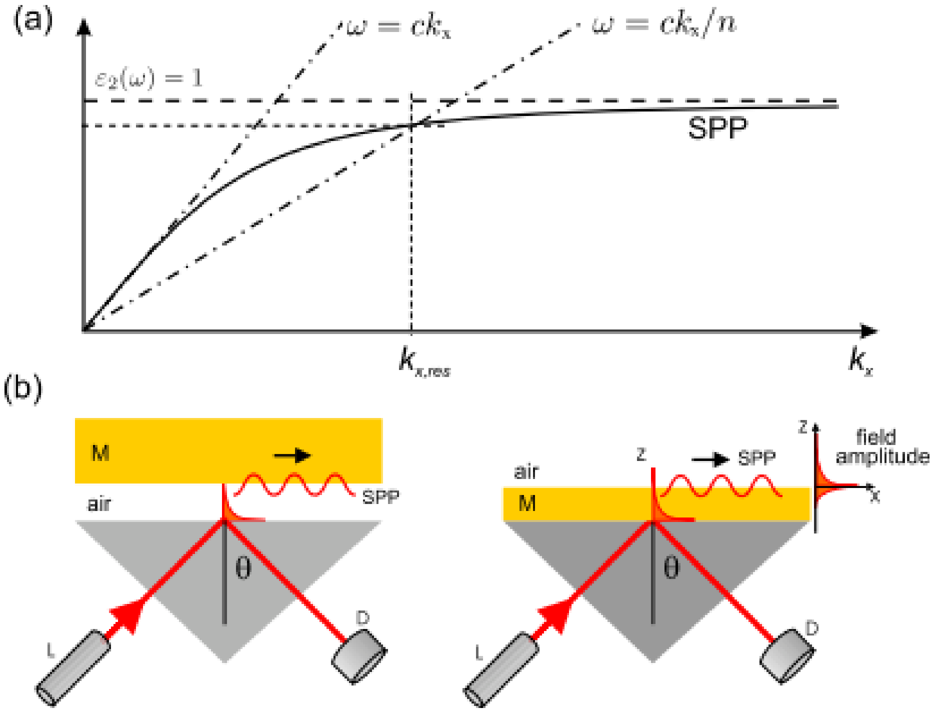

Figure 2.3: (a) Dispersion relation of surface plasmon polariton with light in the free space and the higher refractive index medium. (b) Cartoons of experimental setup to launch surface plasmon polaritons onto the metal surface [83].

wavelength, k_x should be optimized by controlling the incidence angle for the increased momentum of the SPP, as shown in Fig. 2.3b [83]. Based on the surface propagating nature of the SPP, the electromagnetic field can be confined onto the metal surface, and the flow of light on the plasmonic metal surface can be controlled on the nanoscale with various types of photonic devices, such as waveguides [85], bio and chemical sensors [86], and filters [87].

Plasmonic metal nanoparticles are of particular interest for confining the light into nanoscale volumes. When the diameter of the nanosphere is smaller than the wavelength of light, we can define the frequency dependent polarizability $\alpha(\omega)$ from the Clausius - Mossotti relationship [88] given as

$$\alpha(\omega) = 3\mathrm{V}\frac{\epsilon_1 - \epsilon_2}{\epsilon_1 + 2\epsilon_2} \tag{2.9}$$

with the volume of the particle V. As can be seen in Eq. 2.9, the polarizability of metal nanoparticles has a maximum value in the visible frequency when the real part of metal dielectric constant

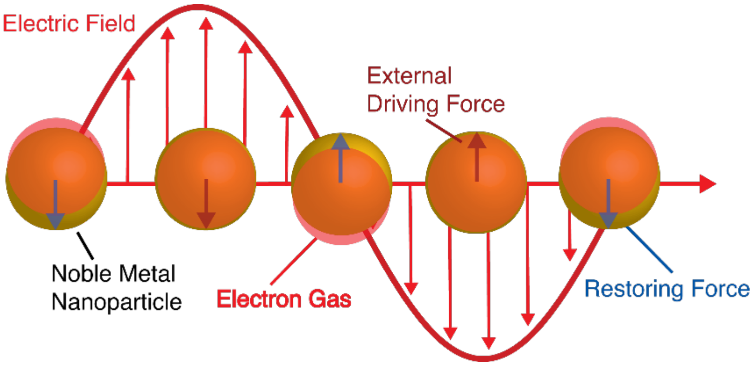

Figure 2.4: Illustration of the localized surface plasmon resonance (LSPR) of metal nanoshpere in response to an external electric field

becomes -2 (we assume $\epsilon_2 \simeq 1$ in air). This resonance behavior is similar to the harmonic oscillator model without a restoring force. Hence, we can imagine an oscillating electron cloud of the plasmonic metal nanoparticles at the resonance frequency of the electromagnetic field as illustrated in Fig. 2.4 [89]. This phenomenon, called localized surface plasmon resonance (LSPR), also induces strong confinement of the electromagnetic field into the metal nanoparticles as a type of evanescent field. This localized evanescent field surrounding the metal surface then induces strong light-matter interaction on the nanoscale when the sample is closely approached to the particles. Hence, we can use this metal nanostructure as a nanoscale source, absorber, or scatterer for various types of nanoscale light-matter interaction beyond the diffraction limit. We can expect this LSPR effect at the apex of the sharp metallic tip of an atomic force microscopy (AFM). Therefore, high spatial resolution optical imaging and spectroscopy are possible by illuminating a light into the apex of the tip, and scanning it onto the sample surface. This is a fundamental principle of scattering type scanning near-field optical microscopy (s-SNOM), which I will describe in the next section.

While the dipole moment induced by LSPR at the apex of the s-SNOM tip provides a localized evanescent field, its field enhancement factor is relatively smaller than that of the nanoparticles due to an overdamped resonance of a semi-infinite tip structure. To achieve stronger local field enhancement at the apex of the plasmonic tip, we can induce another conducting plane below the tip as an image dipole. When the tip is closely approached to a plasmonic surface with unbound

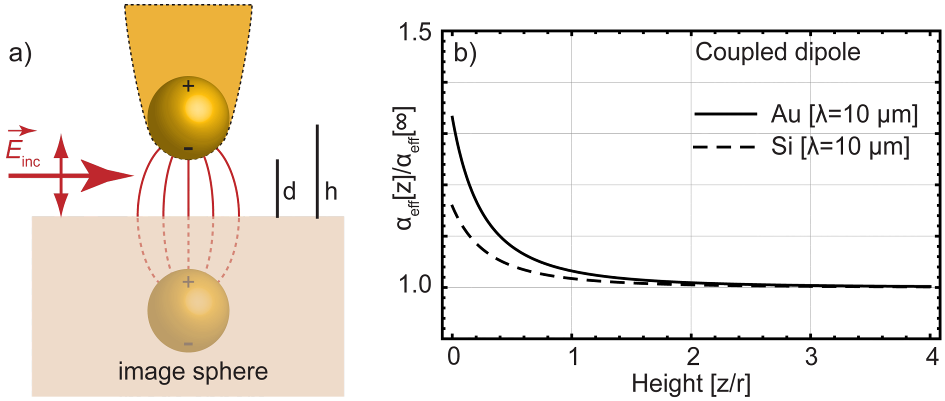

Figure 2.5: (a) Illustration of a coupled dipoles model to calculate polarizability and local field confinement at the gap between tip and substrate. (b) Calculated effective polarizability with respect to the tip - substrate distance for Au and Si substrates [90].

electrons, the localized field at the tip apex induces localized surface charges which give rise to an image dipole of the tip [91]. Therefore, we can induce a dipole-dipole interaction by introducing an image dipole on the metallic substrate as shown in Fig. 2.5a [90]. The polarizability of coupled dipoles can be described by a dipole of the tip (we assume tip polarizability is the same as sphere for simplified model) and an image dipole with polarizability $\beta = (\epsilon_{\mathrm{surf}} - 1)/(\epsilon_{\mathrm{surf}} + 1)$, placed on the substrate with a distance of $-d$. From a dipole-dipole interaction, the polarizability at the nano-gap is given as

$$\alpha_{\mathrm{eff,z}} = \alpha_{\mathrm{sph,z}} \left(1 - \frac{\alpha_{\mathrm{sph,z}}\beta}{16\pi d^3}\right)^{-1}. \tag{2.10}$$

We also derive the localized electric field at the nano-gap as a function of height z (for $z < d$) by adding the field contribution from the external field and the dipole moment of the nano-gap [90]:

$$\begin{aligned} E_{\mathrm{tot,z}}[z] &= E_{\mathrm{inc,z}} + E_{\mathrm{sph,z}} + E_{\mathrm{imsph,z}} \\ &= \left(1 + \frac{\alpha_{\mathrm{eff,z}}}{16\pi(d-z)^3} + \frac{\alpha_{\mathrm{eff,z}}\beta}{16\pi(d+z)^3}\right) E_{\mathrm{inc,z}}. \end{aligned} \tag{2.11}$$

Fig. 2.5 shows an illustration of the coupled dipole model (a) with an example of distance-dependent polarizability (b) for Si and Au substrates for $\lambda = 10$ μm excitation field [90]. As shown in this example, we can actively control the local field enhancement at the nano-gap by inducing and engineering a dipol-dipole interaction. We note that the in-plane polarizability and optical field are also increased in the nano-gap with smaller extents than that of out-of-plane mode [90].

2.2 Scanning near-field optical microscopy

The beginning of near-field optical microscopy is dated to nearly a hundred years ago. An Irish physicist, Edward H. Synge, conceived a simple theoretical idea measuring transmission signals through a nano-aperture to achieve the sub-wavelength optical imaging [92]. Although Albert Einstein reviewed and approved his idea for journal publication in 1928, this idea was not realized experimentally until his death in 1957. It was mainly due to technological limitations in nano-fabrication, nano-mechanics, intense light source, and a high sensitivity detector.

Based upon the technological breakthroughs, scanning near-field optical microscopy (SNOM) or NSOM was experimentally demonstrated in 1984 by a German-Swiss physicist, Dieter Pohl [14]. The first generation NSOM was based on using a tapered optical fiber with a metal-coated aperture (diameter of 50 $\sim$ 100 nm). This apparatus has been widely disseminated for various applications since it provides high spatial resolution optical image with corresponding surface profile. SNOM has opened the way for the nanoscale optical characterization and significantly contributed to materials [93, 94, 95], chemistry [96], photonic devices [97, 98, 99] research, and even to biology [100, 101, 102]. Although it was an extremely powerful method at that time, there were several practical difficulties to obtain reproducible NSOM signals. First, the shear-force AFM feedback is not stable due to low Q-factors when the fiber tip is attached to the tuning fork [38]. The metal coated nano-aperture is easily damaged due to this unstable AFM feedback. In addition, the measurable spectral range is limited due to the narrow spectral bandwidth of an optical fiber. Most importantly, the light transmission efficiency of the nano-aperture is too low. This low efficiency limits the spatial resolution (the diameter of an aperture should be larger than $\sim$50 nm) and applications in inelastic scattering measurements.

For an aperture of radius a in a thin metal substrate, the total power of light transmission P_{trans} is given as [103, 90],

$$P_{\text{trans}}(\lambda, a, E_{\text{inc}}) = \underbrace{\frac{64}{27\pi}\left(\frac{2\pi a}{\lambda}\right)^4 a^2}_{\sigma_{\text{eff}}} \cdot \underbrace{\frac{c}{2}\varepsilon_0 E_{\text{inc}}^2}_{\text{incident irradiance}} , \tag{2.12}$$

where σ_{eff} is the effective transmission cross-section and $c/2 \cdot \varepsilon_0 E_{\text{inc}}^2$ is the incident irradiance to the small aperture. This rapid decrease in transmission power with respect to the decreasing aperture diameter has led us to other approach using a local scatterer, scattering type scanning near-field optical microscopy (s-SNOM) [17, 18]. The fundamental concept of s-SNOM is the same as SNOM measuring a near-field signal simultaneously with a topography. The only difference is using a sharp tip for measuring near-field scattering signals instead of using a fiber aperture. While the tip - sample distance control method in SNOM is limited mainly to the tuning fork based shear-force feedback, s-SNOM uses a conventional tapping mode AFM as well as shear-force AFM. In addition, the shear-force feedback with a short tip in s-SNOM is more stable than SNOM using a long optical fiber. Besides, the measurable spectral range of near-field scattering is not significantly limited. Therefore, the spectral range of near-field microscopies is extended to infrared wavelengths and to the THz regime [104, 105]. Most importantly, the local field enhancement and the scattering cross-section are increased with the decreasing size of the apex of the tip. This allows us to achieve a few nanometers spatial resolution in s-SNOM with intense optical signals. Furthermore, this high sensitivity detection enables us to extend s-SNOM applications to a wide range of different inelastic scattering measurements, such as Raman, IR, photoluminescence (PL), and nonlinear optical responses.

While the near-field signal in SNOM is directly detected through the optical fiber, the near-field signal in s-SNOM is scattered by a tip and delivered to the detector together with the far-field background. Therefore, several methods are used in s-SNOM to reduce far-field background. Simple demodulation of near-field signals with tip oscillating frequency is generally used [106]. The near-field scattering induced by tip-sample dipole-dipole interaction gives a sinusoidal signal with the oscillating frequency of the tip since the polarizability of coupled dipoles are related to the tip-sample distance. Whereas the far-field background is not modulated with this frequency, we can extract only near-field components with a lock-in amplifier. This method is generally used when the AFM tips do not give strong polarizability, e.g., Si or Si_3N_4 tips. On the other hand, when we use noble metallic tips in the visible wavelength range, we can use an optical antenna effect induced by localized surface plasmons. As described in the previous section, the excitation optical field is strongly localized at the apex of metallic tips (Au, Ag, or Cu). Therefore, the excitation rate of the near-field signals is a few orders of magnitude higher than the far-field signals. Hence, we naturally can obtain high contrast near-field images without the demodulation process.

This optical antenna-based near-field detection method is called tip-enhanced near-field microscopy. This method allows us to extend s-SNOM to spectroscopy applications and detect inelastic scattering signals, which have much smaller cross-section. Tip-enhanced Raman spectroscopy (TERS) is a technique to measure Raman scattering signal using tip-enhanced near-field microscopy [31, 107]. Raman scattering signal provides sample information on composite ratio, strain, symmetry, and temperature. However, since the Raman scattering cross-section is much smaller than Rayleigh scattering, it is very difficult to obtain Raman signal from the nanoscale dimension of molecular and material systems. On the other hand, we can obtain single molecule level sensitivity Raman signal using TERS because TERS intensity has a fourth power dependence on the field enhancement given by [89]

$$I_{\mathrm{TERS}} \propto (F(\omega_{\mathrm{out}})F(\omega_{\mathrm{in}}))^2, \tag{2.13}$$

where $F(\omega)$ is a field enhancement factor by an antenna-tip effect, defined as

$$F(\omega) = \frac{E_{\mathrm{loc}}(\omega)}{E_{inc}}, \tag{2.14}$$

where $E_{\mathrm{loc}}(\omega)$ is a frequency-dependent local electromagnetic field. Accordingly, TERS is a powerful method for versatile nanoscale characterizations of various systems. Furthermore, tip-enhanced PL (TEPL) spectroscopy is a promising method to characterize electronic and optical properties of semiconducting materials. For the case of TEPL, the enhanced excitation rate is the same as TERS, but the emission rate is enhanced by the Purcell effect, the enhancement of a spontaneous emission rate by its surrounding environment, at the plasmonic nano-cavity. We will discuss a detailed mechanism of TEPL in Chapter 4. Furthermore, we will discuss the tip-enhanced nonlinear optical nano-crystallography in Chapter 5, as an extension of our tip-enhanced near-field microscopy study.

Chapter 3

Single molecular processes in interacting environments

3.1 Cryogenic tip-enhanced Raman spectroscopy for single-molecule[1]

Structure, dynamics and coupling involving single-molecules determine function in catalytic, electronic or biological systems. While vibrational spectroscopy provides insight into molecular structure, rapid fluctuations blur the molecular trajectory even in single-molecule spectroscopy, analogous to spatial averaging in measuring large ensembles. To gain insight into intramolecular coupling, substrate coupling, and dynamic processes, we use tip-enhanced Raman spectroscopy (TERS) at variable and cryogenic temperatures, to slow and control the motion of a single-molecule. We resolve intrinsic line widths of individual normal modes, allowing detailed and quantitative investigation of the vibrational modes. From temperature dependent line narrowing and splitting, we quantify ultrafast vibrational dephasing, intramolecular coupling, and conformational heterogeneity. Through statistical correlation analysis of fluctuations of individual modes, we observe rotational motion and spectral fluctuations of the molecule. This work demonstrates single-molecule vibrational spectroscopy beyond chemical identification, opening the possibility for a complete picture of molecular motion ranging from femtoseconds to minutes.

3.1.1 Motivation

The investigation of single-molecules allows for the observation of unsynchronized processes and rare events occurring at specific locations in an inhomogeneous sample. As such, single-molecule

---

[1] This section draws significantly from [19]. The experiment was performed by K.-D. Park and analyzed by K.-D. Park and E. A. Muller, and supervised by M. B. Raschke.

spectroscopy provides the systematic basis to reach beyond traditional spectroscopies that average over both the spatial distribution and temporal dynamics of molecules.

Single-molecule spectroscopy can sensitively probe local environment and stochastic dynamics through instantaneous shifts in fluorescence energies and spectral diffusion [1, 26, 27, 28]. Imaging the spatial distribution of an optical excitation [108], disorder in molecular crystals [109] or orientational fluctuations of a biomolecule [110] give insight into electronic and molecular dynamics unresolved in a bulk measurement.

However, single-molecule fluorescence and its variations only indirectly probe the effects of local perturbations such as external fields, intermolecular coupling, conformational states, or strain and are generally not structurally specific [111, 112, 113]. Similarly, multidimensional spectroscopy provides insight into intramolecular structure and dynamics on ultrafast timescales, yet with limited information about slower timescales, oscillator density, or real-space distribution [29].

In contrast, vibrational spectroscopy can directly probe molecular identity through characteristic spectral 'fingerprints.' Vibrational resonances can also serve as exquisitely sensitive and specific reporters of intramolecular dynamics and the local molecular environment, due to the structural specificity of normal modes and their narrow linewidth. Despite the relatively small cross section typically associated with Raman scattering, enhancement by electronic resonance and metal plasmons have enabled single-molecule vibrational spectroscopy with surface-enhanced Raman scattering (SERS) [2, 30] and tip-enhanced Raman spectroscopy (TERS) [31, 32]. The high sensitivity and spatial resolution of TERS enables investigation of localized chemical features and processes even in a dense and heterogeneous system [114, 115].

However, molecules may be highly mobile at room temperature, and single-molecule TERS or SERS sample and average over many adsorbate conformations. Rapid spectral fluctuations associated with different adsorbate orientations and absorption sites that occur faster than the spectral acquisition time contribute to inhomogeneous broadening similar to the ensemble averaged spectra in far-field spectroscopy [2, 33]. Recently, low temperature TERS has allowed for the spectroscopy of single-molecules in specific orientation with frozen degrees of freedom, with the intrinsic linewidth yet unresolved [116, 117]. Temperature dependent line shape measurements in SERS suggest the possibility to distinguish vibrational dephasing on the femtosecond timescale [118]. Low and variable temperature TERS would allow for the selective probing of single-molecule intramolecular vibrational coupling. However, other contributions to the spectrum from orientational motion and spectral fluctuations may also contribute to spectral lineshapes in TERS even in the limit of single-molecules.

Here, we perform cryogenic and variable temperature (90 - 300 K) TERS of malachite green (MG) with high spectral resolution. In order to understand the role of intramolecular coupling, conformational heterogeneity, dephasing, and ensemble effects we perform temperature dependent TERS to observe thermally activated broadening. At low temperatures, we observe intensity fluctuations on the seconds timescale that are both correlated and anti-correlated between modes, as well as frequency fluctuations greater than the intrinsic line width. We attribute these fluctuations to rotational motion and dynamic changes in the local environment of a single-molecule. We demonstrate that at the small-ensemble or single-molecule limit, temperature dependent line shape and time dependent spectral fluctuations are intrinsically linked through multi-timescale dynamic interactions.

3.1.2 Experiment

Fig. 3.1a shows a schematic of our cryogenic TERS setup. A flow cryostat (ST 500, Janis) with vacuum chamber is pumped by a turbo-molecular pump to a base pressure of $< 10^{-6}$ mbar. The sample is held by a round copper block (3 mm diameter) with K-type thermocouple. A cold finger cools the sample to a minimum temperature of 90 K through an oxygen-free high conductivity (OFHC) copper braid connected to liquid nitrogen cryostat.

Temperature is controlled (Model 331 cryogenic temperature controller, Lake Shore Cryotronics) with a resistive heater and K-type thermocouple up to 300 K with a stability of better than 0.1 K.

Au tips are etched electrochemically [119] with $\sim$10 nm apex radius. A shear-force atomic

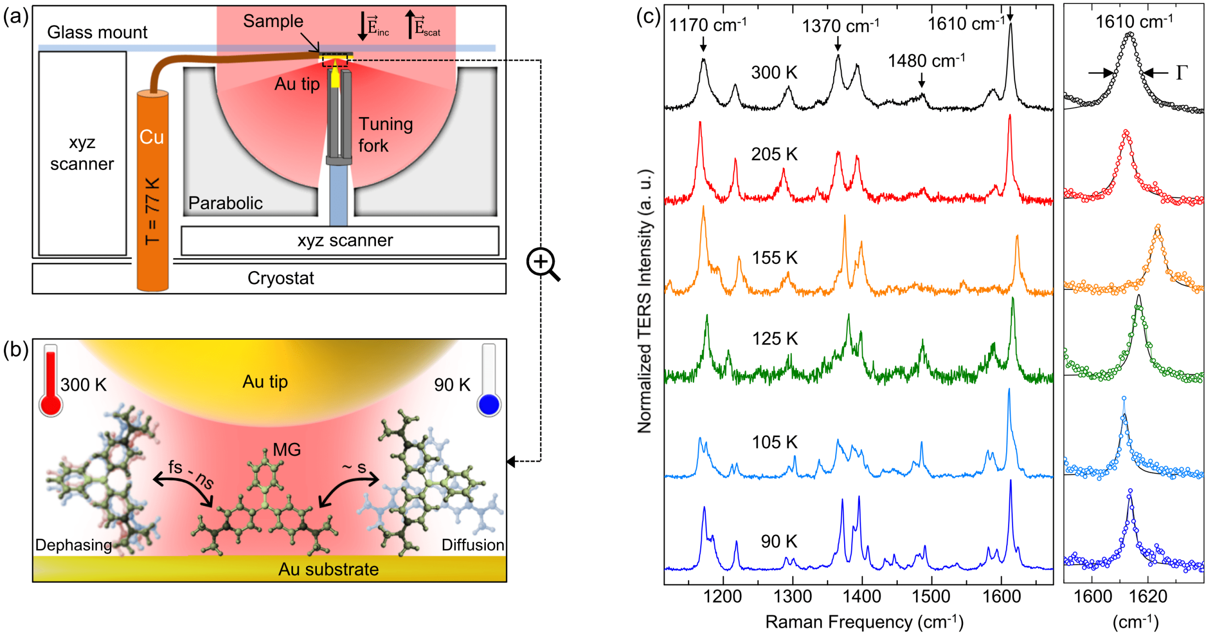

Figure 3.1: (a) Schematic of the cryogenic TERS experiment. Incident laser (E_{inc}) is focused onto the apex of an etched Au AFM tip and Raman signal (E_{scat}) is collected by a parabolic mirror in a back scattering geometry. (b) Illustration of the Au tip-Au substrate junction showing molecular motions of malachite green (MG) with characteristic vibrational signatures at different temperatures. (c) Temperature dependent TERS spectra of MG. Spectra are background subtracted and intensity normalized. Lorentzian line fit analysis of the N-C stretch mode at 1610 cm^{-1} as an example (Right graph of (c), narrowest spectra are selected (Acquisition times: 1-10 s) from full data set apart from spectra of Fig. 3.1c, additional fits shown in Fig. 3.6b in Additional results and discussion section).

force microscope (AFM) based on quartz tuning fork drives the tips at their resonance frequency ($\sim$ 32 kHz) with a dither amplitude of <0.1 nm [120]. Amplitude of the tuning fork in shear-force contact with the sample provides feedback to maintain the tip at a constant tip-sample distance of 1-2 nm [121]. Sample drift for an equilibrated sample at 90 K is observed to be < 1 nm/min. The sample holder is mounted to a glass plate that is attached to a piezoelectric transducer (PZT, Attocube) for xyz sample scanning. AFM operation and tip positioning are controlled by a digital AFM controller (R9, RHK Technology) with a stepper motor (MX25, Mechonics) for coarse positioning.

The tip and sample are positioned in the center of a custom 25 mm parabolic mirror (PM), Ag coated, focal length = 12 mm, and N.A. = 1.0 [122, 123]. A Helium-Neon laser (632.8 nm, P

< 0.3 mW) and liquid-crystal based polarization converter (ARCoptix) provide a radial polarized incident beam [124] aligned with respect to the PM and focused onto the tip apex, with a measured spot size of radius 1 μm.

At the excitation wavelength of 632.8 nm (1.96 eV) MG undergoes a resonance Raman scattering through an electronic transition of the π-conjugated backbone. The tip-sample coupling is enhanced through localized dipole-dipole interaction between plasmonic tip and metallic substrate [32]. Raman signal is collected in the back scattered direction, passed through a long-pass filter (633 nm cut-off) and focused onto the slit of a spectrometer (f=500 mm, SpectraPro 500i, Princeton Instruments) with a LN_2 cooled charge-coupled device (CCD, Spec-10 LN/100BR, Princeton Instruments). Far-field micro-Raman is measured using the same experimental setup with the AFM tip retracted several hundred μm from the sample. The spectrometer is calibrated using hydrogen and mercury lines, with measured spectral resolution of 1.2 cm^{-1} using a 1200 groove/mm grating. Experimental assignments of vibrational modes are made by comparison with DFT calculations using Gaussian98 at the RB3LYP\6-31G(d,p) level.

TERS measurements are performed in a three step procedure. First, laser beam and sample are positioned and aligned for optimal focus on the sample surface. Second, after retracting the sample, the tip is moved into the focus of the laser beam. Lastly, the sample is brought into shear-force AFM feedback for TERS measurements.

The MG sample is prepared by spin coating from an ethanol solution on a 100 nm thick Si-template stripped Au layer (surface rms roughness < 0.5 nm) at a rate of 3000 rpm for 2 minutes. Coverage is calibrated by measuring the visible absorption (Cary 500 Scan UV-Vis-NIR spectrophotometer) of reference samples spin-coated onto glass and calculating coverage from the known optical cross section of MG and monolayer density of 1 molecule nm^{-2} (see Fig. 3.5a in Additional results and discussion section). For the far-field micro-Raman reference measurements, $\sim$0.14 monolayer (ML) sample coverage is used, for the TERS measurements we use $\sim$0.006 ML coverage. Based on this calculation, we probe 4×10^5 MG molecules within the measured micro-Raman spot size of radius 1 μm. In contrast, an AFM tip with radius 10 nm probes an average of

~1–2 molecules in TERS, enabling routine few molecule sub-ensemble measurements. TERS measurements confirm a similarly low surface coverage. TERS signal only occurs at sparsely distributed sample locations, corresponding to less than 10% of locations a 90 K. Assuming molecules are distributed individually or sometimes clustered, single-molecule spectra are possible at this coverage, and approximately a third of spectra at 90 K show the fluctuations associated with single-molecule response in time-series measurements.

3.1.3 Results

We perform cryogenic and variable temperature TERS of MG adsorbed on a flat template stripped Au substrate, using electrochemically etched Au tips with ~10 nm apex radius and high spectral resolution (~1.2 cm^{-1}) in a high vacuum environment as shown in Fig. 3.1a-b. A sparse sub-monolayer coverage enables investigation of small clusters and single-molecules. We compare TERS with far-field Raman spectroscopy (micro-Raman) at each temperature.

Fig. 3.1c shows TERS spectra of sub-monolayer MG in the frequency range 1125-1625 cm^{-1} (full spectrum in Fig. 3.6a in Additional results and discussion section) acquired at different temperatures. At 300 K we observe broad peaks with a line width of 10-20 cm^{-1} full width at half maximum, in agreement with previous room temperature TERS [125]. These peaks result from the spectrally unresolved superposition of inhomogeneously and thermally broadened Raman active vibrational modes. The signal emerges from the only a few molecule within the nanoscale sample volume (average of ~1–2 molecules) as calculated from the near-field spatial localization and surface MG density. TERS line widths are systematically smaller than the ensemble measurements using micro-Raman. The micro-Raman ensemble measurement of a heterogeneous system shows significantly broader line shapes at all temperatures due to inhomogeneous broadening from the ensemble average over $\sim 4 \times 10^5$ molecules. In contrast, TERS spectra contain inhomogeneous broadening contributions from the range of conformations and adsorption sites sampled by a small ensemble of molecules [126].

Shown in Fig. 3.1c, the initially broad peaks narrow with decreasing temperature, and several

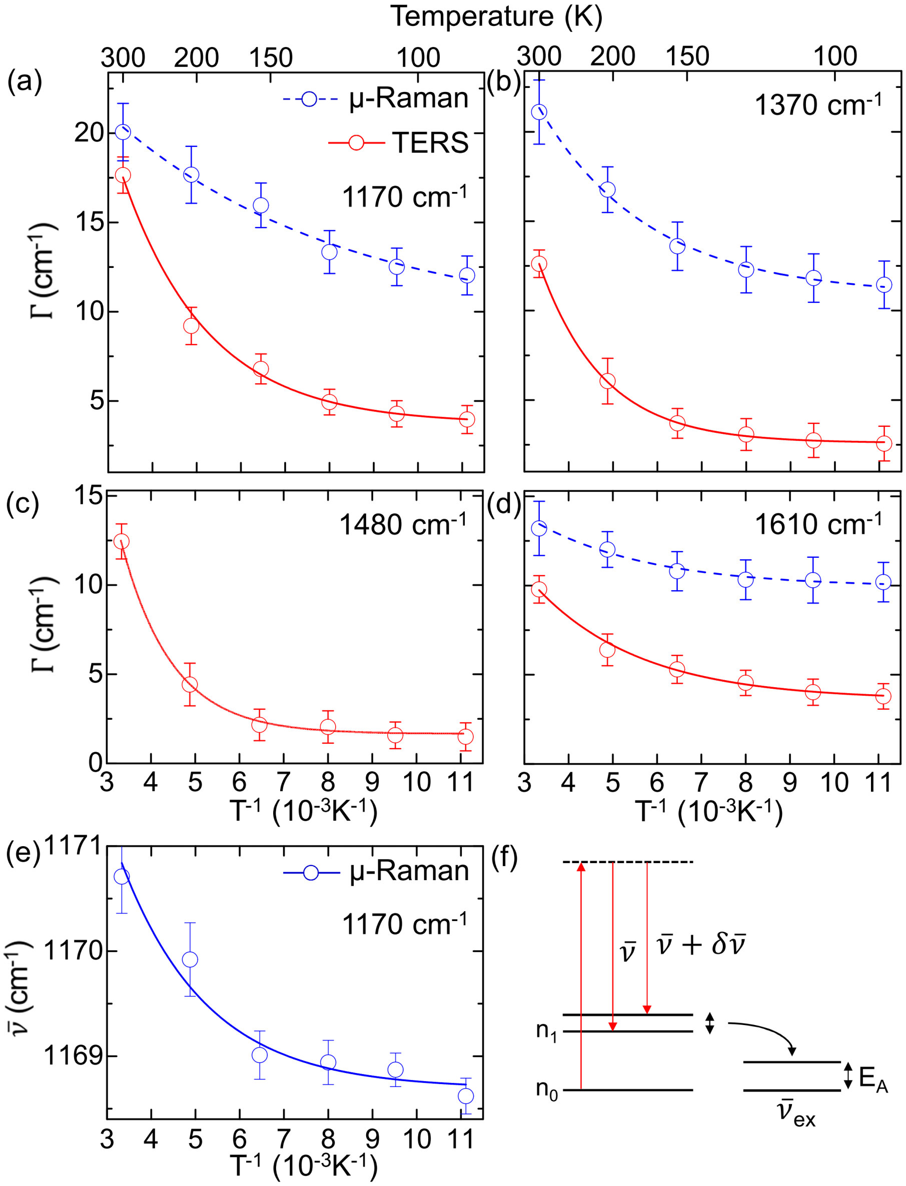

Figure 3.2: Temperature dependent TERS and micro-Raman line width $\Gamma(T)$ (a, b, c, d), and micro-Raman center frequency $\bar{\nu}(T)$ (e) with corresponding exponential fits. (f) Energy diagram of an energy exchange model for vibrational dephasing. A vibrational mode with ground state n_0 and excited state n_1 is coupled to an exchange mode $\bar{\nu}_{ex}$. Dephasing is caused by instantaneous changes $\delta\nu$ of the vibrational Raman frequency $\bar{\nu}$.

of them split, revealing a number of additional modes. At 90 K, narrow line widths allow for the full identification of the normal modes and symmetries of each TERS peak (see Fig. 3.6a in Additional results and discussion section), as otherwise obscured at room temperature. Within the spectral range shown, we assign selected peaks of characteristic normal modes based on density functional theory (DFT) calculations, including C-H in-plane bends (1170 cm^{-1}) and twists (1370 cm^{-1}), bending of the methyl group (1480 cm^{-1}), and an N-C stretching mode (1610 cm^{-1}).

In order to gain insight into the underlying mechanisms, we analyze the temperature dependence of vibrational line widths $\Gamma(T)$ and resonance frequencies $\bar{\nu}(T)$. Fig. 3.2 shows the results for the four selected modes both from TERS and micro-Raman spectroscopy. The line widths $\Gamma(T)$ and uncertainties have been extracted from a Lorentzian line fit analysis (shown in right graph of (c) and Fig. 3.6b in Additional results and discussion section). Since the narrowest peaks are selected from the fluctuating spectra in the time domain, we can select a homogeneous sub-ensemble and thus eliminate heterogeneity otherwise observed in an ensemble measurement [127].

At room temperature, TERS line widths are 2-8 cm^{-1} narrower compared to the line width obtained with micro-Raman, while at 90 K TERS line widths are 6-10 cm^{-1} less than micro-Raman. As an example, the micro-Raman line width of the 1170 cm^{-1} C-H bend narrows only by a factor of 2, from 20 cm^{-1} at 300 K to 12 cm^{-1} at 90 K (Fig. 3.2a) In contrast, the same 1170 cm^{-1} mode measured by TERS narrows by a factor of $\sim$5 over the same temperature range, from 18 cm^{-1} to 3.5 cm^{-1}.

Temperature dependence of the line width is found to follow an Arrhenius behavior. Fig. 3.2a-d shows fits for $\Gamma(T) = \Gamma_0 + A \cdot e^{-E_A/k_b T}$. Fit parameters for activation energy E_A, zero temperature line width Γ_0, and prefactor A from TERS are summarized in Table 3.1.3 (the corresponding micro-Raman results can be found in Table S1). The fitted values obtained for E_A (290-590 cm^{-1}) and A (25-180 cm^{-1}) in TERS are larger than micro-Raman, discussed in detail below.

Accompanying the decreasing line widths, the center frequencies of several modes are found to continuously red-shift with decreasing temperature in micro-Raman. As an example, Fig. 3.2e shows the temperature dependence of the micro-Raman center frequency $\bar{\nu}_F(T)$ of the 1170 cm^{-1} mode with E_A=270±80 cm^{-1}. However, as seen in Fig. 3.1c, center frequencies in TERS typically do not shift in a systematic fashion at low temperatures. While TERS spectra at room temperature are reproducible across the sample and between repeated measurements, low temperature TERS spectra do not have a reproducible center frequency due to inhomogeneity between small sub-ensembles.

Following established procedures derived from early dephasing studies in vibrational spectroscopy, we model the temperature dependent line widths as vibrational dephasing resulting from coupling $\delta\bar{\nu}$ to the thermal bath [128]. An exchange coupling model, illustrated in Fig. 3.2f, approximates system-bath coupling as mediated primarily through a low energy vibrational exchange mode expressed as $\bar{\nu}_{ex}$ [129, 130, 131, 132].

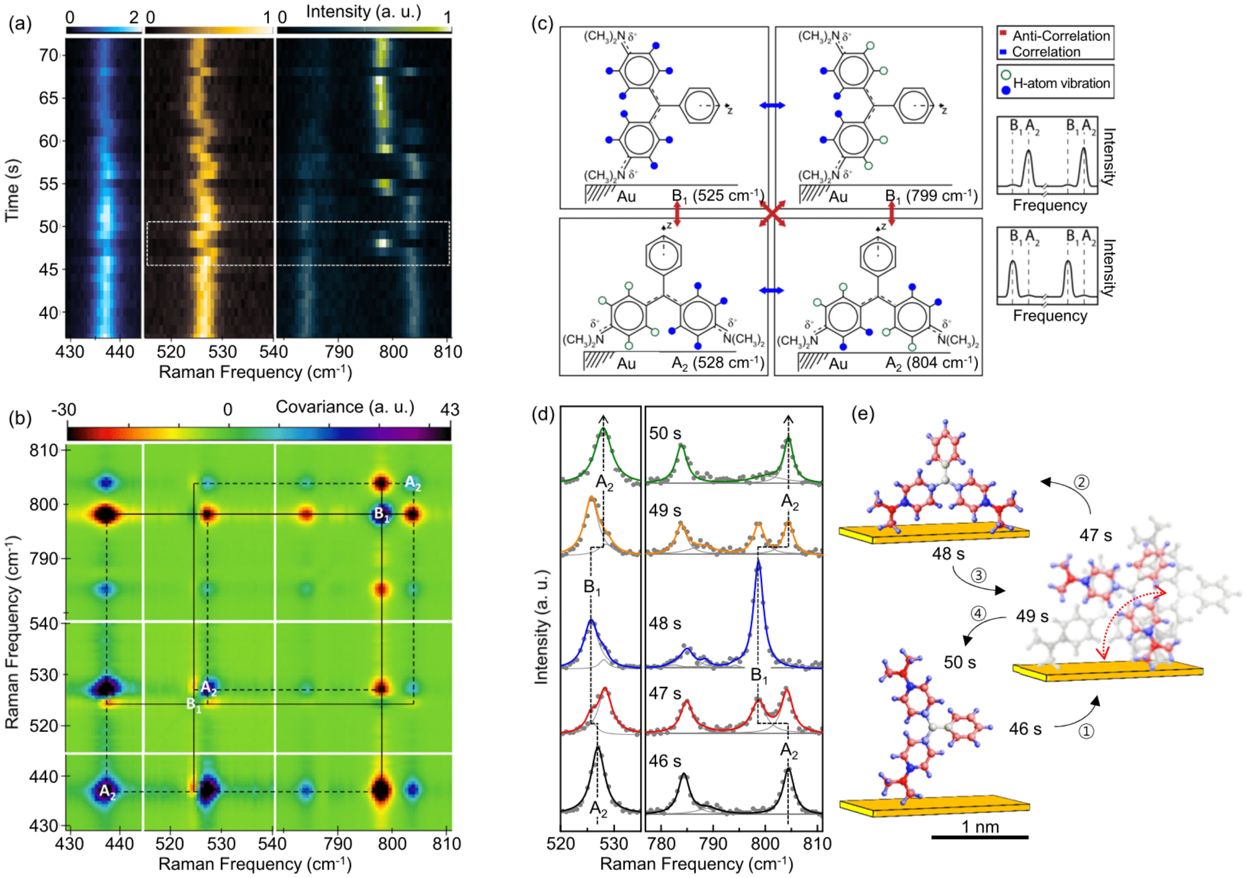

Figure 3.3: (a) Time-series contour plot of 90 K TERS spectra showing spectral fluctuations (For full spectral and temporal data set, see Fig. 3.8a in Additional results and discussion section). (b) Corresponding covariance map of Raman intensities from (a). (c) Symmetry assignment of the four principle vibrational modes, with molecule shown in the orientation in which A_2 or B_1 modes are forbidden, respectively. (Anti-) Correlations from (b) are indicated by red and blue arrows. The C-H out-of-plane bending modes are highlighted by green and blue circles. (d) Subset of time-series spectra (dots), from the region indicated by the dashed box in (a), with Lorentzian fits (solid) exhibit alternating appearance of peaks at 525 and 799 cm^{-1} (B_1) versus 528 and 804 cm^{-1} (A_2). (e) Corresponding molecular orientations at each time slice determined by mode symmetry.

Peak (cm^{-1})	E_A (cm^{-1})	Γ_0 (cm^{-1})	A (cm^{-1})
$\bar{\nu}(1610)$	290 ± 40	3.5 ± 0.4	25 ± 6
$\bar{\nu}(1480)$	590 ± 60	1.5 ± 0.2	180 ± 40
$\bar{\nu}(1370)$	480 ± 20	2.6 ± 0.2	98 ± 8
$\bar{\nu}(1170)$	360 ± 40	3.7 ± 0.6	77 ± 20

Peak (cm^{-1})	E_A (cm^{-1})	$\bar{\nu}_0$ (cm^{-1})	A (cm^{-1})
$\bar{\nu}_F(1170)$	270 ± 80	1168.5 ± 0.2	10 ± 4

Table 3.1: Results from Arrhenius fits to the temperature dependent TERS line width $\Gamma(T)$ for four selected peaks over the temperature range 90-300 K (Top). Corresponding fits to the variation in center frequency $\bar{\nu}_F(T)$ measured by micro-Raman spectroscopy for the 1170 cm^{-1} mode (Bottom).

In the perturbative coupling regime, temperature dependent line width $\Gamma(T)$ and shift in resonance frequency $\Delta\bar{\nu}(T)$ can be expressed as [129]:

$$\Gamma(T) = \Gamma_0 + \frac{(\delta\bar{\nu})^2\tau}{1+(\delta\bar{\nu})^2\tau^2}\exp\left(-\frac{E_A}{kT}\right), \text{ and} \tag{3.1}$$

$$\Delta\bar{\nu}(T) = \frac{\delta\bar{\nu}}{1+(\delta\bar{\nu})^2\tau^2}\exp\left(-\frac{E_A}{kT}\right). \tag{3.2}$$

An Arrhenius temperature dependence arises from the energy E_A associated with the vibrational exchange mode $\bar{\nu}_{ex}$. The observed $\Gamma(T)$ and $\Delta\bar{\nu}(T)$ depend on the exchange coupling strength $\delta\bar{\nu}$ and the lifetime τ of the exchange mode. TERS measurements of $\bar{\nu}(T)$ shift randomly for each sub-ensemble measurement at lower temperatures, and $\Delta\bar{\nu}(T)$ is measured using micro-Raman following established procedures [118]. From the combination of equations (3.1) and (3.2), $\delta\bar{\nu}$ and τ can be estimated [133]. For the 1170 cm^{-1} mode, we find $\delta\bar{\nu}$ =110±50 cm^{-1} and τ =80±20 fs.

TERS spectra at low temperatures exhibit fluctuations in both intensity and frequency of individual peaks between subsequent measurements or even between subsequent spectra in time-series acquisitions. Shown in Fig. 3.3a, we collect time series spectra with high spectral resolution and acquisition times of 1 s (the full data set is shown in Fig. 3.8a in Additional results and discussion section). The high vacuum and low temperature of 90 K allows for measurements times of several minutes without bleaching. As visible in Fig. 3.9a in Additional results and discussion section, while some peaks maintain constant frequency such as the 580 cm^{-1} mode, several other peaks near 525 and 800 cm^{-1} fluctuate between discrete spectral positions.

From the full data set (Fig. 3.8a in Additional results and discussion section), we calculate the covariance $\sigma(i,j)$ between frequencies i and j from the TERS intensities $I(i,t)$ during short time segments t_1 to t_2 using

$$\sigma(i,j) = \frac{1}{N}\sum_{t=t_1}^{t_n}[I(i,t) - \langle I(i)\rangle] \times [I(j,t) - \langle I(j)\rangle]. \tag{3.3}$$

The resulting covariance map from the time range 37-72 s is shown in Fig. 3.3b, with additional time periods shown in Fig. 3.10b-d in Additional results and discussion section. Fluctuations in the total Raman intensity, e.g., from changes in tip-enhancement give rise to an offset with all Raman active modes, appearing as correlated (positive value, blue) on the diagonal. In contrast, off-diagonal features are signatures of mode intensity correlations and anti-correlations (negative value, red). As can be seen, both correlated (blue) and anti-correlated (red) behavior are seen between specific modes.

Fig. 3.3d shows the anti-correlation in the time domain in a subset of consecutive spectra from the time series data (indicated by the dashed area in Fig. 3.3a). We find that modes of particular symmetries are suppressed in individual spectra. Adjacent peaks at 525 and 528 cm^{-1} and 799 and 804 cm^{-1} respectively appear and disappear in an anti-correlated manner. Within the same time-series data, several other MG vibrational modes appear to remain constant in frequency and do not undergo blinking, including the mode at 580 cm^{-1}. From the mode assignment based on DFT, we thus conclude that the appearance of modes of A_2 or B_1 symmetry are mutually exclusive and thus anti-correlated (see 46, 48, and 50 s spectra), except for rare transition events (spectra at 47 and 49 s). In contrast, modes of identical symmetries are correlated, e.g., the 525 and 799 cm^{-1} B_1 symmetry modes.

We model time dependent intensity fluctuations and spectral (anti-)correlations through the tensor polarizability of surface or tip enhanced resonant Raman. Using selection rules developed for surface enhanced resonant Raman spectroscopy, it is possible to assign molecular orientation. In resonant Raman, Franck-Condon enhancement enhances fully symmetric modes, while vibronic (Herzberg-Teller) coupling additionally enhances non-totally symmetric modes and contributes significantly to the observed spectrum when the exciting optical frequency approaches a molecular electronic resonance [134, 135, 136]. Near a metal surface, surface plasmon resonances further enhance the signal [137, 138]. Coupling between vibrations, molecular resonances and the metal substrate introduce more complex selection rules, which can be expressed as $\langle I|\mu^{\sigma}|K\rangle\langle K|\mu^{\rho}|F\rangle\langle F|\, V_{eN}/\,Q_k|\mathrm{I}\rangle$ [135]. Here I, F, and K are initial state, charge transfer state, and excited molecular state, with associated dipole operators for the molecular μ^{σ}, charge transfer μ^{ρ}, and vibronic $V_{eN}/\,Q_k$ coupling. The molecular vibration, molecular electronic resonance and metal substrate thus each contribute to the observed intensity.

For a surface adsorbed molecule, the molecular symmetry is reduced and plasmonic enhancement of modes with particular symmetry can lead to surface selection rules based on molecular orientation [139, 140, 141, 142, 135]. Enhancement or suppression of vibronically enhanced modes in many cases can be used to determine molecular orientation on the surface [140, 141, 143, 144]. For aromatic molecules with $C_{2\nu}$ symmetry such as MG, the A_2, B_1, and B_2 modes are expected to be suppressed (Fig. 3.3c) with the molecular z-axis normal to the surface, z-axis parallel to the surface and aromatic plane normal to the surface, and aromatic plane parallel to the surface, respectively.

Orthonormal vibrational modes are mutually exclusive within a single-molecule or oriented cluster and necessarily appear anti-correlated with time-varying molecular orientation. Following the selection rules observed previously [140, 144], we can assign anti-correlation between modes with A_2 and B_1 symmetries to rotational motion of an adsorbed MG molecule. Details of the coupling to both the surface plasmon and molecular electronic state at the excitation wavelengths may affect the orientational assignment of the molecule, though this is unlikely to affect orthogonality of Raman modes and the resulting anti-correlated fluctuations during rotation.

Fig. 3.3d shows the anti-correlation in the time domain in a subset of consecutive spectra from the time series data (indicated by the dashed area in Fig. 3.3a). Frequency correlation of the time series, defined as normalized covariance $\chi_{ij} = \sigma_{ij}/(\sigma_{ii}\sigma_{jj})$, (Fig. 3.10a in Additional results and discussion section) shows a frequency correlation of 0.6 to -1, while modes with the same symmetry have a correlation of +0.8 to +1 for different spectral regions and time-series, closely matching the idealized (anti-)correlations of -1 and +1 [145, 146]. Similarly, fully symmetric (A_1) modes are positively correlated with all other modes. While small intensity fluctuations would also be possible in time-series measurement of a tip wandering across small clusters of molecules, we observe much larger fluctuations. Individual modes in Fig. 3.3d have intensities which fluctuate discretely between maximum and zero intensity, indicating single-molecule spectra are observed within the time-series.

Although enhancement by electronic coupling may affect the determination of the absolute orientation and angles of rotation, the mechanism of rotation based upon ground-state DFT calcuations is commensurate with our observations. Alternating enhancement between modes can occur as the molecule rotates in a pinwheel fashion with the aromatic plane tilted up from the surface and the phenyl moiety pointing either normal or parallel to the surface as illustrated in Fig. 3.3e.

Additionally, from the studies of a larger time window, spectral fluctuations are observed in the form of frequency shifts. As an example, Fig. 3.4a shows a selection of TERS spectra with short averaging times collected over a 209 s time series, with the full data set shown in Fig. 3.8a in Additional results and discussion section. As can be seen, individual spectra have line widths significantly narrower than the far-field Raman spectrum, yet the sum of TERS spectra approaches the micro-Raman line shape, which ensemble averages over the spectral fluctuations and rotational dynamics.

Fig. 3.4b shows covariance plots of the 780-810 cm^{-1} region for four short segments within the long 209 s time-series (see Fig. 3.10b-d in Additional results and discussion section). Hydrogen out-of-plane bending modes with A_2 and B_1 symmetry show anti-correlated fluctuations during each of the first three time segments. In the final 135-203 s period only a single mode is observed and the molecule appears to remain fixed. Between the time segments, each of the hydrogen out-of-plane modes of A_2 and B_1 symmetry shift by a few cm^{-1}. In contrast, during this same time period of 209 s, several modes with fully symmetric A_1 character remain at nearly constant frequency throughout the acquisition and do not undergo blinking. We discuss below the covariance plots

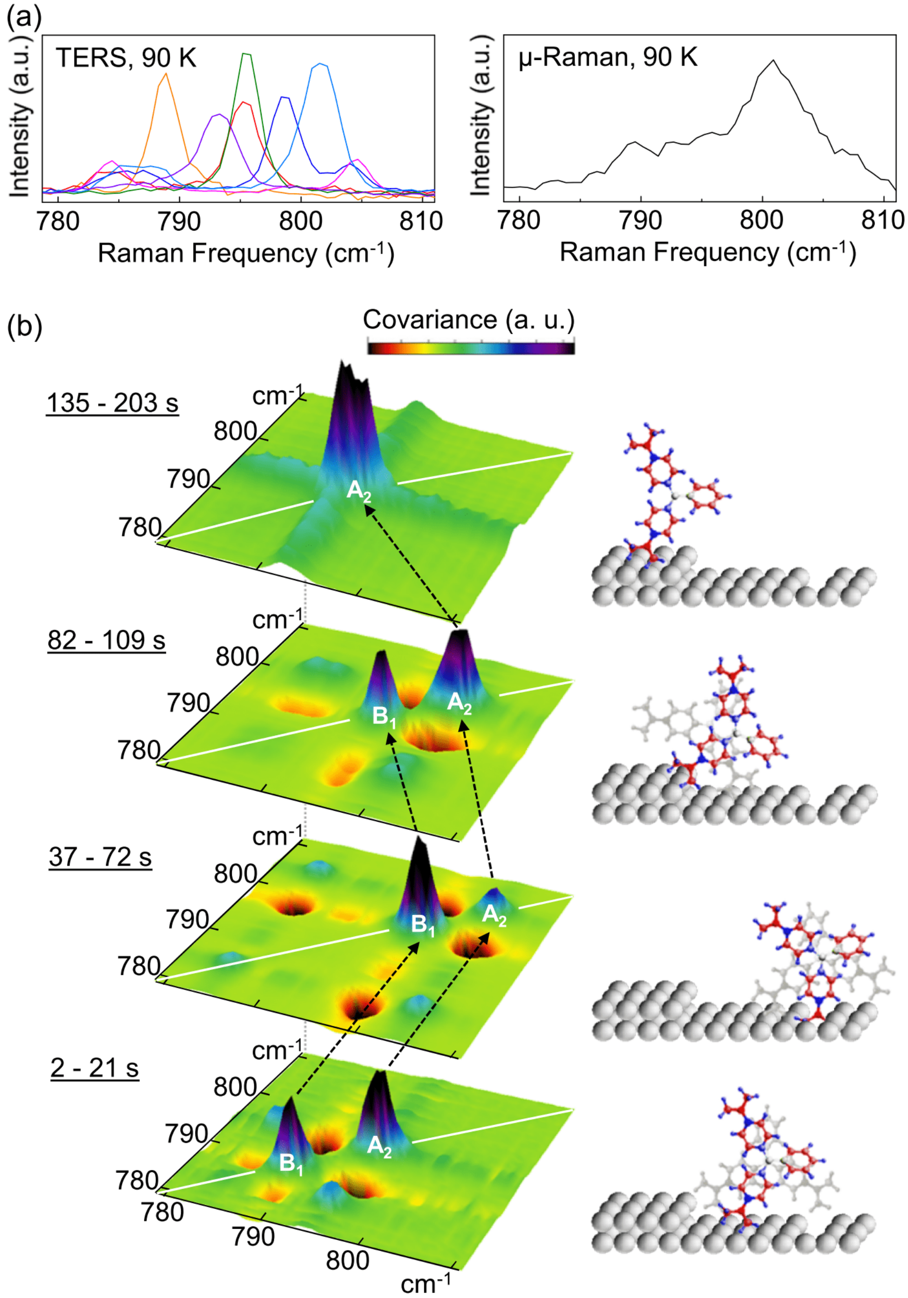

Figure 3.4: (a) Spectral fluctuations as observed in TERS spectra (left), compared with inhomogeneously broadened micro-Raman spectra (right), both at 90 K. (b) Corresponding covariance plots with assigned underlying rotational motion within each of a series of short time segments. Spectral fluctuations appear as jumps in frequency between each time segment.

of short time segments and the correlation between modes with respect to dynamics of rotational motion and spectral fluctuations.

3.1.4 Discussion

In the following we first discuss the temperature dependent spectral narrowing and frequency shifts, followed by analysis of the rotational motion and spectral fluctuations. Temperature activated spectral broadening and shifts are caused by ultrafast vibrational dephasing through intramolecular coupling to low-energy molecular modes. The correlated intensity fluctuations of particular vibrational modes directly record molecular reorientation occurring on the experimental timescale of seconds.

Intramolecular coupling

Temperature-dependent vibrational linewidths range from 20 cm^{-1} for micro-Raman at 300 K to 1.5 cm^{-1} for TERS 90 K, which agree with typical experimental values [147, 148]. Similarly TERS measurements of Γ_0 ranging from 1.5 to 3.5 cm^{-1} compare well with typical values for molecular systems [149].

The observed activated temperature dependence of both narrowing and frequency shifting of the peaks is characteristic of vibrational dephasing. Several studies of molecular materials have observed exchange coupling to low energy intra- or intermolecular vibrations, frustrated rotations, or translations [150, 133, 151], and they have been attributed to substrate modes in temperature-dependent SERS [118]. The four vibrational modes analyzed in Table 3.1.3 exhibit values of E_A corresponding to specific frequencies ranging from 270 to 590 cm^{-1}. A number of low energy torsions of MG are available near the observed E_A, which are more likely exchange modes than phonons of Au because the measured E_A exceeds the highest optical phonon band of Au of $\leq$160 cm^{-1} [152]. The derived coupling strength $\delta\bar{\nu}$ $\simeq$110 cm^{-1} falls within the range of values expected for intramolecular coupling, though it is somewhat larger than observed in previous investigations of vibrational exchange [129, 131] or calculations of typical anharmonic coupling [153].

Temperature dependent TERS must be treated as an upper bound measurement of narrowing and dephasing by anharmonic coupling and exchange mode dephasing. Typically, temperature dependent homogeneous broadening is measured in highly crystalline samples [133] or using line-narrowing time-domain spectroscopies [154]. Single-molecule vibrational spectroscopy has been proposed as an alternative measurement of the homogeneous line width [118, 155], yet this assertion relies on the assumption of a stationary molecule within a well-defined local environment. TERS spectra of even a single-molecule at room temperature are broadened due to rapid frequency fluctuations faster than the integration time of the measurement. For a small ensemble measurement, broadening at high temperatures contains contributions from both femtosecond vibrational dephasing and slower dynamics such that E_A and A are overestimated by the exchange coupling model.

Within the spectral acquisition time, a small ensemble and even single-molecules explore a large phase space and many local environments, such that the line width approaches the micro-Raman ensemble measurement. At 90 K, we observe that molecular motion slows to a timescale observable with the fast 1 s acquisition time, yet at 300 K, the fluctuations in the local chemical environment occur too rapidly and contribute to line broadening. As seen in Fig. 3.4a, a series of 90 K TERS spectra collected with short acquisition times over the course of 209 s have narrow line widths comparable to the expected homogeneous line widths.

Single-molecule motion

With longer acquisition times or at higher temperature, individual acquisitions integrate over rapid fluctuations and broadening is observed similar to the spatial integration and ensemble broadening in far-field micro-Raman. We attribute these frequency fluctuations to two types of dynamic processes, discussed below, rotation of the molecule relative to the surface, and time-dependent changes in the local chemical environment. Indeed we only observe anti-correlated fluctuations on the 1 s timescales of spectral acquisition at 90 K. At room temperature, molecular motion occurs too rapidly, and the acquisition averages over fluctuations such that the spectrum cannot be distinguished from an ensemble measurement.

Statistical analysis of fluctuating spectra through their covariance has been shown to sensitively isolate behavior of small sub-ensembles within even bulk-type experiments [156]. Anti-correlated fluctuations are often used as evidence for single-molecule spectral response in a number of single-molecule methods [157]. In TERS, fluctuations with intensity correlated between all modes have been often observed and attributed to variation in total enhancement [145]. However anti-correlated alternating Raman enhancement of one isotopologue relative to another was used to demonstrate single-molecule response [158, 159, 160]. Intensity fluctuations in isotopologues are attributed to enhancement of the full vibrational spectrum of one molecule relative to another resulting from diffusion of the tip, molecule, or localization of the field enhancement. Anti-correlated fluctuations in the TERS spectrum have also shown isomerization of a single photoswitching molecule on the apex of a TERS tip [161]. Anti-correlated fluctuations in the time-series spectra are able to resolve single-molecule isomerization even within the larger probed ensemble of a self-assembled monolayer. Similar anti-correlated frequency fluctuations of certain modes in surface enhanced Raman spectra of a lipid bilayer were attributed to single-molecule motion of a lipid within a membrane bilayer [162].

Rotational motion has been proposed to be observable through anti-correlated intensity fluctuations in modes with orthogonal polarizability tensors[145]. Recent low temperature single-molecule TERS investigations have primarily reported static molecular orientations [116]. Recently investigations have also associated fluctuations with Franck-Condon enhancement, which attributed anti-correlations between large several hundred cm^{-1} regions of the TERS spectrum to slight changes in the excited electronic state [146]. Near resonance with the molecular electronic state and near resonance with the tip plasmon, however, vibronic Herzberg-Teller enhancement can be larger than Franck-Condon enhancement [143, 163, 139], leading to our observed orientation-dependent Raman scattering from individual modes of different symmetry separated by only a few cm^{-1}.

Spectral diffusion similarly slows to timescales observable between the 1 s acquisition time and 209 s measurement time at 90 K. At several points within the time series A_2 and B_1 modes jump coincidentally and with equal frequency shifts, while other modes remain at nearly constant frequency. Coincident shifts of the A_2 and B_1 are expected, since the observed normal modes all involve C-H out of plane bending of the same atoms. Further, while a change in tip-sample geometry can affect overall enhancement, it is unlikely to play a role here because the change in enhancement only involves difference in symmetry and not the identity of normal modes. Any change in local environment or bond softening is expected to affect these modes similarly. Differences in vibrational frequency have been observed between subsequent single-molecule SERS without time-resolved measurements, which was attributed to differences in a static local environment [127]. Frequency wandering has also been observed in time-series SERS and TERS measurements, and observed motion was attributed to diffusion of liquid water [146, 162]. In vacuum at low temperature, however, frequency jumps are unlikely due to diffusion of residual liquid water and must be activated by the thermal bath. In contrast to the results obtained under atmospheric conditions, in vacuum we observe no fluctuations at room temperature and only minimal differences between repeated measurements at different locations. The disappearance of fluctuations with increasing temperature and associated increase in line width together support that frequency shifts at room temperature occur faster than the 1 s acquisition time and contribute to broadening.

Analysis of mode character and fluctuation during a time series measurement supports assignments of rotational motion and spectral fluctuations and rules out alternate explanations. Instability in the TERS probe or spectrometer can be completely ruled out because several torsional modes are stable to within ≤ 2 cm^{-1} over the same 209 s time-series (Fig. 3.9b-c in Additional results and discussion section) during which the C-H out of plane modes shift by several cm^{-1}. If the tip were to drift, enhancement of separate molecules or clusters with different adsorbate conformation could be observed similar to rotation of a single-molecule. For the sparse coverages used in our experiment, however, sample drift or photobleaching at long times only causes the disappearance of all TERS signal, as sample motion and molecular diffusion are insufficient to bring a new molecule into the TERS hotspot.

A remaining possiblity of a changing chemical enhancement through varying charge transfer between the metal and molecule could be expected to change both the enhancement of modes as well as shift frequency of vibrational modes through the Stark effect [164]. This is an unlikely explanation, however, as the tip and sample are held at ground potential. Discrete frequency switching is also possible in the case of rotation and diffusion of a small cluster in which all molecules move identically. Although we also consider this scenario unlikely, discriminating a single-molecule from two molecules moving completely in tandem is a general limitation in single-molecule spectroscopy and the possibility cannot be completely eliminated. A change in the tip-sample geometry could change the perceived angle if the field angle were to change with drift of the tip, however this is unlikely due to the stable tip-sample positions achieved at low temperatures.

The spectral fluctuations and rotational motion we observe in real-time approach the long-sought goal of measuring single-molecule local dynamics with structural sensitivity. Frequency shifts of vibrations are typically smaller than in fluorescence, yet vibrational modes are both structurally specific and typically more localized within a molecule enabling direct and quantitative investigation of the chemical environment. For a molecule experiencing dynamic fluctuations within a heterogeneous local environment, rapid diffusion can result in a signal integrated over many molecular configurations and interactions with the environment, such that the signal of even a single-molecule approaches that of an ensemble measurement. Selective detection of uncorrelated molecular motion is thus only possible in a highly controlled environment often requiring low temperatures.

Our demonstration of single-molecule dephasing, local dynamics and rotational motion using TERS has not been previously possible in room temperature [115], low but constant temperature, and/or low spectral resolution experiments [116, 117]. Diffusion is slowed from fast room temperature motions to the seconds timescale by cooling below the thermal activation energy, allowing for the observation of how the molecule dynamically samples the local energetic landscape. Because several of the anti-correlated modes are separated by $\leq$10 cm^{-1}, even static orientation may be difficult to ascertain with other methods, for example with lower spectral resolution, spatially averaged far-field Raman, or within the energetically disordered probe regions of SERS. Observation of intramolecular and conformational dynamics becomes possible through the combined high spectral resolution and single-molecule sensitivity of the experiment.

In summary, simultaneous access to disentangled intramolecular structure and dynamics, rotational motion, and spectral fluctuations has been a long-standing goal. Both single-molecule and ultrafast and multi-dimensional spectroscopies have sought to separate and distinguish dynamic components from the heterogeneity of a system to investigate structural evolution and energy flow. Using variable temperature single-molecule TERS, we obtain detailed information on these molecular scale motions even from continuous wave experiments. Here, in vibrational spectroscopy on the single-molecule level with high spectral resolution, molecular fluctuations and their correlations on multiple timescales provide the desired detailed view of molecular motions. The explored fundamental molecular properties in a heterogeneous system are integral to the performance of a variety of functional materials and devices. High resolution temperature dependent TERS opens new means and offers new insights into the intra- and inter-molecular coupling, structural, vibrational dynamics, and molecular motion.

3.1.5 Additional results and discussion

Sample preparation and characterization

Tip-enhanced Raman spectroscopy (TERS) and micro-Raman are both used to observe spectra of malachite green (MG) in sub-monolayer thin films. We calibrate adsorbate thickness using ultra-thin films prepared by spin-coating MG solutions of different concentrations onto glass microscope slides. Visible absorption spectra are measured by a UV-vis-NIR spectrophotometer (Cary 500 Varian) and calibrated by the known cross section of MG. Visible absorption spectra show a linear relationship between solution concentration and film thickness of spin-coated samples for a constant speed of 3000 rpm. Thicknesses were measured for ultrathin films between 1 monolayer and the lowest coverages measurable by UV-vis spectroscopy corresponding to ∼0.05 monolayers, shown in Fig. 3.5a. MG solution concentration for TERS was controlled to produce a coverage of ∼0.006 monolayers, corresponding to 1-2 molecules under the tip, while coverages for micro-Raman were increased to allow sufficient signal-to-noise in far-field data collection.

We characterize the tip-sample geometry by independently imaging the tip and sample. Scanning electron microscope images (Fig. 3.5c) show the expected 20 nm tip radius and a relatively smooth tip geometry for the etched Au tips. We collect high-resolution atomic force microscopy

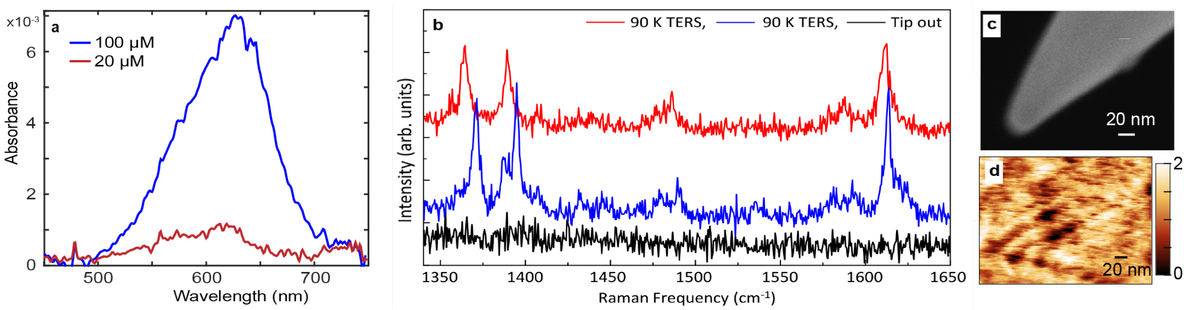

Figure 3.5: (a) UV-vis spectra of MG spin-coated on glass are used to calibrate thin-film thickness. (b) Comparison of low temperature TERS spectra at different spots. Linewidths are varied with respect to the density of molecules in the region of tip apex. (c) Scanning electron microscope image showing AFM tip geometry (d) AFM image of Au substrate imaged with a sharp tip in intermittent contact mode.

images of the sample using silicon tips (Super-Sharp Silicon, NanoWorld, 285 kHz resonance) with nominal tip radius of 2 nm, operated in intermittent contact mode. AFM images (Fig. 3.5d) show the roughness of the polycrystalline template-stripped Au. Typical RMS roughness is $\leq$0.5 nm, and the roughness shown in Fig. 3.5d is 0.35 nm, although individual grains are found to have a small lateral extent. The large area roughness of template stripped Au is also found to be small, with the range of roughness being $\leq$5 nm in a 10 μm image.

MG ultra-thin films consist of randomly distributed molecular adsorbate. In order to locate the regions which contain a small-ensemble of MG rather than larger clusters, several TERS spectra were recorded at each temperature, and the narrowest spectra at each temperature were used. Fig. 3.5b contains repeated TERS spectra at 90 K, showing the expected narrower linewidths (blue) in sub-ensemble or single-molecule spectra relative to a broader linewidth, which may result from spectra collected from a larger MG cluster. Fluctuations attributed to rotation and conformational changes discussed in the Results section were only observed in the narrowest spectra at 90 K.

Comparison between TERS and micro-Raman

Below we present a more through comparison between the temperature dependent TERS and micro-Raman spectroscopy. In order to facilitate a detailed comparison between spectral line shapes in the ensemble-averaged micro-Raman and TERS spectra, spectra for both methods are collected with the same apparatus, with the Au tip brought close to the surface or retracted, respectively. By using same excitation laser, collection optics, and detector, we minimize systematic differences between each method and maintain the spectral resolution of 1.2 cm^{-1}.

Fig. 3.6a shows a comparison between micro-Raman and TERS spectra under identical experimental conditions. Because the range of the charge-coupled device detector is less than the full frequency region of interest, spectra of the full region are collected by superimposing two overlapping spectral regions. The peaks in micro-Raman spectrum narrow when temperature decreased from 300 K to 90 K, however the TERS peaks narrow by a significantly greater amount (Fig. 3.6b). Quantitative comparison with density functional theory (DFT) calculations (bottom of Fig. 3.6a) allows assignment of vibrational modes in the 90 K TERS spectrum, which is more challenging for the micro-Raman or 300 K TERS spectra. The intensities of several Raman active modes are not accurately described by DFT. This is expected from the rotationally averaged DFT polarizability calculations, which do not account for adsorbate geometry, interactions with the substrate, electronic contributions to polarizability or intermolecular interactions in the dense sample used in micro-Raman measurements.

Temperature dependent peak positions and peak widths are measured for four peaks. Fig. 3.6b shows Lorentzian fits for each of the 1170, 1370 and 1480 cm^{-1} peaks (fits for the 1610 cm^{-1} are shown in the Results section). The narrowest spectra with 1-10 s acquisition are selected from the full data set. By selecting the spectra with minimal inhomogeneous broadening within the short acquisition time, TERS spectra are obtained from regions containing only a few or single-molecule sample volumes.

In contrast to the dramatic narrowing in low temperature TERS data, the micro-Raman spectra narrow only slightly as a function of temperature. Fig. 3.6c shows micro-Raman spectra for each temperature. Three peaks of temperature dependent micro-Raman spectra are fit to Lorentzian line shapes in the same manner as the temperature dependent TERS spectra. The peak at 1480 cm^{-1} could not be fit accurately at all temperatures in the micro-Raman spectra. Temperature dependent fits to peak position and linewidth are shown on a logarithmic Arrhenius

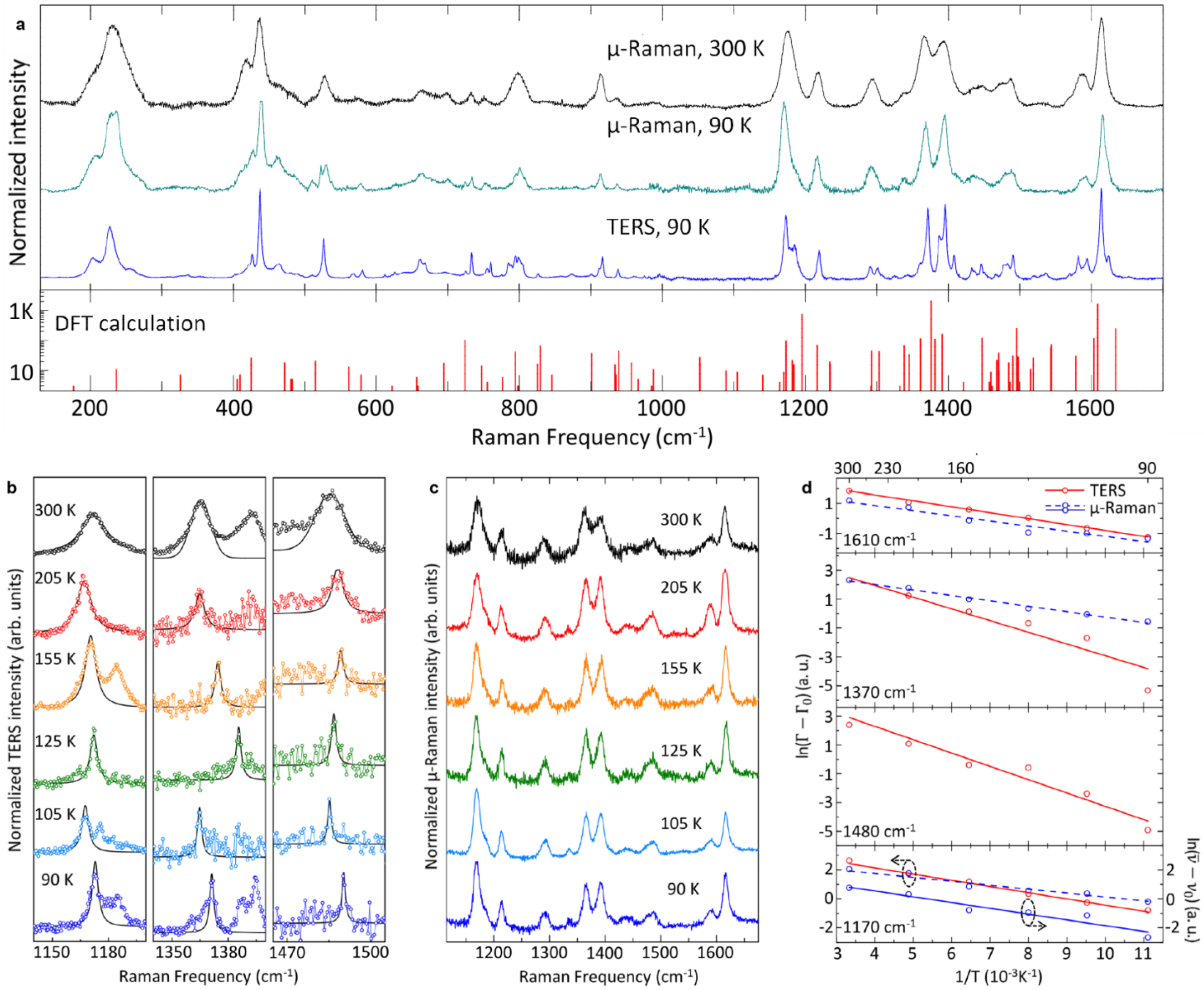

Figure 3.6: (a) Comparison between spectra: micro-Raman spectra at 300 K, micro-Raman spectra at 90 K, and TERS spectra at 90 K. Below, density functional theory calculation exhibiting predicted Raman modes over the full spectral range. (b) Lorentzian line fit analysis of the temperature dependent TERS spectra of MG exhibiting peak narrowing for the peaks at 1170, 1370, and 1480 cm^{-1}. Lorentzian fits for the peak at 1610 cm^{-1} are shown in Fig. 3.1c. (c) Temperature dependent micro-Raman spectra. Spectra are background subtracted and intensity normalized. (d) Arrhenius plot of $\ln(\Gamma(T) - \Gamma_0)$ and $\ln(\bar{\nu}(T) - \bar{\nu}_0)$ versus $1/T$. Data are identical to the exponential graphs shown in Fig. 3.2.

plot in Fig. 3.6d and a linear plot in Fig. 3.2 of the Results section. Exponential temperature dependence of $\ln(\Gamma - \Gamma_0)$ is seen more clearly in the linear fits of Fig. 3.6d, although both plots quantitatively fit the same values.

Fitting results for temperature-dependent miro-Raman are summarized in Table 3.1.5. Comparison of the micro-Raman to TERS fits reveal different temperature dependence. The activation

Peak (cm^{-1})	E_A (cm^{-1})	Γ_0 (cm^{-1})	A (cm^{-1})
$\nu(1610)$	270 ± 60	9.9 ± 0.3	12 ± 3
$\nu(1370)$	280 ± 30	10.8 ± 0.3	39 ± 5
$\nu(1170)$	120 ± 40	8.5 ± 0.9	20 ± 1

Table 3.2: Results from Arrhenius fits to the temperature dependent micro-Raman linewidth $\Gamma(T)$ for three selected peaks over the temperature range 90-300 K.

energy E_A and prefactor A in micro-Raman are much smaller than TERS, while the Γ_0 is 3-5 times wider in micro-Raman. Inhomogeneously broadened peaks can contain multiple unresolved modes at nearby frequencies, and narrowing of individual modes can be masked by the presence of the multiple modes or by heterogeneity greater than the homogeneous linewidth. Micro-Raman spectroscopy is thus considered inadequate and is found to underestimate E_A and $\delta\bar{\nu}(T)$.

Low temperature rotational motion and spectral fluctuations

At room temperature, fast molecular motions blur the spectral signatures of motion for even a single molecule. At cryogenic temperatures, rotational motion and spectral fluctuations are slowed to the timescale of seconds.

Fig. 3.7a shows TERS spectra repeatedly collected at each temperature between 300 K and 90 K with acquisition times $\geq$20 s. Between the measurements, the tip is retracted several μm and brought back in to a different location on the sample. At 300 K and 255 K thermally broadened peaks are well reproduced by repeated TERS measurements, while at 155-90 K individual peaks appear to shift in a random manner between the acquisitions. Spectral fluctuations at room temperature occurs faster than the timescale of the spectral acquisition, resulting in the appearance of inhomogeneously broadened peaks even from a small sample volume. In contrast, slowed or frozen spectral fluctuations appears as an inhomogeneity across the sample and between spectral acquisitions, which we observe as heterogeneity between spectral acquisitions only at low temperatures. Under the conditions investigated, however, TERS spectra of the high frequency region with short acquisition times of 1 s, shown in Fig. 3.7b were not observed to fluctuate significantly in either intensity or frequency.

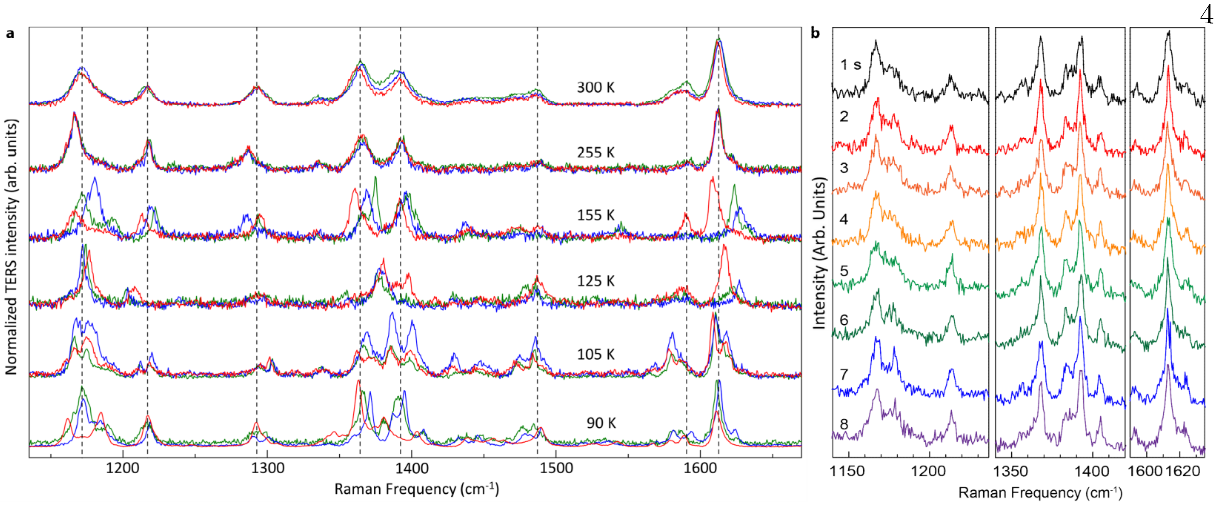

Figure 3.7: (a) Repeated TERS spectra of MG taken at each temperature in the region 90-300 K. Sample inhomogeneity and spectral fluctuations result in significant variation in peak position between the macroscopic areas of the sample. Spectra from different TERS acquisitions under identical sample conditions are identified by color (red, green, blue) and offset to distinguish spectra collected at different temperatures. (b) Time-series TERS spectra at 90 K in the high frequency region with 1 s integration times. TERS spectra of this frequency range were not observed to fluctuate under the conditions used.

In contrast to the high frequency region, low temperature TERS of the low frequency region show significant fluctuations of certain peaks, as discussed in relation to Fig. 3.3-3.4. We present additional data of the low frequency region, with the full time-series collected over 209 s shown in Fig. 3.8a. Fluctuations in total intensity and fluorescence background are observed in addition to fluctuations in intensity of individual modes. Zoomed-in spectra are shown (right of Fig. 3.8a) from the areas indicated by red, yellow, and green dashed boxes. Time-series spectra over the full time range show both the anti-correlated intensity fluctuations associated with rotational motion as well as the slower spectral fluctuations. Covariance plots shown in Fig. 3.3b and Fig. 3.4b of the Results section are taken from the regions indicated by white dotted areas in Fig. 3.4a.

The peak positions of near ∼435, ∼525, and ∼800 cm^{-1} shift by several cm^{-1} between each of the short time segments. Fig. 3.4b shows TERS spectra integrated over each of these time segments. Since the frequencies of a number of modes shift coincidently, quantitative peak assignment is still possible by comparing the full TERS spectrum with calculated DFT Raman frequencies (bottom).

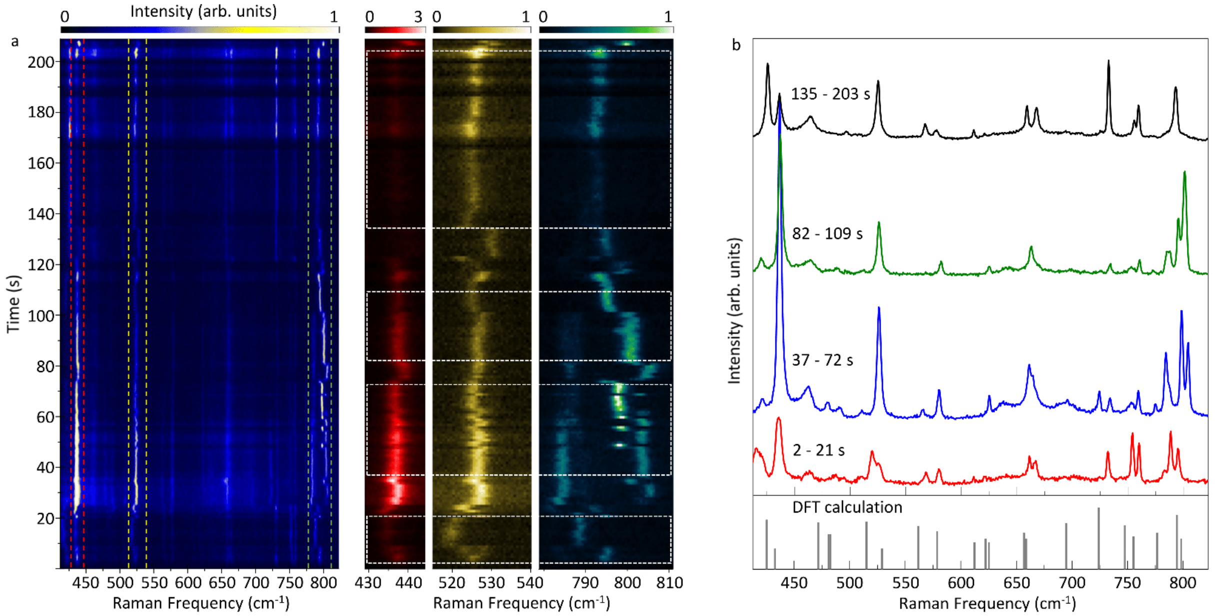

Figure 3.8: (a) Time-series TERS spectra taken at 1 s intervals, showing the full acquisition time of 209 s and full range of the spectrometer. Right, zoomed-in regions showing both rotational motion and spectral fluctuations over the full time-series. (b) TERS spectra averaged over short time integrals from the time-series data compared with DFT calculated normal modes (Bottom).

Only certain modes are observed to shift between different frequencies. Fig. 3.9a shows fits to several peaks which alternate in intensity (525 versus 528 cm^{-1} and 799 versus 804 cm^{-1}). Over the same time period, the mode at 580 cm^{-1} with A_1 symmetry assignment shifts only slightly in frequency and does not undergo blinking during the frequency jumps. Fig. 3.9b-c show two peaks which show similar behavior over this same time period. The overall intensity of these peaks changes randomly over this time period, and these peaks do not disappear or change intensity or frequency in a systematic manner during the frequency jumps of the fluctuating modes. As discussed earlier, a number of modes are stable in both intensity and frequency over the same time-series acquisition during which other modes undergo sharp jumps in both frequency and intensity. These stable modes serve as an ideal reference to clearly demonstrate that of only particular normal modes can only result from the intrinsic molecular response rather than detection artifacts or extrinsic effects.

Fig. 3.10a shows the correlation plot corresponding to the covariance plot shown in Fig. 3.3b of the Results section. Frequency correlation, $\chi_{ij} = \sigma_{ij}/(\sigma_{ii}\sigma_{jj})$, shows normalized intensities

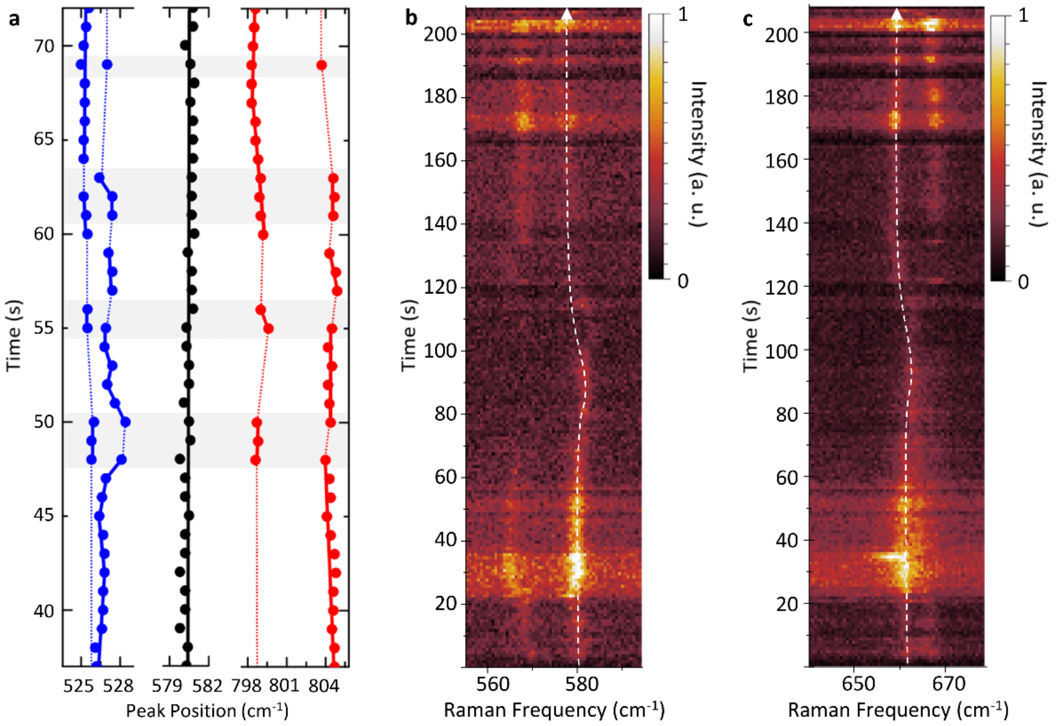

Figure 3.9: (a) Center frequency of three different vibrational modes during 37-72 s. Time-series TERS spectra for the 580 cm^{-1} (b) and 660 cm^{-1} (c) taken at 1 s intervals, showing the full acquisition time of 209 s.

as compared to the covariance plots shown in the Results section. The normalized frequency correlation map enables quantification of correlation or anti-correlation, although the line shape of each peak is obscured by this normalization. As noted earlier, the correlation plot shows that peaks assigned to orthogonal A_2 and B_1 symmetries have correlations of +1 and -1 over this time period. Other spectral ranges and time-periods similarly show correlation and anti-correlation A_2 and B_1 with magnitudes of $| \pm 0.6$ to $1|$. As expected, peaks of fully symmetric A_1 character fluctuate less in intensity and are found to be correlated with all other peaks and with intensity fluctuations of the non-resonant background signal.

Fig. 3.10b-d show covariance plots for each short time segment, showing a larger region of interest than Fig. 3.4b of the Results section. In the covariance plots spanning a larger frequency region, both correlation and anti-correlation are clearly observed for peaks separated by several hundred cm^{-1}. Anti-correlated TERS intensities are seen between A_2 modes and B_1 modes at

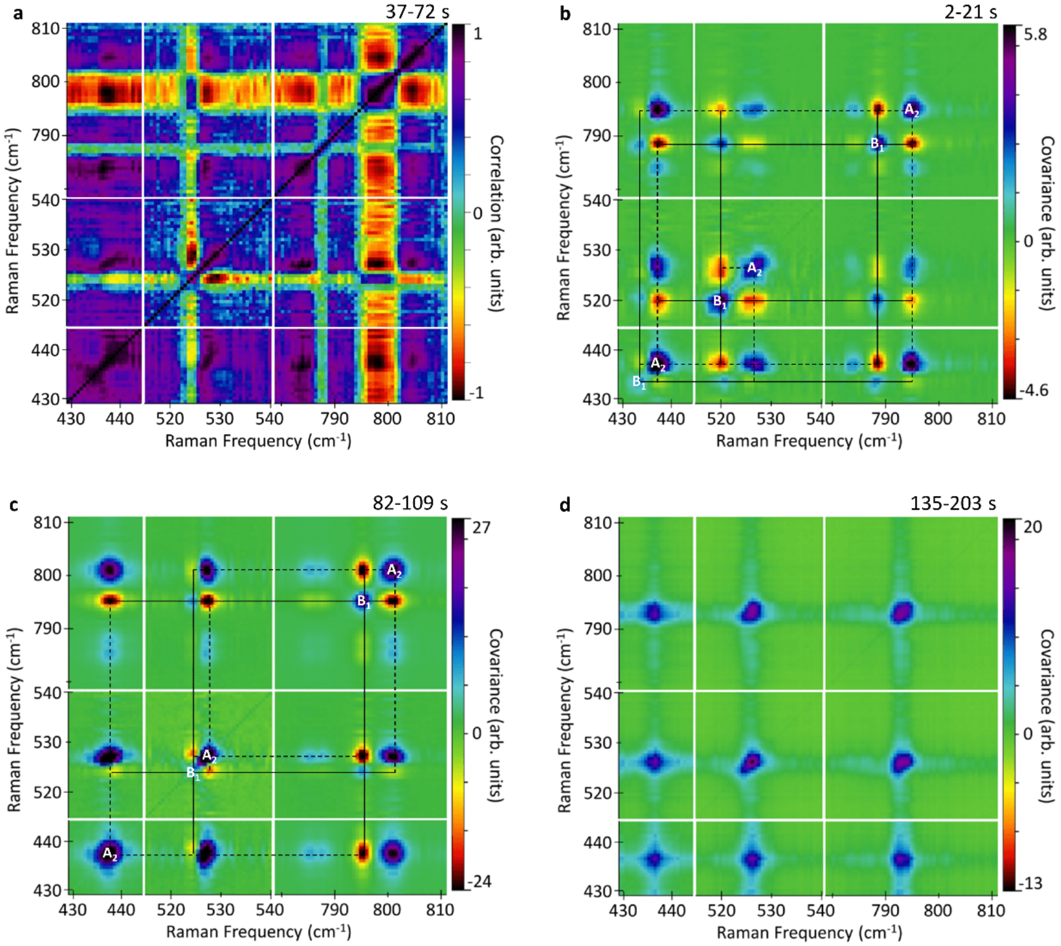

Figure 3.10: (a) Correlation plot of Raman intensity for the time region 37-72 s (Covariance plot is shown in Fig. 3.3b of the Results section). Covariance plots of Raman intensity over three time regions (b) 2-23 s, (c) 82-109 s, and (d) 135-203 s.

$\sim$435, $\sim$525, and $\sim$800 cm^{-1} in Fig. 3.10b-c. Peaks are labeled by their frequency over the time range as shown in Fig. 3.3b of the Results section. Spectral fluctuations cause the slight shift of peak positions between each short-time covariance plot. No fluctuations are observed in the final time segment shown in Fig. 3.10d, corresponding to a static molecular position. Although the explicit causes of spectral fluctuations cannot be concluded here, changes in substrate-adsorbate interaction, e.g. alternately bonding to defects such as atomic vacancies, step edges, or terrace, could contribute to spectral fluctuation. Fig. 3.9d shows the time trace of the center frequency of three different vibrational modes during 37-72 s, quantifying the correlated spectral fluctuation between specific vibrational modes.

3.2 Development of a cryogen-free low-temperature tip-enhanced spectroscopy[2]

3.2.1 Motivation

While we have investigated the intramolecular coupling and single-molecule dynamics with the high-vacuum variable temperature tip-enhanced Raman spectroscopy (TERS) setup introduced in section 3.1, the liquid nitrogen (LN_2) flow cryostat has several remaining issues. In the previous setup, there was no element to isolate the vibration of the cryostat because the TERS head is rigidly mounted on the cryostat. This causes vibrational noise and mechanical drift of the head even when the flow rate of LN_2 is minimal. In addition, the sample did not remain clean during the cooling procedure because multiple layers of water ice can be formed onto the sample surface under high-vacuum conditions. Therefore, for a more detailed understanding of molecular dynamics and intramolecular coupling properties as well as better measurement and control of samples, we build a cryogen-free low-temperature tip-enhanced spectroscopy with an ultra-high-vacuum (UHV) closed cycle helium exchange gas cryocooler extending the temperature range from 20 to 350 K.

3.2.2 Design and instrumentation

We aim to design and set up a cryogen-free low-temperature tip-enhanced spectroscopy, where ′cryogen-free′ means not using liquid helium or nitrogen. Therefore, we design our new low temperature setup with a closed cycle cryocooler. A closed cycle cryocooler is operated by a thermodynamic cycle of a working substance. Its operating principle is similar to a heat engine, but reverses the direction for a cooling system. Fig.3.11 shows a working principle of a closed cycle cryocooler. Basically, the working substance cuts off a large amount of heat energy (Q_w) at a warm temperature (T_w) and simultaneously absorbs a heat energy of the sample (Q_c). In each cycle of cooling, the working substance performs thermodynamic work (W) because Q_c is much smaller than Q_w. We can define the effectiveness of a cryocooler with the ratio W/Q_c, the

---

[2] This section covers instrumentation work performed by K.-D. Park and T. Jiang. The measurement was performed and analyzed by K.-D. Park, and supervised by M. B. Raschke.

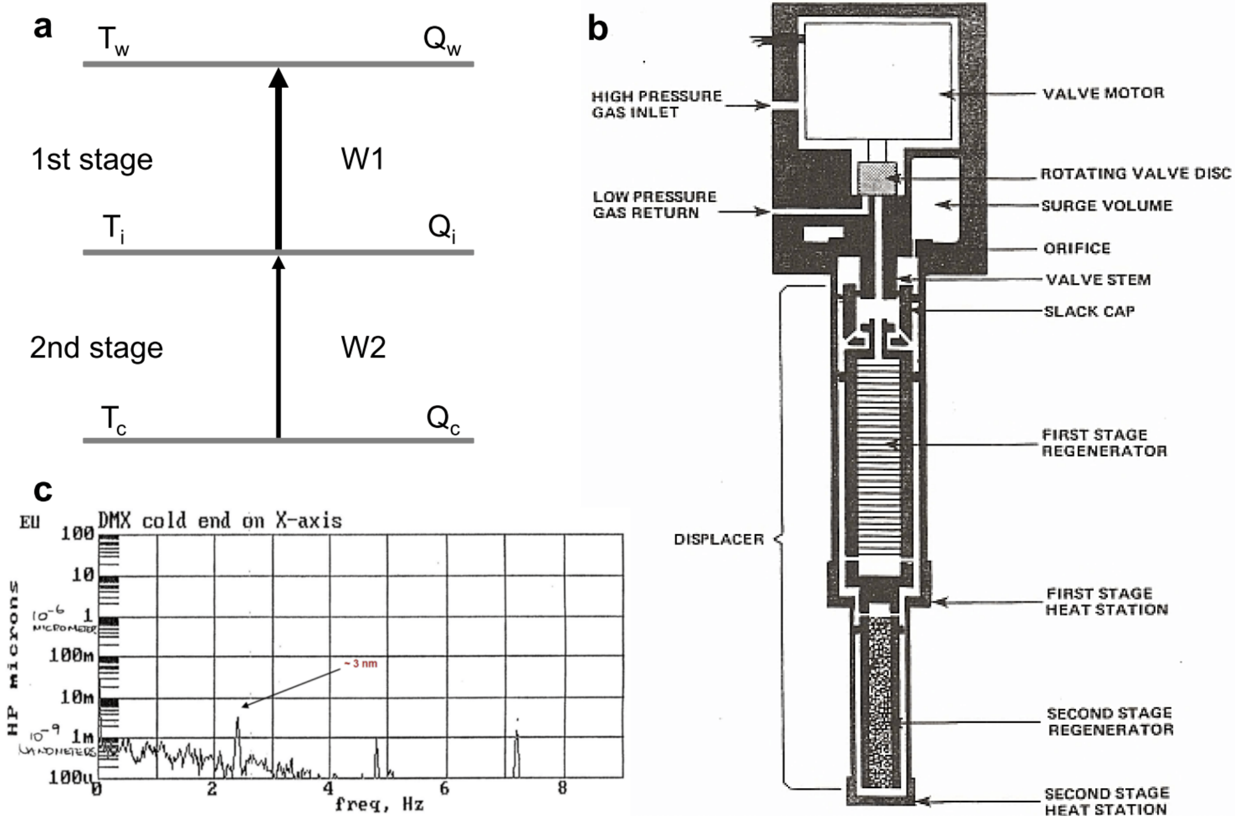

Figure 3.11: (a) Description of a working principle of a closed cycle cryocooler. (b) Schematic illustration of a closed cycle cryocooler consisted of a compressor, a displacer, and a regenerator. (c) A frequency and vibration amplitude curve of a closed cycle cryocooler.

amount of work required to absorb a certain amount of heat from the sample at T$_c$. A closed cycle cryocooler is generally consisted of multiple stages as shown in Fig.3.11. In the second stage, the working substance absorbs a heat energy from the sample at T$_c$ (W1). The absorbed heat energy is transferred to the first stage through the intermediate heat energy (Q$_i$) at the temperature T$_i$. The working substance performs the same work (W2) between Q$_i$ and Q$_w$. With the repeated cycle of this procedure, the sample can be cooled down to a minimum temperature only depending on the environmental heat load.

In general, helium (He) gas is used as a working substance. The temperature of a final cooling stage can reach ~50 K and <10 K with single stage and multi-stage systems, respectively. The temperature of samples in optical measurements are generally higher than these temperatures because there are heat loads from the sample mount, excitation laser, and other experimental components.

We use a commercial multi-stages cryocooler (DE-204PF, Advanced Research Systems, Inc) to build a cryogen-free low-temperature tip-enhanced spectroscopy. For operation of the cryocooler, the Gifford-McMahon (GM) refrigeration principle is used [165]. A cryocooler consists of a compressor (ARS-10HW, Advanced Research Systems, Inc) to compress the He gas, a displacer to move the He gas between cold and warm parts, and a regenerator to enable the heat exchange of He gas between cold and warm parts, as shown in Fig.3.11b. The refrigeration cycle of a closed cycle cryocooler starts with opening the rotating valve disk for the path of high pressure He gas. In this process, the high pressure He gas goes into the expansion space after passing through the regenerating material. Second, the displacer is moved up by the pressure difference expanding the He gas to cool down. Third, the rotating valve disk opens for the path of low pressure He gas, enabling the cold gas to flow through the regenerator to remove heat from the cold stage. Lastly, the displacer is moved down to its original position by the pressure difference, and the cycle is completed.

Our cryocooler is designed to have very low vibrational amplitude at the sample stage. He gas is filled in the space between the cold tip of the cryocooler and the sample mount without mechanical contact between the two. This interface blocks vibrational noise transfer from the cold tip to the sample mount. The manufacturer demonstrates the vibrational level of the sample mount is $\sim$3 nm as shown in Fig. 3.11c even though the vibrational amplitude of the cold tip is 10 - 30 μm.

Fig. 3.12a and b show a schematic and a photo of the designed and built low-temperature cryogen-free tip-enhanced spectroscopy setup. The cryocooler and a home-built atomic force microscopy (AFM) are installed inside the vacuum chamber (MCF800-SphCube-G6F8, Kimball Physics) and nipples. The vacuum chamber has two window ports in the front and at the bottom with 2057.4 mm CF flange. The front port is to access to the AFM to change samples and tips, and the bottom port is for optical access during spectroscopy and imaging measurements. We install

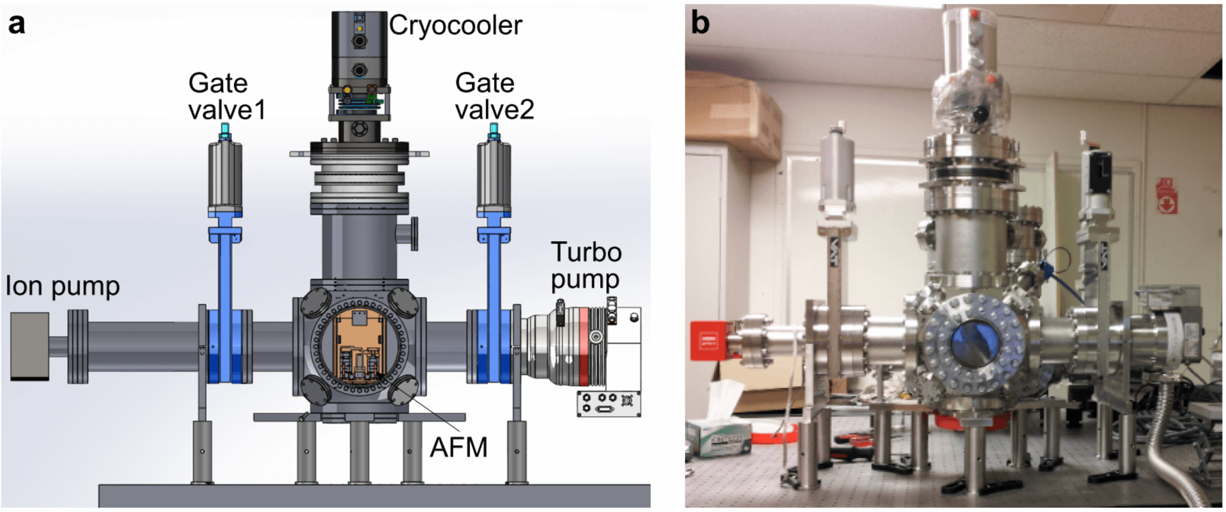

Figure 3.12: A schematic drawing (a) and a photo (b) of the home built cryogen-free low temperature tip-enhanced spectroscopy setup.

a turbo-molecular pump (HiPace 300, Pfeiffer Vacuum) with a rotary pump (Varian) on the right arm to pump down the chamber with pumping speeds of up to 260 l/s for N_2. On the left arm, we install an ion pump combined with a non-evaporable getter (NEG) pump featuring pumping speed in excess of 500 l/s (H_2 and O_2). We add two gate valves (10840-CE01-0005, VAT Valve) on both sides of the AFM to maintain the vacuum on the pumps when we exchange a sample or AFM tip. The chamber and the cryocooler are mounted on an optical table, but the cryocooler is separated from the table with dampers for vibration isolation.

Fig. 3.13a-c show schematics and a photo of the AFM. The outer and inner cold shields are mounted to the first and second stages of the cryocooler, respectively. The sample is held by an oxygen-free high conductivity (OFHC) copper block, and the sample and tip mounts can be moved in x-, y-, and z-directions up to 5 mm using motorized positioners (ANPxyz101, Attocube). A Si diode (LS-DT-670B-S, Lake Shore Cryotronics, Inc.) is mounted near the sample to monitor the temperature. The cold fingers cool the sample to a minimum temperature of 20 K through an OFHC copper braid connected to the second stage of the cryocooler. A CNC-polished aspheric lens (AL 108-B, Thorlabs) with NA = 0.55 is mounted on the base plate using OFHC tubes. For vibration isolation, the AFM is suspended with springs from the ceiling of the inner cold shield.

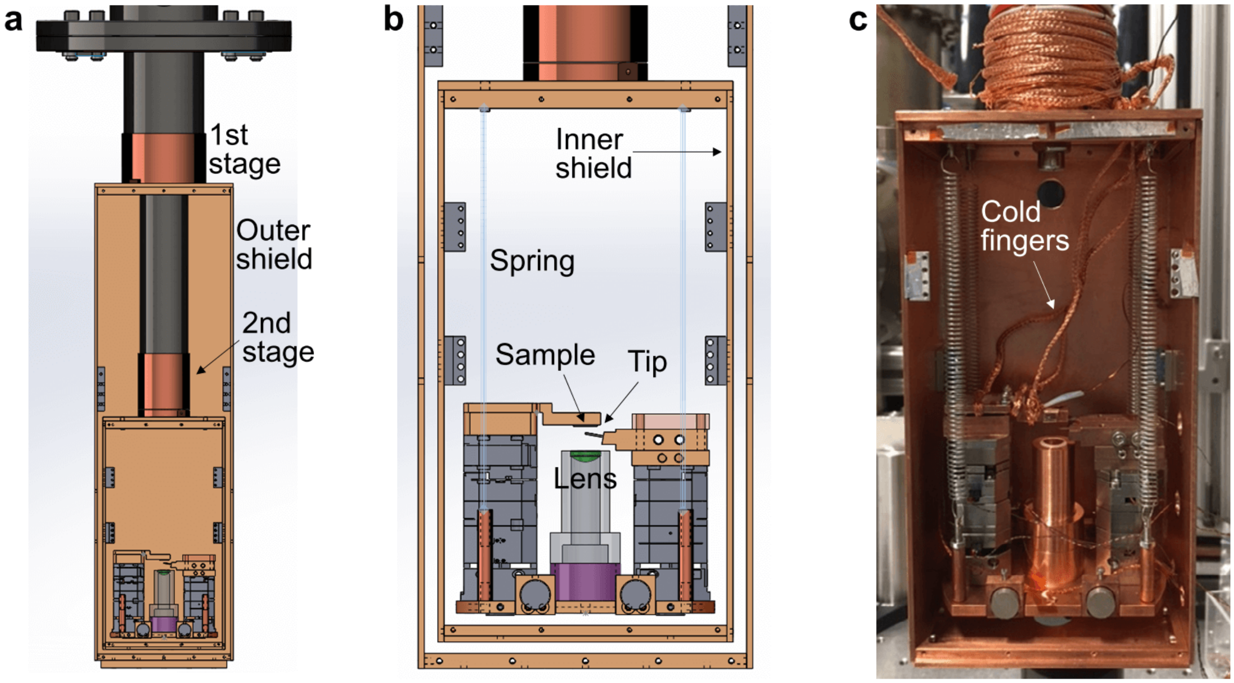

Figure 3.13: Schematic drawings (a, b) and a photo (c) of the home built cryogen-free low temperature AFM setup.

For AFM imaging, Au tips are etched electrochemically [119] resulting in ∼10 nm apex radius. A quartz tuning fork based shear-force AFM is used to control the tip at a constant tip-sample distance of 1-2 nm [121]. The sample holder is mounted to a piezoelectric transducer (PZT, ANSxy100/lr, Attocube) for x- and y-directions sample scanning and tip-sample distance control (ANPz101, Attocube). AFM operation is controlled by a digital AFM controller (R9, RHK Technology). For TERS or tip-enhanced photoluminescence (TEPL) spectroscopy and imaging, a Helium-Neon laser (632.8 nm, $P < 0.3$ mW) provides a linearly polarized incident beam focused onto the tip apex. Raman and PL signals are collected in the back scattered direction, passed through a long-pass filter (633 nm cut-off) and focused onto the slit of a spectrometer (f=500 mm, SpectraPro 500i, Princeton Instruments) with a LN_2 cooled charge-coupled device (CCD, Spec-10 LN/100BR, Princeton Instruments). Far-field micro-Raman and PL are measured using the same experimental setup with the AFM tip retracted several hundred μm from the sample.

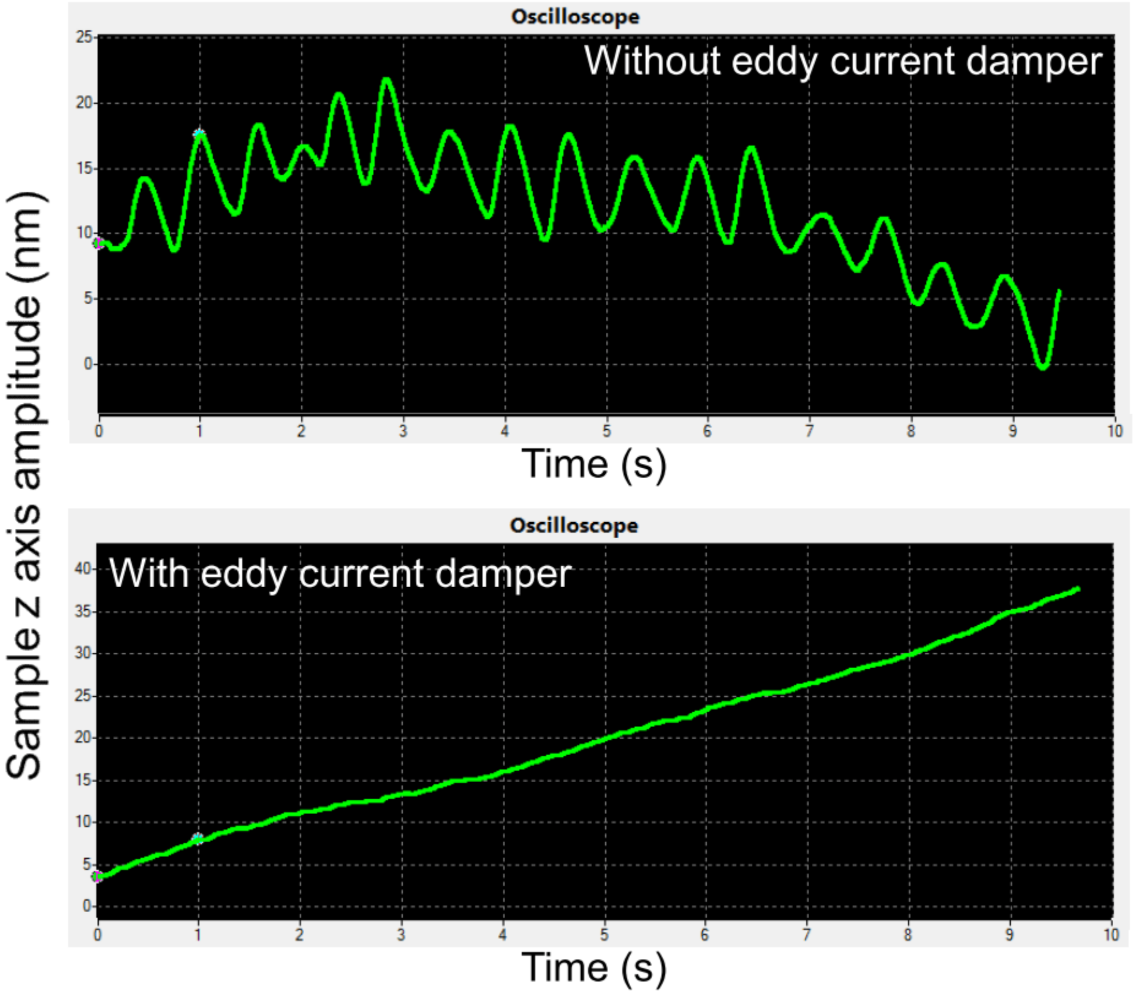

Figure 3.14: Amplitude change of the z axis of the sample with respect to the time when the sample is approached to the AFM tip for without (top) and with (bottom) using eddy current dampers.

3.2.3 Results and discussion

We perform a shear force AFM measurement on a periodic grating to test the stability of our AFM suspended from the ceiling of the cold shield by springs. As can be seen in Fig.3.13b-c, we mount magnets in the front and rear interfaces of the bottom plate of the AFM. When the AFM moves relative to the cold shield, these magnets induce eddy currents (a current loop in a conductor caused by motional electromotive force). These eddy current gives rise to a damping effect of the vibrational noise of the cryocooler, and maintains the AFM stable.

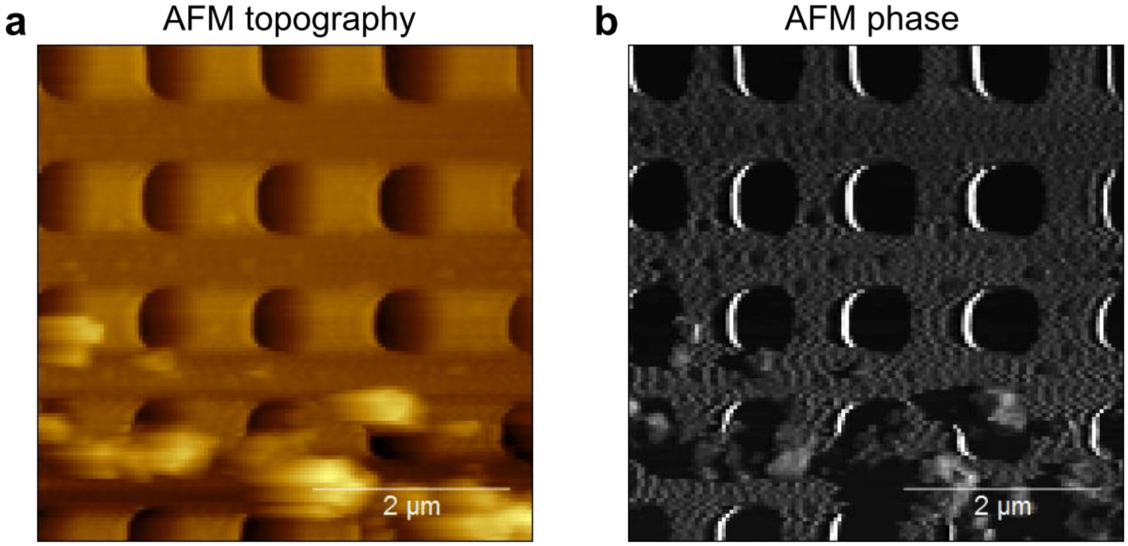

Figure 3.15: AFM topography and AFM phase images measured with eddy current damper.

Fig.3.14 shows the amplitude change of the sample z-axis with respect to the time, when the sample is approached to the AFM tip. The top graph shows vibrational noise (∼8 nm) of the AFM when we take out the magnets. It is difficult to remove this vibrational noise without eddy current damper because the suspension springs are very sensitively influenced by environmental noises. On the other hand, we achieve a low noise shear force feedback condition with eddy current damper as shown in the bottom graph. The measured vibrational amplitude (∼0.5 nm) is comparable to the noise level of a conventional shear force AFM with no spring suspension. We then perform AFM scanning of a periodic grating in this condition. Fig.3.15a and b show measured topography and AFM phase images. We obtain low noise AFM images reproducibly for several hours without any vibrational noise issue of the springs.

During our initial pump down of the chamber, we achieve a vacuum pressure of 3×10^{-8} Torr. Although we use vacuum compatible materials for all the components in our setup inside the chamber, some water vapor and other contaminants are left on the surfaces inside the vacuum. To remove such contaminants, we perform a bake-out process, an artificial acceleration of outgassing. For the bake-out, we wrap heater tapes around the vacuum chamber except for the glass windows. In this procedure, heater tapes are wrapped carefully to not overlap, and several thermocouples are

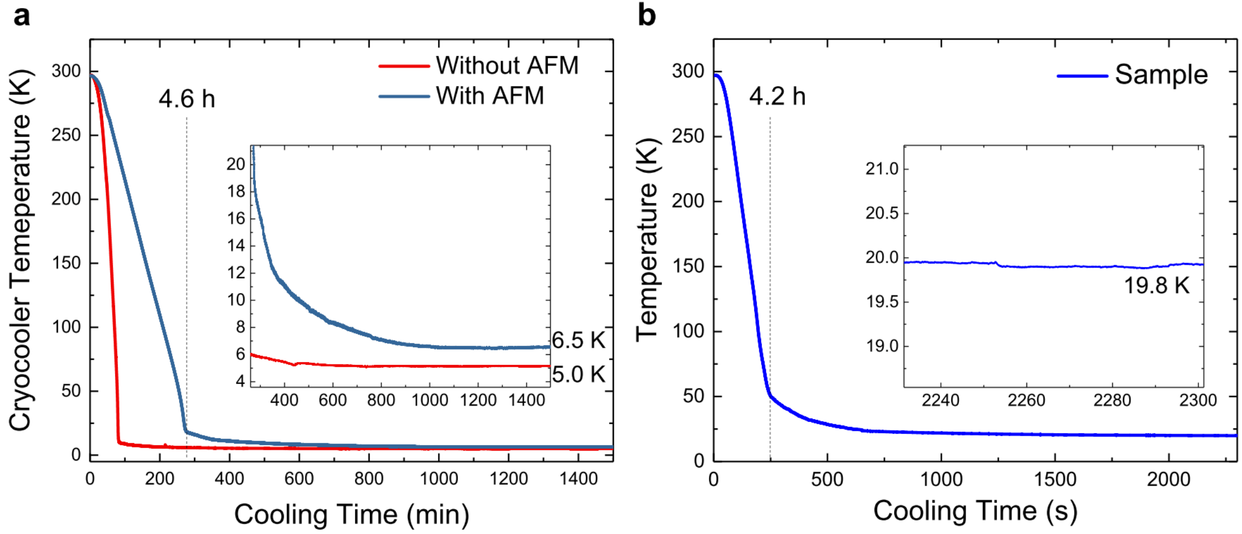

Figure 3.16: A temperature change of the cryocooler (a) and the sample (b) with respect to the cooling time.

installed to monitor the temperature. After wrapping the chamber tightly with aluminum foil for more homogeneous heating, we gradually ramp a heating temperature up to 200 °C for 24 hours, and bake-out for another 48 hours. We then degas the vacuum system to remove residual contaminants at the ion gauge. After pumpdown for another 10 hours, we achieve a vacuum pressure of $< 1 \times 10^{-10}$ Torr.

In this UHV regime, we measure a temperature of the second stage of the closed cycle cryocooler using a Si diode (LS-DT-670B-S, Lake Shore Cryotronics, Inc.). Fig.3.16a shows the temperature of the cryocooler with respect to the cooling time. Red and blue graphs show temperature change curves without and with the AFM installed. With the AFM, the temperature decreases rapidly to 18 K in 275 min, it then gradually decreases to 6.5 K after cooling for ~1000 min. Fig.3.16b shows the temperature of the sample with respect to the cooling time. This shows a similar trend to the cryocooler stage, yet the final temperature is as low as 19.8 K due to the limited cooling power of the closed cycle cryocooler. From this minimum temperature, we can control the sample temperature with a resistive heater and a temperature controller (Model 331 cryogenic temperature controller, Lake Shore Cryotronics) up to 350 K with a stability of better

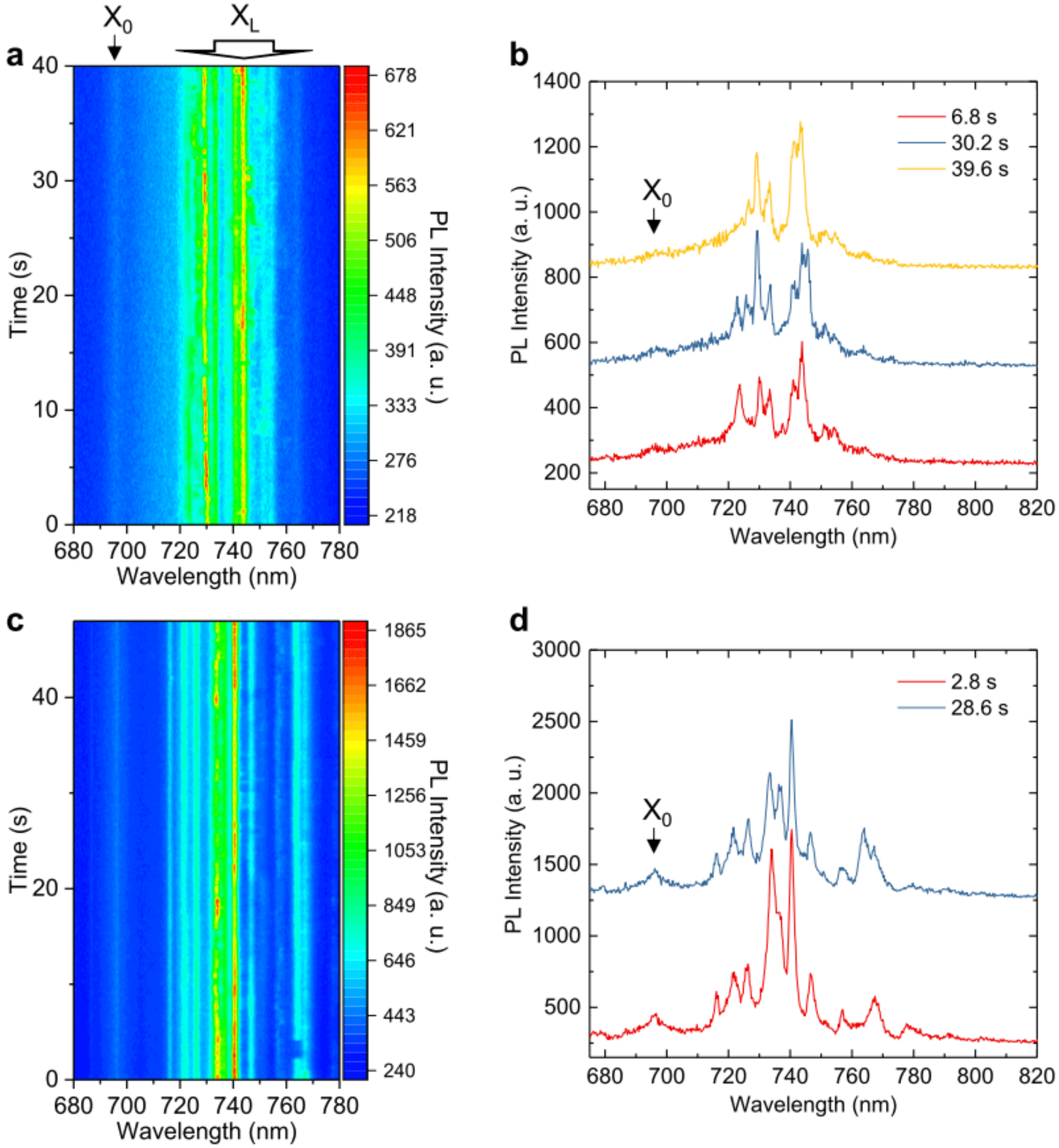

Figure 3.17: Time series far-field PL response (a, c) and selected PL spectra (b, d) of bright and localized excitons of a monolayer WSe_2 measured at 30 K.

than 0.1 K.

As a test optical measurement at low temperature, we perform a far-field photoluminescence (PL) measurement of a monolayer WSe_2 grown on SiO_2/Si substrate at 30 K. Fig. 3.17a and b show time series far-field PL response and selected PL spectra of bright and localized excitons. At low temperature, the PL intensity of the bright exciton is strongly suppressed due to the existence of an optically forbidden dark state [166]. We observe a PL response of the localized excitons in only a few local spots of a WSe_2 crystal. As can be seen in Fig. 3.17, an obvious spectral fluctuation of very narrow peaks is observed with respect to the time in a fixed spot of the sample. In previous studies, these very narrow PL peaks were identified as single exciton states bound to defects [72, 73, 167, 168, 169]. This single photon emission behavior is reproducibly observed in other local spots as shown in Fig. 3.17c and d. We will discuss the localized exciton of a monolayer WSe_2 in more details in section 4.4.

3.2.4 Future works

In the future, we will extend our work on low temperature single-molecule TERS to higher spectral precision and in combination with STM for an extended mode selective study of intramolecular and bath coupling as well as correlation study of tunneling transport and TERS derived molecular orientation, as described below.

Single-molecule dynamics and intramolecular vibrational energy redistribution

The study of vibrational energy flow of local excited states of molecules has long been a central goal to understand many chemical molecular processes [170, 118] and to test different quantum and statistical theoretical models [171, 172]. Conventional techniques rely on ensemble IR or UV pump-probe spectroscopy [173, 174] or femtosecond stimulated Raman spectroscopy [175, 176] as examples. In particular, time-domain multi-dimensional spectroscopy provides, can observe, and distinguishes femtosecond intra- and inter-molecular effects such as intramolecular vibrational relaxation from many interactions with the bath and heterogeneity in the local chemical environment [177, 178].

Single-molecule variable temperature TERS can complement these approaches. TERS measures signals from a small ensemble by spatially localized excitation and detection of a small sub-ensemble within the larger bath, while multi-dimensional spectroscopy separates signal from sub-ensembles by their characteristic frequencies. Single-molecule TERS opens inquiry to entirely new time windows. While femtosecond multi-dimensional spectroscopy interrogates fluctuations on the

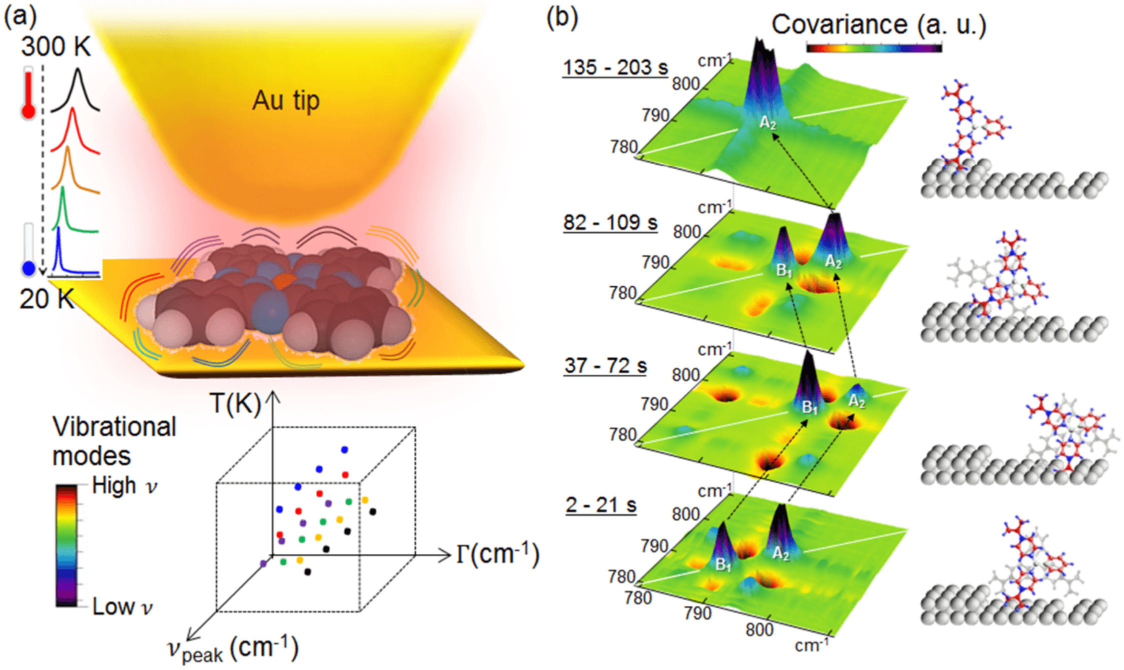

Figure 3.18: Variable temperature single-molecule TERS (a) probing bath coupling from the correlative study of a large number of vibrational modes and their temperature dependence of peak position and linewidth. (b) Our data of spectral diffusion of malachite green represented as covariance plots with assigned underlying rotational motion. Spectral fluctuations appear as jumps in frequency between each time segment.

timescale of femtoseconds to picoseconds, anything slower is observed as heterogeneous broadening and slow dynamics cannot be distinguished from static structure. TERS opens a new route of inquiry into dynamical fluctuation in the time window of milliseconds to minutes, observable through jumps in the frequency spectrum. Meanwhile, single-molecule TERS provides frequency-domain insight into femtosecond-nanosecond dynamical processes that contribute to spectral shifts and line broadening. Single-molecule TERS offers a powerful route to address questions of static and dynamical structure including ensemble averaging and the effects of intermolecular interactions.

We applied a variable temperature TERS for investigation of few-molecule and single-molecule vibrational spectra in both the frequency and time domains with high spectral resolution [19]. We found that the adsorbate conformation is unstable at room temperature and rapidly fluctuates due to the significant thermal rate constant, while at low temperatures, conformational fluctuations are slowed and intramolecular vibrational energy redistribution (IVR) provides a dominant contribution to the observed line shape. From temperature dependent Raman linewidth and frequency shift, we could derive activation energy, coupling strength, and exchange mode lifetimes that contribute to IVR within a few-molecule sub-ensemble.

With our newly built variable temperature TERS (20 - 350 K) using a closed cycle cryostat, we will investigate IVR of poly-aromatic molecules at the single-molecule level to understand the role of molecular fluctuations and local environment on vibrational dynamics, as illustrated in Fig. 3.18. As a model system, we study single molecules and coupled 2D aggregates of large flat aromatic molecules such as porphyrin and phathalocyanines [179, 180, 181, 182] that are recently becoming more important for a range of optoelectronic applications such as novel light harvesting materials [183], molecular electronics [184], and organic semiconductors [185]. These molecules have well understood conformation on the surface, allowing us to distinguish IVR processes as a function of local chemical environment. We will compare single-molecules to 2D aggregates to understand the role of intermolecular coupling and vibrational delocalization [186, 187]. We will investigate temperature dependent vibrational dephasing of high-frequency modes versus low frequency modes as sensitive probes of intra-molecular versus inter-molecular dephasing processes. Finally, we can explicitly investigate the relationship between IVR dynamics and conformation by a careful investigation of molecules with more than one stable adsorbate configuration or internal degrees of freedom [188, 189, 190]. These detailed studies of large molecules will provide better understanding for the fundamental nature of IVR phenomena and related chemical process such as the positron annihilation. We will also seek to model these systems using statistical models for system-bath interaction and vibrational energy and coherence transfer.

Single-molecule electronics

With the recent advancement of the single-molecule detection technologies [116, 19], investigating electronic properties of single molecules at metal-molecule-metal junctions has become a prior work for their potential applications for molecular electronics. To capture single molecules in metallic junction, various technological approaches were developed such as mechanically controlled break junction (MCBJ) [191] and scanning tunneling microscopy (STM) break junctions [192, 193],

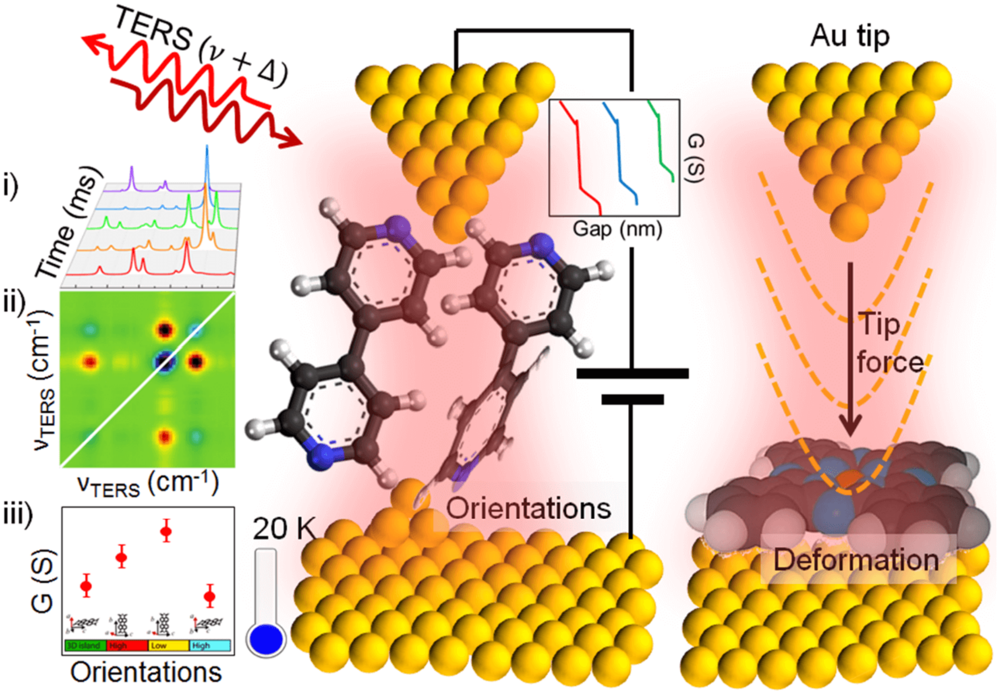

Figure 3.19: Combination of TERS with STM based tunneling (left) for measurements of time series TERS (i), providing molecular orientation and fluctuation information (ii), and correlated with transport conductivity (iii). Tip-molecule force interaction (right) allows for probing nano-mechanical molecular response and its anisotropy from symmetry selective vibrational frequency shifts.

the latter with the benefit of precise distance calibration and transport measurement with the opportunity for single molecule vibrational spectroscopy in UHV low temperature environments [116, 117].

Recent studies showed a range of interesting phenomena including single-molecule diode behavior [194], control of strain [195], protein sequence dependence [196], gap renormalization [197], and molecular switching [198]. Several experiments revealed evidence that the electronic transport properties of molecules depend on their orientations using UV excited cis-trans transition molecule [199], statistical investigation [200], and combined with TERS analysis in ambient condition [201]. In ambient condition fishing mode TERS [201], molecules are diffusing rapidly and the specific orientation cannot be controlled. In addition, inhomogeneous Raman linewidth from intramolecular couplings makes it hard to analyze the correlation of fluctuating vibrational modes.

Therefore, a comprehensive understanding of correlated properties of transport and orientation of various molecules in a stable measurement environment is desired. We will extend our UHV low temperature TERS experiments to complement previous studies and to provide a complete picture of those properties for fixed or stably rotating single molecules, and further interesting open questions: how bias tunneling and voltage, tip-sample forces, and temperature affect the molecular orientation, conformation, and metal-molecule bonding and vice versa of interest. We will use π-conjugated biphenyl systems as a model molecule [200, 201]. As illustrated in Fig. 3.19(left), time series TERS spectra (i) and conductance (G=I/V) will be measured at low temperature with STM based distance and tunneling control. The orientation of molecules will be controlled with temperature and laser fluence, and the specific orientations of molecules will be analyzed from the covariance analysis (ii) of fluctuating TERS peaks of time series spectra. Then, we can derive detailed correlation properties of transport and orientation of single molecules (iii).

In addition, we will explore the deformation of intramolecular atomic bonding for the applied electromagnetic field, bias current and voltage, and tip-induced mechanical force as illustrated in Fig. 3.19 (right). We expect to observe Raman frequency shift from modified strain and energy of atomic bonds. This experiment is feasible for single molecules at low temperature since the homogeneous linewidth of Raman peaks can be observed with suppressed intra- and inter-molecular interactions. For this experiment, we will use porphyrazine and phthalocyanine molecules, which are stationary flat on the surface at low temperatures [179].

3.3 Near-field imaging of cell membranes in liquid[3]

Despite the power of far-field super-resolution microscopies for three-dimensional imaging of biomolecular structures and processes, its application is challenged in dense and crowded samples and for certain surface and membrane studies. While near-field imaging with its ability to provide intrinsic sub-diffraction limited spatial resolution at any optical modality, its application to biological systems has remained limited because of the difficulties of routine operation in liquid environments. Here we demonstrate stable and sensitive near-field scanning optical microscopy (NSOM) in liquid based on a new mechanical resonance control and an optimization of the tip length, achieving high quality factor (>2800) force sensing of the near-field probe. Through near-field imaging of the spatial distribution of epidermal growth factor receptors (EGFRs) on the membrane of A431 cancer cells as an example, we reveal nanoscale correlations between surface EGFR and intracellular organelle structures with ~50 nm spatial resolution. The method provides a new avenue for surface imaging in viscous liquid media to complement super-resolution microscopy for studies of biological membranes, nanostructures, and interfaces.

3.3.1 Motivation

Recently, a range of super-resolution fluorescence microscopies have opened the door for studying biomolecular processes with sub-diffraction limited spatial resolution. For example, stimulated emission depletion (STED) increases spatial resolution by selectively deactivating fluorophores [26, 34]. Likewise, photoactivated localization microscopy (PALM) and stochastic optical reconstruction microscopy (STORM) overcome the diffraction barrier by using photoswitchable fluorescent probes [35, 36].

However, these super-resolution microscopies require not only specific fluorophores optimized for the targets but also low density labeling to decrease localization uncertainty, limiting spatial resolution and imaging speed [202, 203]. In addition, high excitation fluence is needed to obtain

---

[3] This section draws significantly from [101]. The experiment was performed and analyzed by K.-D. Park in collaboration with Inha University, and supervised by M. B. Raschke and S. G. Lee.

the number of photons necessary for accurate position localization of the emitters. Therefore, photobleaching appears to be an unavoidable limiting factor [204]. Also based on a far-field sectioning method, they are not necessarily ideal to investigate non-planar surface and interfaces (Fig. 3.20a).

Near-field imaging, on the other hand, provides intrinsically diffraction-unlimited spatial resolution and is applicable to essentially any optical modality beyond fluorescence, including linear, inelastic, and nonlinear spectroscopies [20]. Applied with great success to a wide range of material systems especially with the advent of scattering scanning near-field optical microscopy (s-SNOM) [18, 205, 83], it provides single molecule sensitivity [19], few nanometer spatial resolution, and in the extension to ultrafast spectroscopy even few-femtosecond temporal resolution [206].

On the one hand limited to surfaces and interfacial regions accessible by the near-field probe, this on the other hand can make near-field imaging ideal for the study of membranes and protein nano-structures, with near-field localization profiling the surface thus discriminating against bulk signals (Fig. 3.20b). In addition, based on force-feedback controlling the near-field probe interaction, it provides simultaneous high resolution topographic information and multimodal imaging of membrane mechanical properties, e.g., viscoelasticity and adhesion force [207], as well as a wide range of optical modality.

However, a major limitation of near-field imaging for biological applications, has long been the difficulty of operation in liquid environments. Typically based on scanning probe microscopy (SPM) techniques, several attempts have been made for operation of near-field scanning optical microscopy (NSOM) and tip-enhanced Raman spectroscopy (TERS) in liquid, in particular for the study of cell membranes and electrochemical interfaces [208, 209, 210, 211, 212, 213, 214]. However, the near-field probe is operated based on a scanning probe force sensor, where its mechanical resonance deteriorates in frequency stability and quality (Q) factor in a liquid medium, sensitive to viscosity, density, and temperature [215]. Yet, with the near-field signal very sensitive to tip-sample distance, high precision and stability in the force-feedback is required to avoid imaging artifacts.

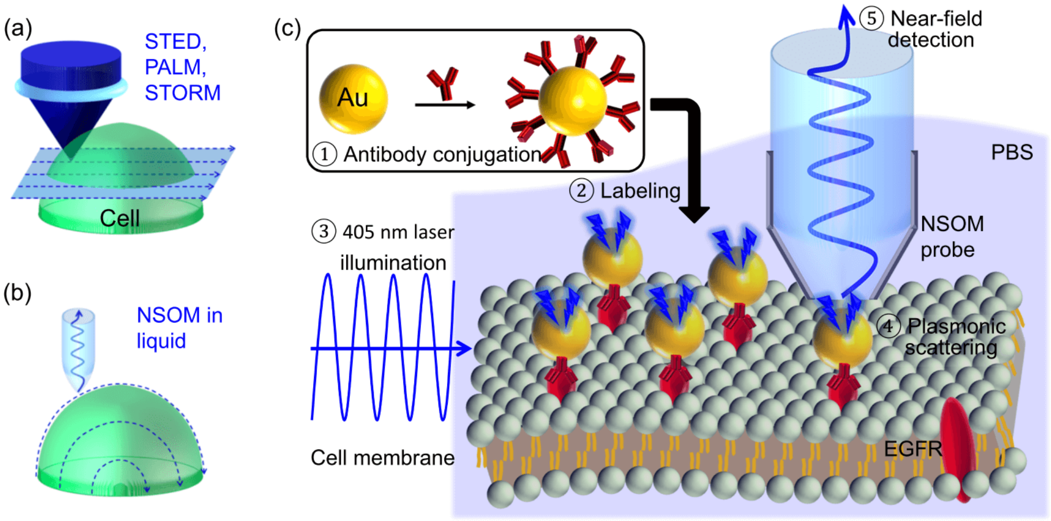

Figure 3.20: Comparison of optical nano-probe imaging methods: typical super-resolution microscopy based on far-field sectioning (a), and NSOM based on near-field profiling (b). (c) Procedure for NSOM imaging of EGFRs on the cell membrane in liquid. Anti-EGFRs are conjugated to AuNPs for labeling to the A431 cell membrane. Near-field scattered light from the AuNPs is collected by a NSOM probe under 405 nm laser excitation.

A refined approach for optimal force control in liquid as a basis for advanced near-field imaging of cell surfaces and membrane proteins is thus desired. Here, we demonstrate a new approach of mechanical resonance control of the near-field probe providing stable and sensitive imaging in liquid. It is based on a combination of length and nodal point optimization of the mechanical force sensor (tuning fork/fiber probe assembly) to achieve high Q-factor and sensitive force control in liquid. As application example, we label gold nanoparticles (AuNPs) to the biomolecules on the cell membrane as nano-plasmonic antennas to overcome the low sensitivity of the nano-apertured near-field probe, as illustrated in Fig. 3.20c. Through high resolution (∼50 nm) near-field imaging of the spatial distribution of epidermal growth factor receptors (EGFRs) on the membrane of A431 cancer cells in liquid, we reveal nanoscale heterogeneity of surface EGFRs, as demonstating experiment representing a typical bioimaging application.

Following the description and characterization of the force sensor design, we show the results of its use for in liquid cell membrane imaging, and conclude with a short perspective of the approach for a broad range of nano-bioimaging applications.

3.3.2 Experiment

Our method is in principle based on established quartz tuning fork shear force sensing to control and scan the near-field probe at and across the cell membrane. However in a conventional implementation, the Q-factor of the NSOM probe is reduced to <100 when the tip is immersed in liquid. To overcome this probelm, we recently developed a method to control the Q-factor of the quartz tuning fork based NSOM probe as shown in Fig. 3.24a [38]. In that method, the resonance frequency and the Q-factor of the NSOM probe are controlled by introducing two nodal wedges (Node 1: knife edge point, Node 2: pin point) and adjusting their positions like fingering a guitar. When the positions of the two nodal wedges are optimized, a high Q-factor is achieved since the vibrational energy of the tuning fork is efficiently transferred to the NSOM probe (l_1 and l_2) due to the effective vibration isolation at Node 1. In addition, we provide a novel physical concept to operate near-field microscopy in liquid by optimizing the tip length, l_3, to minimize the resistance from liquid viscosity. This optimization is a key enabling step for nano-bio imaging applications, and it was not yet discussed in our previously published two nodal wedges method [38].

Modeling of the high-Q NSOM head

The high-Q oscillator is divided into five vibration sections (Fig. 3.21): Rods 1, 2, and 3 corresponding to the fiber probe have lengths of l_1, l_2, and l_3, respectively, and their lengths are adjusted by changing the positions of two nodal wedges. Rods 4 and 5, corresponding to two prongs of the tuning fork, have equal length of l_4. The amplitude function for the five sections can commonly be specified with the mathematical expression as $U(l) = a\cos(\beta l) + b\sin(\beta l) + c\exp[\beta(l - l_{in})] + d\exp[\beta(l_{in} - l)]$ where a, b, c, d are unknown coefficients of the displacement function. The variable l is the distance measured from the base of the tuning fork for Rods 4 and 5, and the distance measured from the pin point support for other sections.

The parameter β is defined as $\beta = \omega^2\rho S/EI$ (ω is a natural frequency, ρ is a density, S is a cross sectional area, E is a Youngs modulus, and I is a moment of inertia) with specific values determined from references [120, 216]. To suppress numerical error, the initial coordinate l_{in} of

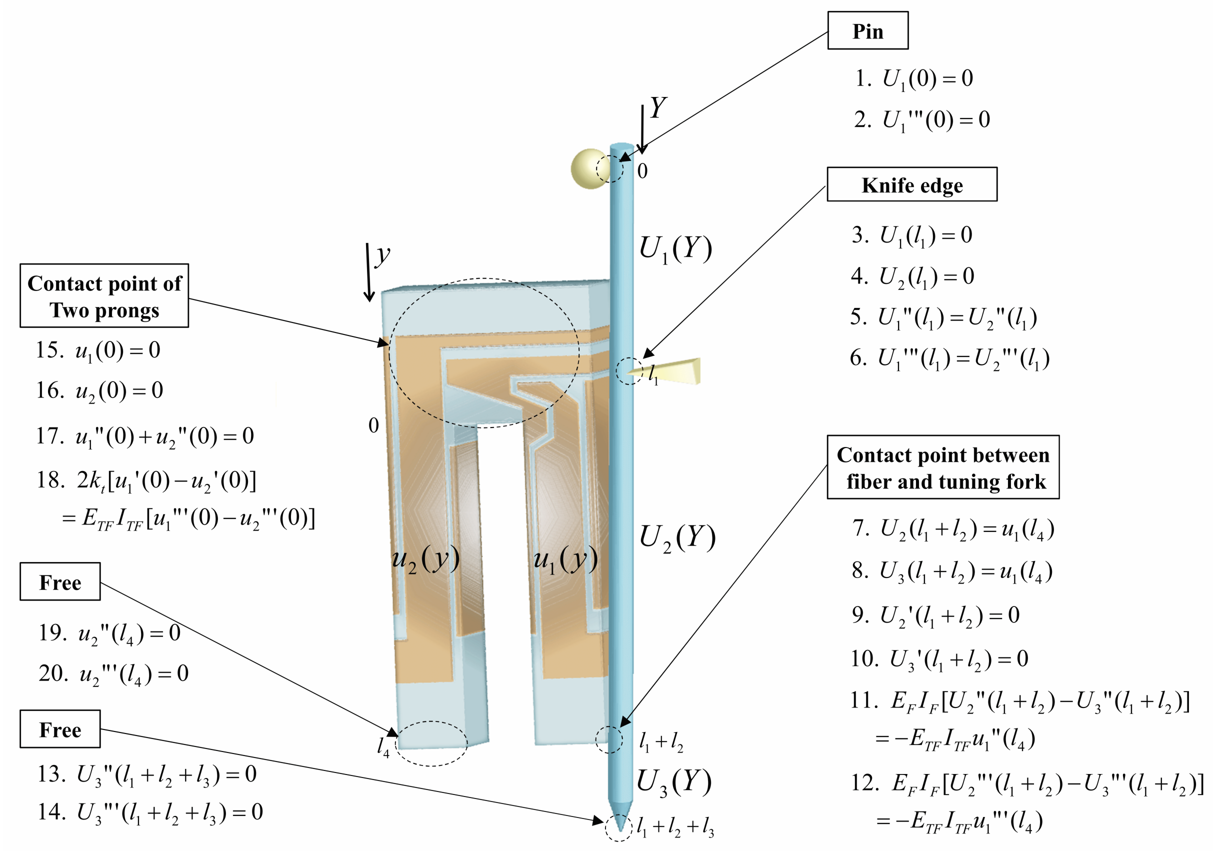

Figure 3.21: Modeling of the tuning fork/fiber probe coupled oscillator. A total of 12 boundary conditions are applied at the six vibration points of the five vibration sections. The boundary conditions in the two *free* parts are deduced based on the bending vibration of beam theory. Other boundary conditions are carefully derived by considering mechanical properties of each part.

each vibrating section is introduced into the exponent of the displacement function.

The system of equations for unknown coefficients is derived by applying boundary conditions to six boundary points (Fig. 3.21). The boundary conditions in tip-end and tuning fork-end are deduced based on the theory for bending vibration of a beam [217]. Other boundary conditions are carefully derived by considering the mechanical properties of each part. Since the system of equations can have nontrivial solutions only when the determinant of the coefficient matrix becomes zero, the frequency having a zero determinant is chosen as a resonance frequency (ω_R) for the high-Q oscillator.

NSOM setup

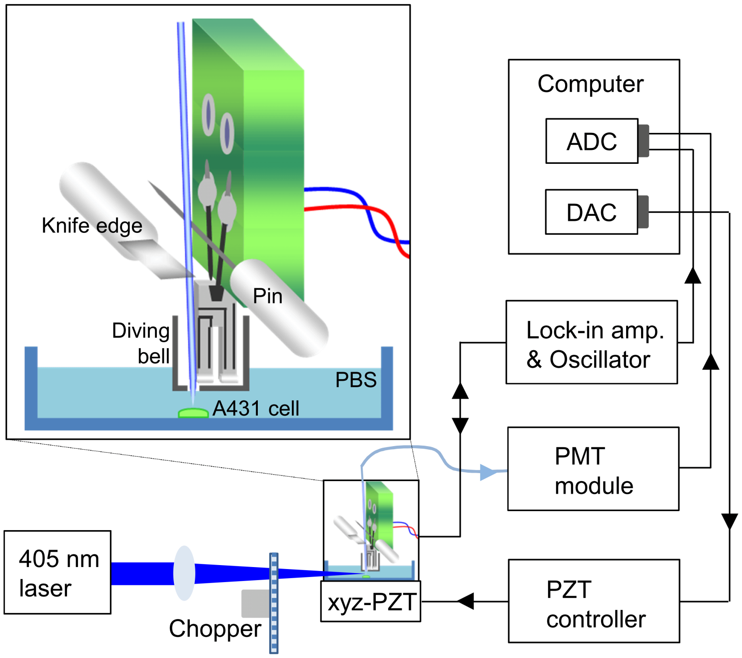

Figure 3.22: Schematic of the NSOM system. The tuning fork is electrically driven by an oscillator (function generator) and the voltage, which is proportional to the mechanical amplitude of tuning fork, is monitored by a lock-in amplifier. The excitation laser is modulated by a chopper to remove noise signal in PMT detection. The high-Q oscillator and diving bell structure are fixed and the sample (cell and culture dish) is scanned by a xyz PZT.

As shown in Fig. 3.22, a 405 nm laser is used as an excitation source and the near-field signal is collected using a commercially available Al-coated tapered fiber having an aperture diameter of ∼50 nm, and is then converted into an electric signal by a photomultiplier tube (R2027 from Hamamatsu) that is placed at the opposite end of the fiber. The position of the sample is changed using a piezoelectric transducer (PZT, P-611.3 from Physik Instrumente) that has a 0.1 nm resolution; its lateral positions (along the x- or y-axis) are also scanned using a PZT with a 10 nm position repeatability against a 100 μm total moving range. The height and near-field signal are acquired using an express data acquisition board (PCI-6229 from National Instruments). An office straight pin and a knife edge (cutter) are used as two nodal wedges and their materials do not play crucial roles in determining resonance characteristics as long as they are sufficiently hard.

Sample preparation

The EGFRs are labeled with the anti-EGFR antibody conjugated AuNPs. AuNPs are synthesized via a seed-mediated growth method using $HAuCl_4{\cdot}3H_2O$ and tri-sodium citrate [218]. The synthesized AuNPs have a spherical shape (diameter: ∼30 nm, smaller diameter AuNPs are not used for not reducing scattering intensity). The nanoparticles are diluted in 20 mM 4-(2-hydroxyethyl)-1-piperazineethanesulfonic acid (HEPES) solution (pH = 7.4) and anti-EGFR antibodies are added to another HEPES solution. Then the gold solution is added to the antibody solution with the volume ratio of 10:1 while being stirred. After stirring 5 mins, the solution is left to react for 20 mins. The mixture solution is centrifuged at 6000 rpm for 30 mins after adding 1% Polyethylene glycol (PEG) to prevent aggregation. Then the anti-EGFR conjugated AuNPs are re-dispersed in PBS buffer solution. The binding mechanism between antibody and AuNP has not been investigated exactly although it is suggested that the antibody could be adsorbed perpendicular on the nanoparticle surface at pH = 7.4 [219]. Finally, by pouring the anti-EGFR conjugated AuNPs solution onto the surface of A431 cancer cell, an antigen-antibody reaction occurred, i.e., the AuNPs are attached to the EGFRs. The samples are kept at 4°C for 12 h. After that the samples are rinsed by PBS buffer solution 3 times to remove residual AuNPs which are not bound to the EGFR.

To confirm the labeling state of the sample, confocal laser scanning microscopy (LSM 510 META, Zeiss) measurement is done using a commercial setup, and the result show general features of fluorescence imaging (Fig. 3.23). It should be noted that since the AuNPs are coated by PEG and antibody, we believe the prepared cells are nontoxic [220].

3.3.3 Results

Modeling and simulation

In the following we describe results of mechanical force sensor design and its characterizations. Fig 3.24b shows simulations of the vibrating amplitude of the oscillators. Since the position of the knife edge (Node 1) corresponds to the node of fiber oscillation, when the length l_2 is $(2n-1)\lambda_F/4$, where n is an integer and λ_F is fundamental wavelength given by the natural resonance frequency of the fiber (∼6 mm), the glued point becomes an anti-node and has a maximum amplitude owing

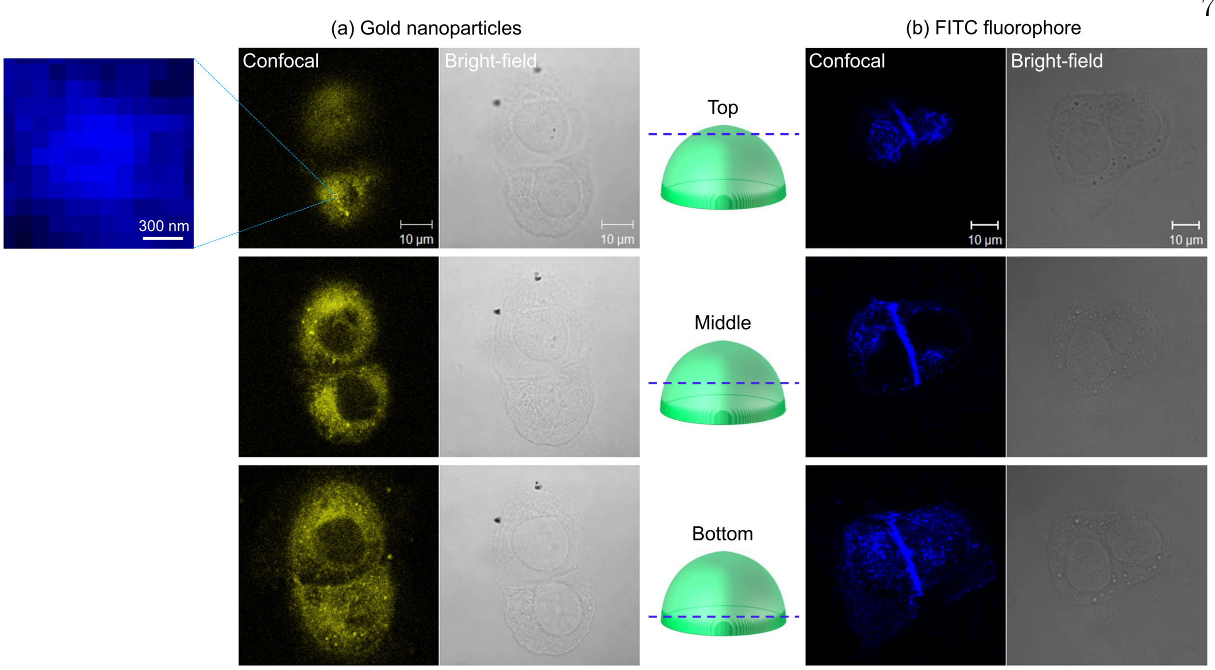

Figure 3.23: (a) Confocal laser scanning microscope images of the A431 cells, where EGFRs are labeled by (a) AuNPs and (b) FITC fluorophores. A 405 nm laser is used for measuring scattering (of AuNPs) or fluorescence (of FITC fluorophores) signals of the A431 cells. The EGFR imaging is done with a 100x magnification, 1.3 NA oil immersion objective lens by changing a focal plane from top to bottom of the cell. The left zoomed-in image is used in Fig. 3.27e to compare spatial resolution with NSOM image.

to the efficient coupled oscillation between the fiber probe and the tuning fork. On the other hand, the glued point becomes a node of the fiber oscillation when l_2 is $n\lambda_F/2$. In this case, the tuning fork loses a significant amount of vibrational energy because the fiber acts as a large damper. Therefore, we set l_2 to $5\lambda_F/4$ to make the high-Q state. Then we compare the amplitude of the tip-end for different values of l_3 lengths (1.5, 2.0, and 3.0 mm) to find an optimized length (smallest amplitude), which minimize a damping effect in viscous medium. For the tip oscillation (l_3), the glued point is regarded as the node irrelevant to the l_2 oscillation because the glued point has a boundary condition of partially fixed-end beam, whereas the tip-end has a free-end beam. The variation of resonance frequency and Q-factor are calculated as a function of lengths l_1 and l_2 ($l_1 + l_2$ is maintained to 14.0 mm) for three different lengths of the protruded tip (l_3 = 1.5, 2.0, and 3.0 mm) to understand the influence of tip length to the resonance characteristics of oscillator

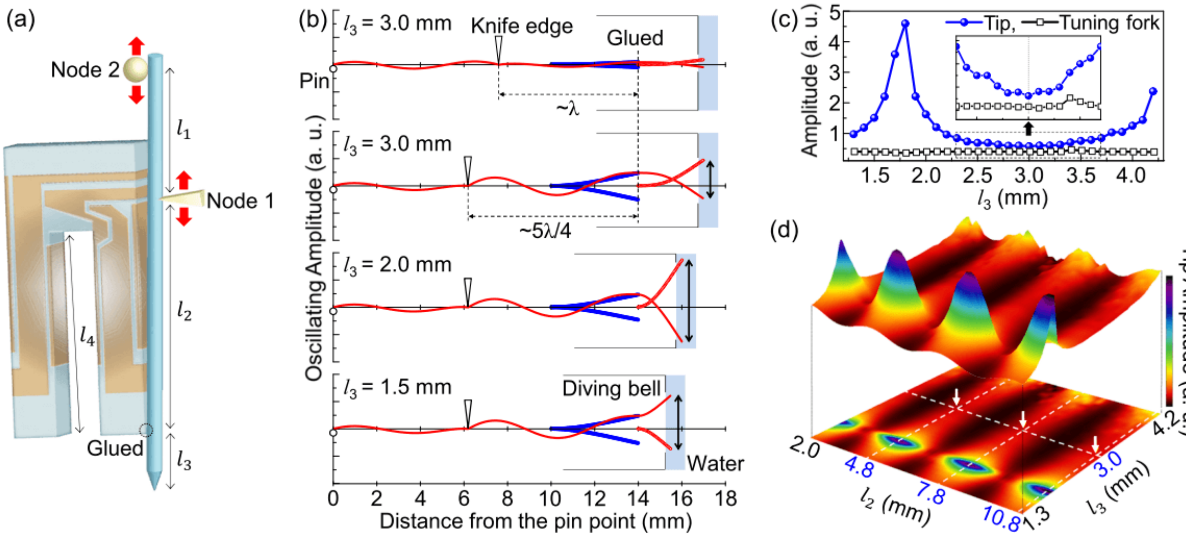

Figure 3.24: (a) Illustration of high-Q oscillator controlled by introducing two nodes at variable distances. (b) Calculated oscillating amplitudes of the tuning fork (blue lines) and the fiber probe (red line). (c) Calculated amplitude variation of the tuning fork-end (black squares) and tip apex (blue circles) as a function of l_3 while maintaining $l_1 = 6.2$ mm and $l_2 = 7.8$ mm. (d) 3D plot of amplitude variation of tip apex as a function of l_2 and l_3.

(Fig. 3.25). While three oscillators have different resonance frequencies, variation tendencies of them are not significantly different and their Q-factors are almost same. From these vibration behaviors, we make a conclusion that the resonance condition is dominantly determined by the lengths l_1 and l_2, but nearly irrespective to the l_3. However, the tip length (l_3) is significant when it is dipped into the liquid because the dithering amplitude of tip is dramatically changed with respect to l_3 and it affects to the Q-factor of oscillator in liquid. Accordingly, the position of the anti-node of l_3 is about 1.5 mm distant from the point of attachment. Thus, the end of 1.5 and 2.0 mm tips is closer to the anti-node and has large amplitude. On the other hand, the end of 3.0 mm tip is exactly set to the node since $\lambda_F/2$ is 3.0 mm, therefore it has smallest amplitude.

Fig. 3.24c shows the modeled amplitude variation of tip apex and tuning fork-end as a function of l_3 (l_1 and l_2 are set to 6.2 mm and 7.8 mm, respectively). Despite the amplitude of the tuning fork terminals for fiber with $l_3 = 1.8$ mm and $l_3 = 3.0$ mm being almost identical, the tip-apex amplitude of the $l_3 = 1.8$ mm tip is ~9 times larger than the $l_3 = 3.0$ mm tip due to the antinodal and nodal locations of tip-end from the point of attachment (see Fig. 3.26 for detail).

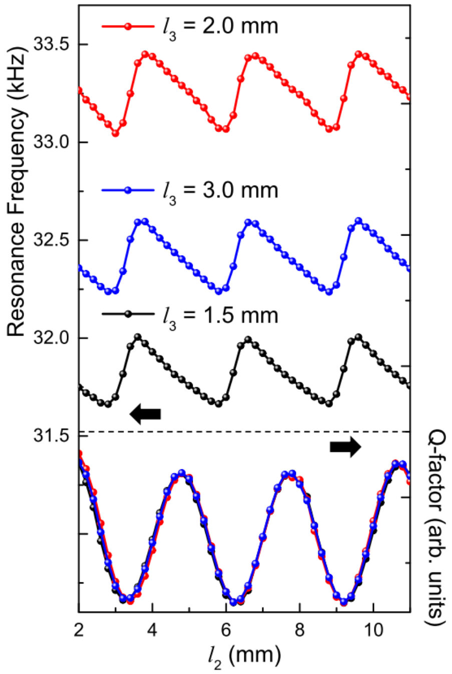

Figure 3.25: Calculation results of the variation of resonance frequency and Q-factor for three different tip lengths ($l_3 = 1.5$, 2.0, and 3.0 mm) with respect to the change of l_1 and l_2 ($l_1 + l_2$ are maintained to 14.0 mm). While the resonance frequencies of three NSOM probes are different, the variation is very similar and Q-factors are almost the same.

This approach thus provides an optimized length of tip (l_3) to maximize force sensitivity when NSOM measurement is performed in liquid by minimizing the resistivity of tip vibration to the viscous medium damping.

Fig. 3.24d shows amplitude variation of tip apex as a function of l_2 and l_3. The operating condition of NSOM in liquid environment is optimized by making the highest Q-factor with l_2 length (4.8, 7.8, or 10.8 mm) and smallest liquid damping with l_3 length (3.0 mm).

Near-Field imaging of cell membranes

In order to enhance the optical sensitivity of the NSOM probe for biomolecular imaging on the cell membrane, plasmon labeling by anti-EGFR conjugated AuNPs attached to the EGFRs is used. AuNPs are excited by a 405 nm laser in side on illumination to enhance the Rayleigh scattering intensity (scattering intensity $\propto 1/\lambda^4$), and the plasmonic scattering signal is collected through the aperture of an optical fiber probe.

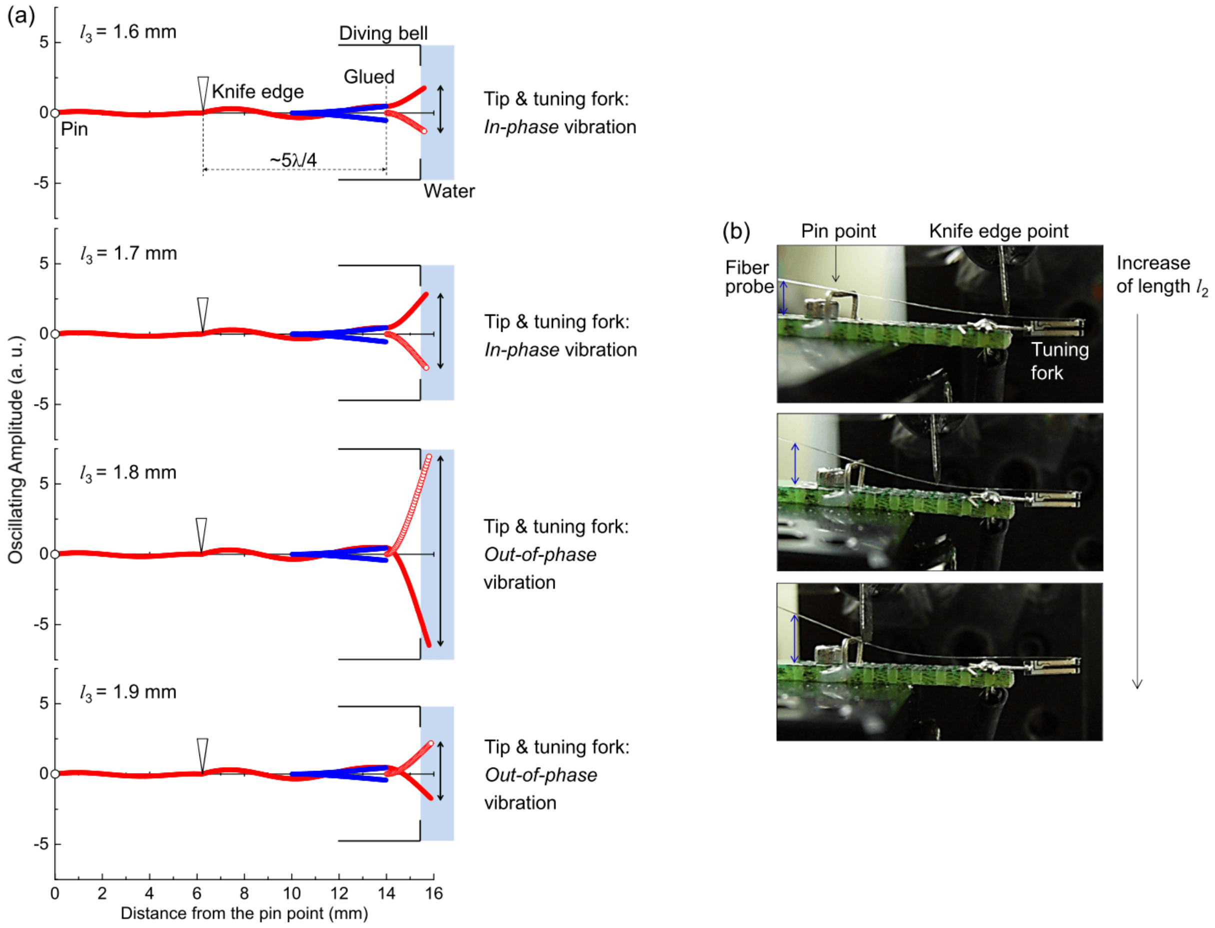

Figure 3.26: (a) Calculated oscillating amplitude curves of the tuning fork (blue lines) and the fiber probe (red line) as a function of l_3 while maintaining $l_1 = 6.2$ mm and $l_2 = 7.8$ mm. Note that the maximum tip-end amplitude ($l_3 = 1.8$ mm) is calculated at the first out-of-phase vibration. Because the amplitude of an out-of-phase vibration is generally larger than in-phase vibration, and the tip-end of $l_3 = 1.8$ mm tip is most closed to the antinode position among the out-of-phase vibrations ($l_3 \geq 1.8$ mm). (b) Photos of test setup for the two nodal wedges method (pin and knife edge positions are not matched with the data). The experimentally observed discrepancy of the resonance frequency and the Q-factor between $l_2 = \sim 3$ mm and $l_2 = \sim 9$ mm (Fig. 3.24a) is attributed to the relatively different compressive force at the pin point, which depends on the position of knife edge. That is to say, despite the compressive force of the knife edge is held constant, the compressive force of the pin point is slightly varied depend on the position of knife edge. This effect makes systematic increase of resonance frequency and Q-factor as a function of l_2.

Fig. 3.27 shows the resulting topography (a) and near-field intensity image (b) of a A431 cell measured in PBS. Several textural features can be identified and distinguished with the EGFR distribution and its local density on the cell membrane possibly related to intracellular organelle locations and stuctures. In general, the axial resolution of NSOM is <10 nm due to the exponential

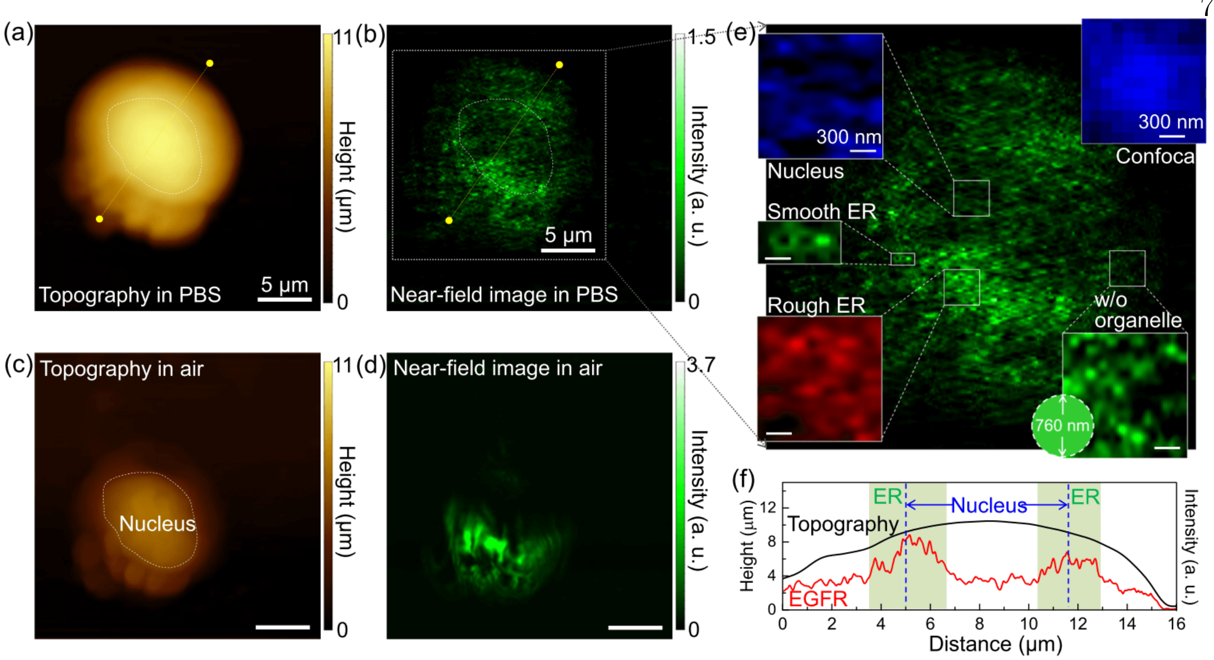

Figure 3.27: Topography and EGFR distribution on the membrane of the A431 cell. Topography (a) and NSOM image (b) of the A431 cell immersed in PBS, and topography (c) and NSOM image (d) of the A431 cell in air after evaporation of PBS. (e) Local variation of surface EGFR distribution corresponding to intracellular nucleus, rough endoplasmic reticulum (ER), smooth ER, and normal region without organelle. The confocal laser scanning microscope image is derived from Fig. 3.23a. (f) Line profiles of topography and EGFR distribution derived from (a) and (b) which show the density distribution of EGFR on the membrane depend on intracellular organelle composition.

decrease of locally confined light intensity with increasing distance to the aperture of NSOM probe [221]. Since the thickness of membrane is 7.5 - 10 nm and the EGFR resides only on the membrane, Fig. 3.27 does not show intracellular image but an EGFR distribution within the membrane, correlated only to the extent that intracellular organelles.

It appears that a lower local density of surface EGFR is observed associated with location of cell nucleus. The high density EGFR region on the membrane is possibly associated with the intracellular endoplasmic reticulum (ER), especially rough ER, because the main function of rough ER is the synthesis and transportation of proteins between the nucleus and cell membrane, and those proteins highly interact with EGFRs [222]. This suggests that the heterogeneous EGFR distribution on the membrane at the zoomed region in red in the left bottom inset corresponds to a structural imprint of intracellular rough ER region.

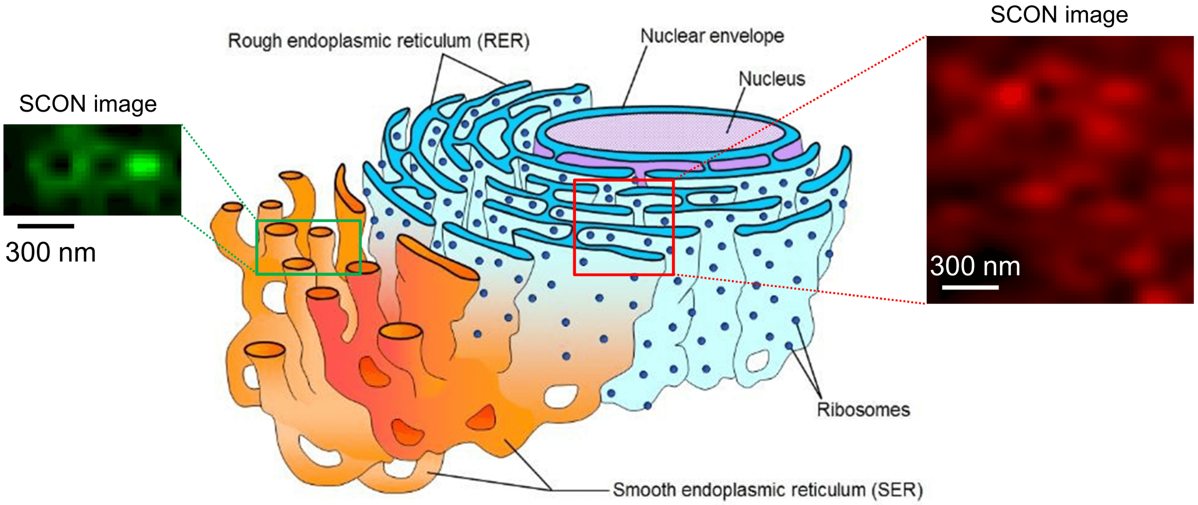

Figure 3.28: Cartoons of organelle structures in the cells. The endoplasmic reticulum (ER) forms an interconnected network of flattened, membrane-enclosed sacs or tubes known as cisternae. It is known that the membranes of ER are continuous with the outer membrane of the nuclear envelope. There are two types of ER: rough ER and smooth ER. The main function of rough ER is the synthesizing and transporting proteins between the nucleus and cell-membrane, and those proteins highly interact with EGFRs. The structure of rough ER is known to be folded like a pile of folded papers. Therefore, we believe the red image zoomed in the left bottom inset is the rough ER region. On the other hand, the observed nanoscale mesh like distribution (green image) is matched with the well known structure of smooth ER: tube shaped like a pipeline with many twists and turns. The organelle structure in the figure is taken from Cronodon.com, and is used with the permission of Cronodon.com.

On the other hand, the zoomed region of surface EGFRs in the left center in green is suggestive to correspond to a structural imprint of intracellular smooth ER region for several reasons. First, the observed nanoscale mesh structure of surface EGFRs matches well with the well known structure of smooth ER (see also Fig. 3.28). Second, smooth ER has no ribosomes and functions in lipid metabolism, carbohydrate metabolism, and detoxification [223]. Therefore, EGFRs on the cell membrane have relatively low local density in the region of smooth ER due to the lack of highly interacting molecules.

Despite the EGFR density on the membrane corresponding to nucleus region is much lower than the membrane region corresponding to the rough ER region (Fig. 3.27f), the cluster diameter is ∼200 nm in both cases as seen in Fig. 3.27e. Note that from the comparison of the EGFR distribution with the membrane regions on the intracellular non-organelles, we confirm the cluster

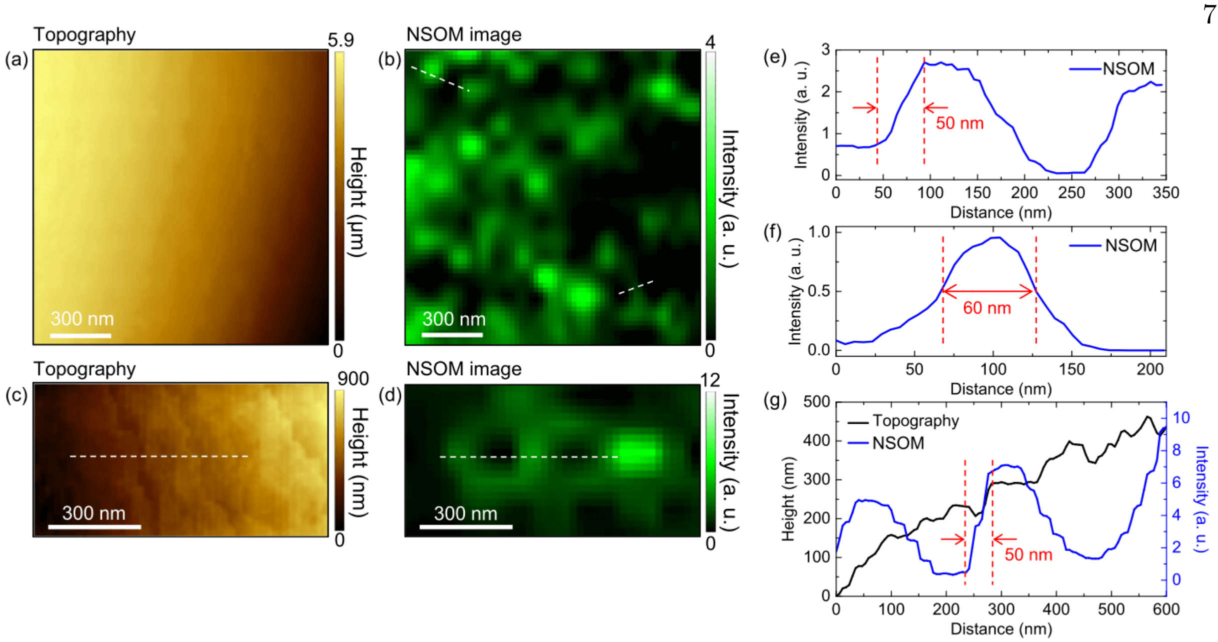

Figure 3.29: Topographies (a, c) and NSOM images (b, d) of the A431 cell immersed in PBS. (e-g) Line profiles derived from the topography and the NSOM images. The ∼50 nm spatial resolution is confirmed, and the NSOM images are not correlated with the surface structure.

size of nucleus and ER is not limited by the spatial resolution of the near-field probe. In the membrane regions without intracellular organelles, ∼50 nm size spots are resolved, which we believe to be a single or a few EGFRs (see also Fig. 3.29 to verify spatial resolution). The correlation of the heterogeneous EGFR distribution on the cell membrane with intracellular organelle composition implies that some proteins residing at the cell organelles possibly interact with the EGFR on the membrane. In contrast, all these spatial features disappear when the cell is dried as shown in Fig. 3.27c and d. We guess the observed EGFR distribution in air is possibly resulted from the aggregation of EGFRs due to the volume contraction of cell during evaporation of water.

In previous studies, the ER structure (inside of cell membrane) was visualized to demonstrate the performance of newly developed super-resolution microscopy [224]. Beyond previous super-resolution imagings of organelle structures, our work visualizes the nanoscopic heterogeneity of membrane biomolecules correlated with intracelluar organelles.

3.3.4 Discussion

There was a considerable body of work to improve the Q-factor under aqueous conditions. Rensen et al. reported the Q-factor could be improved based on the optimized dipping depth of the NSOM probe (Q$\sim$60) [225]. A similar study was carried out by Lee et al. for imaging soft samples immersed in liquid (Q$\sim$400) [226]. However, these studies showed limitations in enhancing the Q-factor beyond a certain level. Höppener et al. reported a significant Q enhancement by attaching a very short fiber probe to a tuning fork and using another optical fiber for laser coupling into the short fiber probe [221]. However, this configuration cannot be applied to a collection-mode NSOM. On the other hand, our method is a versatile tool for collection and illumination modes as well as achieves an extremely Q-factor.

In addition to the high-Q factor, maintaining a stable resonance condition under aqueous conditions is also significant. Recently, we used the stable resonance zone of fiber probe and the resonance tracking method to overcome the resonance change issue when the immersion depth of fiber probe is changed due to the evaporating liquid [215, 227]. Despite these methods are useful for small area scanning, they are inappropriate to apply to large samples such as biological cells. Thus, we adopt the diving bell structure to maintain a stable resonance condition regardless of liquid evaporation and scanning time [228].

Recently, several groups achieved reliable near-field fluorescence imaging on the cell membrane under aqueous conditions [210, 229], yet the spatial resolution was limited to $\sim$100 nm due to the insufficient collection efficiency of the smaller aperture NSOM probes for fluorescence signal. To increase the optical sensitivity and to improve the spatial resolution to $\sim$50 nm, we label plasmonic AuNPs to the EGFRs on the membrane and measure the Rayleigh scattering instead of fluorescence signal. This idea is an inverse approach to the use of plasmonic nanostructures at the near-field probe aperture [212, 230]. From combinatorial optimization of these requisites, we enable the near-field imaging of biomolecules on the cell membrane under buffered conditions.

Several studies have applied NSOM to the biomolecular imaging of dried cells due to the technical difficulties under buffered conditions [231, 232, 233]. However, we believe that cell membrane structures and protein distributions could be deformed due to evaporation of water as seen in Fig. 3.27. Therefore, NSOM application in liquid environments is highly required for in-depth nano-biology study.

Nowadays anti-EGFR cancer therapy is widely administered to patients [234]. However, a large portion of patients do not respond to the therapy for unknown reasons. Therefore, better understanding of the complex network of signaling pathways between EGFRs and intracellular biomolecules is required. Fluorescence resonance energy transfer (FRET) and time-resolved spectroscopy have been used to investigate the EGFR mechanisms [235, 236, 222]. However, these diffraction-limited characterization methods leave many open questions requiring molecular imaging techniques to understand more quantitative properties. Since the proposed method can be easily combined with other optical modality such as Raman, time-resolved, and absorption spectroscopies [237, 98, 238], we expect the NSOM-FRET or other kinds of combined techniques will be used to explore unexamined nanoscale dynamics on the cell membrane as well as the detailed nanoscale processes.

In summary, we demonstrated a new near-field imaging approach based on the control of the nano-mechanical near-field probe resonance by optimizing the tip length of NSOM probe for improved near-field imaging performance in liquid. A very high Q-factor (2800 in water) is achieved by a 3 mm tip as well as two nodal wedges method and a stable resonance condition is maintained by applying a diving bell structure. To overcome the low optical sensitivity of general fluorescence detection, AuNPs are labeled to the EGFR and the plasmonic scattering signal is probed with $\sim$50 nm spatial resolution. In the cell membrane imaging of A431 cell, we reveal the nanoscale correlation between the local distribution of EGFR on the membrane and intracellular organelle composition such as nucleus, rough ER, and smooth ER. The approach is generally applicable for both aperture and scattering type scanning near-field microscopy and TERS, and might lead the way to a greater utility of near-field imaging as a complementary technique to other super-resolution imaging techniques for biological applications in liquid conditions.

3.4 Strong coupling of tip plasmon with a single quantum dot[4]

3.4.1 Motivation

Photoluminescence (PL) is a spontaneous process following photoexcitation [239]. PL characterization allows us to understand electronic structure, impurity, doping, and defect states of materials [240]. When semiconductors are excited by a laser with a photon energy above the photonic bandgap, excitons form with a coherent polarization at the excitation laser frequency [241]. In general, the coherent polarization dephases due to electron- and phonon-scatterings, which induce electron and hole populations in the conduction and the valence bands, respectively [242]. Some of the populated carriers recombine as a form of exciton, with PL emission with the energy of material′s bandgap [243]. On the contrary to this radiative recombination (γ_r), the other populated electrons and holes recombine without photon emission, i.e., non-radiative recombination (γ_{nr}).

To better understand PL in semiconductors, we shall briefly discuss fundamental concepts of excitons, a Coulomb-correlated electron-hole pair, and the exciton binding energy, the required energy to decouple electron and hole, defined by a Russian theorist Yakov Frenkel [244]. In the Wannier and Mott picture [245, 246], excitons in semiconductor crystals are described as weakly bound and delocalized electrons and holes. Delocalization of the electrons and holes is modeled by the effective mass of electrons (m_e) and holes (m_h), in a material with dielectric constant ε. The wave function $f(r)$ is given by the Schrödinger equation:

$$-\frac{\hbar^2}{2\mu}\triangle f(r) - \frac{e^2}{\varepsilon r} f(r) = E f(r), \tag{3.4}$$

where μ is the reduced mass ($\mu = m_e m_h/(m_e+m_h)$) and r is the electron-hole distance. By solving this equation, we can derive the $f(r)$ for the $1s$ state of exciton:

$$f_{1s}(r) = \frac{1}{\sqrt{\pi a_B^3}} e^{-r/a_B}, \tag{3.5}$$

---

[4] This section covers measurements performed and analyzed by K.-D. Park, and supervised by M. B. Raschke. This work was performed in collaboration with H. Leng and M. Pelton from the University of Maryland at Baltimore County.

where a_B is the Bohr radius:

$$a_B = \frac{\hbar^2 \varepsilon}{\mu e^2}. \tag{3.6}$$

The exciton binding energy is defined as:

$$E_B = \frac{\mu e^4}{2\hbar^2 \varepsilon^2} = \frac{\hbar^2}{2\mu a_B^2}. \tag{3.7}$$

We can estimate the exciton binding energy is much less than Rydberg constant by taking into account the reduced mass divided by the dielectric constant square in Eq. 3.7. From these descriptions, we expect that the exciton binding energy is relatively weak in typical bulk inorganic crystals.

As we mentioned in Chapter 1, the dimensional reduction and associated increased quantum confinement in materials give rise to significant modifications in material properties. When the size of semiconductor is smaller than the twice of exciton Bohr radius, the excitonic bandgap and exciton binding energy change significantly due to quantum confinement effect [40]. We can expect high PL quantum yield ($\gamma_r/(\gamma_r+\gamma_{nr})$) in low-dimensional semiconductors, such as quantum wells (2D), wires (1D), and dots (0D). As can be expected, 0D systems, quantum dots (QDs), give rise to most significant changes in excitonic properties due to the strongest quantum confinement [243, 247]. For example, we can systematically control the PL energy and quantum yield by tuning the size of QDs [248].

These PL properties of semiconductors are strongly influenced also from the interacting environments [39]. Specifically, the 0D nature of QDs with its a few nanometers dimension allows us to significantly modify PL properties by an environmental control. Therefore, careful environmental control gives access to manipulating emission properties of QDs for a broad range of photonic and electronic device applications. Most importantly, understanding and control of the environmentally modified PL properties of single QDs are highly desirable since they give rise to new physical properties distinct from those at a bulk crystal.

In this section, we further extend our tip-enhanced spectroscopy study to the single QDs. We place a single CdSe/ZnS QD within a nanoscale gap between a Au tip and Au substrate, and measure single QD PL using tip-enhanced PL (TEPL) spectroscopy. Here, we observe not only the high PL enhancement but also the double PL peaks split by the coupling between exciton and plasmon at the strong coupling regime.

3.4.2 Results and discussion

We prepare samples for single QD measurements in several steps. We first deposit Au film on to the silicon wafer with 100 nm thickness by thermal evaporation. To decrease the PL quenching of QDs to the Au film, we then add a dielectric cover layer, Al_2O_3, on to the Au film with 0.5 nm thickness by using atomic layer deposition (ALD) method. Then, chemically synthesized CdSe/ZnS core-shell QDs are carefully drop cast onto the Al_2O_3 from a dilute solution of QDs with very low density to make a single dot state. The density is confirmed as ∼20 to 30 QDs in a 10 μm × 10 μm area by a far-field PL imaging and an atomic force microscopy (AFM) measurement. Since the single dots are expected to be unstable due to surface diffusion in ambient conditions, we add another 0.5 nm thickness Al_2O_3 cover layer on to the QDs as shown schematically in Fig. 3.30a. Since the electric dipole of the deposited QDs is randomly oriented with respect to surface normal of the substrate, we expect significant heterogeneity in the coupling between the single QD PL and the gap plasmon induced Au PL (*out-of-plane*), as illustrated in Fig. 3.30b.

The TEPL spectroscopy experiment is based on side illumination of tilted Au tip manipulated in a shear-force AFM as illustrated in Fig. 3.30c. This tilting tip geometry gives rise to better optical field confinement than a conventional surface normal oriented tip geometry due to the localized surface plasmon resonance (LSPR) antenna effect. We will discuss more details of this tilting tip effect in chapter 5. In the TEPL spectroscopy setup, the QD sample is mounted to a piezoelectric transducer (PZT, P-611.3, Physik Instrumente) with sub-nm precision positioning. Electrochemically etched Au tips (∼10 nm apex radius) are attached to a quartz tuning fork (resonance frequency = ∼32 kHz) [20]. To regulate the tip-sample distance, the AFM shear-force amplitude is monitored and controlled from the electrically driven tuning fork [120]. Coarse tip positioning is performed using a stepper motor (MX25, Mechonics AG), and shear-force feedback

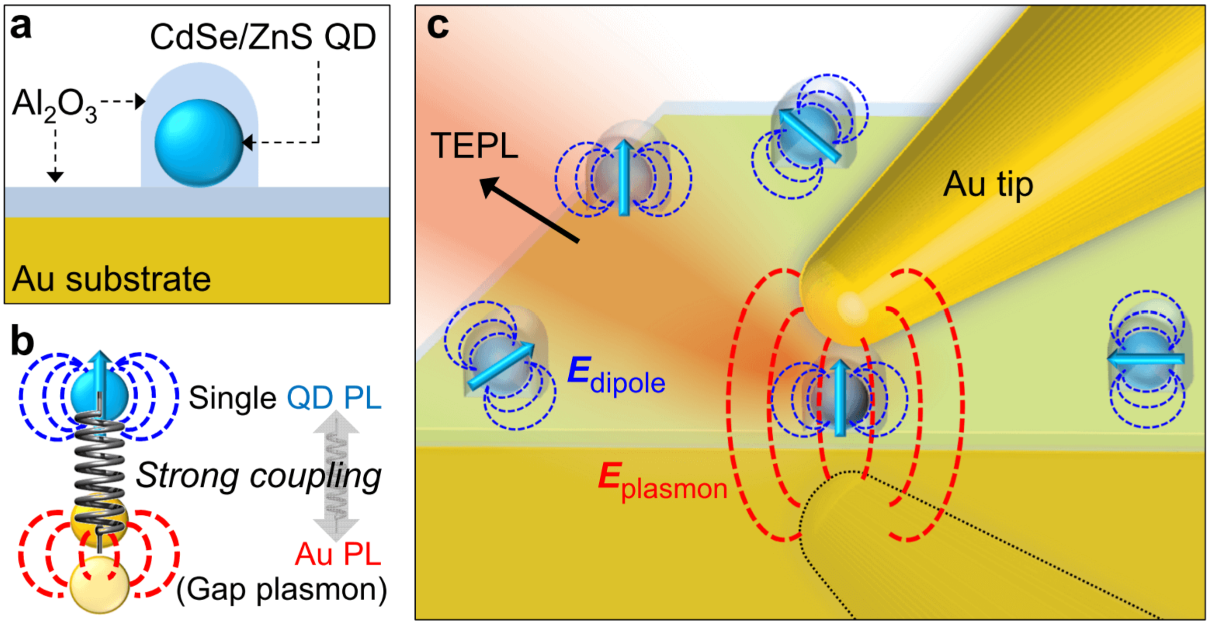

Figure 3.30: (a) Schematic illustration of a sample structure. CdSe/ZnS quantum dot on the Au substrate with Al_2O_3 cover layer. (b) Illustration of the strong coupling between photoluminescence responses of the quantum dot and the gap plasmon. (c) Schematic illustration of TEPL setup for single quantum dots with tilted Au tip.

and sample position are controlled by a digital AFM controller (R9, RHK Technology). A Helium-Neon laser beam (632.8 nm, $\leq$ 0.3 mW), after passing through a half wave plate for polarization control, is focused into the junction between the Au substrate and the tip apex by an objective lens (NA=0.8, LMPLFLN100×, Olympus). TEPL signal is collected in backscattered direction, passed through an edge filter (633 nm cut-off) and detected using a spectrometer (f = 500 mm, SpectraPro 500i, Princeton Instruments) with a thermoelectrically cooled electron-multiplied charge-coupled device (CCD, ProEM+: 1600 eXcelon3, Princeton Instruments). All experiments are performed at room temperature.

We first investigate far-field PL characteristics of single QDs sample. Fig. 3.31a shows time series far-field PL response of single CdSe/ZnS QD measured at a single sample location. We observe an obvious fluctuation in intensity and spectral peak position. This PL fluctuation is in good agreement with a general blinking behavior of single QDs associated with an illumination-induced charging effect or a non-radiative Auger recombination [249]. From the observed blinking,

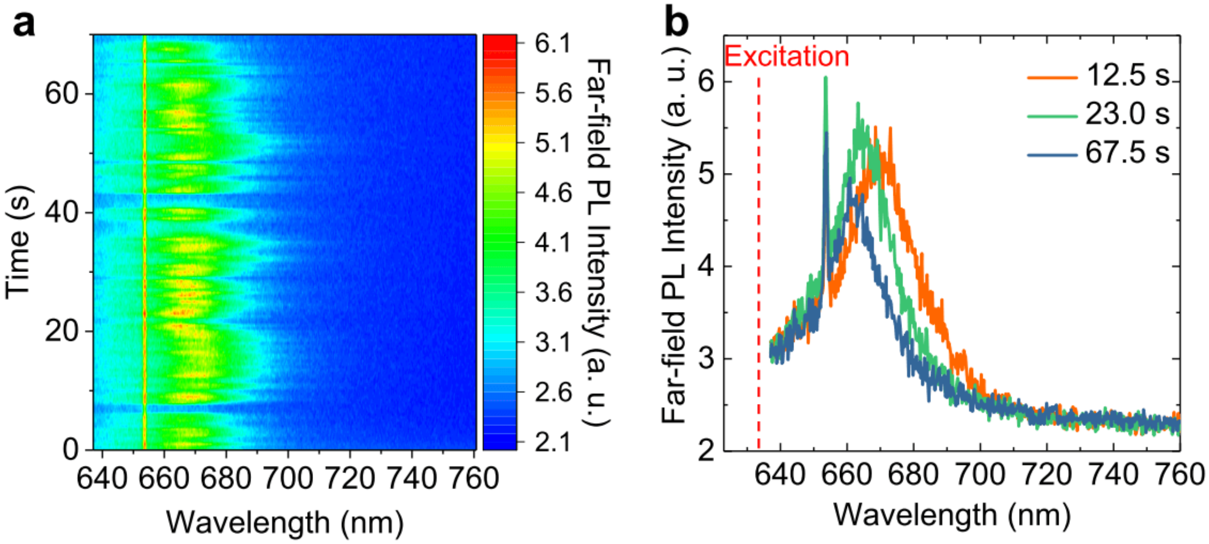

Figure 3.31: (a) Time series far-field PL response of a CdSe/ZnS quantum dot on the Au substrate. (b) Selected far-field PL spectra from (a) exhibiting spectral fluctuation.

we confirm the single QD states of our samples on the substrate. In addition, as can be seen in Fig. 3.31a, this single QD state provides non-quenched PL response for a few minutes owing to the suppressed spectral diffusion by a dielectric cover layer. Fig. 3.31b shows selected PL spectra from time series data (Fig. 3.31a) exhibiting peak energy variation and linewidth change in blinking process. We observe a symmetric spectral shape in measured far-field PL spectra meaning no coupling effect between the QD PL and the plasmon response of Au film. The narrow peak at ∼653 nm is a Raman scattering response of a Al_2O_3 cover layer.

We then perform TEPL spectroscopy experiment on the same sample to understand coupling behaviors between the QD PL and the Au PL of gap plasmon. Fig. 3.32a shows time series TEPL response measured for 30 s. Strong and stable gap plasmon response from the dipole-dipole interaction between Au tip and its image on the Au substrate is observed. TEPL response of a single CdSe/ZnS QD is reproducibly observed during the measurement even though the signal fluctuates more than the far-field response. Fig. 3.32b shows gap plasmon PL and selected TEPL spectra derived from the time series data. Here we can directly compare the intensity of TEPL spectra with far-field PL spectra in Fig. 3.31b under identical experimental conditions. We observe

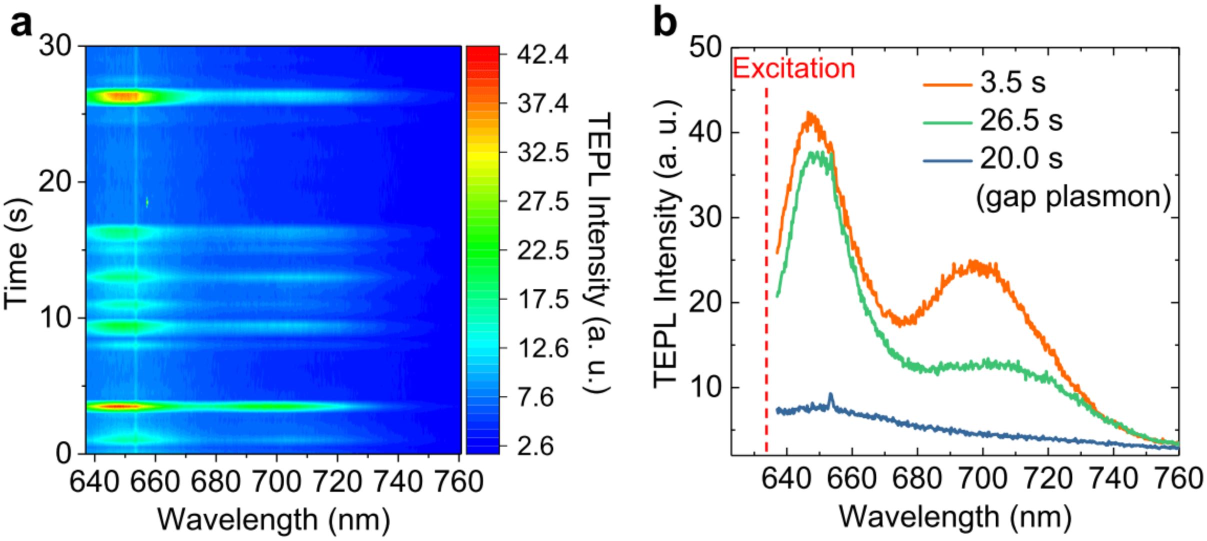

Figure 3.32: (a) Time series TEPL response of a CdSe/ZnS quantum dot on the Au substrate. (b) Selected TEPL spectra from (a) exhibiting PL peak splitting by a strong coupling.

modified PL characteristics of a single QD including enhanced PL due to the tip-Au substrate gap plasmon resonance at ∼650 nm. We can control the Au PL intensity by regulating the tip-sample distance based on a shear-force feedback mechanism. We maintain the tip-sample distance with ∼1 nm during the measurement, and the intensity of this Au PL (at 20.0 s, blue in Fig. 3.32b) is comparable to the far-field PL intensity of a single QD (Fig. 3.31). The QD PL is also highly enhanced resulted from the largely increased excitation rate and emission rate at the Au tip-Au substrate nano-gap. We will discuss more about the TEPL mechanism in Section 4.3. In addition to the enhanced PL, we observe splitting of the PL peak, which we attribute to coupling between the QD PL and the Au PL. We measure the splitting to be ∼160 meV in obtained TEPL spectra. This large energy splitting in the PL suggest coupling between tip and QD is in the strong coupling regime. The higher energy peak near the plasmon resonance shows stronger PL emission than the lower energy peak. This feature is also an evidence of Au PL interaction with the QD PL.

To better understand the coupling, we measure TEPL of other QDs on the sample. We slowly move the sample position with maintaining the tip-sample distance. We often observe non- or small-enhanced TEPL spectra from some QDs even though they show blinking behaviors. We believe this

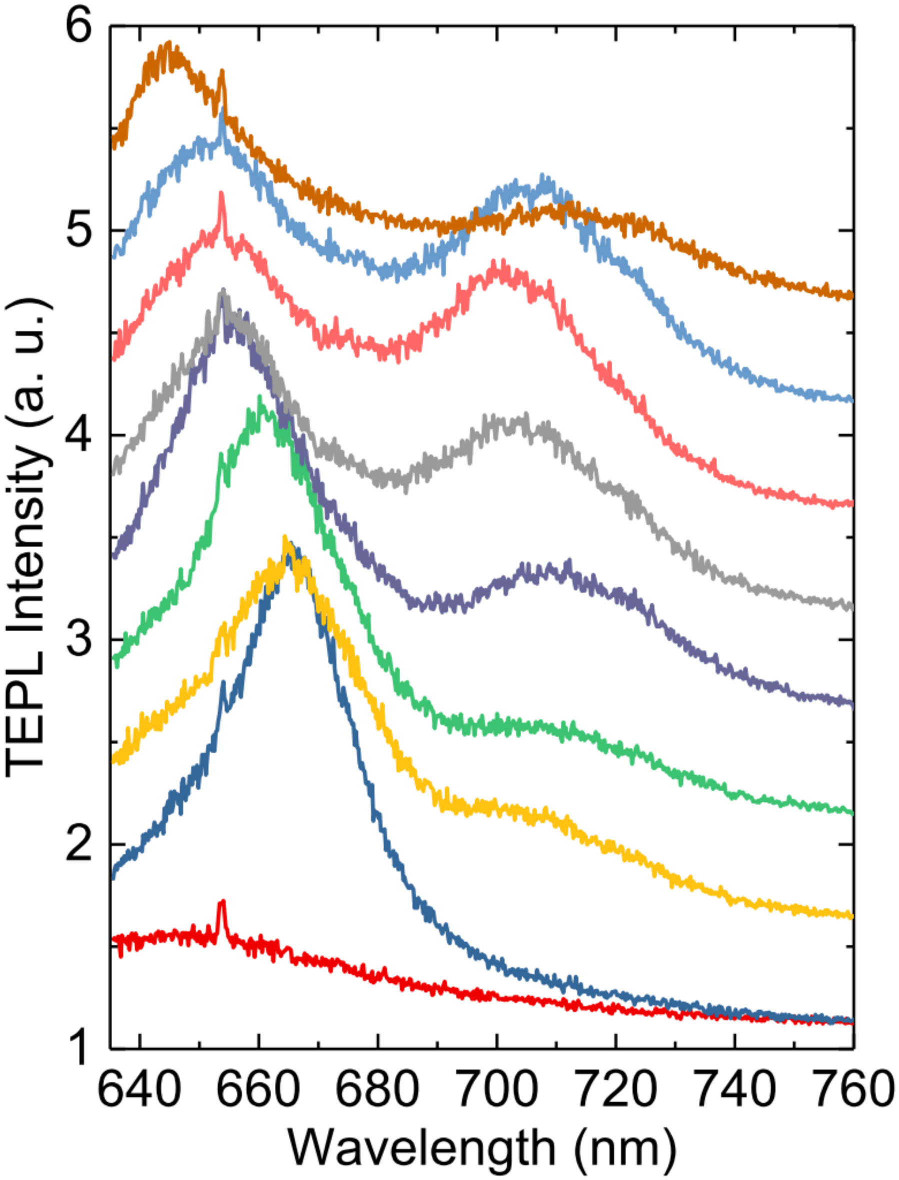

Figure 3.33: Selected TEPL spectra of different single CdSe/ZnS quantum dots on the Au substrate measured while changing the sample position.

variation in the QD PL is associated with a heterogeneous QD orientation on the substrate. Because PL of QDs with non-vertically oriented transition dipole moment can be expected to give rise to weak coupling to the gap plasmon response. Fig. 3.33 shows TEPL spectra measured at different QDs with a same Au tip. We can see strong gap plasmon PL (red) when there is no QD in the tip-substrate gap. The second curve from bottom (blue) shows non-split TEPL spectrum. While the peak energy is in good agreement with the far-field PL peak, the spectrum shows asymmetric shape with largely enhanced intensity. This asymmetric spectral shape is possibly attributed to Fano interference. We select several TEPL spectra in the strong coupling regime to understand the overall trend in PL energy splitting. As we observed in Fig. 3.32b, the lower energy peaks show weaker intensity compared to the higher energy peak. We observe variation in the PL peak splitting and plasmon-QD coupling correlated with the lateral distance between the tip and QD positions since the tip height above the sample is constant during measurements. The PL energy splitting by a strong coupling is observed up to 200 meV in this measurement.

This work demonstrates a significant modification of the spontaneous emission characteristics of 0D semiconductors induced by optical coupling to nano-optical antenna-tip in the strong coupling regime. Recently, strong coupling phenomena in various confined systems were observed [250, 251, 252]. However, most of these observations were measured as changes in the absorption spectrum. The coupling between PL signals we observe implies a much stronger coupling strength that is observable even at room temperature. In addition, we envision that the demonstrated antenna-tip approach for tip-enhanced strong coupling in a single QDs provides greater understanding of modified optical properties of semiconductors as well as a new path for design of photonic devices.

Chapter 4

Probing and control nanoscale processes in van der Waals materials

4.1 Probing bilayer grain boundaries in large area graphene[1]

As contrasted with small graphene flakes, relatively little is known about the lattice and electronic structures of grain boundaries in large area graphene sheets, and their optical and Raman properties, despite their increasing significance for technological applications. Here we identify that grain boundaries in chemical vapor deposition-grown large area graphene possess a twisted bilayer structure, as determined from correlated analyser of topography, near-field scattering, and multispectral tip-enhanced Raman spectroscopy (TERS) imaging with $\sim$18 nm spatial resolution. In addition, we determine the misorientation angle of the bilayer grain boundaries from a detailed quantitative analysis of the phonon scattering properties associated with the modified electronic structure at the K-point of the Brillouin zone. We also investigate the distinct Raman characteristics of other defects such as wrinkles and nucleation sites, which are strongly correlated with nanoscopic structural curvature effects and atomic scale carbon hybridization. This work not only reveals the detailed properties of the defects in large area graphene at the nanoscale regime, but also demonstrates the potential of correlated analysis of multispectral TERS imaging as generally applicable to a wide range of two-dimensional materials beyond graphene.

---

[1] This section draws significantly from [253]. The experiment was performed and analyzed by K.-D. Park in collaboration with Sungkyunkwan University, and supervised by M. B. Raschke and M. S. Jeong.

4.1.1 Motivation

Large area graphene sheets grown by chemical vapor deposition (CVD) have been proposed as a route to realize mass production and commercialization of near-ballistic transport electronic devices [53, 54]. So far, most large area synthetic graphene is polycrystalline. The associated grain boundaries (GBs) [53, 55, 56, 57] have been identified as a major limitation in device applications due to their modified electronic structure and inhibiting carrier transport [58, 59]. Therefore, understanding the detailed characteristics of GBs is a prerequisite for better design of graphene sheets.

Despite the greater applicability of large area graphene sheets compared to graphene flakes, most theoretical and experimental studies of GBs have focused on the analysis of atomic defects observed in adjacent crystal faces [60], which show significant differences from larger-scale deformations of GBs in large-area graphene. Scanning tunneling microscopy (STM) and transmission electron microscopy (TEM) can investigate structural defects, electrical conductivity, and strain associated with GBs with atomic scale spatial resolution [254, 255, 256, 56]. However, these high-resolution local probes provide only a limited field of view, without optical and chemical information. In contrast, Raman spectroscopy and imaging studies of GBs in large area graphene have shown both an increase and decrease in the G$'$ peak intensity at GBs [53, 57, 257], and thus have left a confusing picture regarding their lattice structure and vibrational properties, in part due to the diffraction-limited spatial resolution and a low sensitivity [60] of conventional Raman spectroscopy.

In order to complement STM, TEM, and conventional Raman spectroscopy and to bridge their length scales, here we present $\sim$18 nm spatial resolution tip-enhanced Raman spectroscopy (TERS) and imaging to understand lattice and electronic structure, as well as elastic and phonon scattering properties of GBs in CVD grown large area graphene. Through correlated analysis of topography, near-field scattering, and multispectral TERS imaging, we reveal bilayer GBs in the form of twisted stacking at the boundary between two misoriented crystal facet. We also determine the misorientation angles of the bilayer GBs from a detailed quantitative investigation of the Raman

G and G′ peak properties, which varying with respect to the misorientation angle associated with the modified electronic structure at the K-point of the Brillouin zone.

Further, we investigate the distinct Raman characteristics from a wrinkle, a different type of line defect. In contrast to the GBs, only the G′ peak exhibits significant changes in intensity with no associated spectral shift in the vicinity of the wrinkle, which directly correlated with a nanoscopic structural curvature effect. From multispectral TERS mapping, we also resolve the chemical variation associated with nucleation sites (NSs), where we confirm AB stacking bilayer structures at the NS and find an unexpected phonon scattering response of the D′ peak, which is associated with sp^3-type carbon hybridization defects. Beyond the newly revealed properties of the defects, these results may provide clues to understand the growth mechanism of large area graphene and the formation of nanoscale defects. Furthermore, our work demonstrates the potential of correlated analysis of multispectral TERS imaging as a generally applicable approach for the investigation of the wide range of two-dimensional materials beyond graphene.

4.1.2 Experiment

We study large area graphene grown on a 100 μm thick copper foil using CVD. The chamber was heated up to 1100 °C in 1000 sccm of Ar and 200 sccm of H_2 environment, then annealing was maintained for 20 min. CH_4 gas was then injected at a reduced pressure of H_2 to nucleate and grow graphene. The sample was cooled down to room temperature with an optimized cooling rate. The as-grown sample was then transferred onto a glass cover slip. Details can be found in ref [258].

Fig. 4.1a and b show a schematic of TERS setup. The multispectral TERS imaging system used in these experiments is based on a modified commercial confocal Raman imaging system (NTEGRA spectra, NT-MDT). The sample is mounted to a piezoelectric transducer (PZT) for xyz scanning, with a digital controller. Au tips were electrochemically etched with ∼10 nm apex radius, and glued to a quartz tuning fork (resonance frequency = ∼32 kHz) [32]. For shear force feedback, the tuning fork/Au tip assembly is mechanically driven at its resonance frequency and the amplitude is monitored for tip-sample distance control. A Helium-Neon laser (632.8 nm, $P < 2$ mW) is focused

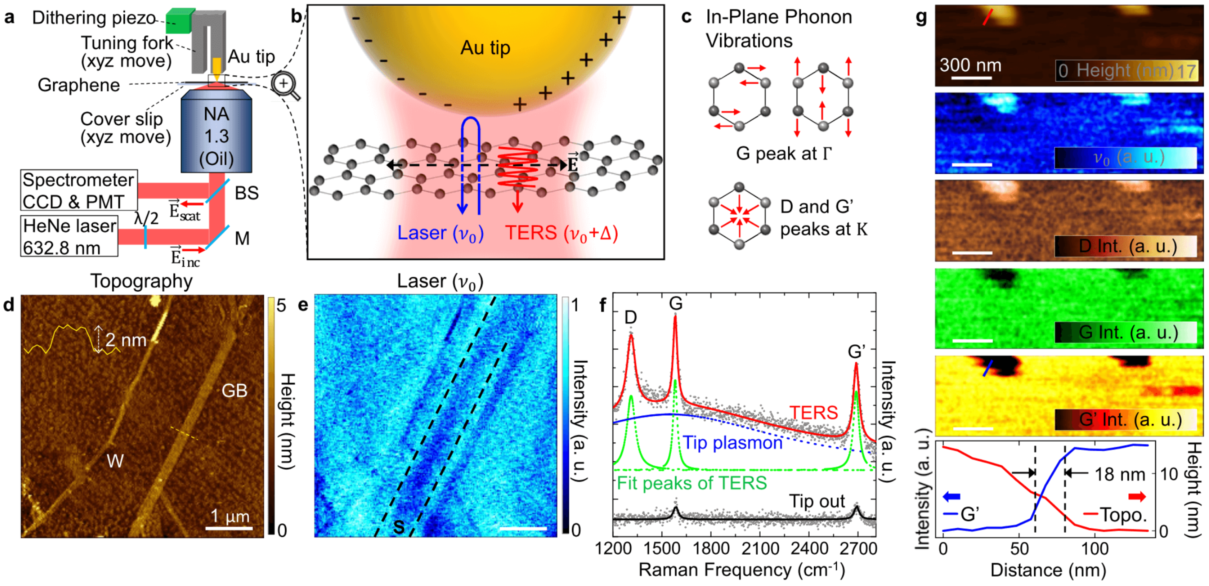

Figure 4.1: (a) Schematic of multispectral TERS imaging (BS: beam splitter, M: mirror). (b) Illustration of plasmon-enhanced light-matter interactions at the tip-graphene junction. (c) Illustration of in-plane phonon modes of graphene. (d) Topography of a CVD grown large area graphene measured by shear force AFM exhibiting wrinkle (W) and grain boundary (GB) structures. (e) Simultaneously measured tip-enhanced Rayleigh scattering image. (f) TERS (red line) and confocal Raman spectra (black line) with Lorentzian line fit analysis. Blue and green dashed lines are tip plasmon and Raman spectra, respectively. (g) Simultaneously measured multispectral TERS images of local defects (contaminations) exhibiting ∼18 nm spatial resolution.

onto the transferred monolayer (ML) graphene sample by an oil immersion objective lens (NA = 1.3), with the linear polarization effectively exciting in-plane vibrational modes (Raman D, G, and G′ peaks) as described in Fig. 4.1b and c. The Au tip of the shear-force atomic force microscopy (AFM) is positioned in the focal spot to enhance the Raman scattering signal by localized surface plasmon resonance (LSPR) and to increase the spatial resolution for nanoscale TERS imaging. The near-field Rayleigh scattering signal from the Au tip is simultaneously measured, providing an approximate measure of the absorption of the thin graphene films. Confocal Raman measurements are performed with the Au tip retracted from sample.

For pre-characterization, topography and near-field Rayleigh scattering images of a wrinkle (indicated by W) and grain boundary (indicated by GB) structure on transferred ML graphene are measured as shown in Fig. 4.1d and e. The scattering intensity is decreased at both wrinkle and

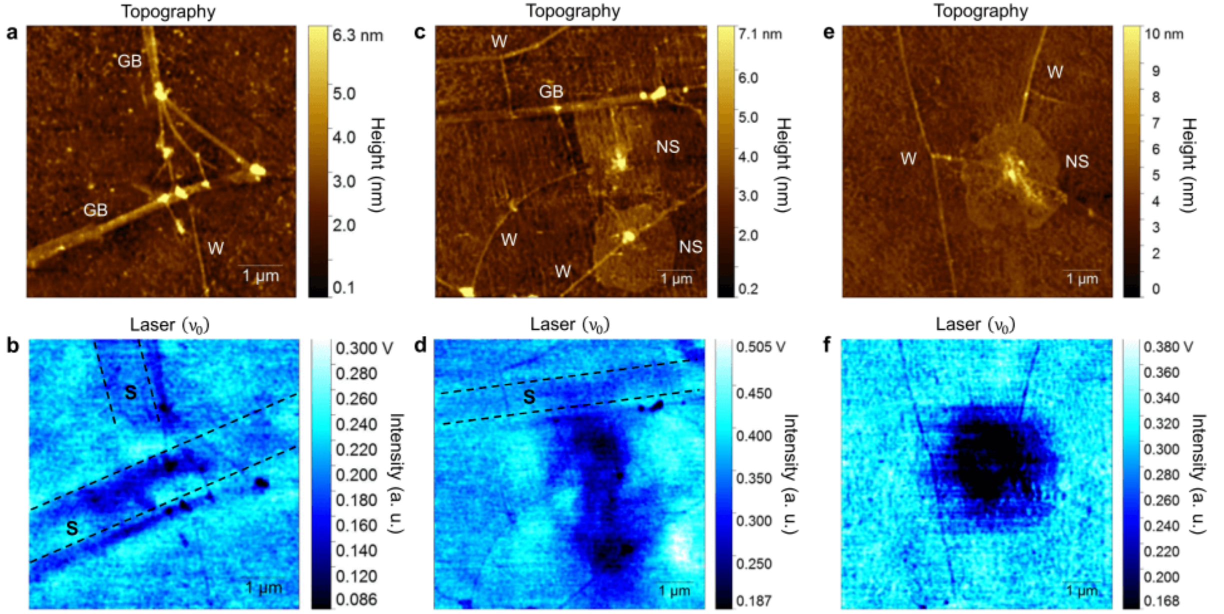

Figure 4.2: (a, c, e) Topographies of CVD grown large area graphene measured by shear force AFM exhibiting wrinkle (W) and grain boundary (GB) structures. (b, d, f) Simultaneously measured tip-enhanced Rayleigh scattering images.

GB structures due to the stronger absorption compared to ML regions. An additional dark stripe (indicated by S, between the black dashed lines) is observed next to the GB in the scattering signal, but does not appear in the AFM topography. This dark stripe is generally observed for other GBs as well in our experiment (see Fig. 4.2 for measurement results of other GBs).

Fig. 4.1f shows a Lorentzian line fit analysis of the TERS and confocal Raman spectra obtained for a single-crystal grain region. The blue and green dashed lines show the tip plasmon spectrum and fit peaks of the three vibrational modes, derived from the TERS spectrum. The G peak intensity is weaker than the G′ peak in the confocal Raman measurement, but it is more enhanced in TERS due to a resonance Raman effect by the tip plasmon [19, 20]. In addition, the Raman D peak in the TERS spectrum appears consistently, though with varying intensity. A large contribution to the D peak likely arises due to an induced artificial defect, from the highly localized electromagnetic field at the tip apex [259].

To confirm the instrumental spatial resolution of the multispectral TERS imaging setup, we perform test measurements of local defects on graphene as shown in Fig. 4.1g, as a similar

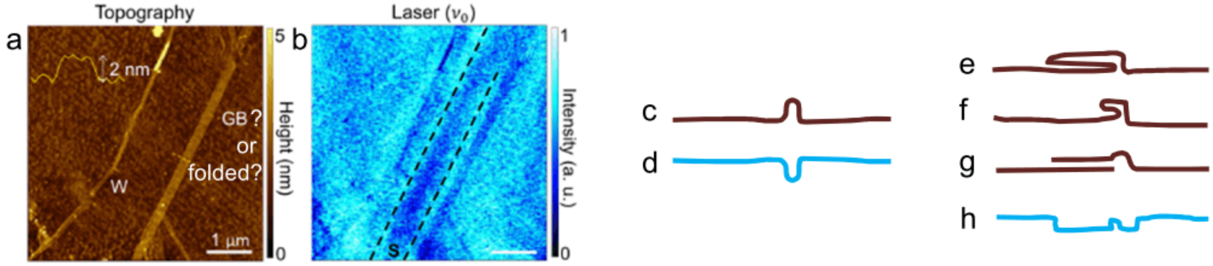

Figure 4.3: (a) Topography of a CVD grown large area graphene measured by shear force AFM exhibiting line defects. (b) Simultaneously measured tip-enhanced Rayleigh scattering image. Expected cross-sections of the wrinkle structures (c), and its optical signal (d). Expected cross-sections of the folded or grain boundary structures (e-g), and optical signal (h) for the structures (e) and (g).

experiment to previous TERS study [260]. A ∼18 nm spatial resolution is achieved in the G′ peak intensity image, and the smooth change in height in the simultaneously measured topography confirms that this optical spatial resolution is not resulted from topographic artifacts.

4.1.3 Results

Classification of the wrinkles, grain boundaries, and folded structures

For type classification of the line defects in large area graphene, we consider four analysis stages: (1) Topographic feature (AFM), (2) Expected cross-section, (3) Optical feature, (4) Raman feature.

1. Confirmation of the other line defects: grain boundary (GB) and folded

(1) Topographic feature (AFM): wide width (∼200 nm).

(2) Expected cross-section: from the measured AFM image, we can infer the cross-section of both the folded structures such as Fig. 4.3e and f and grain boundary structure such as Fig. 4.3g. The folded structures should be trilayer with AB or 0° (near 0°) stacking angles. While the grain boundary should be bilayer with random stacking angles.

(3) Optical feature: from the measured near-field scattering image (Fig. 4.3b) similar to Fig. 4.3h, we can exclude the possibility of the expected cross-section (f).

(4) Raman feature:

a) Folded (Fig. 4.3e): for AB trilayer graphene, according to the group theory analysis, fifteen Raman G′ peaks are allowed since there are multiple electron-phonon scatterings from K to K′ point which occurred by three different iTO phonon branches [261]. Experimentally, the FWHM of AB trilayer graphene should be clearly broader than monolayer graphene with asymmetric spectral shape, and also the G′ peak intensity should be weaker than monolayer [261]. Raman properties of the 0° (near 0°) stacking angle trilayer graphene should also be similar to AB trilayer graphene.

b) Grain boundary (Fig. 4.3g): from the bilayer with random misorientation angles, various combinations of Raman D, G, and G′ peaks should be observed. Therefore, the line defects in Fig. 4.4 are bilayer grain boundaries.

From these correlated analysis, we classify the grain boundaries and folded structures from various line defects.

2. Confirmation of the wrinkles

(1) Topographic feature (AFM): narrow width (∼50 nm).

(2) Expected cross-section: from the measured AFM image, we can infer the cross-section of the wrinkle similar to Fig. 4.3c.

(3) Optical feature: from the expected cross-sectional structure, we can infer the cross-section of the optical image similar to Fig. 4.3d, which could be observed due to stronger absorption compared to the monolayer crystal face. Fig. 4.3d is also in good agreement with the measured near-field scattering image (Fig. 4.3b).

(4) Raman feature: the G′ peak intensity should be decreased due to the structural curvature effect with no change in D and G peaks (see Fig. 4.9).

From these correlated analysis, we classify the wrinkle from various line defects.

Multispectral TERS imaging of grain boundaries

Fig. 4.4b-f show the near-field Rayleigh scattering image and TERS responses, which re-

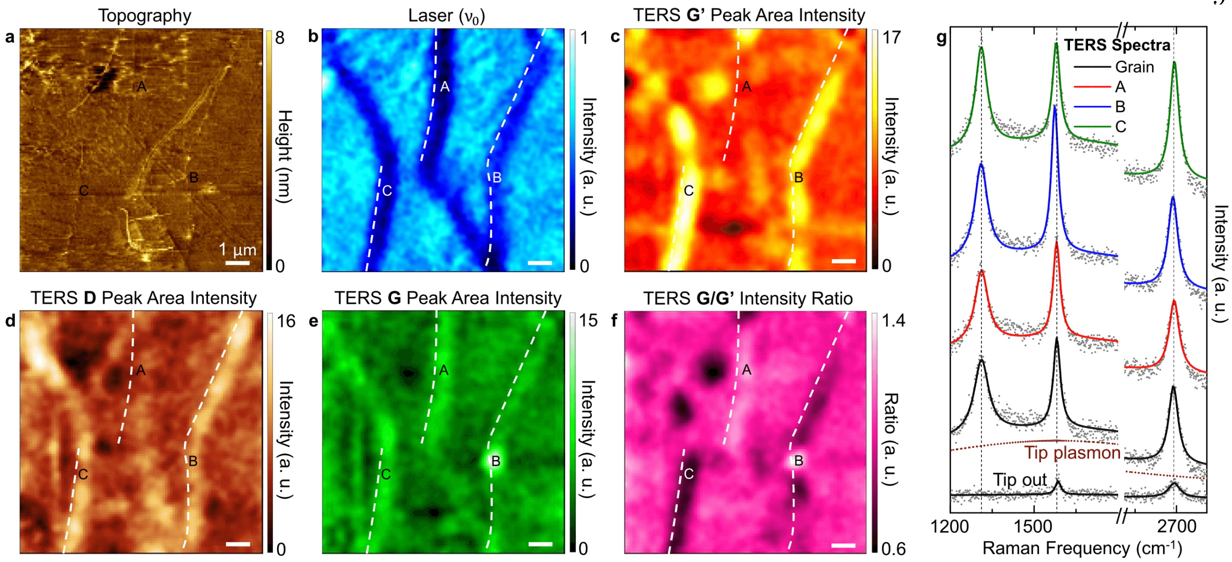

Figure 4.4: (a) Topography of a CVD grown graphene exhibiting structural defects such as wrinkles and grain boundaries. (b) Tip-enhanced Rayleigh scattering image. Distinct grain boundary structures of the topography (a) are marked with white dashed lines. G′ peak area intensity (c), D peak area intensity (d), G peak area intensity (e), and TERS images of G/G′ intensity ratio (f) are derived from multispectral TERS imaging (0.5 s acquisition time per pixel), measured simultaneously with (a) and (b). (g) Lorentzian line fit analysis of the TERS and confocal Raman spectra for grain and GBs A, B, and C with an acquisition time of 5 s.

veal structural properties of complex GB formations not readily resolved in the AFM topography (Fig. 4.4a). The distinguishable line structures from topography are indicated by white dashed lines in the Rayleigh scattering (Fig. 4.4b) and TERS images (Fig. 4.4c-f). As can be seen in Fig. 4.4b, several GBs show a $\sim$1 μm scale modification of Rayleigh scattering on one side of them. In addition, TERS images of D, G, and G′ peaks show distinct Raman response at various GBs, labeled A, B, and C. The TERS G/G′ intensity ratio image (Fig. 4.4f) best exemplifies the heterogeneity of the GBs. For fast TERS mapping, a large pixel size (100 nm per pixel) is used, yet the observed length scales at GBs are not limited by spatial resolution. Fig. 4.4g shows TERS spectra and Lorentzian line fit analysis at A, B, C, and grain regions. In contrast to the TERS images, confocal Raman images measured as same experimental conditions do not give a clear fingerprint of GBs due to the weaker intensity and lower spatial resolution than TERS as shown in Fig. 4.5.

It should be noted that the line defects of folded grains are possibly produced in large area

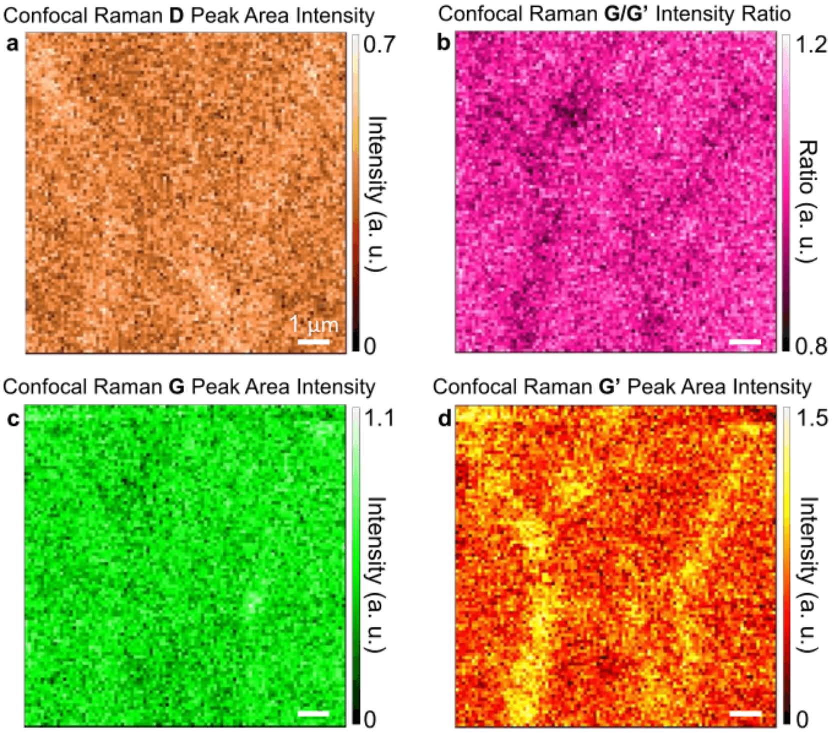

Figure 4.5: Confocal Raman images of D peak area intensity (a), G/G′ intensity ratio (b), G peak area intensity (c), and G′ peak area intensity (d) are derived from multispectral confocal Raman imaging (0.5 s acquisition times per pixel). This measurement is performed as same condition as Fig. 4.4 after retracting the Au tip from sample.

CVD-grown graphene [262]. However, the possibility of folded structures could be explicitly excluded for the line defects A, B, and C from the correlated analysis of topography, near-field scattering, and TERS properties. While we could not observe the folded structures in the measured area of Fig. 4.4, we could find the folded line defect in other measured area as shown in Fig. 4.8.

Fig. 4.6a-d show detailed vibrational properties at GBs A, B, and C, compared to the ML grain region. The distinguishing features of Rayleigh scattering and Raman responses at GBs A, B, and C suggest a bilayer structure. In general, the Raman response of Bernal (AB) stacked bilayer graphene shows an asymmetric G′ peak, with decreased intensity, and broader FWHM [263]. However, the observed G′ peaks at GBs exhibit neither weaker intensity nor distinctly broader FWHM compared to the G′ peak inside a grain. Therefore, the measured GBs A, B, and

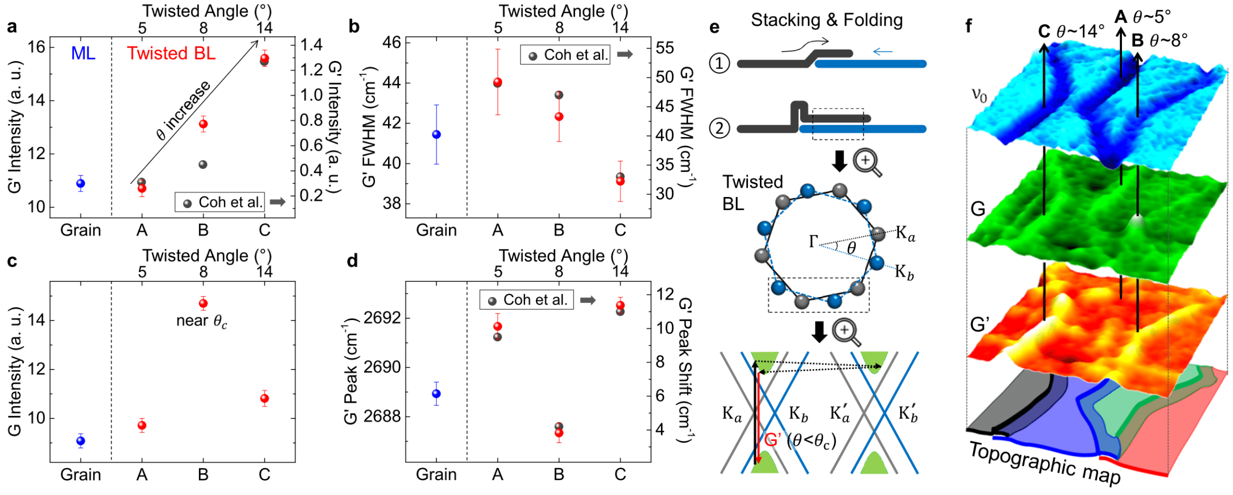

Figure 4.6: (a-d) Quantitative analysis of vibrational properties for grain and GBs A, B, and C (all values are derived from Lorentzian line fitting of Fig. 4.4g). Measured values of G′ peak at GBs (red circles) are compared with the calculated ones (gray circles) from Coh et al. [264]. (e) Illustration of formation and G′ peak Raman process at GBs in CVD grown large area graphene. (f) Determined misorientation angles of GBs A, B, and C.

C are possibly formed as a twisted bilayer with varying misorientation angle θ. As seen in Fig. 4.6a and b, the G′ peak intensity and FWHM are anti-correlated for A to C. In contrast, the G′ peak position at B is distinctly lower than A and C, as shown in Fig. 4.6d.

From the quantitative analysis of relative vibrational properties, the stacking angles of bilayer GBs A, B, and C can be determined. The alternation of the G′ peak intensity in bilayer graphene with respect to the stacking angle was demonstrated experimentally [265, 266] and theoretically [264] in previous studies. Since the magnitude of band structure modification in bilayer graphene is dependent on the overlapping ratio of the Dirac cones of the top and bottom layers, the G′ peak intensity of bilayer graphene gradually increases with the misorientation angle θ (from 0° to 30°) [265]. The FWHM of the G′ peak is generally inversely proportional to the peak intensity except for the narrow zone near critical angle θ_c, where the excitation photon energy (E_{laser}) is same as the energy between the conduction and valence Van Hove singularities [265, 266]. The G′ peak position is also strongly influenced by the resonance near θ_c, based on the general tendency of blueshift at small misorientation angles ($< 7°$) [264]. From comparison between the measured vibrational properties of G′ peak and the calculated data by the super-cell tight-binding method [264], the misorientation angles of the observed GBs are determined as shown in Fig. 4.6a, b, and d. In the case of the boundary A, the G′ peak is slightly weaker in intensity and larger in FWHM compared to ML region as results from the significantly modified band structure. In contrast, the G′ peak intensity is significantly increased at boundary C with a decreased FWHM due to the relatively weak interlayer coupling. From the best matching of the G′ peak intensity and FWHM with the calculated data, we determine the misorientation angle of boundary A (5°), B (8°), and C (14°). Despite we do not consider G′ peak position in the angle determination, the spectral shift tendency of boundary A, B, and C is in good agreement with the calculated data. For 1.96 eV excitation, a critical angle of ∼10° is calculated by a Dirac dispersion relation given by [265]

$$\theta_c = \frac{\Delta k}{K} = \frac{3aE_{laser}}{\hbar\nu_f 4\pi}, \tag{4.1}$$

where a and ν_f are the lattice parameter (2.46 $\mathring{A}$) and the Fermi velocity (10^6 m/s) of monolayer graphene, and $\hbar$ is the reduced Planck's constant. When the misorientation angle of bilayer graphene is close to the θ_c, a drastic increase in G peak intensity have been observed due to the resonance excitation of electron-hole, whereas the FWHM and position are not significantly changed with respect to the misorientation angle [265, 264, 267]. This suggests that the observed strong G peak intensity at B (Fig. 4.4e and Fig. 4.6c) is possibly resulted from the resonance Raman effect near θ_c.

In order to demonstrate the complete picture of the measured region, we also analyze several other line defects other than GBs A, B, and C such as the line between B and C, and the line to the left of the A as shown in Fig. 4.7.

In case of the GBs in regions D (indicated by black dashed lines), the G peak is slightly stronger in intensity compared to monolayer with the comparable intensity of the G′ peak, whereas the D peak intensity is remarkably increased in the overall regions D. Therefore, the GBs in the regions D are bilayer structures with small misorientation angles. However, the TERS properties of G and G′ peaks are not clearly measured due to the surface contaminants, which cause intensity

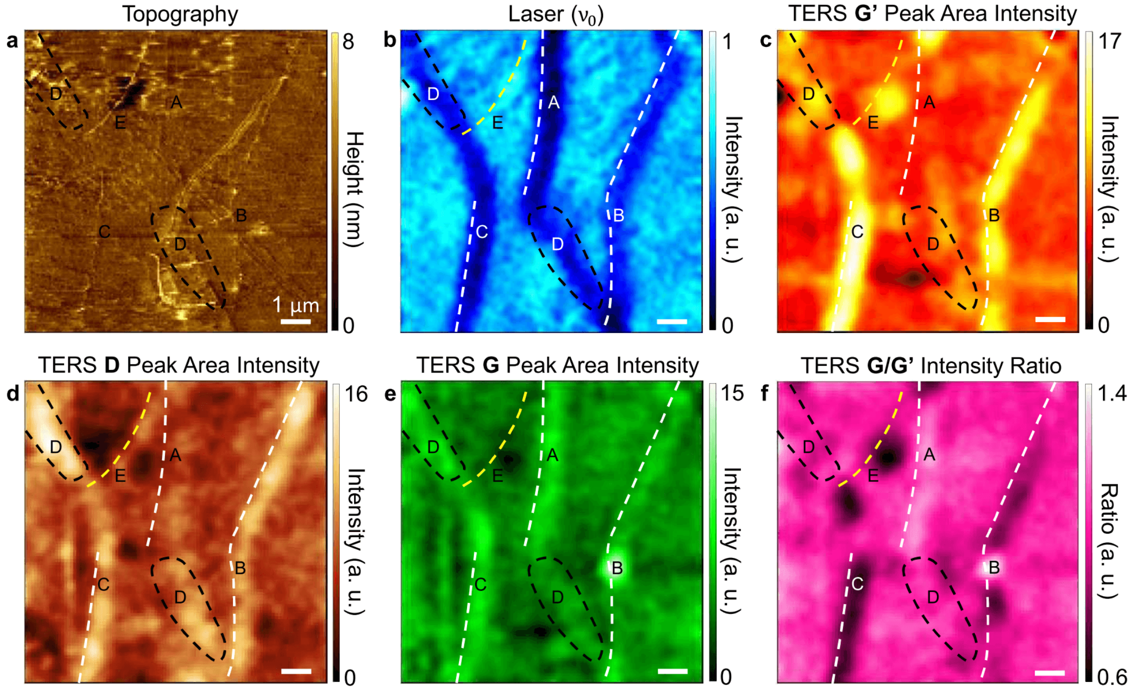

Figure 4.7: (a) Topography of a CVD grown graphene exhibiting structural defects such as wrinkles and grain boundaries. (b) Tip-enhanced Rayleigh scattering image. G′ peak area intensity (c), D peak area intensity (d), G peak area intensity (e), and TERS images of G/G′ intensity ratio (f) are derived from multispectral TERS imaging (0.5 s acquisition time per pixel), measured simultaneously with (a) and (b).

increase of the D peak. From the topography (a), we confirm the surface contaminants in these regions, which are not observed in the regions of A, B, and C. On the other hand, the line defect E is interpreted as a non-carbon defects on the monolayer crystal surface since intensities of the near-field scattering and the Raman D peak are increased with the slightly decreased G peak intensity. Intensity decrease of the G peak cannot be observed in any cases for the multilayer graphene.

Multispectral TERS imaging of folded structure

Fig. 4.8a-f show the near-field Rayleigh scattering image and TERS responses, which reveal structural properties of line defects observed in CVD-grown large area graphene. The distinguishable line structures from the near-field Rayleigh scattering image are indicated by black dashed lines in the TERS images (Fig. 4.8b-f). As we explained, the dark regions in the near-field scattering image are feature of the multilayer graphene due to the stronger absorption than monolayer

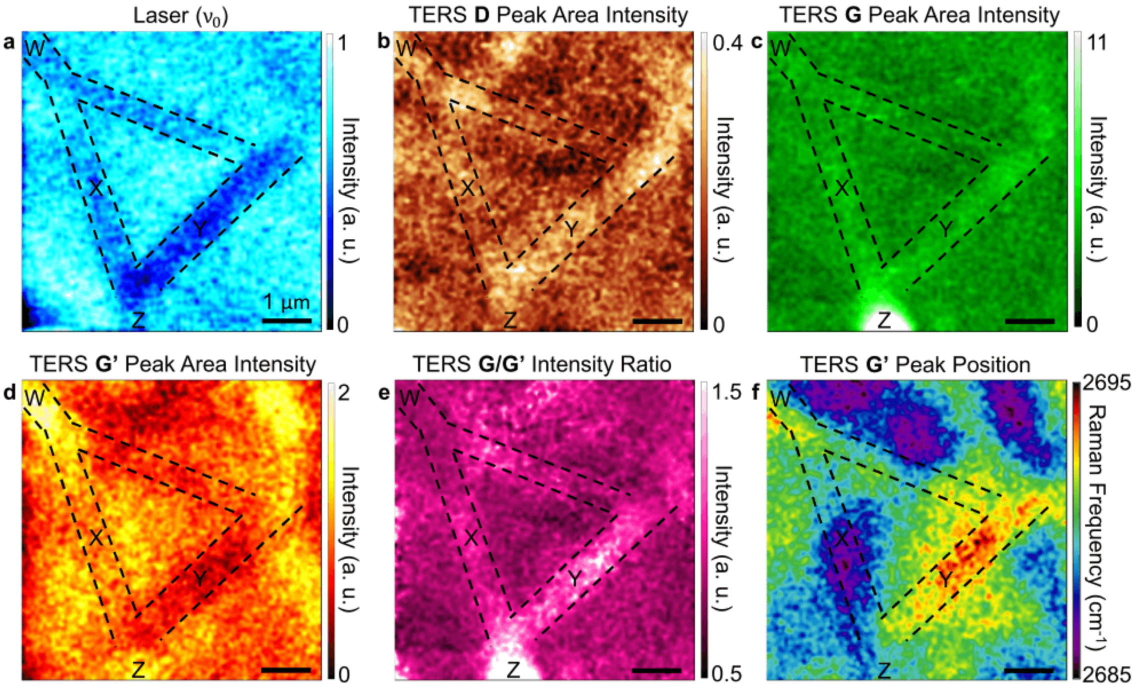

Figure 4.8: (a) Tip-enhanced Rayleigh scattering image of a CVD grown graphene exhibiting line defects such as grain boundaries and folded structure. Tip-enhanced Raman D peak area intensity (b), G peak area intensity (c), G′ peak area intensity (d), TERS images of G/G′ intensity ratio (e), and peak position of G′ peak are derived from multispectral TERS imaging (0.2 s acquisition time per pixel).

regions. TERS images of D, G, and G′ peaks show distinct Raman response at various line defects, labeled W, X, Y, and Z. In the case of the line W, the G′ peak is stronger in intensity and slightly blueshifted in spectral position compared to monolayer region. In contrast, for the line X, the G′ peak intensity is comparable to monolayer region while the G peak intensity is increased. From these features, we can classify the line W and X as bilayer grain boundaries, and estimate the misorientation angles (W $> 13°$, X $< 5°$) as we explained the detailed analysis method. The misorientation angle of indicated bilayer region Z is easily interpreted as ∼10° since the G peak intensity is strongly increased only near the critical angle θ_c. Interestingly, the line defect Y shows decreased G′ peak intensity with evidently more increased G peak intensity than bilayer GBs. These features cannot be explained by the theoretical vibrational properties of the twisted stacking bilayer graphene [264]. In addition, from the near-field Rayleigh scattering image (Fig. 4.8a), we find that absorption in line defect Y is clearly stronger than bilayer GBs. This feature means the line Y is possibly the folded structure of monolayer since it should be a trilayer. Further, the blueshifted Raman frequency of the G′ peak (Fig. 4.8f) also supports this hypothesis.

Multispectral TERS imaging of wrinkle

Furthermore, the other type of line defects in the topography can be resolved, suggesting wrinkle structures in the graphene sheets. We perform multispectral TERS imaging with 6 nm pixel size to investigate the Raman properties of the wrinkles. Fig. 4.9a and b show topography and G′ peak intensity image of a wrinkle in the graphene (D and G peaks intensity images are shown in Fig. 4.10). As can be seen from comparing the TERS spectra (Fig. 4.9c) of the wrinkle and grain regions, and their Lorentzian line fit analysis (Fig. 4.9d), only the G′ peak exhibits significant changes in the vicinity of the wrinkle, with an increase in FWHM and a decrease in intensity, with no associated spectral shift.

Note that the wrinkles are mainly formed in the CVD growth process due to the thermal expansion coefficient difference between underlying substrate (Cu or Ni) and graphene [53, 52]. A small percentage of the wrinkles could be formed during the transfer process which show distinguishing feature of bi-wrinkle formation [52]. Our group have also demonstrated the detailed studies of the origin of wrinkles in the CVD process in previous studies [55, 258]. Since we have used the graphene sample using same CVD growth condition as those references and also not observed the bi-wrinkle formation, we believe the wrinkle we measured was created in the growth process.

Multispectral TERS imaging of nucleation site

NSs in large area graphene are also important defects that can provide valuable information regarding the growth mechanism [258, 55]. Fig. 4.11a-f show the AFM topography, near-field Rayleigh scattering image, and TERS images of a region in the vicinity of an NS. From the modification of near-field scattering properties (Fig. 4.11b), the NS is interpreted as a multilayer graphene region. Specifically, the sub-micrometer region of decreased scattering intensity at the center of the grain is thought to be the origin of nucleation. The strong G peak intensity in the center of the graphene grain (Fig. 4.11c) supports this interpretation. On the other hand, the G′ peak

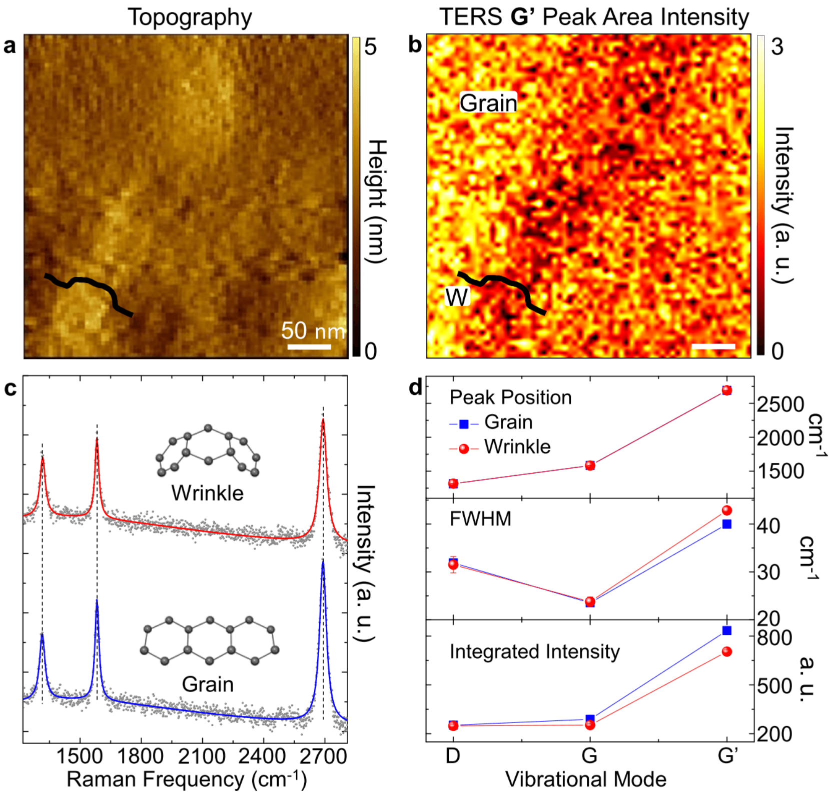

Figure 4.9: (a) Topography of wrinkle structure. (b) TERS image of G′ peak area intensity simultaneously measured with (a). (c) TERS spectra and Lorentzian line fits for wrinkle and grain regions with the acquisition time of 5 s. (d) Peak position, FWHM, and integrated intensity of three vibrational modes for wrinkle and grain.

intensity is decreased in the vicinity of the NS (Fig. 4.11e). Fig. 4.11g shows details of the vibrational properties of the NS region through the spectral line trace (indicated by yellow line in Fig. 4.11e). At the multilayer region (indicated by F), the G′ peak has decreased intensity and increased FWHM, and the peak position is blueshifted in comparison with the ML region (D), with asymmetric spectral shape. The integrated intensity of the G peak is increased, with a slight redshift. These observed Raman properties are in good agreement with those characteristic of AB stacking in bilayer graphene [263]. In addition, the G′ peak intensity is decreased in the region labeled E, with the emergence of an additional Raman peak at ∼1615 cm^{-1} (Fig. 4.11f). This is the D′ peak, generally described as a feature of hydrogen-bonded sp^3 type defects, which depend on the growth conditions [268, 269].

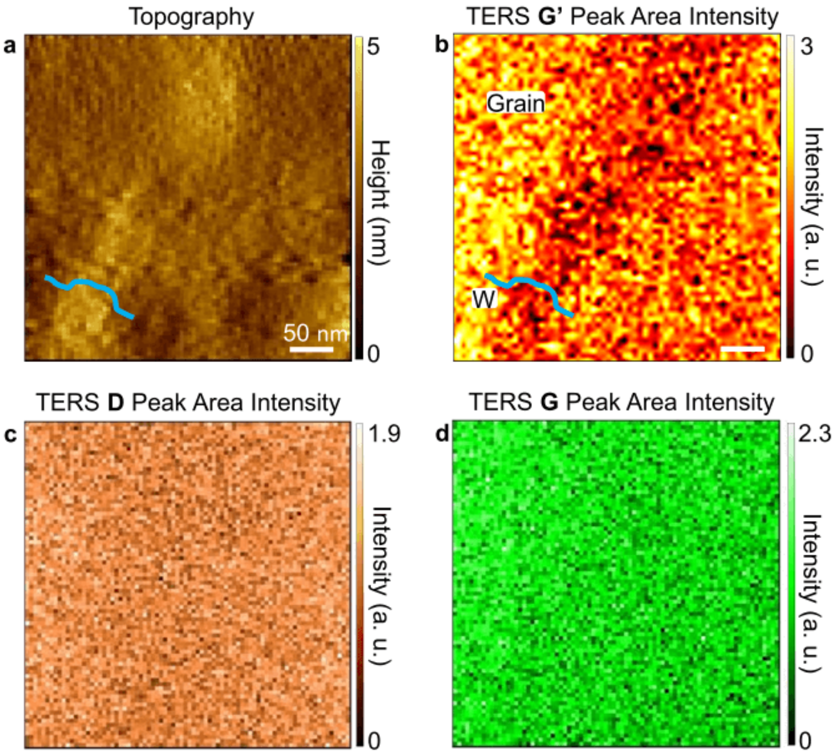

Figure 4.10: (a) Topography of wrinkle structure. Simultaneously measured TERS images of G′ peak area intensity (b), D peak area intensity (c), and G peak area intensity (d).

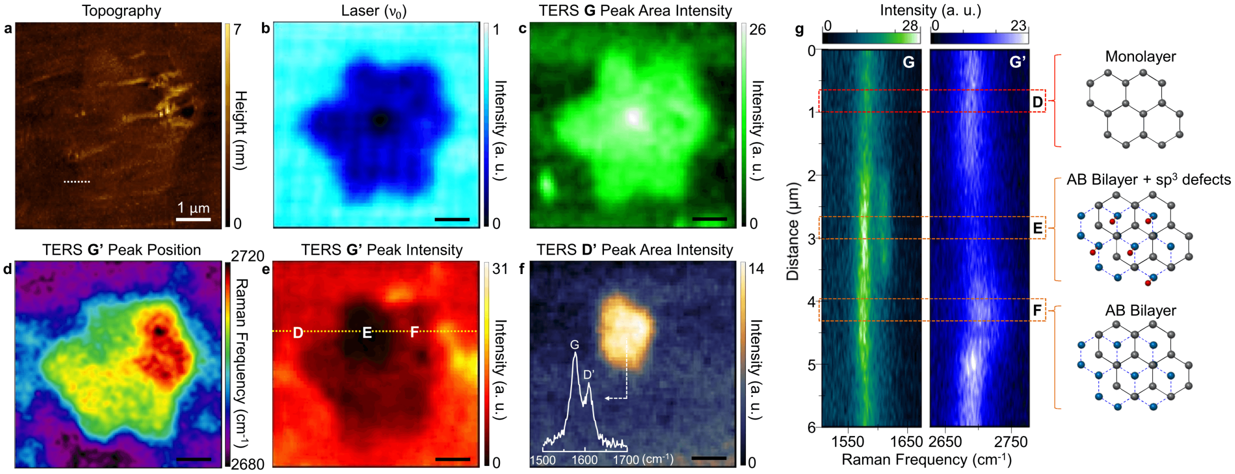

Figure 4.11: (a) Topography of nucleation seed. (b) Tip-enhanced Rayleigh scattering image simultaneously measured with (a). TERS images of G peak area intensity (c), G′ peak position (d), G′ peak intensity (e), and D′ peak area intensity (f) are derived from the multispectral TERS imaging (0.5 s acquisition time per pixel). (g) TERS spectral line traces of G and G′ peaks (yellow dotted line of (e)) with the cartoons of inferred structures at local spots D, E, and F.

4.1.4 Discussion

From these studies, we determine that GB structures in large area CVD-grown graphene are not similar to the well-known atomic vacant defects observed at the boundaries of adjacent graphene flakes. Despite some STM studies showing evidence of bilayer GBs in large area graphene, the structure and formation mechanism had not yet been determined [254, 255]. From correlated analysis of topography, near-field scattering, and multispectral TERS images, we confirm the twisted bilayer structure of GBs, as seen in Fig. 4.6, and can assign misorientation angles for the overlapping regions. The misorientation angles of bilayer GBs are in the range from 0° to 30°, depending on the orientation of the crystal faces. Since the Raman G$'$ peak is originated from an intervalley phonon scattering between K and K' points, its response is sensitively changed with respect to the modified band structure. Thus, we could use the modified Raman properties of G$'$ peak to determine the misorientation angle as seen in Fig. 4.6a, b, and d.

The super-cell tight-binding method of determining the misorientation angle provided a better fit to our data than the continuum method [264]. The misorientation angles of bilayer graphene could be obtained most precisely for angles smaller than 6° or larger than 15°, but there are large uncertainties for θ larger than 6° and smaller than 15° due to the non-monotonic change of peak position and FWHM near the critical angle θ_c. Despite the fact that the physical origin for the modified G$'$ peak responses at the misorientation angles smaller than θ_c is still not reavealed, the possible scattering path between the overlapped Dirac cones was expected as described in Fig. 4.6e [265]. While, for the larger misorientation angles than 15°, the Raman responses would be expected to resemble the monolayer properties since the Raman process occurs in isolated Dirac cones without overlapping [265, 266].

Based on the variation we observe, we infer a formation mechanism for GBs in large area graphene. As described in Fig. 4.6e, one of two facing grains ascends onto the other grain, and makes a twisted bilayer region on the length scale of several hundreds of nanometers. The top and bottom grains stop growing further due to friction, and the part of the top grain above the edge of the bottom grain is pushed up by a surface horizontal compressive force. It should be noted that since the vertical resolution of a shear-force AFM is $\sim$1 nm, we quantify the height of $\sim$2 nm at the pushed up structure of GBs, whereas we cannot clearly quantify the thickness difference of 0.35 nm between monolayer grains and the GBs at the other edges.

Wrinkles are also significant nanoscale defects that degrade the electrical properties of large area graphene. While the structural and electrical properties of wrinkles have been studied by STM [270], the vibrational properties of single wrinkle structures had not previously been investigated. As seen in Fig. 4.9, there are no obvious spectral changes in the D and G peaks at a wrinkle structure, with only the G$'$ peak decreasing in intensity and increasing in linewidth. These modified vibrational properties of the G$'$ peak could be interpreted as a simple curvature effect similar to the suppressed G$'$ peak intensity of carbon nanotubes (CNT) [271]. In addition, the unchanged G$'$ peak position means that the wrinkle structures have monolayer thickness [271].

In the nucleation process of CVD graphene, sp^3 type defects associated with H$_2$ precursor are expected to be formed [268, 269]. Recently, sp^3 defects were experimentally observed by STM [272] and Raman spectroscopy [273], for artificially treated graphene samples. From the D$'$ peak, our results show the first TERS imaging of hydrogen-bonded sp^3 defects at the NS of unmodified graphene (Fig. 4.11f). Note that while the D$'$ peak is also emerged from vacancy type defects, the intensity ratio of D$'$ and G peaks is relatively small in that cases [273]. In addition, since the intensity ratio of D$'$/G (inset of Fig. 4.11f) is comparable to previous study [273], we can conclude that the observed D$'$ at the NSs is a fingerprint of the sp^3 type defects. Additionally, the spectral redshift of the G$'$ peak is also a supporting evidence of the sp^3 type defects, as seen in Fig. 4.11d [273]. Although a complete physical origin of the observed heterogeneous distribution could not be addressed, we expect this observation give clues to understand the initial growth mechanism of graphene and graphane.

Our proposed method shows the potential of correlated TERS analysis as generally applicable to a wide range of 2D layered materials and heterostructures beyond graphene. For example, structures and electronic/vibrational properties at GBs and NS of recently synthesized large area transition metal dichalcogenides (TMDs) [274] could be revealed through correlated TERS analysis.

In summary, we have revealed twisted bilayer structures of grain boundaries in large area graphene and identified misorientation angles from correlated analysis of the high resolution (∼18 nm) multispectral TERS imaging. In addition, we have investigated phonon scattering properties of wrinkles and nucleation sites, which associate with the nanoscopic structural curvature effect and atomic scale carbon hybridization. We expect these results help to better understand nanoscale defects, their impact on function, and growth mechanisms of large area graphene.

4.2 Disordered states and local strain control of WSe_2 monolayer[2]

Many classes of two-dimensional (2D) materials have emerged as potential platforms for novel electronic and optical devices. However, the physical properties are strongly influenced by nanoscale heterogeneities in the form of edges, grain boundaries, and nucleation sites. Using combined tip-enhanced Raman scattering (TERS) and photoluminescence (TEPL) nano-spectroscopy and -imaging, we study the associated effects on the excitonic properties in monolayer WSe_2 grown by physical vapor deposition (PVD). With ∼15 nm spatial resolution we resolve nonlocal nanoscale correlations of PL spectral intensity and shifts with crystal edges and internal twin boundaries associated with the expected exciton diffusion length. Through an active atomic force tip interaction we can control the crystal strain on the nanoscale, and tune the local bandgap in reversible (up to 24 meV shift) and irreversible (up to 48 meV shift) fashion. This allows us to distinguish the effect of strain from the dominant influence of defects on the PL modification at the different structural heterogeneities. Hybrid nano-optical and nano-mechanical imaging and spectroscopy thus enables the systematic study of the coupling of structural and mechanical degrees of freedom to the nanoscale electronic and optical properties in layered 2D materials.

4.2.1 Motivation

Layered two-dimensional (2D) transition metal dichalcogenides (TMDs) have emerged as a new platform for studying quantum confined semiconductor physics [275, 276, 277, 274, 278]. As the TMD crystals are thinned to the monolayer (ML) limit, new properties emerge including an indirect-to-direct bandgap transition [49, 48, 279], valley-specific circular dichroism [64, 280, 281, 282], or an enhanced nonlinear optical response [75, 283]. The direct semiconducting gap, large spin-orbit coupling, and valley-selectivity provide several advantages for the use of TMDs in photodetector and other optoelectronic device applications.

A prevailing theme in TMDs and other layered van der Waals systems is the complex inter-

---

[2] This section draws significantly from [20]. The experiment was performed and analyzed by K.-D. Park, and supervised by M. B. Raschke. This work was performed in collaboration with G. Clark and X. Xu from the University of Washington at Seattle.

action between fundamental excitations inherent to the materials themselves, and extrinsic factors associated with surface morphology and the underlying substrate. The reduced dimensionality invites strong interference from charged impurities, defects, and disorder, creating much difficulty in isolating the intrinsic quantum properties of the material system [67]. The resulting electronic properties are consequently highly inhomogeneous and sensitive to structural variations near internal and external boundaries [68, 69]. To explore these heterogeneities and how they control the optical and electronic properties, a comprehensive multi-modal nano-scale imaging and spectroscopy approach is desired.

High-resolution local probes such as scanning tunneling microscopy (STM) and transmission electron microscopy (TEM) uncover the specific nature of structural defects and grain boundaries (GBs) that may lead, for example, to an increase or decrease in the electrical conductivity [68, 284, 285]. However, despite atomic-scale spatial resolution, these experimental techniques provide limited information of the associated electronic, spin, or optical response. To this end, a series of recent studies applying confocal [68, 69, 286] and near-field photoluminescence (PL) mapping [287, 288], with spatial resolution reaching as high as ∼60 nm, have addressed the question of the local modification of the optical and electronic properties at GBs. However, both increases and decreases in PL quantum yield have been observed for different crystal geometries and sizes [68, 69, 287, 288]. The range of studies have left a confusing picture regarding the relative role of doping, defects, mid-gap exciton states, or strain controlling the PL intensity, lineshape, and spectral position associated with structural heterogeneities.

Here we present a new hybrid nano-opto-mechanical tip-enhanced spectroscopy and imaging approach combining nano-Raman (tip-enhanced Raman scattering, TERS), nano-PL (tip-enhanced photoluminescence, TEPL), and atomic force local strain control to investigate the correlation of local structural heterogeneities with nanoscale optical properties with enhanced ∼15 nm spatial resolution. Using a novel tilted tip approach for in-plane near-field polarization control, we study the excited state PL response in twinned WSe_2 ML physical vapor deposition (PVD) grown microcrystals. A combination of PL quenching and selective spectral changes at nanoscale defects is resolved on 10's nm length scales. Specifically, local PL quenching and a spectral blueshift are observed at crystal edges and nucleation sites (NS) attributed to energy funneling in the heterogeneous system and non-uniform composite ratio between W and Se, respectively. On the other hand, only PL quenching is observed without a change in energy at twin boundaries over ~30 nm length scales correlated with exciton diffusion into non-radiative recombination center. In addition, through controlled tip-sample force interaction we can tune the bandgap reversibly (up to 24 meV) and irreversibly (up to 48 meV) through local nanoscale strain engineering (0 - 1%). The combined results allow for the separation of the effect of strain from controlling the PL modification at edges, NS, and internal twin boundaries, and suggest defects and stoichiometry as the primary factors modifying the PL at the structural heterogeneities, yet in distinctly different ways. These results clarify many of the apparent inconsistencies of earlier studies. This shows the potential of combined nano-optical and nano-mechanical spectroscopy and imaging with nanometer spatial resolution, few cm^{-1} spectral resolution, and nN force sensitivity as generally applicable to a wide range of systems beyond 2D materials.

4.2.2 Experiment

We use WSe_2 monolayers grown by physical vapor transport using powdered WSe_2 as precursor material. Source material (30 mg) in an alumina crucible is placed in the hot zone of a 25.4 mm horizontal tube furnace, and an SiO_2 substrate is placed downstream in a cooler zone at the edge of the furnace ($750 - 850$ °C). Before growth, the tube is evacuated to a base pressure of 0.13 mbar and purged several times with argon. The furnace is then heated to 970 °C at a rate of 35 °C/min and remains there for a duration of 5-10 min before cooling to room temperature naturally. A flow of 80 sccm argon and 20 sccm hydrogen is introduced as carrier gas during the 5-10 min growth period. Details can be found in Ref. [289].

As shown schematically in Fig. 4.12a and Fig. 4.13a, the experiment is based on a confocal microscope setup, with top illumination of a shear-force AFM tip for combined TERS and TEPL. A Helium-Neon laser beam (632.8 nm, < 0.5 mW), after passing through a half wave plate for

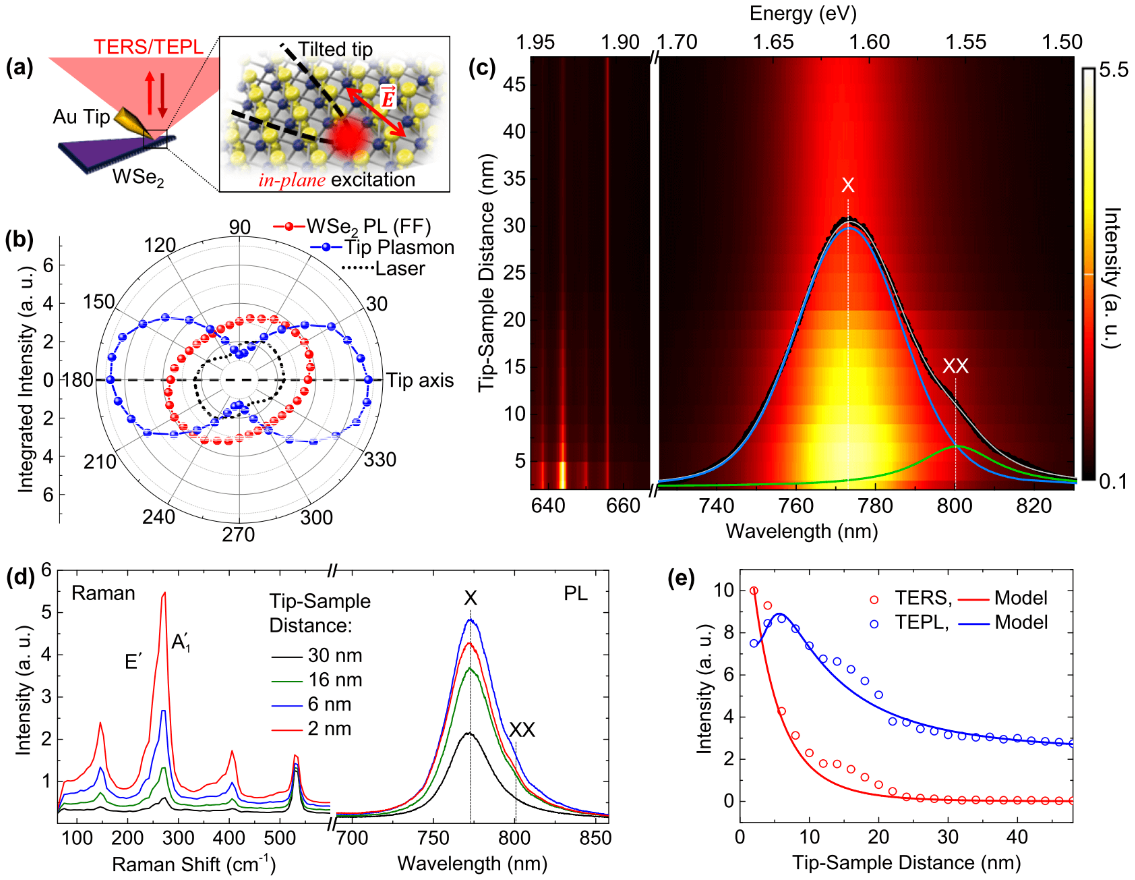

Figure 4.12: Schematic of multi-modal TEPL/TERS (a) with polar plot of the integrated intensity (b) for the tip plasmon (blue line), WSe_2 PL (red line), and excitation laser (black line). (c) Tip-sample distance dependence of TEPL and TERS of monolayer WSe_2. Overlapped TEPL spectrum (black) at 6 mm distance with Voigt profile fit (gray) decomposed into exciton (blue, X), and possibly biexciton (green, XX) emission. (d) Selected TERS and TEPL spectra for different tip-sample distances. (e) Peak intensity dependence of WSe_2 Raman (273 cm^{-1}) and WSe_2 PL response (772 nm) with respect to the tip-sample distance, derived from (c), with fit to rate equation model as described in the text.

polarization control, is focused onto the WSe_2 sample by an objective lens (100×, NA=0.8). The sample is mounted to a piezoelectric transducer (PZT, Attocube) for xyz scanning. The electro-chemically etched Au-tip with typical apex radius (r ∼ 15 nm) is then positioned in the focal area [119]. Tip positioning is operated by a stepper motor (MX25, Mechonics), and shear-force feedback and scanning conditions are controlled by a digital AFM controller (R9, RHK Technology). With the tip tilted by ∼40° with respect to the surface normal, confocal far-field or TERS and TEPL imaging and spectroscopy can then be performed alternatively, by simply retracting or engaging

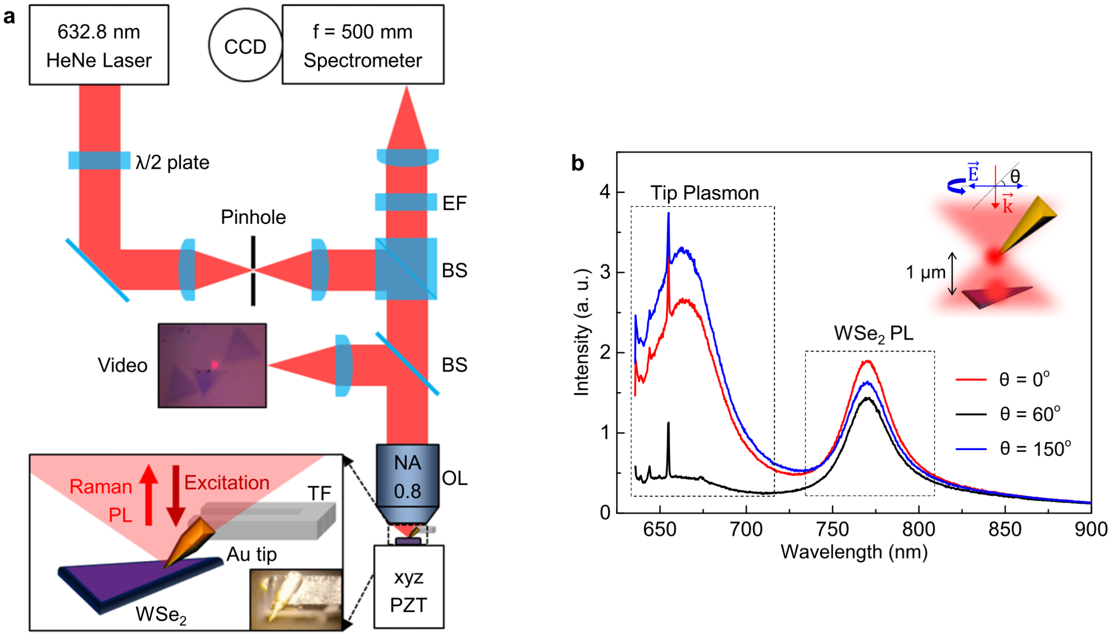

Figure 4.13: (a) Schematic of the multi-modal TEPL/TERS setup. EF: edge filter, BS: beam splitter, OL: objective lens. (b) Confocal far-field tip plasmon and WSe_2 PL spectra for three different polarization angles of incident laser.

the plasmonic Au-tip with the sample. The resulting localized surface plasmon resonance (LSPR) excitation in the axial detection of the tip with *in-plane* sample projection of the locally enhanced near-field leads to effective excitation of the *in-plane* Raman and exciton modes as characteristic for layered 2D materials, in contrast to conventional surface normal excitation for normal tip orientation (see Fig. 4.13b). Fig. 4.12b shows the resulting anisotropy of the tip scattered plasmon response (blue) and far-field WSe_2 PL (red) as a function of excitation polarization (black, slightly asymmetric due to the polarization-dependent incident optics) exhibiting the expected optical antenna behavior with excitation polarization parallel with respect to the tip axis.

Fig. 4.13a and b show experimental setup, and tip plasmon and WSe_2 PL spectra with respect to the incident polarization angle θ as defined in the inset. The incident beam is focused onto the tip apex, and the WSe_2 sample is initially located out of focus at 1 μm distance below the tip. The tip plasmon intensity is strong for P_{in} excitation ($\theta = 150°$) and substantially decreased ($>$ 10 times) for S_{in} excitation ($\theta = 60°$). The far-field PL intensity of WSe_2 is not affected by the tip plasmon and the small change of intensity for the different angle results from the polarization dependent reflectivity of the beam splitter.

Fig. 4.12c shows the distance dependence of TEPL and TERS of the ML WSe_2 with representative PL spectrum (black) acquired at 6 nm distance, with Voigt profile fit dominated by the exciton response ($\sim$1.61 eV) and a longer wavelength shoulder ($\sim$1.55 eV). Fig. 4.12d shows the near-field localization of both the TEPL and TERS responses for representative distances. The most prominent Raman peaks observed correspond to a superposition of $E^{'}$ (in-plane) and $A_1^{'}$ (out-of-plane) modes at $\sim$273 cm^{-1} [290], and first- and third-order LA phonons (M point in the Brillouin zone) at $\sim$150 cm^{-1} and $\sim$405 cm^{-1}, respectively [291]. The shoulder in the TEPL spectra ($\sim$10 - 3 nm distances) may rise from trion[287] or biexciton[292, 281] emissions with the biexciton as the more likely origin for the following reasons: The $\sim$50–60 meV spectral separation from the main exciton (X) peak is in agreement with the observation of biexciton assignment from previous studies [292, 281]. Furthermore, only a single exciton peak is observed in the far-field spectrum for the incident intensity of 10^5 W/cm^2 as shown in Fig. 4.12d. Whereas the additional feature only emerges in the TEPL measurement with the tip-enhanced excitation intensity at the apex of $\sim 10^7$ W/cm^2. This behavior is consistent with the expected super-linear intensity dependence of biexciton emission [293, 294].

It should be noted that biexciton peak is emerged when the tip-enhancement factor is high enough as shown in Fig. 4.17d. Assignment of the high energy shoulder to biexcitons is suggested based on spectral position in comparison with other studies and the emergence of that spectral feature only when the tip-enhancement is sufficiently high, as shown in Fig. 4.17d, suggesting the expected super-linear excitation intensity dependence. Specifically, the $\sim$50–60 meV separation between peaks is consistent with the energy difference between exciton and biexciton peaks as reported in the literature [292, 281]. Observation of biexcitons has been also reported in literature for CW excitation using 0.1 - 10 mW power, which translates into excitation intensities of 10^4 - 10^6 W/cm^2 [294, 293]. In our experiment, for the incident intensity of 10^5 W/cm^2, only a single exciton peak is observed in the far-field measurements (Fig. 1d). The appearance of an additional peak in the near-field, where the local excitation intensity can increase up to 10^7 W/cm^2 due to the local field enhancement at the tip apex on the order of 10, seems consistent with the expected super-linear dependence of biexciton emission on excitation intensity [294, 293].

Following the initially continuous increase in both TEPL and TERS response for $d \lesssim 20$ nm, at distances $d < 5$ nm, the WSe$_2$ PL starts to quench. This behavior is due to a near-field polarization transfer between the WSe$_2$ exciton and the metal tip, giving rise to non-radiative damping and PL quenching. The PL distance dependence observed is well described by a rate equation model with damping rates Γ and quantum yields of radiative emission η corresponding to $1/\Gamma_{\mathrm{s}} \sim 0.5$ ps and $\eta_{\mathrm{s}} \sim 0.1$ for the sample, and $1/\Gamma_{\mathrm{tip}} \sim 30$ fs and $\eta_{\mathrm{tip}} \sim 0.5$ for the tip, and with the resonance energy transfer length of $R_0 \sim 8$ nm. For TERS, the same set of parameters are used except assuming very short ($1/\Gamma_{\mathrm{s}} \sim 5$ fs) lifetime of the excitation to describe the instantaneous character of the Raman process [121].

In order to describe the dependence of TEPL and TERS signals on the tip–sample distance z, we use rate equations for the excited state population of sample (P_{s}) and tip plasmon (P_{tip}) as described in [121]:

$$\frac{dP_{\mathrm{s}}}{dt} = \Gamma_e(z) - \left(\Gamma_{\mathrm{s}} + \Gamma_{\mathrm{RET}}(z)\right) P_{\mathrm{s}} + \Gamma_{\mathrm{RET}}(z)\, P_{\mathrm{tip}},$$

$$\frac{dP_{\mathrm{tip}}}{dt} = -\left(\Gamma_{\mathrm{tip}} + \Gamma_{\mathrm{RET}}(z)\right) P_{\mathrm{tip}} + \Gamma_{\mathrm{RET}}(z)\, P_{\mathrm{s}}.$$

Here, we take into account a spatially integrated, over the near-field probe area, distance-dependent excitation rate $\Gamma_e(z) \propto (1/(R+z))^4$, with tip apex radius R. Damping rates include radiative and non-radiative contributions $\Gamma_{\mathrm{s,tip}} = \Gamma^{\mathrm{rad}}_{\mathrm{s,tip}} + \Gamma^{\mathrm{nrad}}_{\mathrm{s,tip}}$, and the non-radiative resonance energy transfer (RET) rate $\Gamma_{\mathrm{RET}}(z) = \Gamma^{\mathrm{rad}}_{\mathrm{tip}}\,(R_0/z)^m$, with $m = 4$ due to the reduced dimensionality and the characteristic length scale of near-field energy transfer R_0. We solve the equations for steady state and as a function of z, and obtain the PL intensity $I_{\mathrm{PL}}(z) \propto \eta_{\mathrm{tip}} P_{\mathrm{tip}} + \eta_{\mathrm{s}} P_{\mathrm{s}}$, where $\eta_{\mathrm{s,tip}} = \Gamma^{\mathrm{rad}}_{\mathrm{s,tip}}/\Gamma_{\mathrm{s,tip}}$ is the quantum yield of the sample and tip emission.

As shown in Fig. 4.12e, a good agreement between the simulation and the experimental TEPL

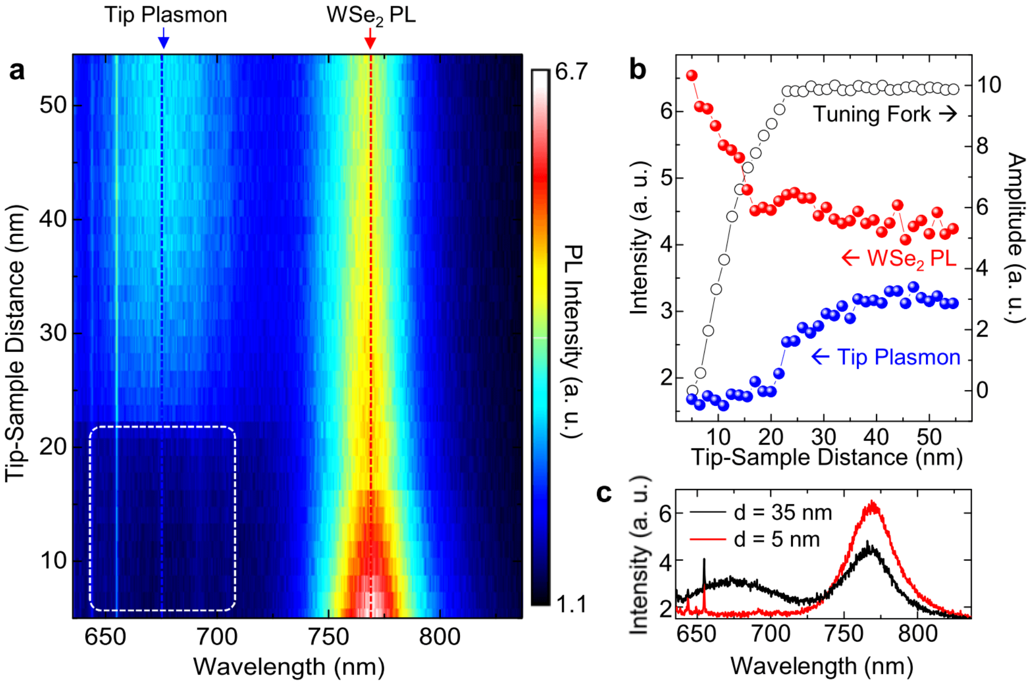

Figure 4.14: (a) Tip-sample distance dependence of TEPL of monolayer WSe$_2$. Spectra are measured in 1.5 nm increments and 0.2 s acquisition time. (b) Amplitude changes of tuning fork and the peak intensity changes of tip plasmon and WSe$_2$ PL (~770 nm) with respect to tip-sample distance derived from the (a). (c) Tip plasmon and WSe$_2$ PL spectra for the different tip-sample distances (35 nm and 5 nm).

data is found for fit parameters with tip radius $R \sim 30$ nm, damping rates and quantum yields of $1/\Gamma_{\rm s} \sim 0.5$ ps, $\eta_{\rm s} \sim 0.1$, $1/\Gamma_{\rm tip} \sim 30$ fs, $\eta_{\rm tip} \sim 0.5$, and a RET length $R_0 \sim 8$ nm. TERS intensity is simulated using the same set of parameters, but assuming very short ($1/\Gamma_{\rm s} \sim 5$ fs) lifetime of the excitation, to describe the near instantaneous character of the Raman process.

Fig. 4.14a shows tip-sample approach behavior with different tip in another sample spot. As the tip is closely approaching to the sample, the PL spectral intensity of WSe$_2$ is enhanced as shown in Fig. 4.14b due to near-field interaction. Notably, the tip plasmon is quenched in this regime (marked with white dashed box in Fig. 4.14a). This tip plasmon quenching can be possibly understood as a result of the optical excitation transfer from the tip to the WSe$_2$ with subsequent non-radiative decay. We find typical tip plasmon resonances in the range between 600 and 800 nm PL but not consistently for all gold tips used. However, for those tips which exhibit a tip plasmon

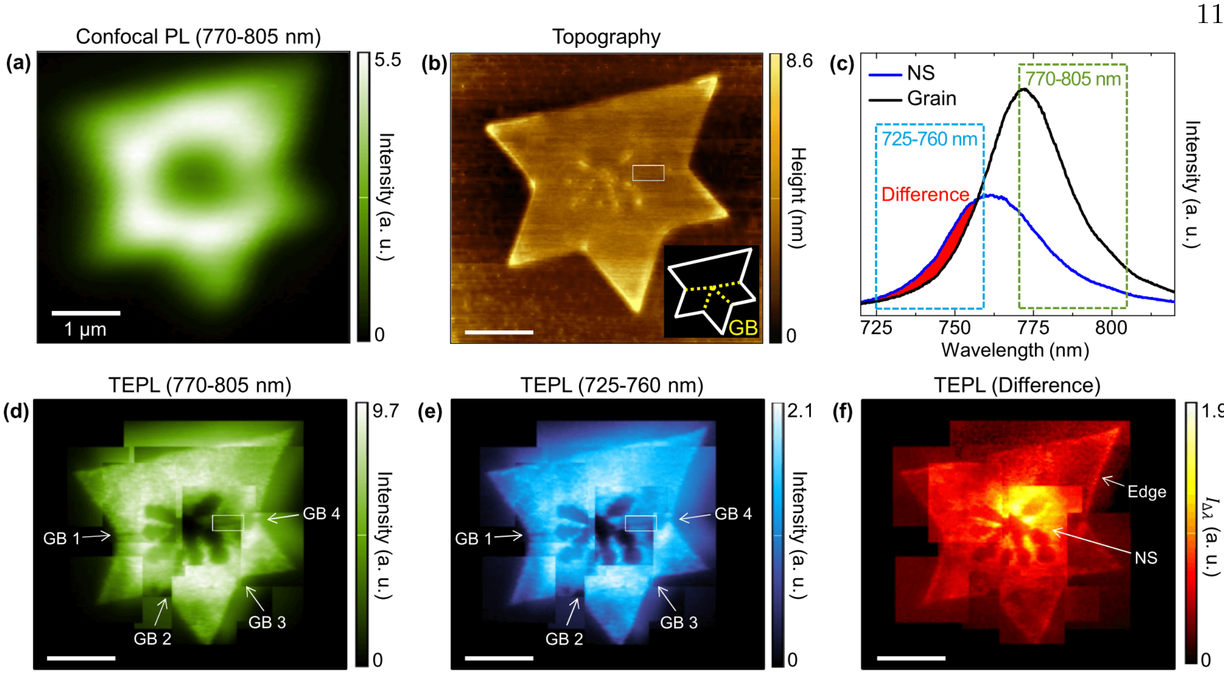

Figure 4.15: (a) Confocal PL images of a ML WSe_2 crystal for the integrated intensity at 770-805 nm (Blueshifted PL (725-760 nm) and spectral difference PL images are shown in Fig. 4.16a and b). (b) Corresponding topography with inset illustrating the crystal and internal GBs. (c) TEPL spectra of the ML WSe_2 for nucleation site (NS) and grain regions. TEPL images for the integrated intensity of 770-805 nm (d) and 725-760 nm (e) spectral regions, and spectral difference TEPL image (f).

resonance, we generally observe tip-enhanced PL of WSe_2.

4.2.3 Results

Multi-modal TEPL/TERS imaging of nanoscale defects

We then image NS, external crystal edges, and internal GBs through their effect on the PL and Raman response. Fig. 4.15a shows a ∼500 nm spatial resolution confocal PL survey of a polycrystalline ML WSe_2 flake with spectrally integrated 770-805 nm acquisition. To visualize the spatial heterogeneity of the PL spectrum, we propose the multi-modal PL imaging method. The integrated intensities for the main PL (770-805 nm) and the blueshifted PL (725-760 nm) are selectively counted at each pixel of sample scanning. However, the spatial heterogeneity of the blueshifted PL is not clearly visualized because the tail of the main PL still significantly affects

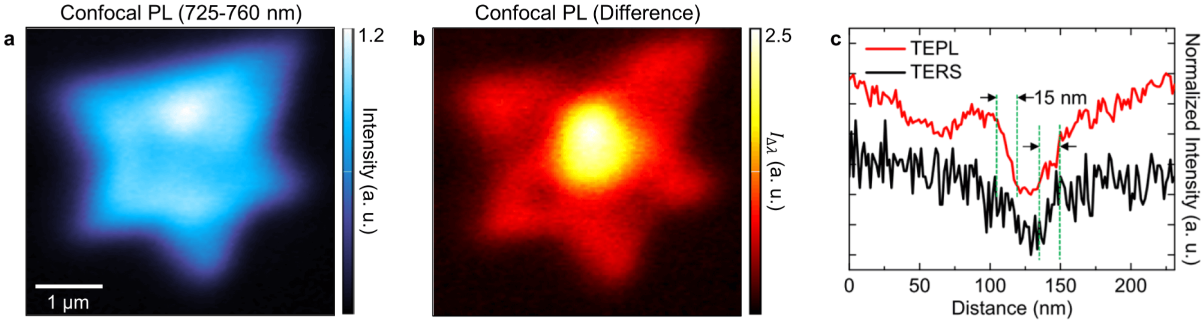

Figure 4.16: (a) Confocal PL image of the ML WSe_2 for the integrated intensity at 725-770 nm (blueshifted PL). Corresponding confocal PL image for the integrated intensity at 770-805 nm is shown in Fig. 4.15a. (b) Corresponding spectral difference confocal PL image. (c) Line profiles for the 770 nm PL peak and 273 cm^{-1} Raman mode which exhibiting 15 ± 5 nm spatial resolution.

the integrated intensity of the blueshifted PL. To solve this problem, we subtract the main PL image from the blueshifted PL image after compensating for intensity discrepancy. Through this method, the blueshifted PL property is clearly visualized in the PL images. For the corresponding blueshifted PL image (725-760 nm), and difference PL image see Figs. 4.16a and b.

Corresponding TEPL images with ~15 nm spatial resolution reveal the influence of the NS region and crystal edge, which are seen to give rise to an associated decrease in PL intensity and spectral blueshift as shown in Fig. 4.15d-f (770-805 nm region, 725-760 nm region, and spectral difference image $I_{\Delta\lambda}$). Where $I_{\Delta\lambda} = \int_{\lambda_1}^{\lambda_2} |I(\lambda)_{\text{i}} - I(\lambda)_{\text{ii}}| d\lambda$, $\lambda_1 = 725$ nm, $\lambda_2 = 760$ nm, and $I(\lambda)_{\text{i}}$ and $I(\lambda)_{\text{ii}}$ are the PL spectra for blueshifted center, edges and grains, respectively.

It should be noted that despite high spatial resolution TEPL images enabled by the strong localized plasmon effect (Fig. 4.15d-f), there is a superimposed weak homogeneous far-field background signal over micron length scale. Note also that it is difficult to obtain 15 nm resolution for large area scanning due to the different thermal expansion of tip and objective lens mounts, as well as overall drift of the scanner (~ 1 nm/min) on the time scale of such a measurement. Although reproducible 50 nm spatial resolution images were obtained in the whole crystal scanning, the presented near-field image is a composite of several 1 μm × 1 μm or 2 μm × 1 μm TEPL image scans to achieve the best resolution images.

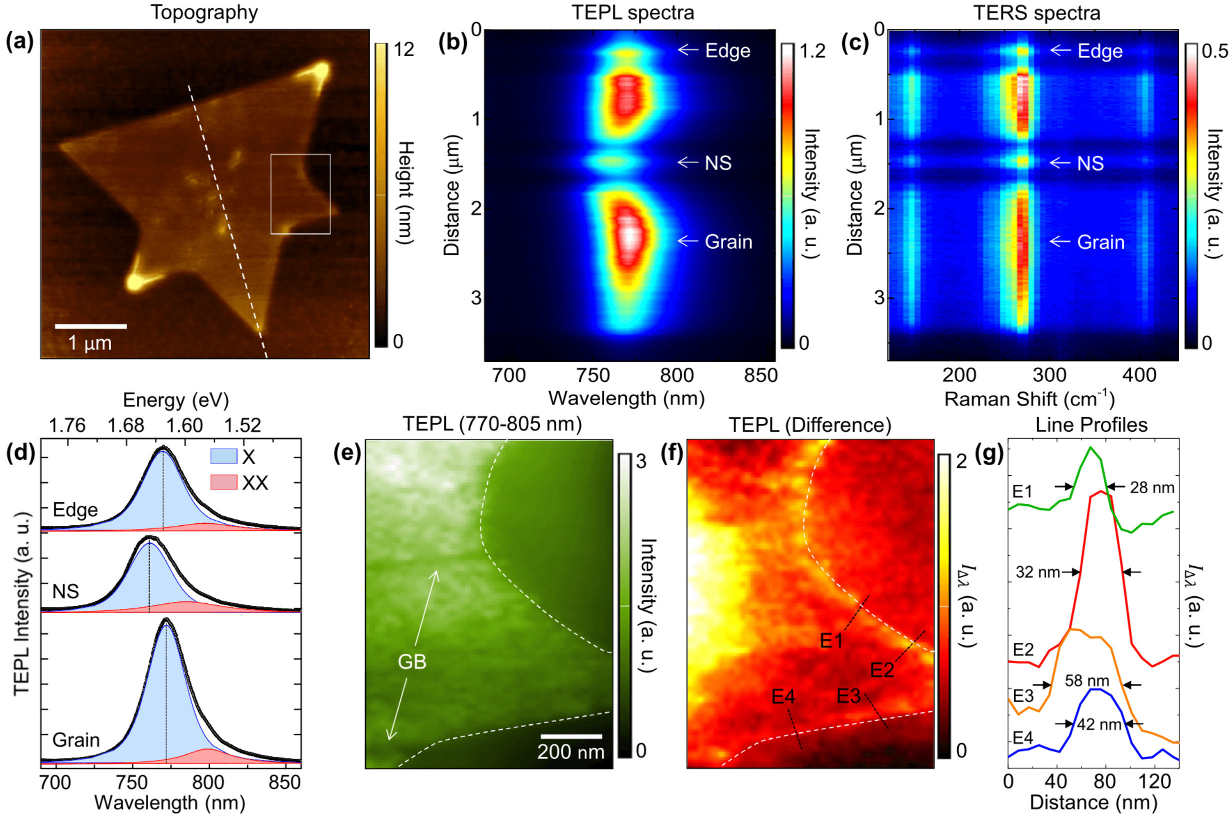

Figure 4.17: Topography (a) of a ML WSe_2 with spectral TEPL (b) and TERS (c) line traces along the center line of the crystal (dashed line in (a)). (d) Distinct TEPL spectra acquired from the edge, nucleation sites (NS), and grain region of crystal. Exciton and possible biexciton peaks are assigned via the Voigt fitting. Peak energies are 1.610 eV at edge, 1.630 eV at center, and 1.606 eV at grain. TEPL images of the spectral region of 770-805 nm (e) and the spectral difference (f). (g) Selected line profiles at the edge derived from (f).

Fig. 4.16c shows line profiles for the 770 nm PL peak and 273 cm^{-1} Raman mode (same data as Fig. 4.18f). We estimated a spatial resolution of 15 ± 5 nm according to the general convention (distance between 5% and 95% of optical intensity at the step edge).

Details of the effect of NS and crystal edges on the PL and Raman characteristics are investigated as shown in Fig. 4.17, revealing in spatially-resolved spectral line traces (b, c) the decrease in PL and blueshift, being more pronounced for the NS compared to the edges (Fig. 4.17d). Intensity variations aside, no change in the corresponding Raman frequency of the $E^{'}$ and $A_1^{'}$ superposition mode is observed (Fig. 4.17c). The spatial variation of the PL at the edges (Fig. 4.17e) is best exemplified in the spectral difference map (Fig. 4.17f), with the PL shift and decrease extending

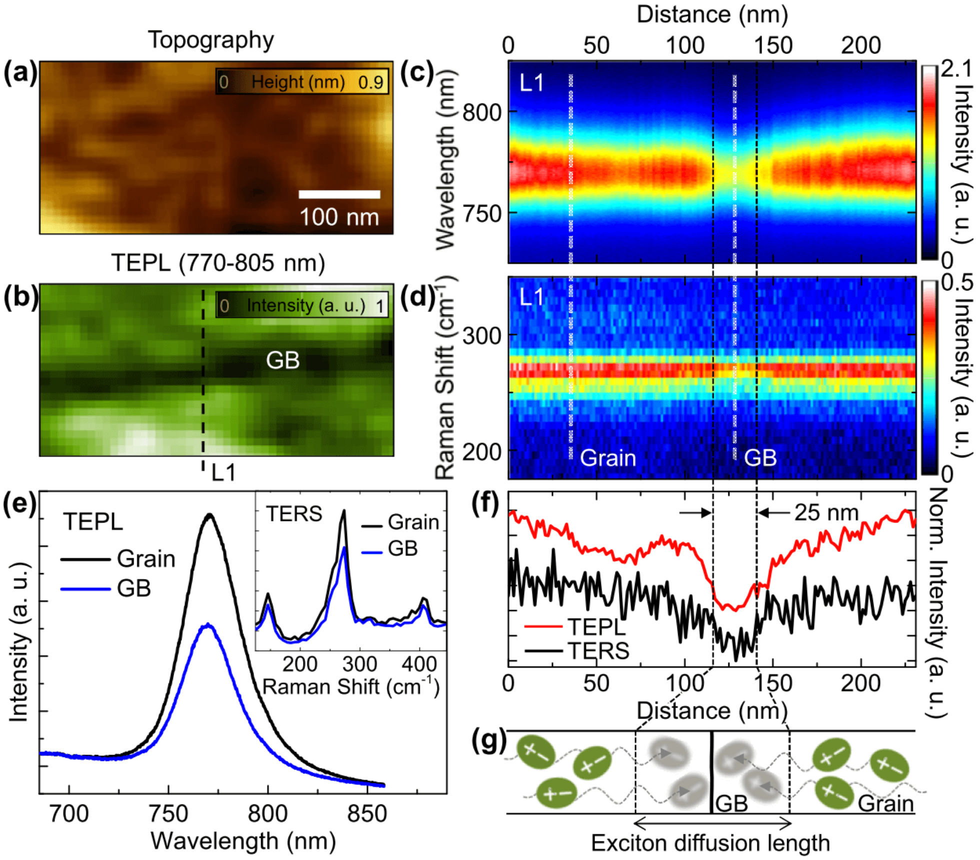

Figure 4.18: (a) AFM topography of GB area (indicated in Fig. 4.15b). (b) TEPL image for the integrated intensity at 770-805 nm (indicated in Fig. 4.15d). Spectral TEPL (c) and TERS (d) trace across GB (L1 indicated in (b)). (e) TEPL and TERS spectra derived from grain and GB regions indicated in (c) and (d) (dashed white lines). (f) Corresponding spectrally integrated line profiles for the 770 nm PL peak and 273 cm^{-1} Raman mode derived from (c) and (d). (g) Illustration of exciton diffusion length at GB.

irregularly along the edges, over a ∼$30-80$ nm wide region, as also seen in representative line traces E1-E4 (Fig. 4.17g).

The corresponding effect of the decrease in PL at the GBs can be clearly seen in the TEPL images Fig. 4.15 and Fig. 4.17e and appears somewhat distinct from the effect of edges and NS, as further analyzed in Fig. 4.18, showing a zoom in to a single GB (white box in Fig. 4.15d). The GB is not discerned in the AFM topography (Fig. 4.18a). Neither PL nor Raman emission exhibit a spectral shift (Fig. 4.18c-e), however both experience a decrease comparable to the case of NS and edges. Yet the PL decrease is quite homogeneous along the grain boundary with a narrow width of

$\sim$25 nm (Fig. 4.18f). Note that although we could not obtain correlated atomic resolution TEM or STM images of our specific samples, the symmetric mirror twinned GB structures were confirmed by TEM studies for TMD crystal under similar conditions [68].

Local strain engineering via nano-mechanical force

In order to investigate the effect of local strain on the PL modification, we use the AFM tip to locally apply a contact force to perturb the sample while simultaneously measuring the TEPL. The tip-sample distance is regulated by controlling the set-point and proportional-integral (PI) gains in feedback [120]. We set a low set-point and a high PI gain to apply mechanical force to the ML WSe_2. In this unusual feedback condition, AFM tip taps the sample with $\sim 10 - 30$ Hz frequency and the tapping force is increased by lowering the set-point. Through this force control of tip, the strain of the as-grown WSe_2 is locally released, as shown in Fig. 4.19. The bandgap of WSe_2 was shown to decrease linearly with increasing strain in the range of 0 - 2% [295]. Thus we can use the energy of the PL peak to estimate the amount of strain for various tip-sample separations. From comparison with far-field PL of both as-grown and transferred WSe_2 we assess that the crystals are initially under a tensile strain of $\sim$0.98%.

The change of direct bandgap energy of ML WSe_2 with respect to the applied tensile strain was calculated previously using the Heyd–Scuseria–Ernzerhof (HSE) density functional theory (DFT) [295]. The bandgap energy of ML WSe_2 is found to change linearly with the tensile strain. The PL peak of the unstrained sample depends on the growth condition and substrates. Our analysis is based on the assumption of the PL peak energy of the transferred WSe_2 crystal having 0% strain. The tensile strain of as grown sample is then calculated based on the linear dependence of the PL energy with strain as shown in Fig. 4.20 [295].

Fig. 4.19a shows that with increasing force exerted by the tip, the TEPL increases and spectral weight is transferred with the appearance of a blueshifted emission by $\sim$48 meV. The nano-mechanical tip interaction gives rise to an almost complete and irreversible strain release. In order to release the local strain and shift local bandgap to $\sim$48 meV as shown in Fig. 4.19a, the tip has to induce a stronger force onto the sample compared to TEPL measurements, and therefore

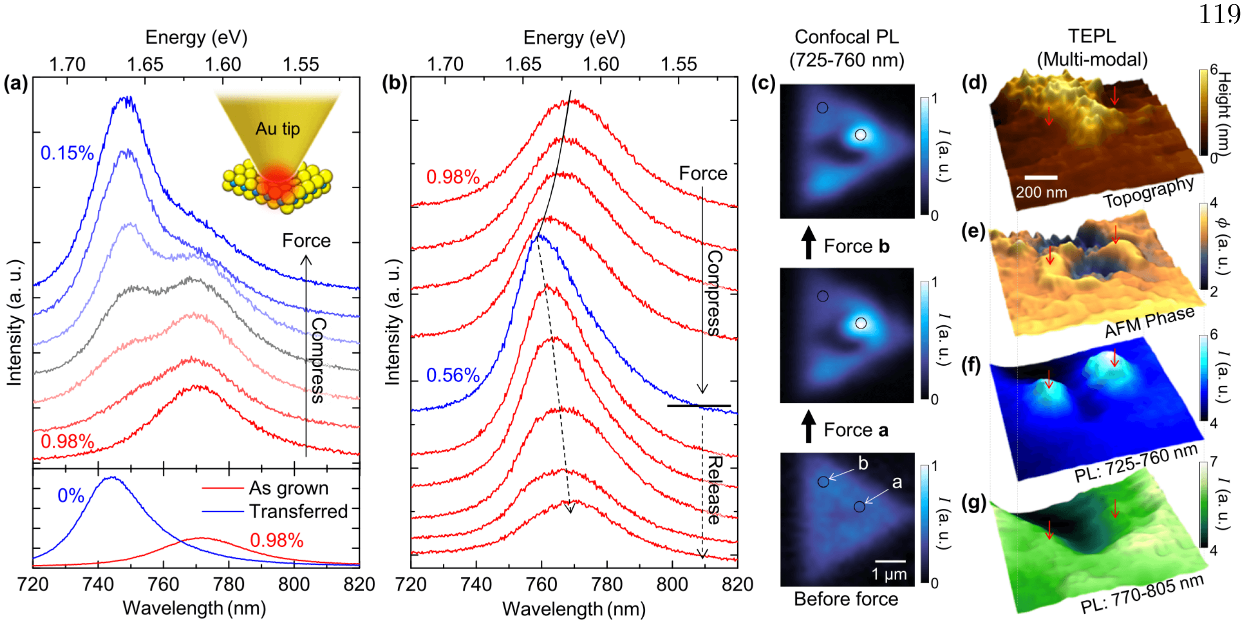

Figure 4.19: (a) Bottom: far-field PL spectra for the as-grown (red) and transferred (blue) ML WSe_2 on the SiO_2 substrates. Top: evolution of PL spectra of the as-grown ML WSe_2 with interacting compressive force of tip, giving rise to an irreversible release of the tensile strain of the crystal. (b) Reversible evolution of PL spectra under modest nano-mechanical tip-sample force interaction. (c) Confocal PL (725-760 nm) images before and after irreversible (a) and reversible (b) strain manipulation. (d) AFM topography, (e) AFM phase, (f) blueshifted TEPL (725-760 nm), and (g) main TEPL (770-805 nm) images for two locations near NS which exhibit low PL prior to nano-mechanical strain release.

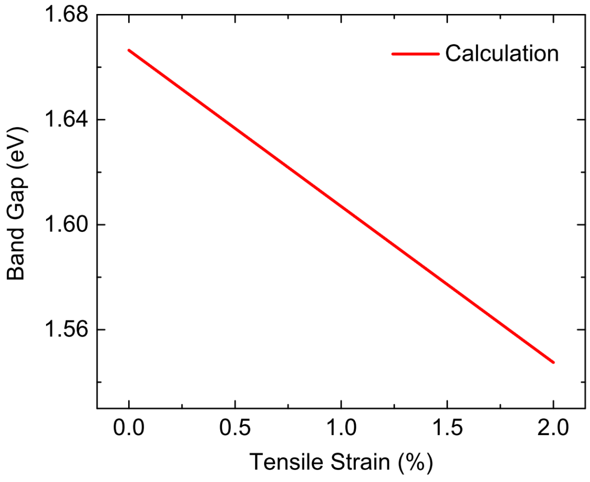

Figure 4.20: Calculation result for the bandgap change of ML WSe_2 with respect to the tensile strain. We assume the PL peak energy of the transferred sample has a 0% strain.

has to be closer to the WSe_2 crystal. This leads to a significant quenching of the near-field PL, such that the red (bottom) curves in Fig. 4.19a are dominated by the far-field response of the nearby strain released area resulting in the double peak structure we observe. The near-field PL signal increases (blue curves) when the strain released area is expanded to ~200 nm^2. The PL modification at the strain released crystal region is seen in the confocal PL imaging before and after the force interaction (Fig. 4.19c). Despite the only few $10'$s nm spatial localization of the apex force interaction, the strain released crystal region extends spatially over a ~1 μm sized area. We estimate the maximum force exerted to ~10 nN, without giving rise to tip apex modifications, as verified by repeated TEPL and TERS measurements.

Under careful and weak force interaction the strain can be partially released in a reversible fashion as shown in Fig. 4.19b, with a spectral shift of ~24 meV corresponding to a maximum release to ~0.56%. In this case the experimental conditions are similar to those used for the TEPL and TERS imaging, thus no discernible permanent PL modification is seen in the confocal PL image (Fig. 4.19c). Both the reversible and irreversible strain release induced by the tip force interaction are generally repeatable with similar results for different flakes.

Fig. 4.19d-g shows TEPL imaging on a WSe_2 flake near a NS region with initially strongly suppressed PL. Force interaction at the two locations indicated shows the appearance of blueshifted and enhanced PL. The associated strain release also manifests itself in a change in the AFM phase signal, yet not in the topography as expected.

4.2.4 Discussion

Our results are generally consistent with the findings of recent studies that have addressed the localized modification of the PL by structural heterogeneities [68, 69, 287, 288], yet add further spatial details and assignment to specific processes. An increase in PL intensity correlated with a spectral blueshift at GBs observed in [69] has been interpreted in terms of a local strain release and structural deformation, associated with the large TMD crystals studied (> 10 μm) and the resulting high substrate strain accumulated in the growth process. Our correlated spectroscopic results and the ease of nano-mechanical both reversible and irreversible local strain release by slight force perturbation would be consistent with this interpretation.

In contrast, recent near-field PL imaging revealed a decrease at GBs for small crystallites ($<$ 5 μm) [287] over a $\sim$120 nm average width and without spectral shifts.

The atomic defects at the twin GBs of ML TMDs have been investigated with transmission electron microscopy (TEM) [68, 284]. These atomic defects of GBs can be further deformed or bonds broken under high strain as a result of the crystal growth procedure [68, 69]. We therefore suggest that in the previous far-field PL imaging studies, which showed clear PL decrease(increase) at the GBs of the large size TMD crystal ($>$ 10 μm), might measure structurally deformed GBs [68, 69]. The large TMD crystals might have particularly high strain effect due to the long growth time and result in significantly large areas of PL modification at GB region. On the other hand, since the small TMD crystals have much less strain effect, PL modification is constrained to the nanoscale areas possibly dictated by exciton diffusion at the mid-gap states. In order to address this hypothesis, we perform far-field confocal PL imaging ($\sim$500 nm resolution) for $\sim$10 μm size polycrystalline WSe_2 crystal, and PL quenching at GBs is clearly revealed as shown in Fig. 4.21a-c. It should be also noted that despite the crystal sizes are small, interflake GBs always showed distinct PL quenching due to the structural deformation as shown in Fig. 4.21d-f.

This, together with our finding of a PL quenching (47%) without changes in structure and bandgap at the internal twin boundaries as concluded from the combined TERS and TEPL imaging, suggests that neither strain nor doping are responsible for the PL quenching, but instead non-radiative recombination process possibly from mid-gap states of defects. Given the atomic-scale lateral extent of the GB, the spatial scale of PL quenching would be related to the exciton diffusion length. Our value for the PL quenching width of $\sim$25 nm would be in good agreement with the expected exciton diffusion length of $\sim$24 nm as estimated from the measured values of exciton diffusivity and lifetime [68].

At the crystal edges our observed decrease in PL intensity, spectral blueshift, and spatial heterogeneity agree with previous studies [287]. Similar to disordered semiconductors [296, 297] the

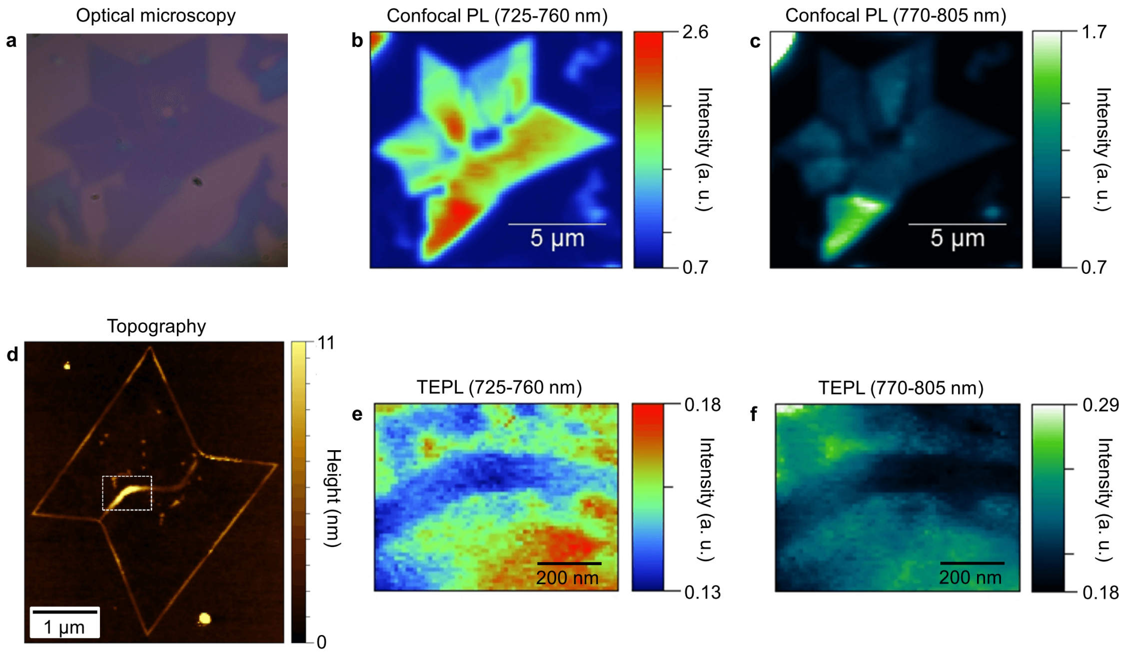

Figure 4.21: (a) Optical microscopy image of a polycrystalline ML WSe_2. (b) Confocal PL image for the integrated intensity at 725-760 nm spectral range. (c) Confocal PL image for the integrated intensity at 770-805 nm spectral range. (d) Topography image of the polycrystalline WSe_2 with dislocated GBs. (e) TEPL image of interflake GB region (indicated in (d) as a white dashed box) for the integrated intensity at 725-760 nm spectral range. (f) TEPL image of sample region for the integrated intensity at 770-805 nm spectral range.

quenching could be due to energy funneling from higher to lower energy states in the inhomogeneous system [287]. Our spatial extent of the disordered PL modification region of $\sim 30-80$ nm at the edges is in good agreement with the edge roughness observed by TEM [68]. Note that our length scale is significantly shorter than the ~300 nm reported in a previous near-field PL study [287]. This difference in length scales could either be due to different crystal structures or growth conditions. Lastly, the significant PL quenching and blueshift at NS can be attributed to the loss of Se [298], and the surface adsorbates are understood as tungsten (W) compounds left in the growth process [299] that can act as non-radiative recombination sites.

The electronic band structure of TMDs is sensitive to tensile strain that causes reduced orbital hybridization due to the weakened ionic bonds [300]. This gives rise to a redshift of the bandgap energy and an associated decrease in PL intensity [299, 301, 302, 295]. Therefore, we believe the

PL energy of transferred WSe_2 is significantly higher than the as-grown sample due to the released tensile strain [69], as confirmed by our force-controlled nano-spectroscopy measurements.

In summary, we have measured modifications of the electronic structure and optical properties of WSe_2 at the nanoscale through high resolution (< 15 nm) multi-modal TEPL and TERS imaging. A nonlocal PL modification at twin boundaries associated with a $\sim$25 nm exciton diffusion length, and $\sim 30 - 80$ nm wide region of optical heterogeneity at edges is observed. Further, we have demonstrated dynamic tuning of the local bandgap of ML WSe_2 by releasing and controlling local strain. Our hybrid opto-mechanical nano-probe technique can be used for tunable nano-electronic devices where the carrier mobility is controlled via strain engineering [299, 301]. We expect this method to help in the design of novel nano-photonic/electronic TMD devices by enabling local bandgap engineering and *in-situ* spectroscopy of 2D materials.

4.3 Radiative control of dark excitons in WSe_2 monolayer at room temperature[3]

Excitons, Coulomb-bound electron-hole pairs, are elementary photo-excitations in semiconductors that can couple to light through radiative relaxation. In contrast, dark excitons X_D show anti-parallel spin polarization with generally forbidden radiative emission. Because of their long lifetimes, these dark excitons are appealing candidates for quantum computing and optoelectronics. However, optical read-out and control of X_D states has remained challenging due to their decoupling from light. Here, we present a tip-enhanced nano-optical approach to induce, switch, and programmably modulate the X_D emission at room temperature. Using a monolayer transition metal dichalcogenide (TMD) WSe_2 on a gold substrate, we demonstrate $\sim 6 \times 10^5$-fold enhancement in dark exciton photoluminescence quantum yield achieved through coupling of the antenna-tip to the dark exciton *out-of-plane* optical dipole moment. This is possible because of the large Purcell factor of the tip-sample nano-cavity, which is $\geq 2 \times 10^3$. Our approach provides a new and facile way to harness excitonic properties in low-dimensional semiconductors offering new strategies for quantum optoelectronics.

4.3.1 Motivation

The two-dimensional (2D) nature of monolayer (ML) transition metal dichalcogenides (TMDs) creates tightly bound excitons with strong Coulomb interactions and an extraordinarily large binding energy [48, 49, 304]. Associated anomalous excitonic properties and strong light-matter interactions suggest a new paradigm for a range of applications in optoelectronics [305, 306, 307, 308].

The broken inversion symmetry and strong spin-orbit coupling (SOC) in ML TMDs lead to spin- and energy-splitting in the conduction band [309, 310, 311]. The electrons with anti-parallel spins in the two respective states of the split conduction band give rise to bright and dark excitons [166, 312, 313] by combining with the holes in the higher-lying valence band. These two

---

[3] This section draws significantly from [303]. The experiments and simulations were performed and analyzed by K.-D. Park, and supervised by M. B. Raschke. This work was performed in collaboration with G. Clark and X. Xu from the University of Washington at Seattle.

distinct states of exciton have orthogonal transition dipole orientation associated with the spin configuration, as demonstrated recently both theoretically [311, 314] and experimentally at low temperature [315, 70, 71, 316].

As known from zero-dimensional quantum dot (QD) studies, dark excitons X_D have a long lifetime due to solely non-radiative decay channels and spin flip processes [317]. This distinct nature of dark excitons in low-dimensional semiconductors has attracted much attention for potential applications as coherent two-level systems for quantum information processing [318], or Bose-Einstein condensation (BEC) [319], yet a full-scale study is hampered by the *out-of-plane* transition dipole moments making them difficult to access optically [315, 70, 71, 316].

In order to induce dark exciton emission in atomically thin TMDs, different approaches were demonstrated in recent low temperature photoluminescence (PL) studies. Following a procedure as established for dark exciton emission in QDs [320, 321], tilting the spin direction by applying a strong external *in-plane* magnetic field ($\geq$ 14 T) induces a weakly allowed in-plane optical transition by the Zeeman effect [315, 70]. Alternatively, by exciting out-of-plane polarized surface plasmon polaritons (SPP) in a TMD-plasmonic device, radiative X_D emission through dark exciton-SPP coupling can be induced [71]. This weak X_D emission can also be observed through polarization-selective detection from the sample edge [316]. However, all these studies have been restricted to cryogenic temperature conditions (T $\leq$ 30 K), because otherwise the small energy difference of $<$ 50 meV between dark and bright exciton leads to thermal excitation into the then overwhelming bright exciton emission channel.

In this work, we demonstrate a new approach for dark exciton spectroscopy based on state selective dark exciton coupling with tip-enhanced PL (TEPL) spectroscopy, as illustrated in Fig. 1a-b. Here, the scanning probe nano-optical antenna-tip selectively couples to the *out-of-plane* transition dipole moment which facilitates Purcell-enhanced dark exciton emission with few-fs radiative dynamics [121]. With this simple and generalizable approach we demonstrate excitation, modulation, and radiative control of dark exciton emission, at room temperature, and with high quantum yield. The combination of the nanoscale localized ($\leq$ 15 nm) effective excitation through

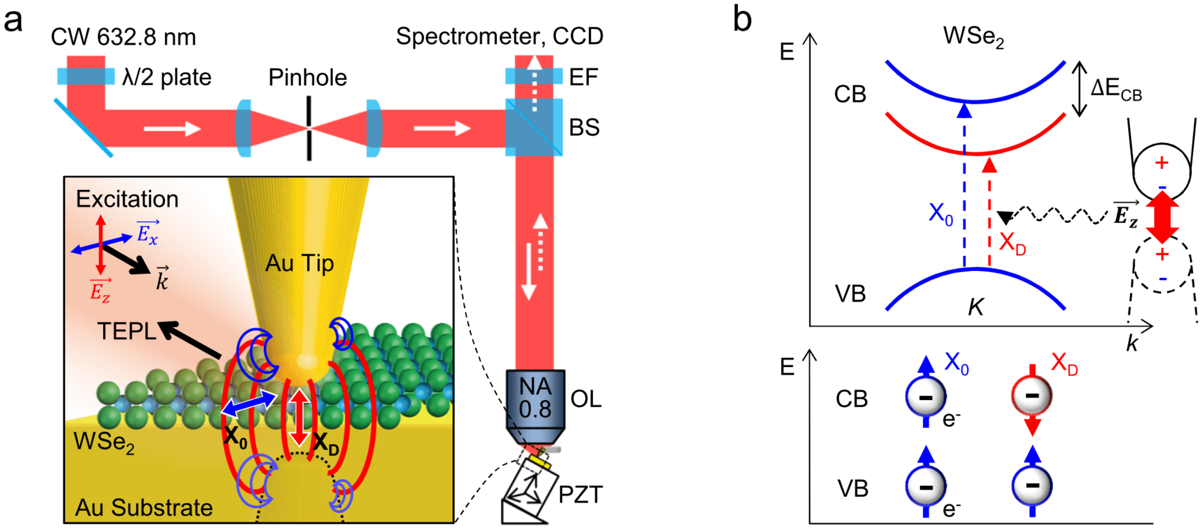

Figure 4.22: Schematic of tip-enhanced photoluminescence spectroscopy and electronic band structure of WSe_2. (a) Selective excitation and probing of the transition dipole moments of dark (*out-of-plane*) and bright (*in-plane*) excitons by polarization control. EF: edge filter, BS: beam splitter, OL: objective lens. (b) Split-band and -spin configurations of bright and dark exciton states. Spin-forbidden optical transition of dark excitons is induced by strongly confined local antenna fields with plasmonic Purcell enhancement at the tip-sample nano-gap. CB: conduction band, VB: valence band.

strongly confined *out-of-plane* optical fields at the tip-Au substrate nano-gap, with antenna-tip mediated near- to far-field mode transformation gives rise to a $\sim 6 \times 10^5$-fold X_D-PL enhancement as we demonstrate in WSe_2 with a Purcell factor $\geq 2 \times 10^3$ enhanced spontaneous emission rate. Through precise control of the distance between the antenna-tip and the sample, the coupling strength of dark excitons to the antenna-tip can be modulated. This method allows active control of the dark exciton *On/Off* states in time and space.

4.3.2 Experiment

WSe_2 monolayers are grown by physical vapor transport using powdered WSe_2 as precursor material. Source material (30 mg) in an alumina crucible is placed in the hot zone of a 25.4 mm horizontal tube furnace, and an SiO_2 substrate is placed downstream in a cooler zone at the edge of the furnace (750 − 850 °C). Before growth, the tube is evacuated to a base pressure of 0.13 mbar and purged several times with argon. The furnace is then heated to 970 °C at a rate of 35 °C/min and remains there for a duration of 5-10 min before cooling to room temperature naturally. A flow of 80 sccm argon and 20 sccm hydrogen is introduced as carrier gas during the 5-10 min growth period. The as-grown WSe_2 crystals are then transferred onto flat template stripped Au substrates using a wet transfer technique. For that purpose, PMMA (6% in anisole) is spin-coated onto the SiO_2 wafer, covering the region with WSe_2 monolayer crystals. The wafer is then placed in a solution of dilute hydrofluoric acid (20% in distilled water), until the SiO_2 layer is etched away and the PMMA membrane with WSe_2 crystals floats free. The membrane is then rinsed in distilled water to remove residual etchant, and scooped up onto a wire loop. The PMMA membrane can then be placed onto the Au sbstrates under an optical microscope, similar to the commonly used dry transfer technique. Once the membrane has been lowered into contact with the substrate, heating the substrate $\geq$ 160 °C melts the PMMA layer releasing it from the wire loop.

The experiment is based on TEPL spectroscopy [20], with side illumination of Au nano-tip manipulated in a shear-force atomic force microscopy (AFM) as shown schematically in Fig. 4.22a. In the TEPL spectroscopy setup, the sample is mounted to a piezoelectric transducer (PZT, P-611.3, Physik Instrumente) with sub-nm precision positioning. Electrochemically etched Au tips (~10 nm apex radius) are attached to a quartz tuning fork (resonance frequency = ~32 kHz) [20]. To regulate the tip-sample distance, the AFM shear-force amplitude is monitored and controlled from the electrically driven tuning fork [120]. Coarse tip positioning is performed using a stepper motor (MX25, Mechonics AG), and shear-force feedback and sample position are controlled by a digital AFM controller (R9, RHK Technology). The sample surface is tilted by ~60° with respect to the incident k-vector for effective excitation. A Helium-Neon laser beam (632.8 nm, $\leq$ 0.3 mW), after passing through a half wave plate for polarization control, is focused into the junction between the Au substrate and the tip apex by an objective lens (NA=0.8, LMPLFLN100×, Olympus). TEPL signal is collected in backscattered direction, passed through an edge filter (633 nm cut-off) and detected using a spectrometer (f = 500 mm, SpectraPro 500i, Princeton Instruments) with a thermoelectrically cooled electron-multiplied charge-coupled device (CCD, ProEM+: 1600 eXcelon3, Princeton Instruments). The spectrometer is calibrated using hydrogen and mercury

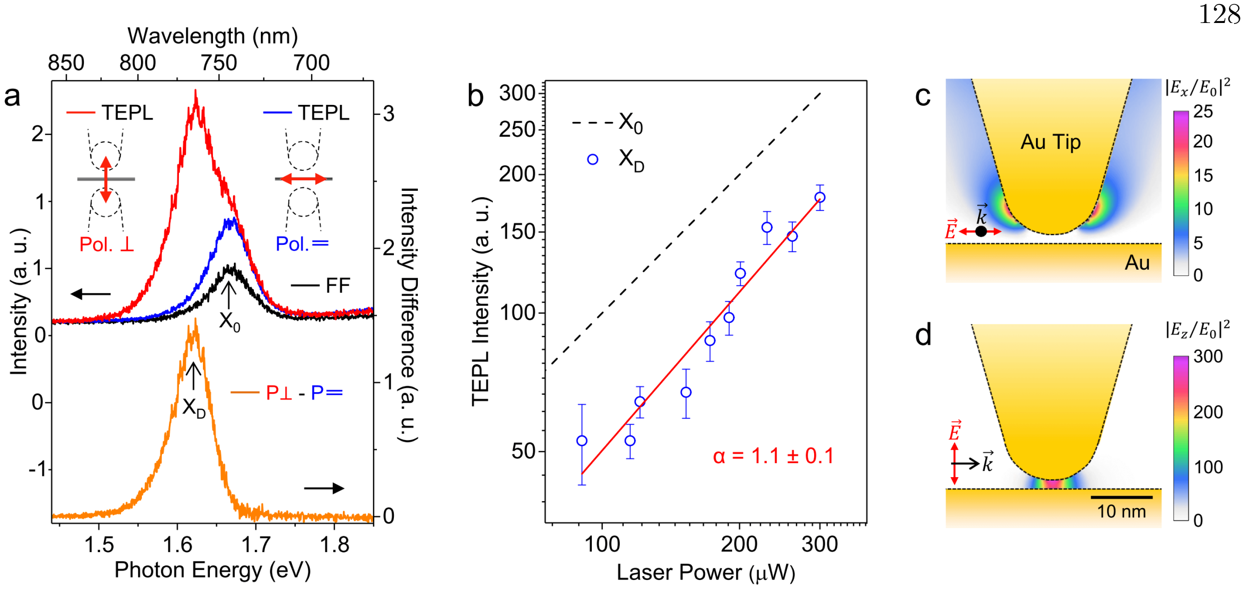

Figure 4.23: Probing radiative emission of dark excitons of WSe_2 through polarization- and power-dependence of tip-enhanced photoluminescence. (a) Excitation polarization dependent TEPL spectra of monolayer WSe_2 on a Au substrate at ∼1 nm tip-sample distance with tip-selective X_D emission (orange). (b) Log-plot of the power dependence of TEPL intensity of dark (X_D) and bright (X_0) exciton. (red line is a fit of the dark exciton emissions exhibiting a linear power dependence). (c-d) Finite-difference time domain (FDTD) simulation of the *in-plane* (c) and *out-of-plane* (d) optical field intensity and confinement under experimental conditions of (a).

lines, and a 150 grooves/mm grating is used to obtain a high bandwidth spectrum for simultaneous measurement of gap plasmon and TEPL spectra. The Au tip is oriented normal with respect to a planar Au substrate. TEPL spectroscopy is then performed by tip-sample distance control between the Au tip and a ML WSe_2 transferred onto the Au substrate. All experiments are performed at room temperature.

4.3.3 Results

Radiative emission of dark excitons at room temperature

Fig. 4.23a shows TEPL spectra at 1 nm tip-sample distance with excitation polarization oriented parallel or perpendicular with respect to the sample surface. A strong X_D emission peak is observed (red). In contrast, the X_D response is suppressed for tip-perpendicular polarization (blue) even though enhanced PL response of X_0 is observed, attributed to an *in-plane* localized optical field effect in agreement with the spectral X_0 characteristics in far-field emission (black). The difference spectrum after polarization correction for X_0 then corresponds to the pure X_D mode emission (orange).

We perform Lorentzian line fit analysis of the bright (blue) and dark (orange) excitons to compare the peak energy and spectral linewidth of them as shown in Fig. 4.24a and b. Lorentzian functions provide for a better line fit for both spectra compared to Gaussian function due to the homogeneous broadening likely dominated by phonon scattering. From Lorentzian fitting of the spectra for X_D and X_0, the dark exciton state is found at $\sim$46 meV below the bright exciton associated with the intravalley energy splitting in the conduction band. While the bright exciton peak shows Lorentzian shape to good approximation, the dark exciton is asymmetric with a shoulder at 780 nm. This shoulder is possibly due to a lifting of the valley degeneracy [314], a Fano resonance resulting from the exciton-plasmon coupling [322], or the dark trions [71, 70]. This result is in good agreement with recent X_D observations facilitated by *in-plane* magnetic field (47 meV) [70], SPP coupling (42 meV) [71], and polarization-selective detection from the sample edge (40 meV) [316]. We note that the energy of bright and dark exciton emission is only minimally perturbed by the Au substrate due to the tightly bound excitons within the monolayer [48, 49, 304, 323].

Further the TEPL linewidth of the X_D emission is more narrow than the bright exciton linewidth, in agreement with previous observation (Fig. 4.24) [71]. The observed TEPL linewidth of the dark exciton emission is more narrow than that of the bright exciton in agreement with recent observation based on surface plasmon polaritons (SPP)-device based probing [71]. On the other hand, the dark exciton emission induced by the Zeeman effect showed the same linewidth as the bright excitons [315, 70]. We believe this feature is attributed to the different (intrinsic vs. extrinsic) spin flip mechanisms of the dark excitons.

To test for a possible contribution from bi-exciton emission, which has comparable photon energy to dark states, we measure the TEPL intensity as a function of the excitation power for X_D and X_0 emissions. Fig. 4.23b shows the resulting TEPL power dependence based on linear fits to the TEPL spectra and plotting the integrated spectral intensities of X_D and X_0 emissions. On the

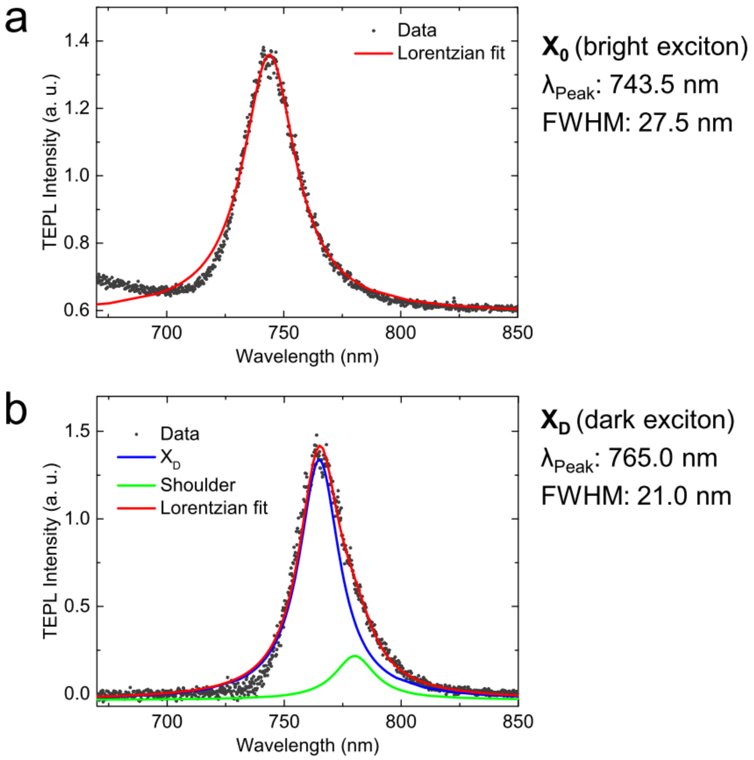

Figure 4.24: TEPL spectra of the bright (a) and dark (b) excitons of WSe_2 monolayer transferred onto the Au substrate with Lorentzian line fit analysis, derived from Fig. 4.23a.

basis of the linear power dependence behavior, we exclude bi-exciton emission [292].

To understand the polarization dependence of the X_D emission, and to model the intensity difference of *in-plane* and *out-of-plane* local fields at the Au tip - Au substrate junction, we calculate the confined optical field intensity using finite-difference time-domain (FDTD) simulation for our experimental conditions (Fig. 4.23a).

As shown in Fig. 4.23c-d, in the nano-gap, the optical field intensity of the *out-of-plane* mode is stronger by a factor of $\geq 3 \times 10^2$ than that of the *in-plane* mode as expected.

For further investigation of the antenna-tip induced dark exciton emission, we perform TEPL measurements under precise nanometer tip-sample distance control. Fig. 4.25a shows contour plots of TEPL spectra of ML WSe_2 with respect to the distance between the Au tip and Au substrate. Bright exciton emission (X_0) at 1.667 eV is observed in the distance region of 4 - 12 nm attributed to the enhanced localized (*in-plane*) near-field excitation at the tip apex. In contrast, for shorter

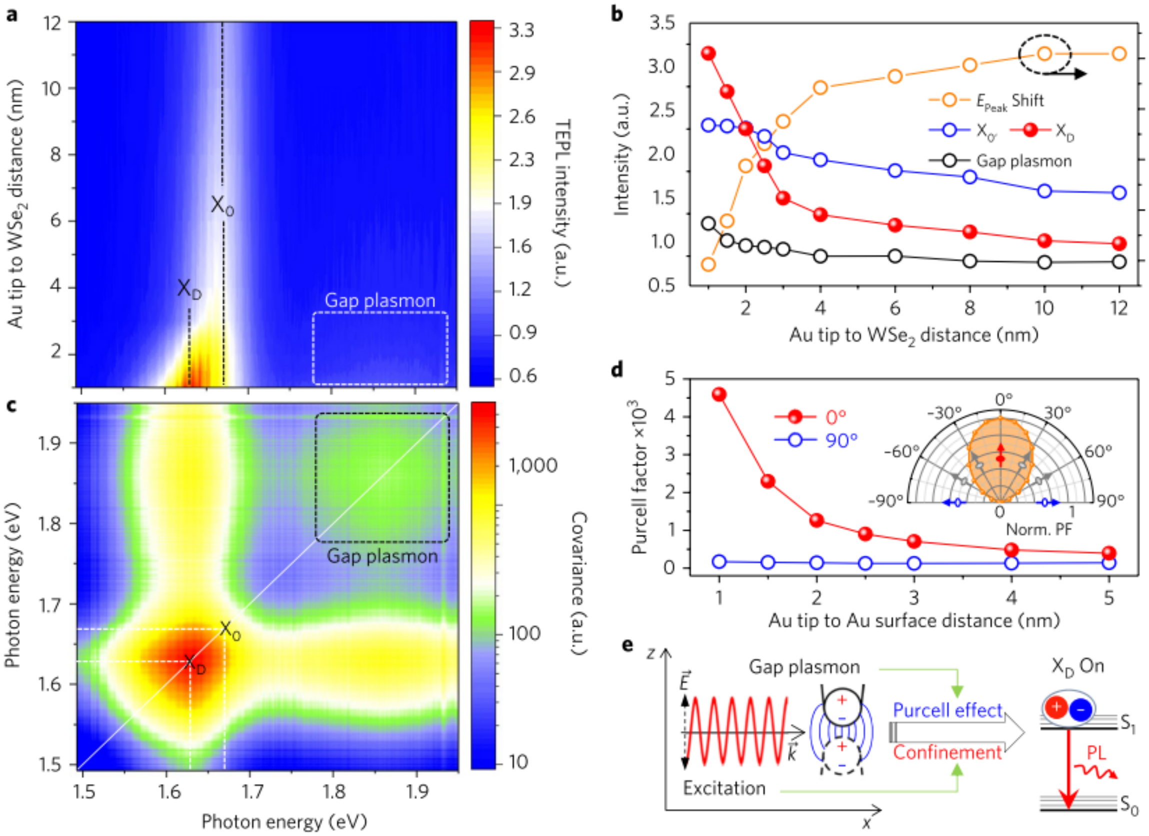

Figure 4.25: Active control of tip-induced radiative emission of dark excitons of WSe$_2$ monolayer. (a) Tip-sample distance dependence of TEPL spectra. (b) Tip-sample distance dependence of peak intensity of TEPL responses (X$_D$, X$_0$, and gap plasmon) with spectral energy shift, derived from (a). (c) 2D covariance map of the distance dependent TEPL spectra from (a), exhibiting strong correlation between the gap plasmon and X$_D$ emission. (d) Simulated plasmonic Purcell factor for *out-of-plane* and *in-plane* spontaneous dipole emitters with respect to the distance between Au tip and Au surface. Inset: Normalized plasmonic Purcell factor with respect to emitter orientation. (e) Illustration of the tip-enhanced emission mechanism of dark excitons as a combination of both enhanced excitation (*out-of-plane* optical field confinement) and antenna-mediated emission (polarization transfer and enhanced radiative decay by Purcell effect) at the plasmonic nano-gap.

distances in the 1 - 3 nm range, dark exciton X$_D$ emission emerges and dominates the spectra at 1.621 eV. In addition, a weak tip-plasmon PL response from the Au - Au nano-gap is seen as described previously [121]. Fig. 4.25b shows corresponding distance dependence in TEPL intensity for X$_D$, X$_0$, and gap plasmon emission. While the X$_0$ peak intensity saturates below 2 nm distances due to polarization and energy transfer and non-radiative relaxation in the metal tip and substrate, the X$_D$ peak intensity continues to rise sharply correlated with an increasing gap plasmon PL intensity. Because the *in-plane* dipole of the X_0 does not couple to the antenna mode, the PL quenching dominates over enhancement at short distances. In contrast, the X_D emission with its *out-of-plane* dipole, when coupled to the antenna mode with its fs-radiative decay, continues to dominate at short distances [121, 324, 4].

This behaviour is most clearly evident in the 2D covariance plot (Fig. 4.25c). From the full data set of Fig. 4.25a, we calculate the covariance $\sigma(i,j)$ between wavelengths i and j from the distance dependent TEPL intensities $I(i,d)$ using

$$\sigma(i,j) = \frac{1}{N}\sum_{d=d_1}^{d_n}[I(i,d) - \langle I(i)\rangle] \times [I(j,d) - \langle I(j)\rangle]. \tag{4.2}$$

The resulting 2D covariance map clearly shows strong (weak) correlation between the *out-of-plane* gap plasmon and the dark (bright) exciton emission. The plasmon PL emission serves as an indicator and metric of the X_D-tip polarization transfer and Purcell enhancement of rapid PL emission as established previously (see Ref. [121]).

Radiative control of dark excitons

As we demonstrated previously [20], the shear-force AFM tip can also act as an active control element to modify excitonic properties of TMDs both spectrally and spatially. In the optical antenna tip-WSe_2-Au surface configuration, the nano-gap is regulated by a shear-force feedback mechanism [38]. This gives rise to sub-nm precise control of the gap plasmon response, and associated strongly correlated dark exciton emission. Fig. 4.26a-c show time-series contour plots of the TEPL response (X_D, X_0, and gap plasmon) during constant (a), discrete (b), and modulated (c) tip-sample distance. The precision of nano-gap control relies on the mechanical quality (Q) factor of the AFM tuning forks. We generally achieve Q-factors of $\geq 4 \times 10^3$ by attaching two Au tips to both prongs of the tuning fork. Using this high-Q sensor, we regulate a tip-sample distance with ~0.2 nm precision, and stably maintain the X_D *On* state under ambient conditions with minimal fluctuations (a). Varying the distance between 1 nm and 5 nm the X_D can be switched discretely between its *On* and *Off* states (b). Correspondingly, by continuously time-varying the tip-sample distance, we can programmably modulate the X_D emission (c). Fig. 4.26d shows the derived time-series of peak

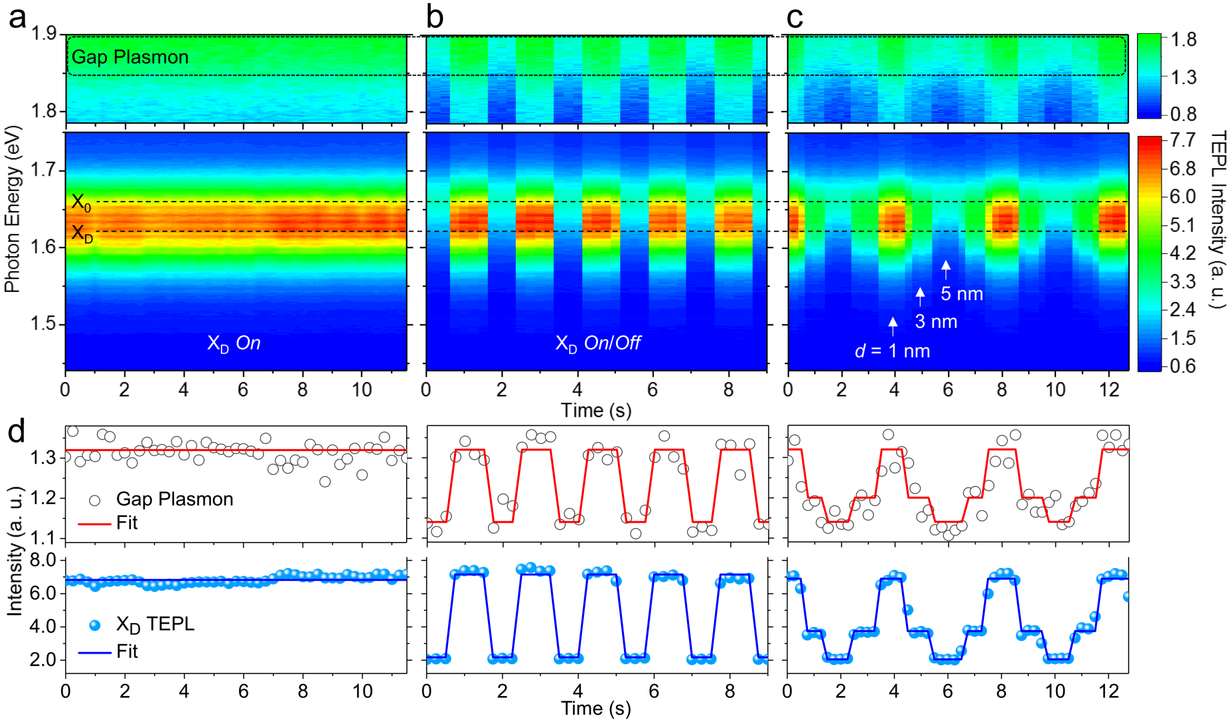

Figure 4.26: Switching and modulation of dark exciton emission. (a) Time-series TEPL response (X_D, X_0, and gap plasmon PL) in continuous *On* state of X_D emission at 1 nm tip-sample distance. (b) Discrete *On/Off* switching of X_D emission with discrete tip-sample distance variation between 1 nm and 5 nm. (c) X_D emission modulation by functional control of tip-sample distance. (d) Time-series of peak intensity of TEPL response with correlation between corresponding X_D emission and gap plasmon, derived from (a)-(c).

intensity of TEPL response from Fig. 4.26a-c, with correlation of X_D PL and gap plasmon, verifying the precise control of the X_D emission.

4.3.4 Discussion

Radiative decay mechanisms of dark excitons

In 2D TMDs, as dictated by the C_{3h} point group and resulting selection rules, only an *out-of-plane* optical transition is allowed with $\sim 10^{-3} - 10^{-2}$ times smaller radiative decay rate compared to an *in-plane* optical transition dipole of the bright excitons [311, 314, 316].

In principle, a spin flip is required to induce radiative decay of the dark excitons [314]. The electron spins can be extrinsically flipped by applying an *in-plane* magnetic field [70]. Using a large field of ≥ 14 T, a radiative decay rate $\Gamma \sim 10^{-3}\Gamma_B$ can be obtained with *in-plane* optical transition by the Zeeman effect [315, 70], where Γ_B is the radiative decay rate of the bright excitons. On the contrary, when the reflection symmetry in the surface normal direction is broken (typical condition for TMD crystals on a flat substrate), an intrinsic spin flip is facilitated by a virtual transition in the conduction band attributed to the SOC mixing. This then induces an *out-of-plane* dipole transition by the perturbation of a local field [325, 314]. Since this transition is between quantum states with identical magnetic quantum number and opposite parity, the transition dipole moments give rise to Bychkov-Rashba coupling to an *out-of-plane* optical field [326]. The associated radiative decay rate $\Gamma_D \sim (10^{-3} - 10^{-2})\Gamma_B$ is estimated theoretically [311, 314], and is independent of an external field.

In our experimental design, a combination of two physical mechanisms of increase in excitation rate by field enhancement as well as Purcell factor induced optical antenna emission (Fig. 4.25e) is responsible for the ability to detect the dark exciton modes via tip-coupling to an *out-of-plane* field. First, a strongly confined *out-of-plane* optical field effectively excites the transition dipole moment of dark excitons with $|E_z|^2$ in the nano-gap enhanced by a factor of $\geq 3 \times 10^2$ compared to the incident field intensity $|E_0|^2$ (Fig. 4.23d). In addition, and most significantly, the spontaneous emission rate is enhanced in the nano-gap due to the plasmonic Purcell effect [327, 323]. Here, as demonstrated previously [121], near-field dipole-dipole coupling and exciton polarization transfer into the tip with its few-fs radiative lifetime of its plasmonic optical antenna mode, gives rise to an increased emission of the dark exciton with decreasing tip-sample distance. To model this effect we computationally design *out-of-plane* and *in-plane* fluorescent model dipole emitters positioned within the nano-gap to calculate the effective Purcell factor ($\gamma_{PF} = \gamma/\gamma_0$, see Fig. 4.27).

We use a commercial FDTD simulation software to estimate the Purcell enhancement (radiative decay rate enhancement) factor of the dark excitons, $\gamma_{PF} = \gamma/\gamma_0$. For the geometry of Au tip (with 5 nm apex radius) in close proximity to the Au substrate, we model the dark exciton of a monolayer WSe_2 as a monochromatic fluorescent emitter (electric dipole, $\lambda = 765$ nm) as shown in Fig. 4.27a. The position of the emitter is fixed at 0.3 nm above the Au substrate. For simulation of

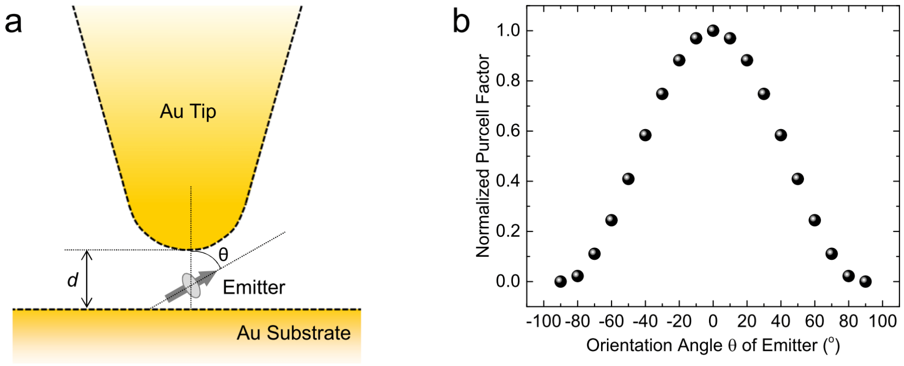

Figure 4.27: (a) Illustration of the computational design of Au tip, Au substrate, and fluorescent emitter (electric dipole) for finite-difference time domain (FDTD) simulation of Purcell enhancement factor. (b) Normalized Purcell enhancement factor of the fluorescent emitter with respect to the orientation angle.

the distance dependent Purcell enhancement factor (Fig. 4.25d), the distance (d) between the Au tip and the Au substrate is controlled by moving the tip position. The orientation of the emitter is set between 0° and 90° to simulate the angle dependent Purcell factor (Fig. 4.27b) as well as the dark and bright excitons.

In FDTD simulations, the Purcell factor is calculated by the ratio of the emission intensity radiated by an electric dipole in the nano-structured environment and in free space emission. Specifically, the Purcell factor is determined by the polarizability of the near-field coupled Au-Au nano-gap, the local density of states of the system defined by the Green's function, and the vector magnitude of the dipole moment.

As shown in Fig. 4.25d, the Purcell factor of an *out-of-plane* spontaneous emitter (0°) in the tip-surface gap exceeds 2×10^3 for ≤ 1.5 nm distances as a result of the polarization transfer and rapid radiative tip emission.

Enhancement factor of tip-induced dark exciton emission

For our experimental condition, the resulting overall TEPL intensity enhancement factor (EF) of the dark exciton emission as a combination of both effects given by

$$< \mathrm{EF} >= |\frac{E_z}{E_0}|^2 \cdot \gamma_{PF}, \tag{4.3}$$

is estimated to be as high as ~6×10^5 at 1.5 nm plasmonic nano-gap. This enhancement factor of the dark excitons is, to the best of our knowledge, the largest enhancement factor for fluorescent emitters investigated to date. In comparison, even refined plasmonic Ag nanocubes coupled to a Ag film achieved ~3×10^4-fold fluorescence enhancement from cyanine molecules as the closest analogue [328, 327]. This extraordinary PL enhancement is due to the strictly *out-of-plane* oriented transition dipole moment in the atomically thin semiconductor sandwiched in the $\leq$ 1.5 nm plasmonic nano-gap.

This *out-of-plane* mode selective enhancement facilitates the room temperature observation of $\mathrm{X_D}$ not readily possible with other techniques. We can quantify the ratio of near-field TEPL intensity of the dark excitons (I_D^{NF}) compared to the far-field PL intensity of the bright excitons (I_B^{FF}) given by

$$\frac{I_D^{NF}}{I_B^{FF}} \approx |\frac{E_z}{E_0}|^2 \cdot \gamma_{PF} \cdot \frac{\Gamma_D}{\Gamma_B} \cdot \frac{\eta_D}{\eta_B}. \tag{4.4}$$

Here, Γ_D and Γ_B represent respective decay rates, modified by the Purcell factor γ_{PF}, and η_D and η_B are relative occupation numbers of thermally populated dark and bright excitons, respectively, with their ratio η_D/η_B given by $e^{\frac{\Delta E}{k_B T}}$ with ΔE the energy splitting between the dark and bright excitons [329]. With the parameters from above, $I_D^{NF}/I_B^{FF} \sim 4\times10^3 - 4\times10^4$ at 300 K, thus facilitating direct probing and active control of the tip-enhanced radiative emission of the dark excitons with strong contrast even at room temperature. In the absence of the antenna-tip polarization and Purcell effect enhancement, the complementary approaches of inducing dark exciton emission by an *in-plane* magnetic field [315, 70], SPP coupling [71], and polarization-selective edge detection [316] do not readily extend to room temperature due to the otherwise dominant spectral weight of the bright exciton.

We note that the Au substrate primarily serves the purpose to allow for the formation of the *out-of-plane* plasmonic nano-cavity by the Au tip inducing a near-field coupled image dipole in the substrate. This nanocavity with $\leq$ 1.5 nm gap gives rise to large Purcell factor (> 2,000) compared to dielectric substrates, which is responsible for the enhancement of the dark exciton emission. With regards to the screening effect, the energy of bright and dark exciton emission is only minimally perturbed by the Au substrate due to the tightly bound exciton within the monolayer. In literature, a slight modification in peak energy has been observed for TMD monolayers using a gold substrate/nanoparticle as results of several effects, e.g., hot-electron induced structural phase transition [330] and n-doping [331] effects. However, these hot-electron induced effects are very weak in our case due to the lower excitation energy as explained in [332].

Our new approach thus gives access to potential applications of dark excitons in quantum nano-optoelectronics over a wide temperature range. We envision the demonstrated tip-antenna platform for room temperature dark exciton emission with or without nano-opto-mechnical control [20] as ideal building block for functional quantum devices. Further, the nanoscale optical switching of the spin states paves way for new design and fabrication of nano-spintronic devices. Specifically, the control of long-lived dark excitons confined in only ~150 nm^3 mode volume can be exploited to create nanoscale devices for integrated quantum-photonic circuits and active quantum information processor such as nano-light emitting diodes, nano-optical switch/multiplexer, high-density memory, and qubit. The nano-confinement further allows for imaging with $\leq$ 15 nm spatial resolution of heterogeneity of dark excitonic properties in 2D TMDs [20], with the possibility for an additional modulation in electronic energy with local strain engineering via nano-mechanical tip force control as we demonstrated recently [20]. The range of dynamic controls including coherent ultrafast excitation and tip/antenna manipulation thus gives access to a range of new phenomena at the sub-10 nm scale regime including room temperature strong coupling [251, 333], interlayer electron-phonon coupling [334], or *out-of-plane* exciton behaviours [335]. Further, the range of application can be extended to dark excitons in semiconducting carbon nanostructures, QDs, and molecular materials beyond TMDs and other van der Waals materials.

4.4 Radiative control of localized excitons in WSe_2 monolayer at room temperature[4]

4.4.1 Motivation

Single photon emitter is a light source that generate particle type light with the antibunching characteristics [336, 337, 338]. This single photon state can be explained only with a quantum mechanical interpretation on the contrary to the coherent light source, which explained by classical interpretations. From the quantization of the electromagnetic field, we can classify three distinguished states of light: i) coherent states, ii) thermal states, and iii) number states (Fock states) [339]. The quantized optical field with a narrow bandwidth is interpreted as a single photon emitter using a definition of the number states [340]. Fig. 4.28 describes different states of light distinguished from the second order coherent function $g^{(2)}(\tau)$.

For coherent states (coherent light), $g^{(2)}(\tau) \equiv$ for all τ, and the thermal states generally show $g^{(2)}(\tau) = 1 + |g^{(1)}(\tau)|^2 \geq 1$. The bunching peak in thermal states is due to the bosonic character of photons in classical light sources. This bunching phenomenon is only observed when the coherence length is smaller than the temporal resolution of the detectors since the temporal width of the bunching peak is approximately the inverse of the spectral linewidth. For the number states $|n\rangle$ of light, the inverse feature $g^{(2)}(\tau) =$ 1-(1/n) (antibunching) is observed, and for the single photon state, $g^{(2)}(\tau) = 0$.

Single photon emitters are key element for scalable quantum computing [340, 341]. These single photon states can be generated using attenuated laser pulses [342], nonlinear crystals [343], and magneto-optical trap (MOT) [344]. However, all these methods require complex and massive experimental setups, which are not ideal to achieve scalable quantum computing. Therefore, naturally generating single photon sources are desirable to use, e.g., epitaxially grown single quantum dots [345].

---

[4] This section covers measurements and simulations performed and analyzed by K.-D. Park, and supervised by M. B. Raschke. This work was performed in collaboration with G. Clark and X. Xu from the University of Washington at Seattle.

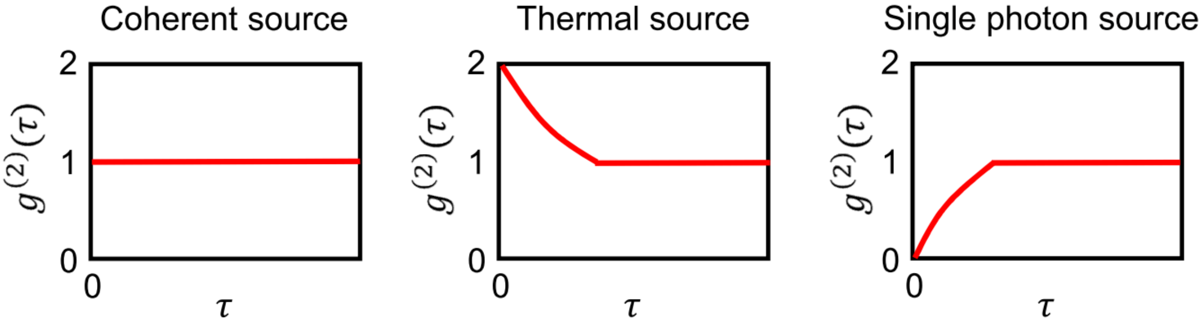

Figure 4.28: Different states of light source distinguished from the second order coherent function $g^{(2)}(\tau)$.

Recently, single quantum emitting states are discovered in atomically thin TMDs when excitons are localized to defects or quantum dot like confined potentials [72, 73, 167, 168, 169]. This new class of single quantum emitter from localized excitons (X_L) in layered 2D materials is promising candidate for potential applications in quantum optics and information technologies. However, all these recent observations were performed in cryogenic conditions due to the dominant bright exciton emission at room temperature in far-field optical measurement.

Here, we perform multispectral TEPL imaging on the radiative emission of localized excitons at room temperature, as an extension study of WSe_2 ML. TEPL allows us to investigate spatial local heterogeneity of X_L modes with ~10 nm spatial resolution. These X_L modes concentrate in the vicinity of the crystal edges in contrast to the bright excitons. This X_L behaviore is associated with the density of structural defects. Furthermore, we control the orientation of their transition dipole moment from precise control of plasmon-exciton coupling using nano-optical antenna-tip.

4.4.2 Results and discussion

Fig. 4.29a shows a schematic illustration of TEPL setup for WSe_2 monolayer (ML) grown on SiO_2/Si substrate and transferred on gold film. Using this tilted tip geometry, we can probe both *in-plane* (bright exciton; X_0, trion; X_T, biexciton; XX) and *out-of-plane* (dark exciton; X_D, localized exciton; X_L) spontaneous emissions of WSe_2. In case of the localized exciton, X_L, transition dipole moment is randomly oriented due to the heterogeneous bounding geometry to the crystal defects.

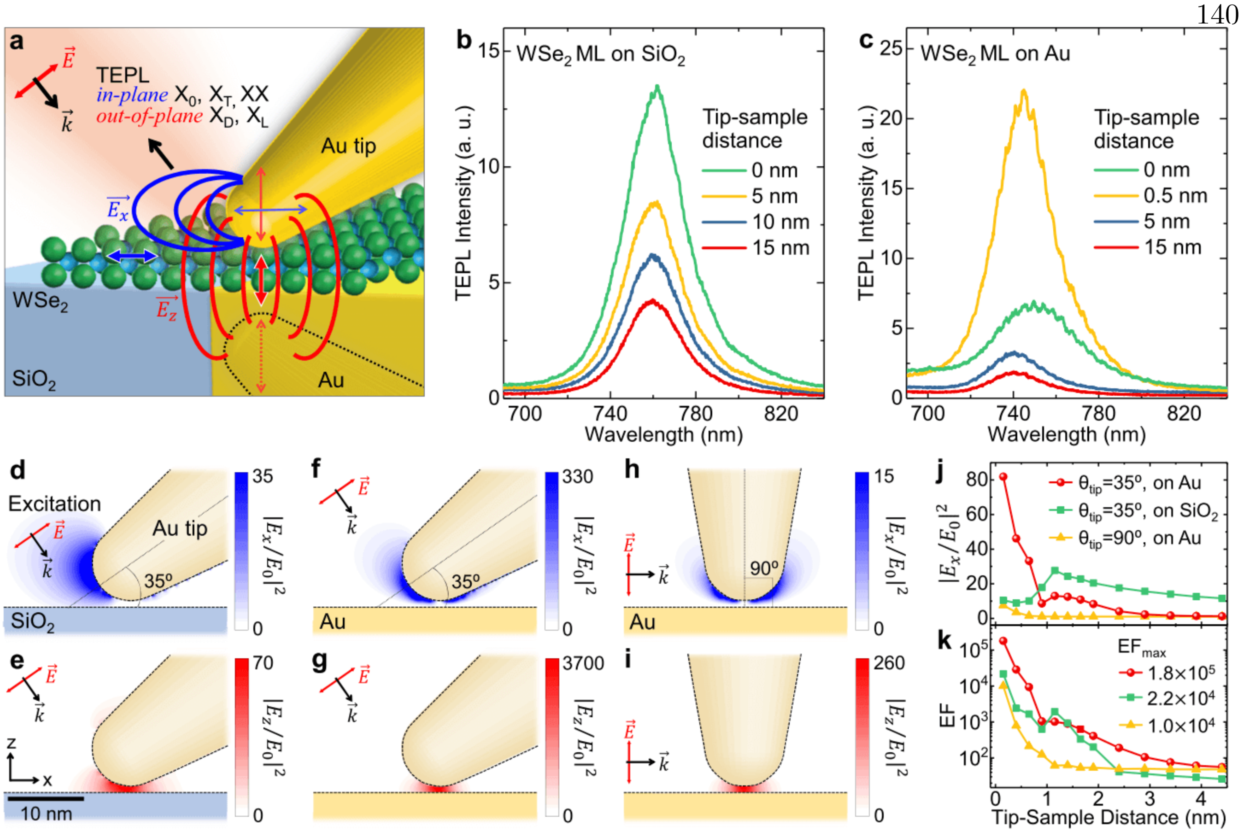

Figure 4.29: (a) Schematic illustration of TEPL setup for WSe_2 monolayer with tilted Au tip. Tip-sample distance dependence of TEPL for WSe_2 monolayer on the SiO_2 substrate (b) and Au substrate (c). (d-i) Simulated *in-plane* (blue, $\boldsymbol{E}_x$) and *out-of-plane* (red, $\boldsymbol{E}_z$) optical field intensity enhancement maps at the tip apex for a tilted tip (d-g) and a conventional surface normal tip (h-i) orientations using finite-difference time-domain (FDTD) method. Tip-sample distance dependence of *in-plane* optical field intensity enhancement (j) and PL enhancement factor (k) at the sample plane for varying tip orientation and substrate.

To understand plasmon-exciton coupling and TEPL enhancement difference between the SiO_2 and the Au substrates, we perform the distance dependent TEPL measurement for the both substrates as shown in Fig. 4.29b-c. From the estimation of the net enhancement factor in observed TEPL spectra and the calculated dimension difference between tip and focused laser spot, we obtain $\sim 2.0\times 10^4$-fold X_0 PL enhancement for WSe_2 ML on the SiO_2 substrate at 0 nm tip-sample distance. For the WSe_2 ML on the Au substrate, we obtain much larger $\sim 8.0 \times 10^4$-fold PL enhancement at the 0.5 nm tip-sample distance. At 0 nm distance, we often observe decreased TEPL intensity with spectral redshift (green curve in Fig. 4.29c) due to competition with the dark exciton (X_D)

emission.

Fig. 4.29d-i show simulated *in-plane* (blue, $\boldsymbol{E}_x$) and *out-of-plane* (red, $\boldsymbol{E}_z$) optical field intensity enhancement maps at the tip apex using finite-difference time-domain (FDTD) method. We model two different tip geometries with a conventional perpendicular ($\theta_{\text{tip}} = 90°$, Fig. 4.29h-i) and an exceptional tilting ($\theta_{\text{tip}} = 35°$, Fig. 4.29d-g) orientations with respect to the sample surface. The tilting tip geometry gives rise to stronger optical field confinement due to the localized surface plasmon resonance (LSPR) antenna effect. We will discuss more details of this tilting tip effect in chapter 5. As can be seen in Fig. 4.29d and f, a much stronger *in-plane* optical field confinement is observed for the Au substrate in comparison with the SiO_2 substrate under the same simulation conditions. This difference in local field enhancement is explained with the coupled dipole model, as we described in Chapter 2 (Fig. 2.5). The *in-plane* local optical field at the tip-substrate gap is increased when the tip-substrate distance is decreased because the polarizability of image dipole is increased. Since the effective polarizability of Au substrate is larger than dielectric substrate SiO_2, we can achieve larger PL enhancement of the bright exciton with the Au substrate.

Fig. 4.29j shows *in-plane* optical field intensity enhancement at the sample plane with respect to the tip-sample distance for varying tip orientation and substrate. The maximum optical field intensity enhancement of tilted tip on the SiO_2 substrate is obtained at 1.15 nm tip-sample distance (green). This is attributed to the decreased *in-plane* localized plasmon at the tip apex in the very small distances (< 1 nm) due to the competition between the localized plasmon mode and the weak dipole-dipole coupling mode on the dielectric substrate. On the other hand, in case of the tilted tip on Au substrate, the optical field intensity enhancement is more increased at the very small distances (< 0.8 nm) owing to the effective polarization transfer of the local antenna mode to the strong dipole-dipole coupling mode on the noble metal substrate (red). The field intensity enhancement of the conventional surface normal oriented tip on the Au substrate shows a gradual increase without an inflection point according to the conventional coupled dipole model (yellow) [90].

We also calculate the Purcell enhancement factor of the bright exciton as a function of tip-sample distance. We model *in-plane* fluorescent dipole emitters positioned within the nano-gap. The position of the emitter is fixed at 0.3 nm above the substrate. For simulation of the distance dependent Purcell enhancement factor, the distance between the Au tip (tilted and surface normal) and the substrate (Au and SiO_2) is controlled by moving the tip position. Using the calculated Purcell factor and the field intensity enhancement (Fig. 4.29j) at each distance, we estimate the distance dependent PL enhancement factor as shown in Fig. 4.29k. We can theoretically achieve maximum 1.8×10^5 and 2.2×10^4 PL enhancement for the tilted tip on the Au and SiO_2 substrate, respectively. This enhancement factor is in reasonable agreement with the experimental results of Fig. 4.29b and c.

As can be seen in Fig. 4.29f-g, the *out-of-plane* optical field confinement is dominant (> 10 times larger than *in-plane* optical field in intensity enhancement) in case of using the Au substrate. On the other hand, the *out-of-plane* optical field intensity enhancement is ~ 2 times larger than *in-plane* mode for the SiO_2 substrate. Therefore, the substrate of WSe_2 ML can be chosen depend on the measurement purpose. For example, the Au substrate is more appropriate to probe radiative emission of dark exciton (X_D) or localized exciton (X_L), whereas the SiO_2 substrate is better to probe *in-plane* mode excitons (X_0, X_T, and XX) as described in Fig. 4.29a.

We first investigate the *in-plane* mode multi-exciton peaks (X_T and XX) using the SiO_2 substrate. Fig. 4.30a shows normalized TEPL (red) and far-field (blue) spectra measured at crystal face and edge regions. TEPL and far-field spectra are normalized by 1.1 and 1.0, and their intensity difference is shown in green curve to more clearly demonstrate the emerging shoulders in TEPL spectrum. We observe distinct multiexciton shoulders in TEPL spectrum measured at crystal edge. We assign X_T, XX, and X_L to the observed shoulders at crystal edge based on their energy difference with bright exciton peak (X_T: 26 meV, XX: 53 meV) as well as the slopes in power dependent linear equations (Fig. 4.30b-c). In log-plots of the power dependent TEPL intensity for X_T, XX, and X_L with respect to the TEPL intensity of X_0, X_T shows linear increase. As we expect from a quadratic relation between XX and X_0 in their population, XX shows superlinear increase even though the derived slope ($\alpha \sim 1.17$) is not quite quadratic due to the homogeneous broadening and

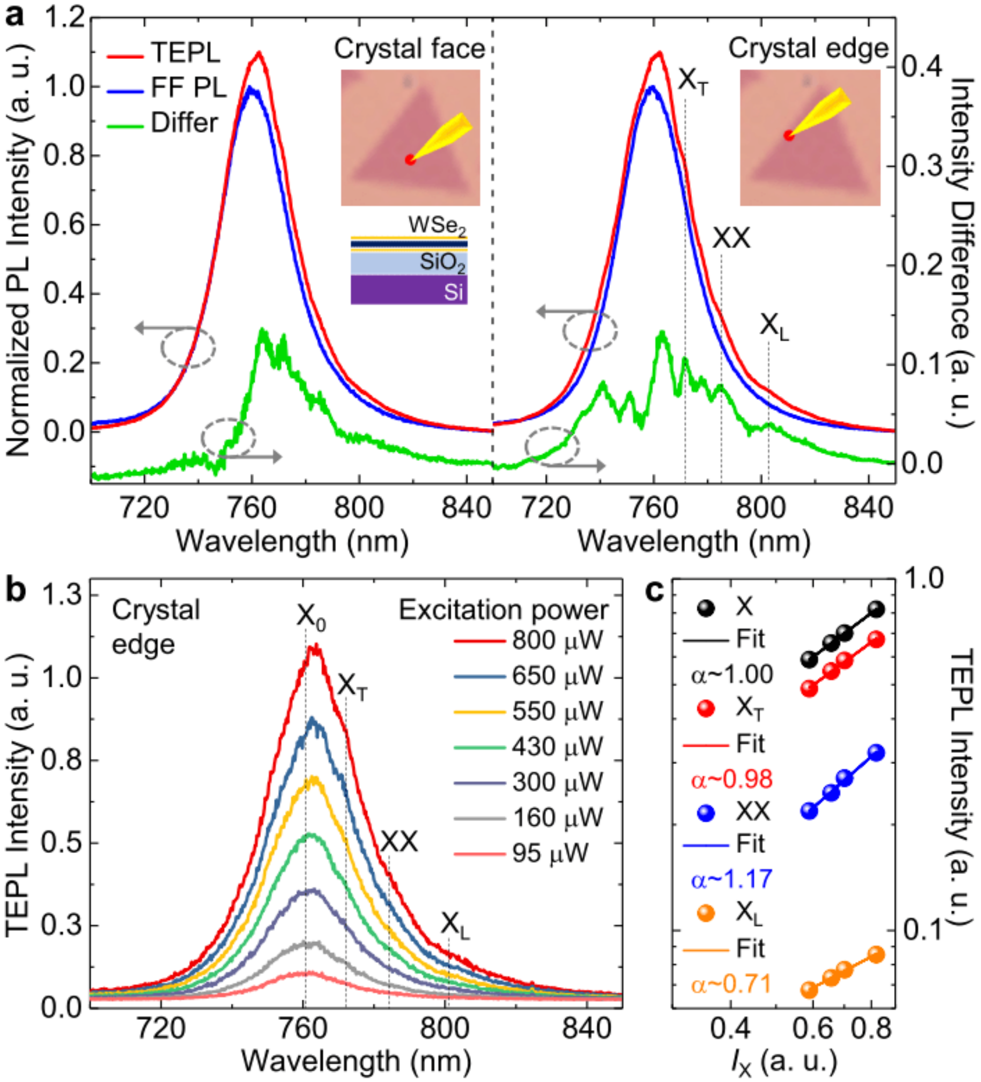

Figure 4.30: (a) Normalized TEPL (red) and far-field (blue) spectra of a WSe_2 monolayer on the SiO_2 substrate measured at crystal face and edge regions. (b) Power dependent TEPL spectra measured at edge. (c) Log-plot of the power dependence of TEPL intensity for X_T, XX, and X_L, with respect to the TEPL intensity of X_0.

spectral overlap at room temperature. On the other hand, the power dependent TEPL intensity of X_L shows sublinear behavior since X_L is saturated at high excitation power when defects are fully populated with excitons.

Additionally, the spectral broadening of bright exciton to the higher energy at crystal edge is observed due to energy funneling in the disordered semiconducting state as we discussed in section 4.2. We also observe a few meV redshift of the bright exciton peak in TEPL spectra measured

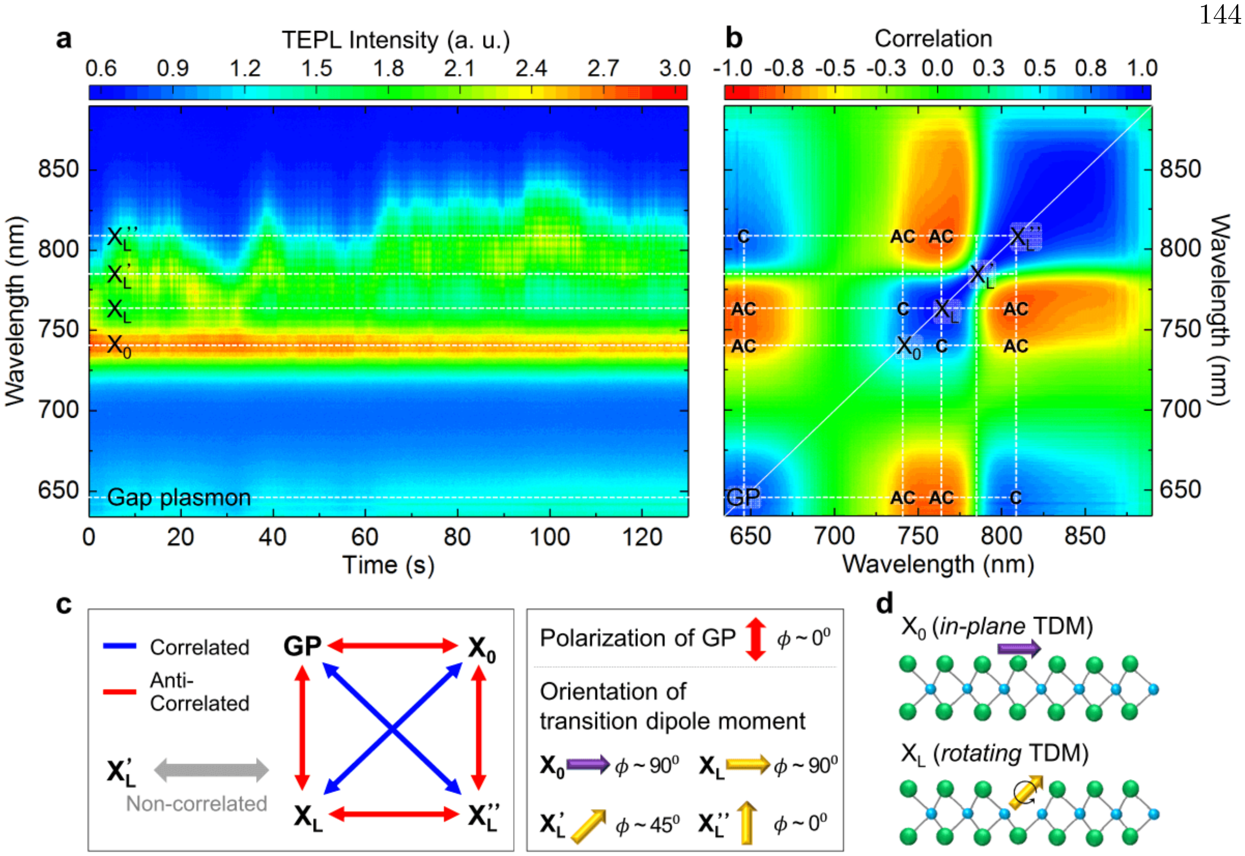

Figure 4.31: (a) Time series TEPL response of a WSe_2 monolayer on the Au substrate. (b) 2D correlation map of the time series TEPL spectra of Fig. 4.31a. (c) The orientations of transition dipole moment of the X_L emission peaks derived from the 2D correlation map (b). (d) Illustration of the *in-plane* and rotating emission dipoles of bright and localized excitons.

both at crystal face and edge. This redshift is possibly due to the photo-excited charge effect from the strong local optical field at the tip apex.

Despite we observe a TEPL shoulder of the localized exciton at room temperature with the SiO_2 substrate, it does not provide any significant spectroscopic properties due to its spectral overlap with *in-plane* modes. As we mentioned earlier, the *out-of-plane* optical field intensity is $>$ 10 times stronger than *in-plane* field when we use the Au substrate (Fig. 4.29f-g). Therefore, to probe distinct localized exciton peak and suppress PL emission of multiexciton peaks, we perform TEPL measurement of a WSe_2 ML transferred on the Au substrate. Fig. 4.31a shows a time series TEPL response of gap plasmon (GP), X_0, and X_L. This obvious X_L emission peak is observed from only a few local spots of crystal. The time dependent spectral fluctuation of X_L peak is observed when the position of tip and sample is fixed during this measurement. In previous low temperature far-field studies, very narrow $\mathrm{X_L}$ peaks were investigated as single exciton states bound to defects [72, 73, 167, 168, 169]. In our measurement, very narrow single photon emission peaks are not observed due to the homogeneous broadening at room temperature. On the other hand, we always observe single $\mathrm{X_L}$ peak in spectrally fluctuating time dependent measurement, i.e., different energy peaks of $\mathrm{X_L}$ are not observed simultaneously. Therefore, our result includes both possibilities that the observed emission peak is resulted from a bunch of $\mathrm{X_L}$ at the defect or homogeneously broadened single photon states.

Fig. 4.31b shows 2D correlation map of the time series TEPL spectra of Fig. 4.31a. We assign the position of GP and $\mathrm{X_0}$, and the representative positions of localized exciton, $\mathrm{X_L}$, $\mathrm{X'_L}$, and $\mathrm{X''_L}$ in the diagonal of the 2D map. The time dependent intensity fluctuation of the GP response is resulted from a small fluctuation of the tip-sample nano-gap in shear-force feedback in ambient condition. The intensity fluctuation of $\mathrm{X_0}$ peak and the spectral fluctuation of localized exciton peak are induced by varying GP intensity. The correlation (blue) and anti-correlation (red) between these peaks are very evident in off-diagonal spots. The GP response shows anti-correlation with $\mathrm{X_0}$ and $\mathrm{X_L}$ peaks, and correlation with $\mathrm{X''_L}$ peak. The $\mathrm{X_0}$ peak shows anti-correlation with $\mathrm{X''_L}$ peak and correlation with $\mathrm{X_L}$ peak. Hence, the $\mathrm{X_L}$ peak shows anti-correlation with $\mathrm{X''_L}$ peak. On the other hand, the $\mathrm{X'_L}$ peak is uncorrelated with any peaks or GP response.

Using 2D correlation map and well-defined dipole orientation of the GP response (*out-of-plane*) and the $\mathrm{X_0}$ peak (*in-plane*), we can derive the orientations of transition dipole moment for $\mathrm{X_L}$, $\mathrm{X'_L}$, and $\mathrm{X''_L}$ peaks as shown in Fig. 4.31c. As explained in previous study [346], the orientation of the emission dipole of localized exciton is randomly varied. Since we observe a spectrally fluctuating single peak in a stationary spot, the orientation of transition dipole moment of localized exciton is rotated by the varying plasmon-exciton coupling strength. Fig. 4.31d shows an illustration of the stationary *in-plane* and rotating emission dipoles of bright and localized excitons.

This result demonstrates the orientation of emission dipole can be controlled by the tip-induced plasmon-exciton coupling. The energy of localized exciton emission is varied in the range

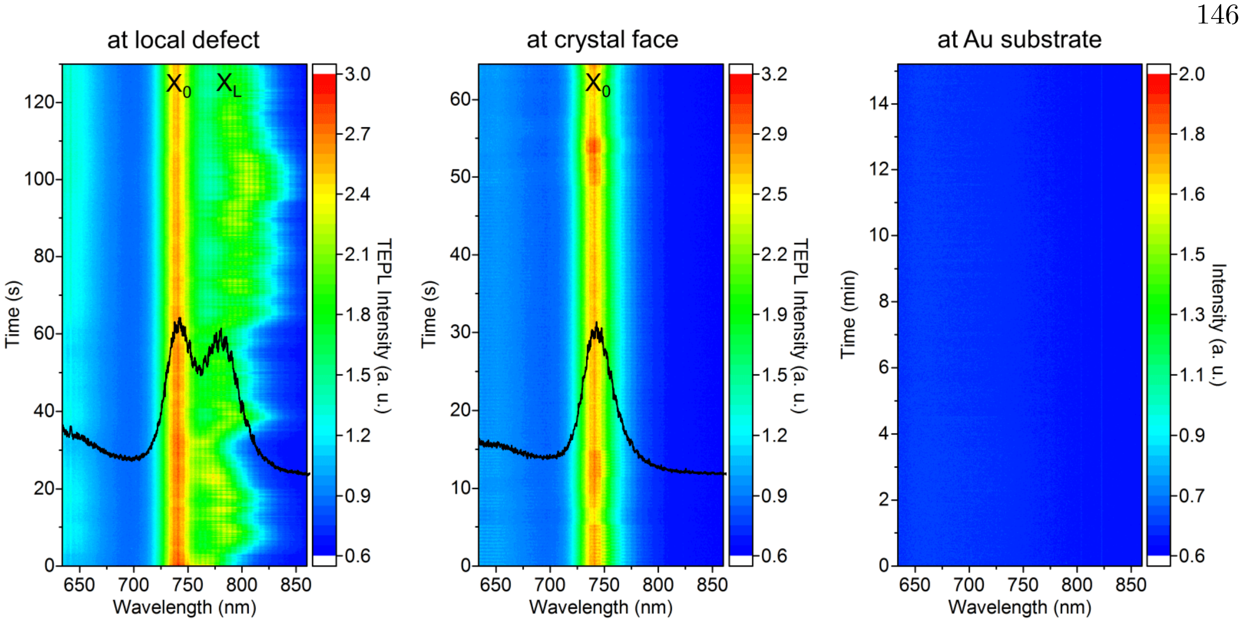

Figure 4.32: Time series TEPL response of a WSe_2 monolayer on the Au substrate measured at local defect (a) and crystal face (b). (c) Time series plasmon response of the Au substrate.

of >100 meV depend on the dipole orientation. Therefore, this approach can be also used for a wide range bandgap engineering of semiconducting 2D materials and regarding device applications. This localized exciton behavior is reproducibly observed in other local spots of other crystals with different tips. As we mentioned, this feature is generally not observed at crystal face as shown in Fig. 4.32b, and observed at only a few local spots of crystal. In Fig. 4.32c, we measured ∼10,000 spectra during scanning the Au substrate with no WSe_2 sample. From this result, we confirm that this X_L is not the plasmon response of Au substrate.

We then perform the multispectral TEPL imaging to understand a spatial heterogeneity of the localized exciton. We do not use the sample transferred on Au substrate for TEPL imaging because the heterogeneous roughness of the Au substrate gives irregular PL enhancement and corresponding non-uniform TEPL image. Fig. 4.33a and b show TEPL image of a WSe_2 ML on SiO_2 substrate with spectrally integrated 710-760 nm and 800-850 nm acquisition, respectively. The integrated intensities for the X_0 PL (710-760 nm) and the X_L PL (800-850 nm) are selectively counted at each pixel of sample scanning. The white dashed lines in Fig. 4.33a and b present crystal

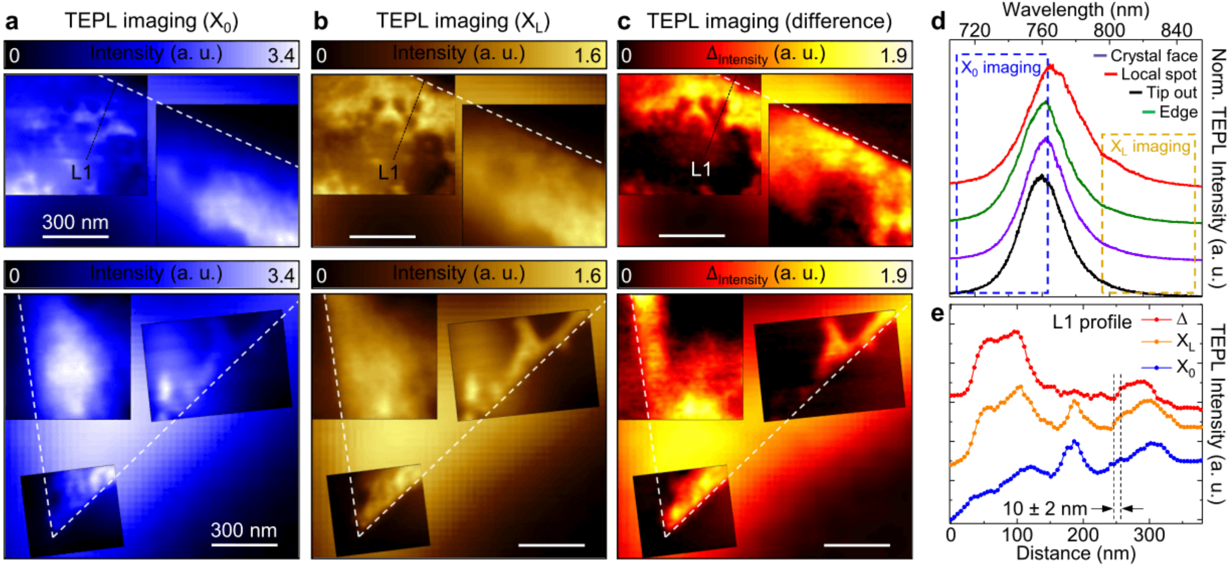

Figure 4.33: TEPL images of a WSe_2 monolayer on the SiO_2 substrate for the integrated intensity of 710-760 nm (X_0, a) and 800-850 nm (X_L, b) spectral regions, and spectral difference TEPL image (c). (d) Distinct TEPL spectra obtained at crystal face, edge, and local spot. (e) TEPL intensity profiles of line L1 in Fig. 4.33a-c.

edges and a ~500 nm spatial resolution confocal PL images are shown as a background image of the several patches of TEPL image. Since the X_L PL response of a WSe_2 ML on SiO_2 substrate is weak, the integrated intensity of the X_L PL can be affected by the tail of the X_0 PL. Therefore, for more clear visualization of the X_L PL, we subtract the X_0 PL image from the simultaneously measured X_L PL image after compensating for intensity discrepancy. Through this method, the spatial heterogeneity of X_L PL is clearly visualized as shown in Fig. 4.33c.

On the contrary to the X_0 emission distribution, the pronounced X_L PL emission is observed at edges. This observation is in good agreement with previous study [72]. This spatial heterogeneity of X_L PL is due to the relatively low crystal quality and corresponding highly dense defects at edges. Therefore, as we discussed in Fig. 4.30a-b, the spectral blueshift of X_0 PL peak is generally accompanied with emerging X_L peak at edge, as can be seen in Fig. 4.33d (compare purple and green curves). Fig. 4.33e shows intensity profiles of line L1 in the measured TEPL images. From these line profiles, we confirm a spatial resolution of 10 ± 2 nm of the TEPL imaging. Since we use the same tip for this TEPL imaging and a distance dependent TEPL measurement in Fig. 4.29b,

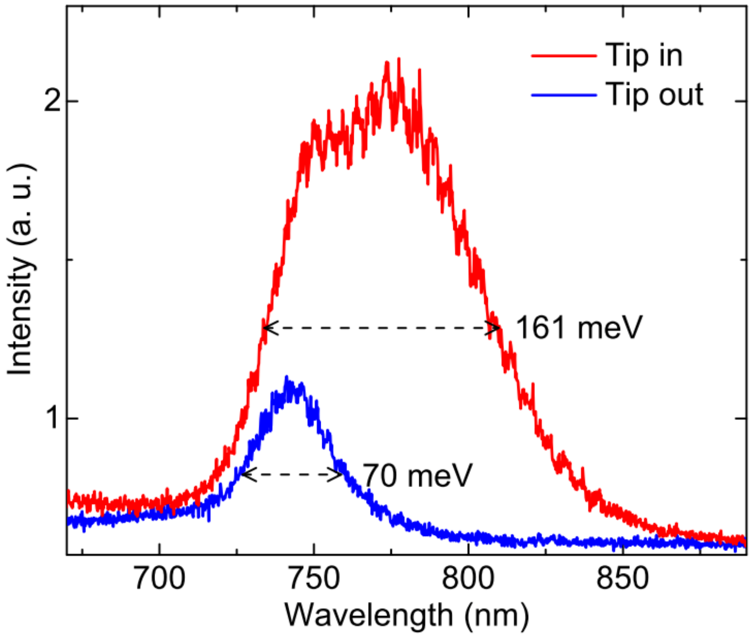

Figure 4.34: Conventional far-field and extraordinarily broad TEPL spectra of a WSe_2 monolayer on the Au substrate.

we have used a diameter of 10 nm to estimate the TEPL emission area in our calculation of the TEPL enhancement factor in Fig. 4.29b.

It should be noted that we often observe a very broad TEPL spectrum from a WSe_2 ML on the Au substrate. As shown in Fig. 4.34, we achieve ∼161 meV TEPL linewidth, which is more than 2 times broader than the far-field PL linewidth (∼70 meV). We believe this broadband emission is generated when the bright, dark, and localized excitons are excited simultaneously. We expect that this can be used as a broadband light source in photonic device applications.

Chapter 5

Tip-enhanced nonlinear optical nano-crystallography

5.1 Vector field control of plasmonic antenna tip[1]

Power gain, sensitivity, and polarization in linear and nonlinear optics are strongly correlated with the excitation vector field because of the anisotropy of light-matter interactions sensitive to structural symmetries. In particular for nano-optics, photonics, and near-field imaging, vector field control requires a combination of intrinsic far-field incident and detection polarization in combination with extrinsic polarization response definitives through non-optical elements. Here we present a novel tilting antenna-tip approach to control the vector field by breaking the axial symmetry of the Au tip in scattering type scanning near-field optical microscopy (s-SNOM). This gives rise to a significantly enhanced optical field confinement with respect to both *in-plane* and *out-of-plane* directions due to localized plasmon antenna effect. We use the nonlinear response of second harmonic generation (SHG) as an example to quantify the enhanced signal sensitivity as well as to investigate the detailed nano-crystallographic properties of quantum materials. In tip-enhanced SHG s-SNOM imaging of monolayer MoS_2 film and single-crystalline ferroelectric $YMnO_3$, we reveal nano-crystallographic details of domain boundaries and domain topology with significantly enhanced sensitivity with < 50 nm spatial resolution. We envision that this simple and generalizable approach of linear and nonlinear optical nano-crystallography provides novel imaging access to structural details in a wide range of quantum materials.

---

[1] This section covers measurements and simulations performed and analyzed by K.-D. Park, and supervised by M. B. Raschke.

5.1.1 Motivation

Molecular vibrations, phonons, excitons, and spin excitations interacting with light give rise to anisotropic linear and nonlinear optical responses sensitive to the direction of the wavevector and the polarization of the optical field and strongly correlated with the structural symmetries of the material [347, 348, 75]. In reflection or transmission measurements of far-field optical imaging and spectroscopy, the vector projection of the optical field into the orientation directions determined by the laws of linear and nonlinear refraction gives access to the optical selection rules associated with the materials symmetries [349, 350], yet with limited degrees of freedom under the wavevectors conservation in far-field optics. On the other hand, these wavevectors conservation requirements are lifted in near-field scattering depend on the structure and orientation of the nano-objects. Hence, in principle, scanning near-field optical microscopy (SNOM) and spectroscopy can increase these degrees of freedom and actively control the near-field polarization from choice of incident and detected wavevector together with independent control of local polarization through engineered antenna-tip response. However, to date, most SNOM studies have explained polarization and tip control to a limited extent having focused primalily on improving sensitivity and spatial resolution. Therefore, to broadly extend the range of SNOM application to provide for a generalized approach to optical nano-crystallography and imaging [347], an extended antenna-tip vector field control is desired.

In general, a surface normal oriented antenna-tip is used in scattering type SNOM (s-SNOM). On the one hand, this conventional tip geometry is useful to selectively detect *out-of-plane* polarized optical responses by a strongly confined optical field. However, it typically has a weak optical confinement in other polarization angles, which reduces the detection sensitivity for the *in-plane* optical responses. On the other hand, engineering tip for enhanced *in-plane* sensitivity limits spatial resolution and universal applicability with complex tip fabrication processes [351, 352, 353, 354]. These limitations restrict the range of applications to the various quantum materials, especially two-dimensional (2D) samples, e.g., graphene [79, 355, 356], transition metal dichalcogenides (TMDs)

[20], epitaxial thin films [357], and important classes of transition metal oxides of layered crystals, manganites, etc.

Here, we demonstrate a generalizable approach to control and enhance the excitation and detection polarizability for both *in-plane* and *out-of-plane* vector fields in nano-imaging, without loss of spatial resolution. We break the axial symmetry of a conventional Au wire tip by varying its tilt angle with respect to the sample surface. This active control of the broken axial symmetry increases the degrees of freedom of both *in-plane* and *out-of-plane* polarizability. In addition, this gives rise to a significantly enhanced optical field confinement with respect to both directions by creating a confined structure for free electron oscillation and associated localized plasmon antenna effect [358, 359].

We demonstrate the local vector field maps at the tip apex using a finite-difference time-domain (FDTD) simulation to provide basic principles on the broken axial symmetry of the antenna-tip. From the FDTD simulation, we find an optimized tilting angle of Au tip (35°) giving rise to $\sim$30 ($\sim$70) times enhanced *in-plane* (*out-of-plane*) excitation rate for nonlinear optical response (second harmonic generation, SHG) compared to a conventional tip geometry.

As application examples of a novel tilted tip approach, we demonstrate SHG s-SNOM imaging results for various quantum materials not only to quantify the enhanced signal sensitivity of the tilted tip, but also to investigate the detailed nano-crystallographic properties of samples. As a model system of layered 2D materials, we study on monolayer MoS_2 film and obtain a full grain boundary (GB) map, which cannot be taken in far-field SHG imaging. This is achieved by the modified nonlinear optical susceptibility and broken selection rule at the nanoscale boundaries. In addition, we study on a $YMnO_3$ single crystal, which has both *in-plane* and *out-of-plane* $\chi^{(2)}_{xyz}$ components [77, 21]. From the ferroelectric domain imaging facilitated by the local phase-sensitive detection [21], we confirm appreciably enhanced SHG sensitivity with 35° tilted tip compared to a conventional s-SNOM modality. Consequently, these experimental results demonstrate this simply implementable approach enables to study nonlinear nano-optical properties of a range of materials.

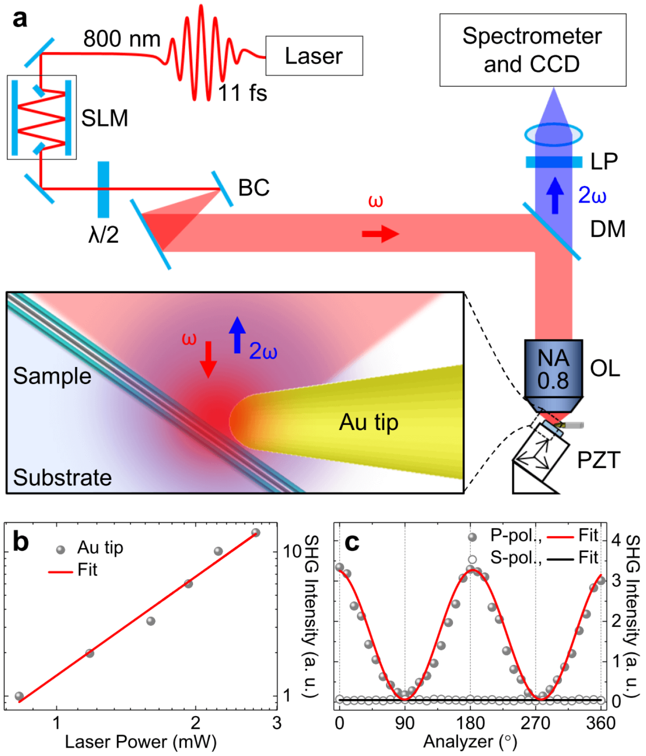

Figure 5.1: (a) Schematic of SHG s-SNOM setup, SLM: spatial light modulator, $\lambda/2$: half wave plate, BC: beam collimator, DM: dichroic mirror, OL: objective lens, LP: linear polarizer (analyzer). (b) Log-plot of the power dependence of SHG intensity of Au tip in $P_{in}P_{out}$ configuration. (c) Polarization dependence of SHG intensity of Au tip for P- (red) and S- (black) polarized excitation.

5.1.2 Experiment

The experiment is based on tip-enhanced spectroscopy [20], with side illumination to the Au tip manipulated in a shear-force AFM as shown schematically in Fig. 5.1a. The sample surface is tilted by 35° with respect to the tip axis with capable tilting angle variation from 0° to 90°. Excitation beam provided from a Ti:sapphire oscillator (Femtolasers Inc., with $\tau \sim 11$ fs pulse duration, center wavelength of 800 nm, 78 MHz repetition rate, and < 2 mW power) is focused onto the tip-sample junction, and the backscattered SHG signals are polarization selected and collected using a spectrometer (f = 500 mm, SpectraPro 500i, Princeton Instruments) with a charge-coupled device (CCD, ProEM+: 1600 eXcelon3, Princeton Instruments).

In excitation and detection, we define the P and S polarization as light polarized parallel and perpendicular with respect to the plane formed by k-vector and tip axis. In $P_{in}P_{out}$ (P polarized excitation and P polarized detection) configuration, weak but appreciable SHG signal is generated from an asymmetric nanostructure of the Au tip [119], as seen in power dependence (Fig. 5.1b) and polarization dependence (Fig. 5.1c) measurements. Therefore, to eliminate a possible contribution from SHG response of the tip to the sample signal, we only use $P_{in}S_{out}$ configuration in the tip-enhanced SHG s-SNOM imaging.

5.1.3 Results

Optical antenna properties of tilted tip

To understand the local optical field enhancement with respect to the tilt angle of Au tip, we map the optical field intensity ($|\boldsymbol{E}|^2$) and charge (Re[$\boldsymbol{E}$]) distribution theoretically using FDTD simulations (Lumerical Solutions, Inc.) for our experimental conditions. Fig. 5.2a and d show calculated *in-plane* optical field maps ($|\boldsymbol{E}_x|^2$ and Re[$\boldsymbol{E}_x$]) for surface normal tip orientation ($\theta_{\text{tip}} = 90°$) with excitation (800 nm) polarization perpendicular with respect to the tip axis. Despite this excitation polarization condition gives weak electrostatic lightning rod effect, a decent amount of $\boldsymbol{E}_x$ field is confined at the apex resulting from the localized surface plasmon resonance (LSPR) antenna effect [358, 359]. While the local field enhancement for the excitation polarization parallel to the tip axis is smaller than this condition due to the weakened LSPR effect.

To achieve an efficient local plasmon antenna effect together with the lightning rod effect, we model tilted tip with excitation polarization parallel with respect to the tip axis. As shown in Fig. 5.2c and f, for the small ($10° \leq \theta_{\text{tip}} \leq 30°$) and large ($60° \leq \theta_{\text{tip}} \leq 90°$) tilting angles, the field confinement is not significantly enhanced compared to the conventional tip orientation (Fig. 5.2a) because the Au tip cannot sustain antenna-like *in-plane* and *out-of-plane* plasmon [359]. On the other hand, the field confinement is significantly enhanced for the tilting angles between 30° and 60° since the bound electrons are effectively confined at the tip apex which give rise to an appreciable LSPR effect with the dense electric charges by the lightning rod effect.

Fig. 5.2b and e show calculated $|\boldsymbol{E}_x|^2$ and Re[$\boldsymbol{E}_x$] distributions for the 35° tilted tip orientation ($\theta_{\text{tip}} = 35°$) exhibiting the strongest *in-plane* vector field confinement. In addition, in this

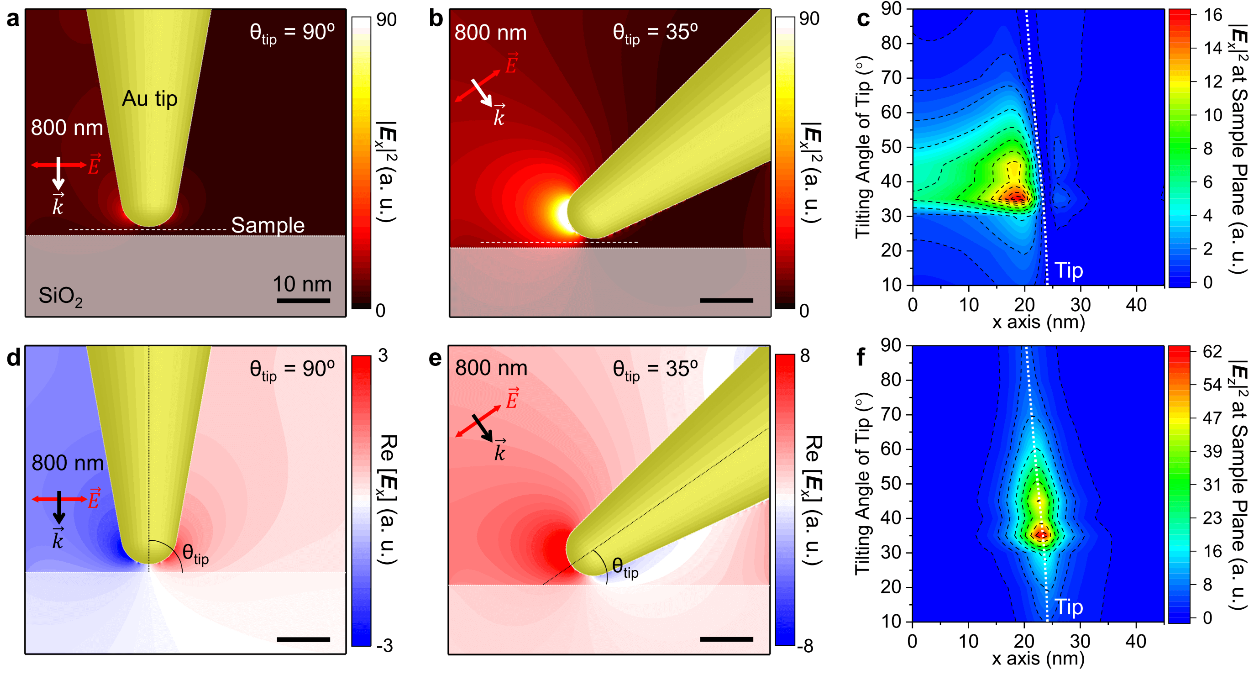

Figure 5.2: Simulated *in-plane* electric field intensity and charge distribution maps for surface normal tip orientation ($\theta_{\text{tip}} = 90°$, (a) $|\boldsymbol{E}_x|^2$, (d) Re$[\boldsymbol{E}_x]$) and for optimized tilted tip orientation ($\theta_{\text{tip}} = 35°$, (b) $|\boldsymbol{E}_x|^2$, (e) Re$[\boldsymbol{E}_x]$). Simulated *in-plane* (c) and *out-of-plane* (f) electric field intensity profiles at sample plane with respect to the tip tilting angle (θ_{tip}).

	$\lvert\boldsymbol{E}_x/\boldsymbol{E}_0\rvert^2$ (*in-plane*)		$\lvert\boldsymbol{E}_z/\boldsymbol{E}_0\rvert^2$ (*out-of-plane*)	
	$\theta_{\text{tip}} = 90°$	$\theta_{\text{tip}} = 35°$	$\theta_{\text{tip}} = 90°$	$\theta_{\text{tip}} = 35°$
$\lambda_{\text{exc}} = 532$ nm	28	290	40	630
$\lambda_{\text{exc}} = 633$ nm	23	180	42	250
$\lambda_{\text{exc}} = 800$ nm	16	90	25	100

Table 5.1: Comparison of *in-plane* and *out-of-plane* optical field intensity enhancement for conventional ($\theta_{\text{tip}} = 90°$) and tilted ($\theta_{\text{tip}} = 35°$) tip at different excitation wavelength.

tilting angle, the *out-of-plane* vector field confinement is more significantly enhanced as shown in Fig. 5.2f. This notable *out-of-plane* field enhancement is attributed to the SiO_2 substrate, which gives rise to the electromagnetic coupling between the tip charges and the induced charges on the surface of dielectric [360].

To investigate this enhanced field confinement is attributed to the LSPR effect, we calculate the optical field intensity enhancement for *on-resonance* and slightly *off-resonance* excitation wavelength. Table 5.1 shows comparison of *in-plane* and *out-of-plane* optical field intensity enhancement for conventional ($\theta_{\text{tip}} = 90°$) and tilted ($\theta_{\text{tip}} = 35°$) tip at different excitation wavelength. To compare these two tip orientations with their maximum enhancement condition, the excitation polarization is set perpendicular and parallel to the tip axis for $\theta_{\text{tip}} = 90°$ and $\theta_{\text{tip}} = 35°$, respectively. As can be seen in Table 5.1, the tilting tip gives much larger optical field enhancement at 532 nm excitation for both $|\boldsymbol{E}_x/\boldsymbol{E}_0|^2$ and $|\boldsymbol{E}_z/\boldsymbol{E}_0|^2$ compared to longer wavelength excitations. For the polarizability of a gold ellipsoid model, it has been demonstrated that the plasmon resonance peak is redshifted with increasing aspect ratio because the ohmic damping is decreased as the plasmon resonance is tuned away from the interband transition of gold [90]. Therefore, we conclude that the tilting tip induces strongly localized plasmon resonance to both *in-plane* and *out-of-plane* axes by suppressing overdamped resonance of the semi-infinite tip structure. This effect gives strongest optical field enhancement at 532 nm excitation similar to gold nanosphere and significantly enhanced optical field confinement for all excitation wavelength in visible and near-infrared compared to the conventional surface normal tip geometry.

SHG s-SNOM imaging using tilted tip

The broken inversion symmetry of TMDs with the reduced dimensionality provides remarkably large nonlinear optical responses with purely *in-plane* polarizability [65], which play an important role for device applications [361] as well as material characterizations [75]. While SHG microscopy provides informative knowledge on nonlinear optical response such as the crystalline symmetry, orientation, defect states, stacking angle, and the number of layers, little is known about their nanoscale properties due to its limited spatial resolution [74, 66, 76]. To characterize these subwavelength nonlinear optical properties, we use the SHG s-SNOM apparatus.

As illustrated in Fig. 5.3a, we perform the tip-enhanced nano-SHG imaging with the 35° tilted tip for single-layer MoS_2 film grown on the SiO_2/Si substrate, as a model system of $\bar{6}m2$ point group with possessing pure *in-plane* $\chi^{(2)}_{xyz}$ tensor elements [65]. As for the comparison with the near-field image, we first follow a conventional far-field imaging procedure as established for determining orientation angle (θ_{co}) and grain boundary of the TMD crystals [75, 283].

Fig. 5.3b and c show the far-field SHG images with polarization selections of $P_{in}P_{out}$ and

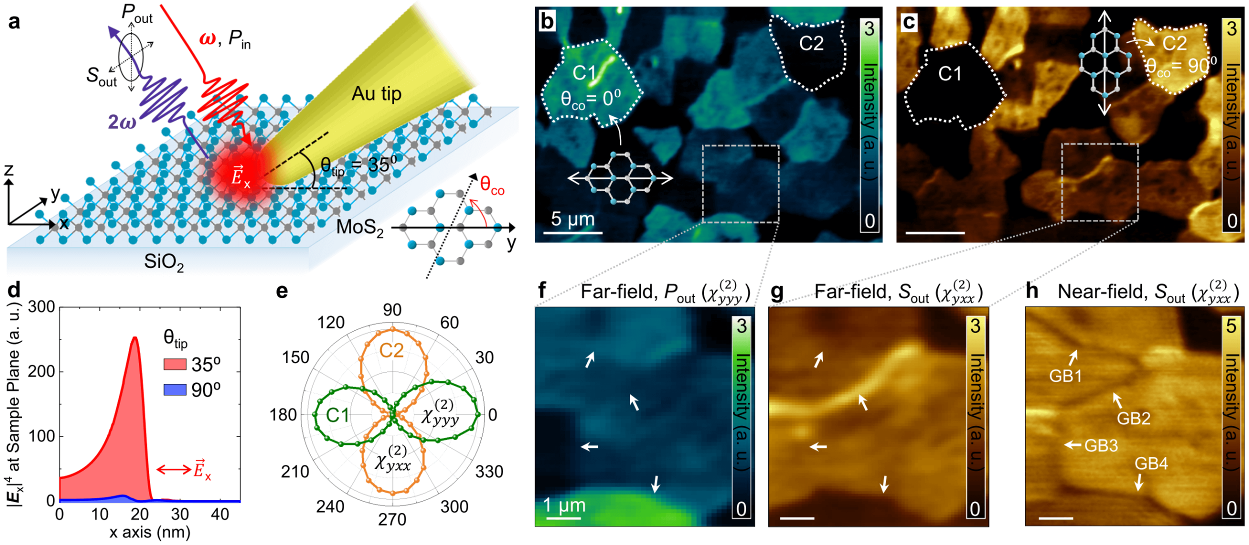

Figure 5.3: (a) Schematic of SHG s-SNOM measurement for monolayer MoS$_2$ film on a SiO$_2$ substrate. Far-field SHG images measured in $P_{in}P_{out}$ (b) and $P_{in}S_{out}$ (c) configurations. (d) Simulated $|\boldsymbol{E}_x|^4$ profile at sample plane for tilted ($\theta_{\text{tip}} = 35°$) and conventional ($\theta_{\text{tip}} = 90°$) tip orientations. (e) Far-field SHG polarization dependence of crystals C1 and C2 in (b) and (c). (f)-(g) Magnified far-field SHG images of small area in (b)-(c). (h) Tip-enhanced SHG s-SNOM image of the same area measured in $P_{in}S_{out}$ configuration.

$P_{in}S_{out}$, respectively, displaying crystal orientations. From the nonvanishing $\chi^{(2)}_{xyz}$ tensor elements and excitation condition, the induced second order polarization for crystals with $\theta_{\text{co}} = 0°$ (C1 of Fig. 5.3b-c) is given by $\boldsymbol{P}_y(2\omega) = 2\varepsilon_0\chi^{(2)}_{yyy}\boldsymbol{E}_y(\omega)^2$, where $\boldsymbol{E}_{i=x,y,z}(\omega)$ are the electric field components at the laser frequency. In detail, for the MoS$_2$ crystals with $\theta_{\text{co}} = 0°$ (C1 of Fig. 5.3b-c), the induced second order polarization can be written as

$$\boldsymbol{P}(2\omega) = 2\varepsilon_0\chi^{(2)}_{xyz}\boldsymbol{E}_z(\omega)\boldsymbol{E}_y(\omega). \tag{5.1}$$

Using the nonvanishing $\chi^{(2)}_{xyz}$ tensor elements for the $\bar{6}m2$ symmetry class, $\boldsymbol{P}(2\omega)$ is given by

$$\begin{bmatrix} \boldsymbol{P}_x(2\omega) \\ \boldsymbol{P}_y(2\omega) \\ \boldsymbol{P}_z(2\omega) \end{bmatrix} = 2\varepsilon_0 \begin{bmatrix} 0 & 0 & 0 & 0 & 0 & -\chi^{(2)}_{xxy} \\ -\chi^{(2)}_{yxx} & \chi^{(2)}_{yyy} & 0 & 0 & 0 & 0 \\ 0 & 0 & 0 & 0 & 0 & 0 \end{bmatrix} \times \begin{bmatrix} 0 \\ \boldsymbol{E}_y(\omega)^2 \\ \boldsymbol{E}_z(\omega)^2 \\ 2\boldsymbol{E}_y(\omega)\boldsymbol{E}_z(\omega) \\ 0 \\ 0 \end{bmatrix}, \tag{5.2}$$

$$\boldsymbol{P}_y(2\omega) = 2\varepsilon_0\chi^{(2)}_{yyy}\boldsymbol{E}_y(\omega)^2. \tag{5.3}$$

Therefore, the SHG signal of crystals with $\theta_{\text{co}} = 0°$ is polarized parallel to the excitation polarization (ω) and clearly observed in $P_{in}P_{out}$ configuration, as shown in Fig. 5.3b.

In contrast, the crystals with $\theta_{\text{co}} = 90°$ (C2 of Fig. 5.3b-c) are seen most clearly in $P_{in}S_{out}$ configuration (Fig. 5.3c) since the induced SHG polarization is given by $\boldsymbol{P}_y(2\omega) = \text{-}2\varepsilon_0\chi^{(2)}_{yxx}\boldsymbol{E}_x(\omega)^2$. In detail, in case of the MoS$_2$ crystals with $\theta_{\text{co}} = 90°$ (C2 of Fig. 5.3b-c), $\boldsymbol{P}(2\omega)$ is given by

$$\begin{bmatrix} \boldsymbol{P}_x(2\omega) \\ \boldsymbol{P}_y(2\omega) \\ \boldsymbol{P}_z(2\omega) \end{bmatrix} = 2\varepsilon_0 \begin{bmatrix} 0 & 0 & 0 & 0 & 0 & -\chi^{(2)}_{xxy} \\ -\chi^{(2)}_{yxx} & \chi^{(2)}_{yyy} & 0 & 0 & 0 & 0 \\ 0 & 0 & 0 & 0 & 0 & 0 \end{bmatrix} \times \begin{bmatrix} \boldsymbol{E}_x(\omega)^2 \\ 0 \\ \boldsymbol{E}_z(\omega)^2 \\ 0 \\ 2\boldsymbol{E}_x(\omega)\boldsymbol{E}_z(\omega) \\ 0 \end{bmatrix}, \tag{5.4}$$

$$\boldsymbol{P}_y(2\omega) = -2\varepsilon_0\chi^{(2)}_{yxx}\boldsymbol{E}_x(\omega)^2. \tag{5.5}$$

Therefore, the second harmonic signal (2ω) of crystal C2 is polarized perpendicular to the excitation polarization (ω).

This polarization selection rule on the crystallographic orientation is also confirmed in far-field SHG anisotropy measured by rotating linear analyzer (Fig. 5.3e). As dictated in the selection rule, only $\boldsymbol{E}_x(\omega)$ component affect to the detected SHG intensity ($\boldsymbol{I}_{2\omega}$) in $P_{in}S_{out}$ configuration. Therefore, according to a power law $\boldsymbol{I}_{2\omega} \propto |\boldsymbol{P}(2\omega)|^2 \propto |\boldsymbol{E}(\omega)|^4$, we can calculate the enhanced SHG intensity using the 35° tilted tip ($\boldsymbol{I}^{35^\circ}_{2\omega,MoS_2}$) compared to the conventional surface normal oriented tip ($\boldsymbol{I}^{90^\circ}_{2\omega,MoS_2}$) from the FDTD simulation. As shown in Fig. 5.3d, the spatially integrated $|\boldsymbol{E}_x(\omega)|^4$ for the 35° tilted tip at sample plane is ∼28 times larger than that of the surface normal oriented tip ($\theta_{\text{tip}} = 90^\circ$). Consequently, we estimate the tip-enhanced SHG intensity ratio $\boldsymbol{I}^{35^\circ}_{2\omega,MoS_2}/\boldsymbol{I}^{90^\circ}_{2\omega,MoS_2}$ ~ 28.

Fig. 5.3h shows the measured tip-enhanced nano-SHG image in $P_{in}S_{out}$ configuration for a small area of the far-field image. Far-field images of P_{out} and S_{out} detection are magnified in Fig. 5.3f and g for comparison. As demonstrated previously [75, 283], some GBs are visualized in the far-field SHG images resulted from the constructive (or destructive) interference between SHG signals of two facing crystals in the laser focal spot. However, these interference patterns are observed only when the two crystals have same crystal orientation.

In the tip-enhanced SHG image, on the other hand, a full GB map is obtained with more pronounced SHG contrast. For example, while the GB2 is observed in both far- and near-field images, the others (GB1, GB3, and GB4) are not seen in far-field images. This is because the tip-enhanced SHG signal is detected dominantly from nanoscale dimension at the tip apex. Thus, the detected SHG signal at GBs is weaker than crystal face due to the modified nonlinear optical susceptibility and broken selection rule.

In order to assess a benefit of the increased *out-of-plane* field confinement (Fig. 5.2f), we then perform the tip-enhanced nano-SHG imaging on a single-crystalline x-cut YMnO_3, as a model system of *6mm* point group with possessing both *in-plane* and *out-of-plane* nonlinear optical susceptibility [77, 21]. We first deduce the sample orientation from far-field SHG anisotropy measurement, as shown in Fig. 5.4a. Therefore, we probe the ferroelectric $\chi^{(2)}_{zxx} = \chi^{(2)}_{zyy}$ tensor elements in $P_{in}S_{out}$ s-SNOM configuration. The corresponding SHG polarization is then given by $\boldsymbol{P}_z(2\omega) = 2\varepsilon_0\chi^{(2)}_{zxx}(\boldsymbol{E}_x(\omega)^2+\boldsymbol{E}_y(\omega)^2)$ as dictated by selection rule. In detail, for the single-crystalline x-cut

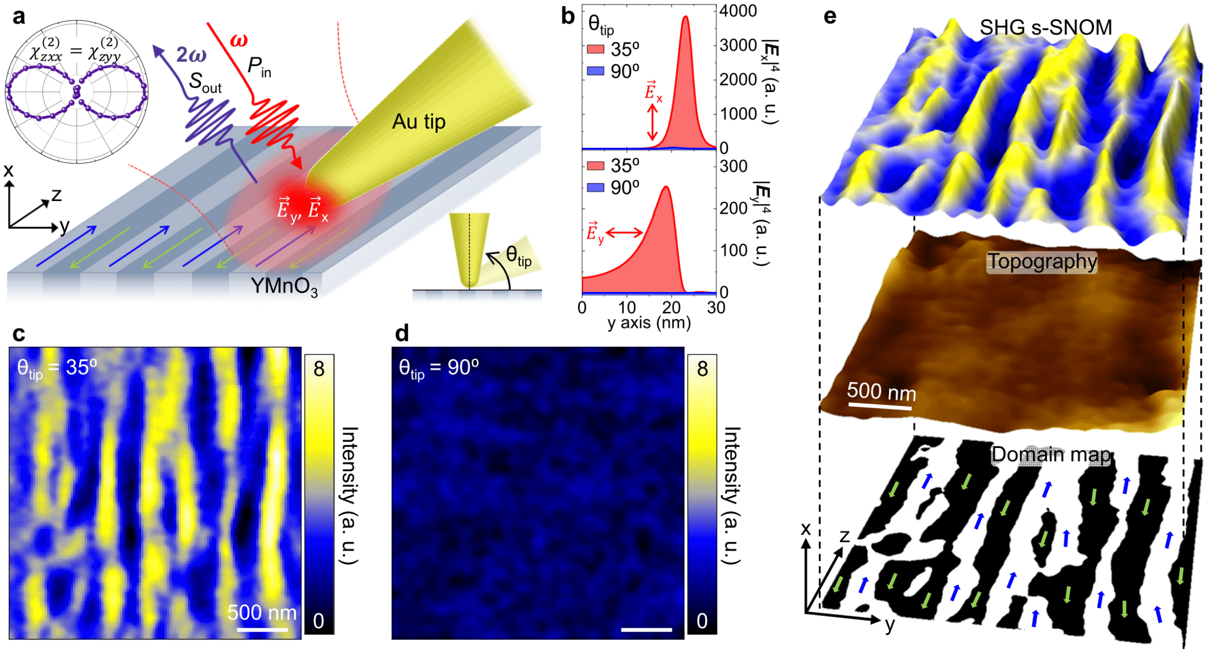

Figure 5.4: (a) Schematic of SHG s-SNOM measurement for single-crystalline x-cut YMnO$_3$. (b) Simulated $|\boldsymbol{E}_x|^4$ (*out-of-plane*) and $|\boldsymbol{E}_y|^4$ (*in-plane*) profiles at sample plane for tilted ($\theta_{\text{tip}} = 35°$) and conventional ($\theta_{\text{tip}} = 90°$) tip orientations. Tip-enhanced SHG s-SNOM image measured by tilted (c, $\theta_{\text{tip}} = 35°$) and conventional (d, $\theta_{\text{tip}} = 90°$) tip. (e) Three dimensional representation of SHG s-SNOM image and topography, together with the corresponding ferroelectric domain map.

YMnO$_3$ (Fig. 5.4a), the induced second order polarization can be written as

$$\boldsymbol{P}(2\omega) = 2\varepsilon_0 \chi^{(2)}_{xyz} \boldsymbol{E}_x(\omega) \boldsymbol{E}_y(\omega) \tag{5.6}$$

Using the nonvanishing $\chi^{(2)}_{xyz}$ tensor elements for the *6mm* symmetry class, $\boldsymbol{P}(2\omega)$ is given by

$$\begin{bmatrix} \boldsymbol{P}_x(2\omega) \\ \boldsymbol{P}_y(2\omega) \\ \boldsymbol{P}_z(2\omega) \end{bmatrix} = 2\varepsilon_0 \begin{bmatrix} 0 & 0 & 0 & 0 & \chi^{(2)}_{xxz} & 0 \\ 0 & 0 & 0 & \chi^{(2)}_{yyz} & 0 & 0 \\ \chi^{(2)}_{zxx} & \chi^{(2)}_{zyy} & \chi^{(2)}_{zzz} & 0 & 0 & 0 \end{bmatrix} \times \begin{bmatrix} \boldsymbol{E}_x(\omega)^2 \\ \boldsymbol{E}_y(\omega)^2 \\ 0 \\ 0 \\ 0 \\ 2\boldsymbol{E}_x(\omega)\boldsymbol{E}_y(\omega) \end{bmatrix}, \tag{5.7}$$

$$\boldsymbol{P}_z(2\omega) = 2\varepsilon_0 \chi^{(2)}_{zxx} (\boldsymbol{E}_x(\omega)^2 + \boldsymbol{E}_y(\omega)^2). \tag{5.8}$$

Therefore, the second harmonic signal (2ω) is polarized perpendicular to the excitation polarization (ω).

Then, the measured intensity $\boldsymbol{I}_{2\omega}$ is proportional to $|\boldsymbol{E}_x(\omega)^2+\boldsymbol{E}_y(\omega)^2|^2 = |\boldsymbol{E}_x(\omega)|^4 + |\boldsymbol{E}_y(\omega)|^4 + 2|\boldsymbol{E}_x(\omega)|^2|\boldsymbol{E}_y(\omega)|^2$, and we can estimate the tip-enhanced SHG intensity ratio of tilted and normal tip $\boldsymbol{I}^{35^\circ}_{2\omega,YMnO_3}/\boldsymbol{I}^{90^\circ}_{2\omega,YMnO_3} \sim 27$, from the spatially integrated $|\boldsymbol{E}_x(\omega)|^4$, $|\boldsymbol{E}_y(\omega)|^4$, $|\boldsymbol{E}_x(\omega)|^2$, and $|\boldsymbol{E}_y(\omega)|^2$ at sample plane for the 35° tilted and surface normal oriented tips, as shown in Fig. 5.4b.

Fig. 5.4c and d show the resulting tip-enhanced SHG images taken by tilted ($\theta_{\text{tip}} = 35^\circ$) and non-tilted ($\theta_{\text{tip}} = 90^\circ$) tip. As expected from FDTD simulations, we observe a high contrast image of the domain walls with the tilted tip. Other than the strong confinement of optical fields, this is also achieved by the interference effect between the tip-enhanced SHG from a single domain and the far-field SHG from multiple domains giving rise to a local phase-sensitive signal [21]. Using the tip-enhanced SHG image, we can obtain the corresponding ferroelectric domain map exhibiting a 180° phase alternation between domains (Fig. 5.4e). The simultaneously measured topography shows no correlation with the SHG image meaning the surface-induced SHG signal probably weak and does not influence to the domain wall imaging.

5.1.4 Discussion

A conventional s-SNOM tip oriented normal to the sample surface gives limited polarization control. Furthermore, the *out-of-plane* antenna mode driven into a semi-infinite tip structure results in the weak vector field confinement due to overdamped resonance. In order to increase the LSPR effect at the tip apex, several ways have been suggested, e.g., fabricating nano-antenna [362], spherical apex [359], and groove near apex [363]. However, these methods require complicated fabrication process, lose a spatial resolution, and decrease the lightning rod effect. In this work, we present a simple but powerful solution to control the localized plasmon and the vector field of nano-optical antenna-tip, complementing all the drawbacks of previous methods. We find the field confinement can be sensitively controlled by tuning the tip orientation angle with respect to the sample surface. This idea was initially conceived to enhance the *in-plane* optical field $\boldsymbol{E}_x$ confinement for investigation of 2D materials. However, it turned out the *out-of-plane* optical field $\boldsymbol{E}_z$ is also highly enhanced even larger than $\boldsymbol{E}_x$. This brings up an interesting new aspect that this 35° tilted tip modality with the broken axial symmetry provides much more sensitive near-field signals than conventional s-SNOM for all samples beyond 2D materials.

Although we only perform the SHG nano-crystallography study to best demonstrate the strength of tilted tip through the well-defined samples and selection rule, this approach is also applicable to tip-enhanced Raman/photoluminescence spectroscopy (TERS/TEPL) with much larger enhanced plasmon resonance with the typical excitation wavelengths of 532 nm and 633 nm. In addition, we envision that this strongly confined vector field gives access to anomalous nanoscale light-matter interactions such as exciton-plasmon coupling [303], electron-phonon coupling [334], and strong coupling [251] in a range of molecules and materials.

5.2 Second harmonic generation nano-crystallography of ferroics[2]

5.2.1 SHG s-SNOM imaging of $BaTiO_3$-$BiFeO_3$ multiferroics

Multiferroic materials can exhibit simultaneous ferroelectric, ferromagnetic, and ferroelastic order [365, 366]. They have been proposed for the conversion of light at optical frequencies into THz frequencies [367], DC polarizations [368], and for the fabrication of multifunctional devices [365, 369]. $BiFeO_3$ (BFO) is a single phasemultiferroic and has attracted a lot of interest due to its high Neel and Curie temperatures, as well as its ferroelectric and anti-ferromagnetic properties [370, 371, 372]. In BFO based systems, optically induced birefringence, optically induced strain waves [373, 374], and electrical control of acoustic phonons [375] have been observed. One inherent challenge in utilizing BFO for multifunction devices is that the large leakage currents, due to increased conductivity from oxygen vacancies and Fe ions, degrade its ferroelectric properties. In this work we focus on a solid-state solution of $BaTiO_3$-$BiFeO_3$ (BTO-BFO) where the addition of another perovskite material reduces the conductivity of the composite material [376, 377]. We study second harmonic generation (SHG) measurements of (1-x)BTO-(x)BFO ($x = 0.725$), a multiferroic material with improved magnetoelectric properties to understand underlying domain order.

We use the symmetry selectivity of SHG both in far-field, and for near-field nano-imaging, in s-SNOM geometry, to determine symmetry characteristics and the ferroelectric (FE) domain texture of the BTO-BFO films as described previously [21, 90]. Fig. 5.5a shows the schematic of the experiment, based on a combination of a parabolic mirror based excitation and detection scheme [122], with axial illumination and detection and a shear-force AFM based near-field SHG imaging implementation [21]. Pump radiation provided from a Ti:sapphire oscillator (Femtolasers Inc., with broadband ∼10 fs pulse duration and 78 MHz repetition rate, power < 8 mW) is focused onto the scanning probe gold tip, with polarization controlled by a half-wave plate. The tip-enhanced and

---

[2] This section draws significantly from [364, 357]. The second harmonic generation experiment was performed and analyzed by K.-D. Park, and supervised by M. B. Raschke. $BaTiO_3$-$BiFeO_3$ multiferroics work was performed in collaboration with B. A. Magill and G. Khodaparast from Virginia Tech. $PbTiO_3/SrTiO_3$ superlattices work was performed in collaboration with A. Damodaran, R. Ramesh, and L. Martin from the University of California at Berkeley.

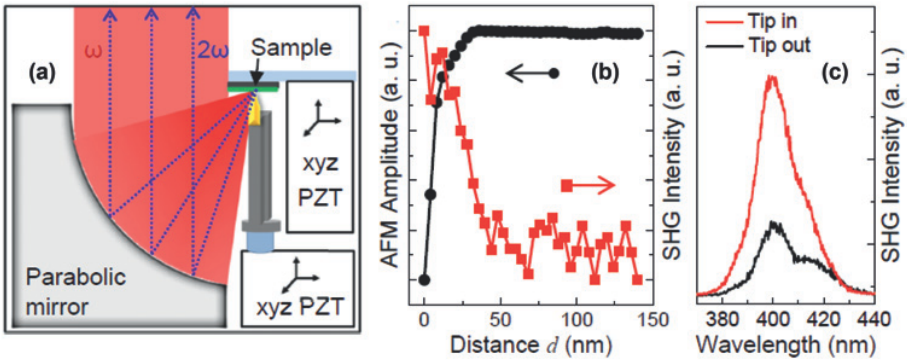

Figure 5.5: (a) Schematic of the experimental setup for SHG nano-imaging. (b) Approach curve of Au tip to the BTO-BFO surface with near-field increase of SHG intensity in shear force regime. (c) Near- and far-field SHG spectra.

backscattered SHG signals are polarization selected, filtered using dichroic optics, and detected using a spectrometer with a LN_2 cooled charge-coupled device (CCD). Specific combinations of input and output polarizations and the predominant enhancement of the tip-parallel polarization allow one to select specific nonlinear susceptibility components, characteristic to the ferroelectric domains, and their orientation [21, 90]. Fig. 5.5b-c shows spatial and spectral characteristics of the near-field SHG signal.

Fig. 5.6a shows a far-field rotational SHG anisotropy detected in the reflection mode with P- and S-polarized excitation (P_{in} and S_{in}), and indicates a significant net sample ferroelectric polarization (offset angle due to arbitrary sample orientation with respect to incident polarization). The S_{in} SHG signal is larger than for P_{in} due to the loss of in-plane electric field component due to the angle of incidence. The finite signal is the result of incomplete domain cancelation due to the small laser focus, angle of incidence, and retardation effects. However, no specific domain contrast is observed in the far-field SHG response (Fig. 5.6b). It is also of note, that we do not observe the presence of any magnon side bands which have been previously observed in BFO [378]. On the other hand, distinct ferroelectric (FE) domain contrast is observed in near-field SHG imaging (Fig. 5.6c-d) under both $S_{in}S_{out}$ and $P_{in}P_{out}$ polarization combination as a superposition of amplitude and heterodyne phase contrast SHG due to interference with the far-field SHG background,

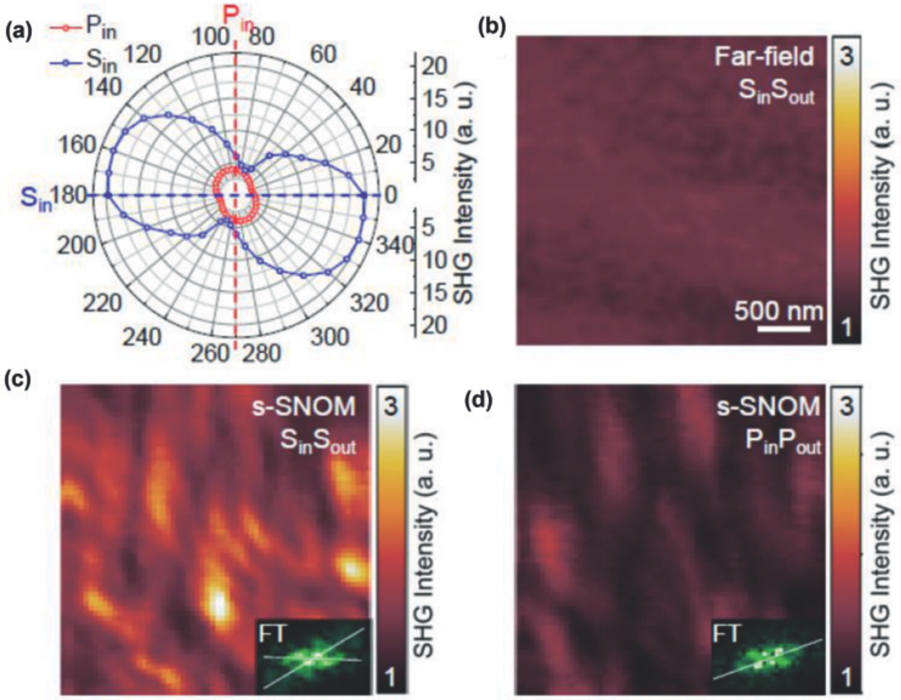

Figure 5.6: (a) Far-field SHG polar plots of BTO-BFO for P_{in} and S_{in} excitations. (b) Far-field SHG image for SinSout polarization selection. Near-field SHG images for $S_{in}S_{out}$ (c) and $P_{in}P_{out}$ (d) polarization exhibiting disordered, but generally typical, complex FE domain order. Inset: 2D image Fourier transform, indicating the primary domain orientations.

as described previously [21, 90]. Despite the polycrystalline film structure, distinct FE contrast is observed with domains extending over multiple crystallites. The FE domains are highly disordered but otherwise exhibit predominantly two ($S_{in}S_{out}$), or one ($P_{in}P_{out}$) dominant orientations, as also seen in the 2D Fourier transformed image (inset). These FE features are generally observed over extended sample regions. The spatial features are similar to the complex domain structures of BFO thin films and other multiferroics systems as observed previously by TEM and piezoresponse force microscopy (PFM) [366].

5.2.2 SHG s-SNOM imaging of $PbTiO_3/SrTiO_3$ superlattices

Understanding the nature of symmetry breaking in phase coexistence materials is of fundamental significance. Using the tip-enhanced SHG s-SNOM, we explore the second order nonlinear optical response of ferroelectric-phase and vortex-phase regions in $PbTiO_3/SrTiO_3$ superlattices.

Superlattices of $(PbTiO_3)_n/(SrTiO_3)_n$ are synthesized on 5 nm $SrRuO_3$-buffered, single-crystalline $DyScO_3$ $(110)_o$ $[(001)_{pc}]$ substrates via pulsed-laser deposition (where $_{pc}$ indicates pseudocubic indices) [379]. Growth of the $SrRuO_3$ is accomplished at a growth temperature of 700°C and an oxygen pressure of 50 mTorr. The growth temperature and oxygen pressure during growth of the superlattices is 630°C and 100 mTorr, respectively, to ensure stoichiometric transfer of both $PbTiO_3$ and $SrTiO_3$. All depositions are performed at a laser fluence of 1.5 J/cm^2 in an on-axis geometry. The growth is monitored using reflection high-energy electron diffraction (RHEED) to assure maintenance of a layer-by-layer growth mode throughout the growth process which, in turn, enables controlled growth of the superlattices with different periodicities while achieving the same 100 nm total thickness. The RHEED oscillations are monitored for specular spots along the $[\bar{1}10]_o$ of the $DyScO_3$ $(110)_o$ substrate. After the growth, the samples are cooled to room temperature in 50 Torr of oxygen to promote oxidation.

A typical reflection mode geometry is used for the far-field SHG anisotropy measurement, with specific combinations of input and output polarizations selected by an achromatic half-wave plate and a polarizer. The backscattered SHG intensity is then measured while keeping the polarization optics stationary and rotating the sample. For near-field SHG imaging, a shear-force atomic force microscopy (AFM) based scattering scanning near-field optical microscopy (s-SNOM) setup is used in a tilted tip geometry as described previously. The Au tip is illuminated from the top by broadband ~10 fs pulses derived from a Ti:Sapphire oscillator (Femtolasers Inc., 800 nm center wavelength, 78 MHz repetition rate), with tip-parallel polarization and average incident power of 3 mW. The tip-enhanced SHG signals are collected by a microscope objective (100×, NA=0.8) in the back-reflection geometry and detected with a spectrometer and a charge-coupled device (Princeton Instruments).

The azimuthal dependence of SHG response of the ferroelectric *a1/a2* and the vortex phases is measured using far-field SHG setup in the reflection mode geometry, and polar maps for the $S_{in}S_{out}$ and $S_{in}P_{out}$ configurations are obtained as shown in Fig. 5.7a-b. This measurements

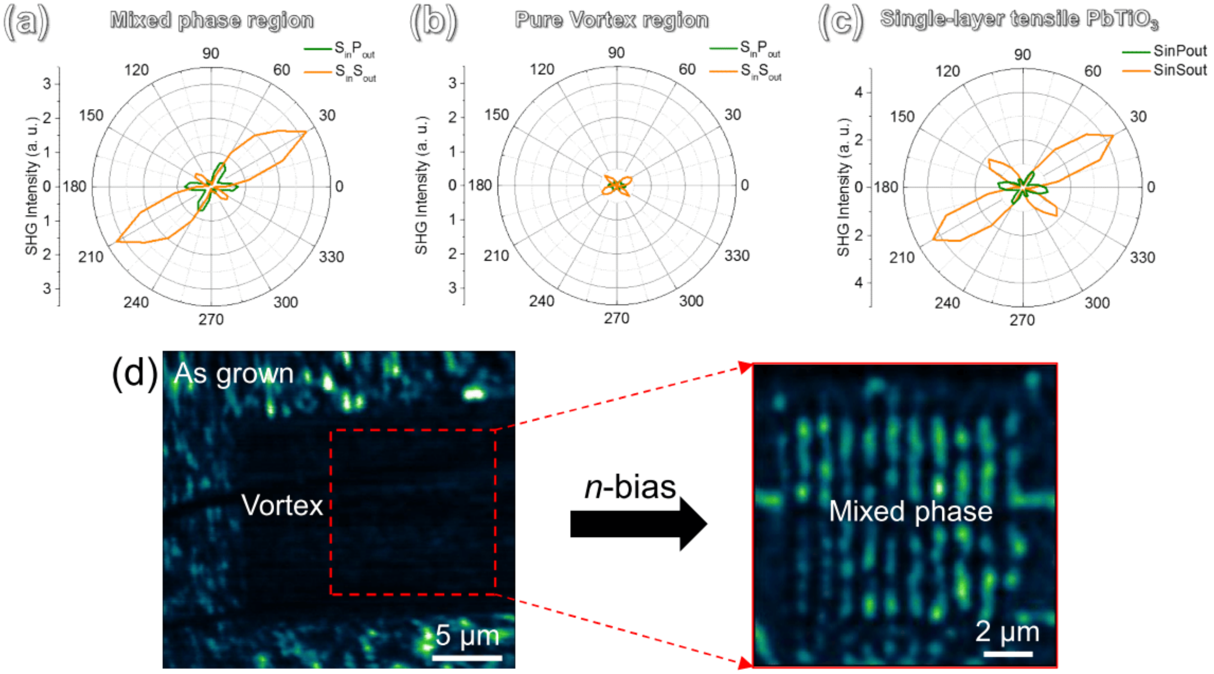

Figure 5.7: The azimuthal dependence of SHG response obtained from regions with the as-grown mixed-phase structure of $PbTiO_3/SrTiO_3$ superlattices (a), the electrically-poled pure vortex structure (b), and a tensile-strained $PbTiO_3/SmScO_3$ (110) thin film possessing in-plane polarized *a1/a2* ferroelectric domain structure (c). (d) Microscopic SHG image of the electrically-poled phase switching region of $PbTiO_3/SrTiO_3$ superlattices.

are performed for as-grown regions and regions that are poled to the pure vortex phase on a representative n = 16 superlattice, as well as a single-layer $PbTiO_3$ film grown on a $SmScO_3$ $(110)_o$ substrate possessing an *a1/a2* domain structure (Fig. 5.7c). The form of the polar maps obtained from the as-grown regions matches well with those from the single-layer $PbTiO_3$ films indicating predominant contributions from the ferroelectric *a1/a2* phase [380]. A highly diminished SHG response is observed from the vortex regions and is indicative of highly reduced anisotropy in the vortex-phase as compared to the ferroelectric phase. This difference in SHG intensity is clearly observed with microscopic SHG imaging of the phase switching region as shown in Fig. 5.7d.

In order to understand the microscopic details of how the ferroelectric phase evolves into the vortex phase, we first focus on a single $PbTiO_3$ layer within the superlattice near the phase boundary as extracted from phase-field models (Fig. 5.8a). As expected, the *a1/a2* domains (labeled

FE (*a1/a2*) wherein the color scale shows the polarization component along the $[100]_{pc}$) exhibit uniform polarization along the $[100]_{pc}$ and $[010]_{pc}$ resulting in a net polarization along the $[110]_{pc}$ (white arrow, Fig. 5.8a). As one transitions into the vortex phase (labeled Vortex wherein the color scale corresponds to the magnitude of $\bigtriangledown \times P$), the polarization evolves into polarization vortices with axes aligned along the $[100]_{pc}$. More insight into the nature of this phase boundary, can be obtained by tracking the evolution of the polarization components ($<P_{100}>$, $<P_{010}>$, and $<P_{001}>$) as well as the magnitude of the axial electric toroidal moment ($<|\boldsymbol{G}|>$, averaged across the section) as one transitions from the ferroelectric to vortex structure (Fig. 5.8b). Starting with the ferroelectric phase, we observe constant in-plane polarization components and near zero $\boldsymbol{G}$. The transition to the vortex phase occurs over ~20 unit cells and is characterized by complex polarization rotation pathways (reminiscent of Bloch- and Neel-like walls in ferromagnets) along with a continuously increasing $\boldsymbol{G}$ that eventually saturates to a large value of 0.2 e$\cdot\mathring{A}^{-1}$ which arises from the continuous rotation of polarization within the vortex structures (blue box, Fig. 5.8a and in color-maps of the polarization components P_{100} (Fig. 5.8c), P_{010} (Fig. 5.8d), and P_{001} (Fig. 5.8e) for the same section). We also note that the clockwise and counter-clockwise vortices are arranged in an alternating fashion, such that the toroidal moment $\boldsymbol{G}$ periodically switches direction.

Also notable is that while the spatial average of the non-axial polarization components ($<P_{001}>$, $<P_{010}>$) go to zero within the vortex phase, a sizable axial component ($<P_{100}> \approx$ 0.1 C/m^2) is observed (Fig. 5.8b); the direction of which is related to the component of net polarization in the adjacent ferroelectric phase. In turn, this produces a screw-like character to the vortex phase and suggests that the vortex structure is characterized by a multi-order-parameter state consisting of axial ferroelectric polarization that coexists with $\boldsymbol{G}$. This is also observed in second-principles calculations for an n = 14 superlattice and is consistent with previous predictions for low-dimensional ferroelectrics [381, 382, 383, 384]. Such axial polarization can be experimentally observed by focusing on a region of phase coexistence (i.e., alternating ferroelectric *a1/a2* and vortex stripes, Fig. 5.8f). Using piezoresponse force microscopy (PFM), it is again observed that the amplitude of the piezoresponse (Fig. 5.8g) is higher in the ferroelectric *a1/a2* regions than in

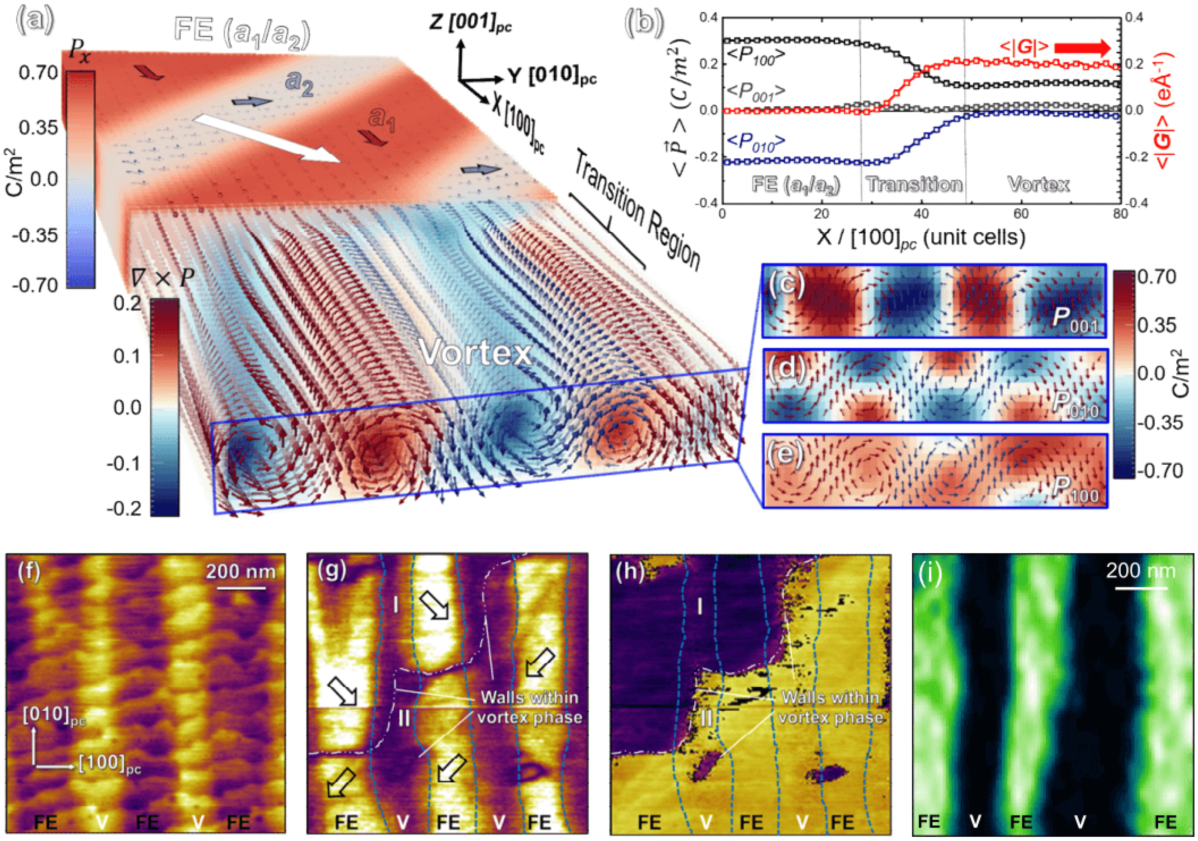

Figure 5.8: Exploring the phase boundary between *a1/a2* and vortex phases. (a) A zoom-in of the phase-field calculation focusing on a single $\mathrm{PbTiO_3}$ layer near the phase boundary and revealing that the ferroelectric *a1/a2* superdomain (labelled FE(*a1/a2*), color-scale showing polarization component along $[100]_{pc}$ or the X-direction) smoothly transitions to the vortex phase (labelled Vortex, color-scale corresponding to magnitude of $\bigtriangledown \times P$) comprising of alternating clockwise and anti-clockwise polarization vortices. (b) Plot showing the spatially-averaged ferroelectric polarization components ($<P_{001}>$, $<P_{010}>$ and $<P_{100}>$) and the averaged magnitude of the axial electrical toroidal moment ($< |\boldsymbol{G}| >$) as we traverse across the phase boundary along [100] from the ferroelectric to the vortex phase. (c)-(e) Color-maps showing spatial distribution of the P_{001}, P_{010} and P_{100} components, respectively, for a cross-section (blue box, a) of the vortex phase and highlight the coexistence of toroidization and an axial component ($P_{100} \approx 0.1$ C/m^2) of polarization, the direction of which is related to polarization in the adjacent *a1/a2* phase. Lateral piezoresponse force studies showing topography (f), lateral amplitude (g), and lateral phase (h) showing the nanoscale distribution of *a1/a2* and vortex phases, and highlighting the presence of domain-wall-like features within the vortex phase that is indicative of axial polarization components. (i) SHG s-SNOM image of the as-grown region showing similar nanoscale distribution of *a1/a2* and vortex phases.

the vortex regions which, along with the topography, allows for clear demarcation of the regions. The phase of the piezoresponse (Fig. 5.8h) shows two contrasts across the same area. By combining the amplitude and phase data, the fact that the cantilever axis is aligned along the $[010]_{pc}$, and our understanding of the 5.8 structure, the net in-plane polarization for each area can be extracted (arrows, Fig. 5.8g). Consistent with the phase-field predictions, the axial polarization component of the vortex phase is set by the direction of the polarization in the adjacent *a1/a2* stripe (e.g., region I, Figs. 5.8g, h). There are situations, however, when adjacent *a1/a2* stripes on either side of a vortex region possess opposite net in-plane polarization, and in this case we observe an inversion of the lateral phase signal in the vortex region indicative of a *domain wall-like* feature (e.g., region II, Figs. 5.8g,h).

Such effects are also resolved in nonlinear optical study. The SHG response from the as-grown regions (Fig. 5.7a) is found to be consistent with that observed for the purely ferroelectric *a1/a2* phase in a single-layer $PbTiO_3$ film (Fig. 5.7c). The ability to electrically switch to a purely vortex state results in a strong reduction of the second-harmonic intensity (Fig. 5.7b). In turn, realizing that the presence of the vortex phase results in a reduction of SHG intensity and by normalizing the as-grown signal based on the volume of the two phases, we estimate nearly an order of magnitude reduction in the SHG signal in the vortex phase as compared with the ferroelectric phase. Such effects are also resolved at the nanoscale in near-field SHG nano-imaging (Fig. 5.8i) obtained using shear-force atomic force microscopy-based s-SNOM where the ferroelectric and vortex regions provide alternating strong and weak signals, respectively.

Either way, the phase-field models, PFM, and SHG data suggest that the vortex structures possess an axial component of polarization that is correlated with the polarization in the surrounding ferroelectric phase.

Chapter 6

Conclusions and outlook

In previous chapters, I described a range of new photon-induced phenomena of low-dimensional materials (from single-molecule to van der Waals materials and ferroics), which revealed and controlled using the advanced tip-enhanced nano-spectroscopy and nano-imaging techniques we have developed beyond the current instrumental limits. This chapter provides a summary of the main scientific discoveries and instrumental achievements demonstrated in the thesis. In addition, I discuss the outlook of this work as well as possible follow-up experiments.

6.1 Summary

6.1.1 Single molecular processes in interacting environments

In order to understand zero-dimensional (0D) molecular/material systems in interacting environments, we demonstrated intramolecular dephasing, local dynamics and rotational motion of a single-molecule using cryogenic high spectral resolution tip-enhanced Raman spectroscopy (TERS). Diffusion is slowed from fast room temperature motion to the seconds timescale by cooling below the thermal activation energy, allowing for the observation of how the molecule dynamically samples the local energetic landscape. Observation of intramolecular and conformational dynamics becomes possible through the combined high spectral resolution and single-molecule sensitivity of the experiment. These single-molecule behaviors have not been previously possible in room temperature [115], low but constant temperature, and/or low spectral resolution experiments [116, 117]. For the first time we have achieved the long standing goal of a molecular movie, recording snapshots of a single molecule as it rotates and diffuses across the energetic surface of an atomically rough metal substrate. This work demonstrates low temperature and high resolution TERS as a new and powerful methodology paving the way to investigate detailed intra- and inter-molecular properties with single-molecule sensitivity.

In addition, we built a cryogen-free low-temperature tip-enhanced spectroscopy with an ultra-high-vacuum (UHV) closed cycle helium exchange gas cryostat extending the temperature range from 20 to 350 K. This instrument development work is performed for more detailed understanding of molecular dynamics and intramolecular coupling properties as well as better measurement and control of samples.

We extended this single-molecule spectroscopy study to the biomolecular imaging study. We have demonstrated a new mechanical resonance control method for stable and sensitive near-field scanning optical microscopy (NSOM) in viscous liquid media. A very high Q-factor (2800 in water) is achieved by a 3 mm tip as well as two nodal wedges method and a stable resonance condition is maintained by applying a diving bell structure. To overcome the low optical sensitivity of general fluorescence detection, the epidermal growth factor receptors (EGFRs) are labeled with gold nanoparticles and the plasmonic scattering signal is probed with $\sim$50 nm spatial resolution. From the NSOM imaging of an A431 cancer cell in liquid, nanoscale correlation between the EGFRs distribution and organelle composition is revealed. We believe this method provides new avenue for near-field membrane imaging to complement super-resolution microscopy for bio-nano-imaging of membranes and other biological interfaces under in situ and in liquid conditions.

We further extended our tip-enhanced spectroscopy study to single quantum dots (QDs) to understand modified spontaneous emission properties of single QDs coupled strongly with localized plasmon. We placed a single CdSe/ZnS QD at the junction of an Au tip and Au substrate, and have performed tip-enhanced photoluminescence (TEPL) spectroscopy experiment. Through this experiment, we observed the PL peak splitting from strong coupling between the exciton and plasmon as well as giant PL enhancement of a single QD.

6.1.2 Probing and control nanoscale processes in van der Waals materials

As a first work of tip-enhanced nano-spectroscopy and nano-imaging study on van der Waals two-dimensional (2D) materials, we demonstrated multispectral TERS imaging on large area graphene grown by chemical vapor deposition (CVD) method. We revealed twisted bilayer structures of grain boundaries in large area graphene and identified misorientation angles from correlated analysis of the high resolution ($\sim$18 nm) multispectral TERS imaging. Further, we investigated phonon scattering properties of wrinkles and nucleation sites, which associate with the nanoscopic structural curvature effect and atomic scale carbon hybridization.

We extended our work to the semiconducting 2D materials, the transition metal dichalcogenide (TMD) monolayer. We measured modifications of the electronic structure and optical properties of WSe_2 on the nanoscale through high resolution (< 15 nm) multi-modal TEPL and TERS imaging. We observed a non-local PL modification at twin boundaries associated with a $\sim$25 nm exciton diffusion length, and $\sim 30 - 80$ nm wide region of optical heterogeneity at edges. Further, we demonstrated dynamic tuning of the local bandgap of ML WSe_2 by releasing and controlling local strain. We believe our hybrid opto-mechanical nano-probe technique can be used for tunable nano-electronic devices where the carrier mobility is controlled via strain engineering [299, 301].

We further extended this approach to probe and control the radiative emission of dark exciton and localized exciton of the TMD monolayer at room temperature. We used a novel generalizable approach demonstrating excitation, modulation, and radiative control of dark exciton emission of WSe_2 monolayer transferred on gold film. Based on nano-tip enhanced spectroscopy with $\sim 6 \times 10^5$-fold PL enhancement induced by the plasmonic Purcell effect and few-fs radiative dynamics of the optical antenna tip, we directly probed and actively modulated the dark exciton emission in time ($\sim$ms) and space ($<$15 nm) at room temperature.

Additionally, we performed multispectral TEPL imaging of the localized excitons. Through this experiment, we investigated spatial local heterogeneity of localized exciton modes with $\sim$10 nm spatial resolution, concentrated in the vicinity of the crystal edges in contrast to bright excitons which is associated with the density of structural defects. Furthermore, we could control the orientation of their transition dipole moment through precise control of plasmon-exciton coupling using nano-optical antenna-tip.

6.1.3 Tip-enhanced nonlinear optical nano-crystallography

Lastly, we extended the range of tip-enhanced nano-spectroscopy and nano-imaging studies to nonlinear nano-crystallography and imaging. We presented a simple but powerful solution to control the localized plasmon and the vector field of the nano-optical antenna-tip. We demonstrated the broken axial symmetry of a conventional Au tip by engineering its tilting angle with respect to the sample surface. From theoretical simulations, we showed the field confinement can be sensitively controlled by tuning the tip orientation angle. In addition to the tuning ability, we found that the tilted tip gives rise to a significantly enhanced optical field confinement with respect to both vertical and horizontal directions by creating a confined structure for free electrons and associated localized plasmon antenna effect. Using this advantage of the tilting tip, we have demonstrated nonlinear optical second harmonic generation (SHG) nano-crystallography imaging for MoS_2 monolayer film, ferroelectric $YMnO_3$, $BaTiO_3$-$BiFeO_3$ multiferroics, and $PbTiO_3/SrTiO_3$ superlattices.

6.2 Outlook

High spectral resolution variable temperature TERS offers new insights into the intra- and inter-molecular coupling, structural and vibrational dynamics, and molecular motion. We can extend this work on i) an extended mode-selective study of intramolecular and bath coupling, ii) a correlation study of tunneling transport and TERS derived molecular orientation, and iii) probing plasmonic hot electron photochemistry on the single particle level. For these follow-up studies, we will use a recently built cryogen-free low-temperature tip-enhanced spectroscopy with an UHV closed cycle helium exchange gas cryostat extending the temperature range from 20 to 350 K.

A new mechanical resonance control of the near-field probe provides a way to a greater utility of near-field imaging as a complementary technique to other super-resolution imaging techniques for biological applications in liquid conditions. The approach is generally applicable for both aperture and scattering type scanning near-field microscopy and TERS, and can be easily combined with other optical modalities, such as time-resolved and absorption spectroscopies [98, 238]. Membrane proteins are particularly significant in biomedical research because they are the target of over 60% of all modern medicinal drugs [37]. Specifically, anti-EGFR cancer therapy is widely administered to patients recently [234]. However, a large portion of patients do not respond to the therapy for unknown reasons. Conventional far-field sectioning super-resolution fluorescence microscopies are unable to investigate membrane biomolecules. Therefore, we expect our *in-liquid* NSOM modality will provide a better understanding for the membrane proteins and incurable diseases.

We expect the demonstrated multispectral TERS imaging study on graphene will help to better understand nanoscale defects, their impact on function, and growth mechanisms of large area graphene. This study shows the potential of correlated TERS analysis as generally applicable to a wide range of 2D layered materials and heterostructures beyond graphene. For example, structures and electronic/vibrational properties at grain boundaries and nucleation site of recently synthesized large area TMDs [274] could be revealed through correlated TERS analysis.

A new hybrid nano-optomechanical tip-enhanced spectroscopy and imaging approach combining TERS, TEPL, and atomic force local strain manipulation is expected to help in the design of novel nano-photonic/electronic TMD devices by enabling local bandgap engineering and *in-situ* spectroscopy of 2D materials. We will extend our hybrid TERS/TEPL experiments i) to probe interlayer exciton and Raman modes of TMD heterostructures [335] and ii) to probe length scale of interdiffused exciton in lateral (in-plane) heterostructures [385, 386].

Our demonstration on the radiative control of dark exciton gives access to potential applications of dark excitons in quantum nano-optoelectronics over a wide temperature range. We envision the demonstrated tip-antenna platform for room temperature dark exciton emission with or without nano-opto-mechnical control [20] as an ideal building block for functional quantum devices. Further, the nanoscale optical switching of spin states paves way for new design and fabrication of nano-spintronic devices. Specifically, the control of long-lived dark excitons confined in only $\sim$150 nm^3 mode volume can be exploited to create nanoscale devices for integrated quantum-photonic circuits and active quantum information processor, such as nano-light emitting diodes, nano-optical switch/multiplexer, high-density memory, and qubit. The nano-confinement further allows for imaging with $\leq$ 15 nm spatial resolution of heterogeneity of dark excitonic properties in 2D TMDs [20], with the possibility for an additional modulation in electronic energy with local strain engineering via nano-mechanical tip force control as we demonstrated recently [20]. The range of dynamic controls including coherent ultrafast excitation and tip/antenna manipulation thus gives access to a range of new phenomena at the sub-10 nm scale regime including room temperature strong coupling [251, 333], interlayer electron-phonon coupling [334], or *out-of-plane* exciton behaviors [335]. Further, the range of application can be extended to dark excitons in semi-conducting carbon nanostructures, QDs, and molecular materials beyond TMDs and other van der Waals materials.

The demonstrated tilting tip idea, controlling vector field of the nano-optical antenna-tip, was initially conceived to enhance the *in-plane* optical field $\boldsymbol{E}_x$ confinement for investigation of 2D materials. Interestingly, it turned out the *out-of-plane* optical field $\boldsymbol{E}_z$ is also highly enhanced even larger than $\boldsymbol{E}_x$. This brings up an interesting new aspect that this tilted tip modality provides much more sensitive near-field signals than a conventional scattering-scanning near-field optical microscopy (s-SNOM) tip for all samples beyond 2D materials. SHG nano-crystallography using tilted tip paves way to harness little known linear and nonlinear nano-optical properties of a wide range of samples beyond layered 2D and ferroic materials.

Although we only performed the SHG nano-crystallography study to best demonstrate the strength of the tilted tip through the well-defined samples and selection rule, this approach is also applicable to TERS/TEPL spectroscopy and imaging with much larger enhanced plasmon resonance with typical excitation wavelengths of 532 nm and 633 nm. We expect that this strongly confined vector field gives access to anomalous nanoscale light-matter interactions in a range of molecules and materials.

Bibliography

[1] William E Moerner and Lothar Kador. Optical detection and spectroscopy of single molecules in a solid. Phys. Rev. Lett., 62(21):2535, 1989.

[2] Katrin Kneipp, Yang Wang, Harald Kneipp, Lev T Perelman, Irving Itzkan, Ramachandra R Dasari, and Michael S Feld. Single molecule detection using surface-enhanced Raman scattering (SERS). Phys. Rev. Lett., 78(9):1667, 1997.

[3] Bingqian Xu and Nongjian J Tao. Measurement of single-molecule resistance by repeated formation of molecular junctions. Science, 301(5637):1221–1223, 2003.

[4] Pascal Anger, Palash Bharadwaj, and Lukas Novotny. Enhancement and quenching of single-molecule fluorescence. Phys. Rev. Lett., 96(11):113002, 2006.

[5] Arpad A Bergh and PJ Dean. Light-emitting diodes. Proceedings of the IEEE, 60(2):156–223, 1972.

[6] Sebastian Reineke, Frank Lindner, Gregor Schwartz, Nico Seidler, Karsten Walzer, Björn Lüssem, and Karl Leo. White organic light-emitting diodes with fluorescent tube efficiency. MRS Online Proceedings Library Archive, 1212, 2009.

[7] Anders Hagfeldt and Michael Grätzel. Molecular photovoltaics. Acc. Chem. Res., 33(5):269–277, 2000.

[8] Sergei A Akhmanov, Viktor A Vysloukh, and Anatolii S Chirkin. Optics of femtosecond laser pulses. Moscow Izdatel Nauka, 1988.

[9] JD Kmetec, CL Gordon III, JJ Macklin, BE Lemoff, GS Brown, and SE Harris. MeV x-ray generation with a femtosecond laser. Phys. Rev. Lett., 68(10):1527, 1992.

[10] AC Ferrari and J Robertson. Resonant Raman spectroscopy of disordered, amorphous, and diamondlike carbon. Phys. Rev. B, 64(7):075414, 2001.

[11] Eleonora Petryayeva, W Russ Algar, and Igor L Medintz. Quantum dots in bioanalysis: a review of applications across various platforms for fluorescence spectroscopy and imaging. Appl. Spectrosc., 67(3):215–252, 2013.

[12] Samuel T Hess, Shaohui Huang, Ahmed A Heikal, and Watt W Webb. Biological and chemical applications of fluorescence correlation spectroscopy: a review. Biochemistry, 41(3):697–705, 2002.

[13] Shaul Mukamel. Principles of nonlinear optical spectroscopy. Number 6. Oxford University Press on Demand, 1999.

[14] Dieter W Pohl, W Denk, and M Lanz. Optical stethoscopy: Image recording with resolution $\lambda/20$. Appl. Phys. Lett., 44(7):651–653, 1984.

[15] E Betzig, M Isaacson, and A Lewis. Collection mode near-field scanning optical microscopy. Appl. Phys. Lett., 51(25):2088–2090, 1987.

[16] Robert C Dunn. Near-field scanning optical microscopy. Chem. Rev., 99(10):2891–2928, 1999.

[17] F Zenhausern, MP Oboyle, and HK Wickramasinghe. Apertureless near-field optical microscope. Appl. Phys. Lett., 65(13):1623–1625, 1994.

[18] Bernhard Knoll and Fritz Keilmann. Enhanced dielectric contrast in scattering-type scanning near-field optical microscopy. Opt. Commun., 182(4):321–328, 2000.

[19] Kyoung-Duck Park, Eric A Muller, Vasily Kravtsov, Paul M Sass, Jens Dreyer, Joanna M Atkin, and Markus B Raschke. Variable-temperature tip-enhanced Raman spectroscopy of single-molecule fluctuations and dynamics. Nano Lett., 16(1):479–487, 2016.

[20] Kyoung-Duck Park, Omar Khatib, Vasily Kravtsov, Genevieve Clark, Xiaodong Xu, and Markus B Raschke. Hybrid tip-enhanced nanospectroscopy and nanoimaging of monolayer WSe_2 with local strain control. Nano Lett., 16(4):2621–2627, 2016.

[21] Catalin C Neacsu, Bas B van Aken, Manfred Fiebig, and Markus B Raschke. Second-harmonic near-field imaging of ferroelectric domain structure of ymno 3. Phys. Rev. B, 79(10):100107, 2009.

[22] H Peter Lu, Luying Xun, and X Sunney Xie. Single-molecule enzymatic dynamics. Science, 282(5395):1877–1882, 1998.

[23] Shimon Weiss. Measuring conformational dynamics of biomolecules by single molecule fluorescence spectroscopy. Nat. Struct. Mol. Biol., 7(9):724, 2000.

[24] Kengo Adachi, Kazuhiro Oiwa, Takayuki Nishizaka, Shou Furuike, Hiroyuki Noji, Hiroyasu Itoh, Masasuke Yoshida, and Kazuhiko Kinosita. Coupling of rotation and catalysis in f 1-atpase revealed by single-molecule imaging and manipulation. Cell, 130(2):309–321, 2007.

[25] Erwin Schrödinger. Are there quantum jumps? Part I. Br. J Philos. Sci., 3(10):109–123, 1952.

[26] Stefan W. Hell and Jan Wichmann. Breaking the diffraction resolution limit by stimulated emission: stimulated-emission-depletion fluorescence microscopy. Opt. Lett., 19(11):780, June 1994.

[27] Eric Betzig, George H Patterson, Rachid Sougrat, O Wolf Lindwasser, Scott Olenych, Juan S Bonifacino, Michael W Davidson, Jennifer Lippincott-Schwartz, and Harald F Hess. Imaging intracellular fluorescent proteins at nanometer resolution. Science, 313(5793):1642–5, September 2006.

[28] Wei Min, Sijia Lu, Shasha Chong, Rahul Roy, Gary R Holtom, and X Sunney Xie. Imaging chromophores with undetectable fluorescence by stimulated emission microscopy. Nature, 461(7267):1105–9, October 2009.

[29] Daniel E Rosenfeld, Zsolt Gengeliczki, Brian J Smith, T D P Stack, and M D Fayer. Structural dynamics of a catalytic monolayer probed by ultrafast 2d ir vibrational echoes. Science, 334(6056):634–9, November 2011.

[30] S. Nie. Probing single molecules and single nanoparticles by surface-enhanced Raman scattering. Science, 275(5303):1102–1106, February 1997.

[31] Raoul M. Stöckle, Yung Doug Suh, Volker Deckert, and Renato Zenobi. Nanoscale chemical analysis by tip-enhanced Raman spectroscopy. Chem. Phys. Lett., 318(1-3):131–136, February 2000.

[32] Catalin C Neacsu, Jens Dreyer, Nicolas Behr, and Markus B Raschke. Scanning-probe Raman spectroscopy with single-molecule sensitivity. Phys. Rev. B, 73(19):193406, 2006.

[33] W. Zhang, B.S. Yeo, T. Schmid, and R. Zenobi. Single molecule tip-enhanced Raman spectroscopy with silver tips. J. Phys. Chem. C, 111(4):1733–1738, February 2007.

[34] Katrin I Willig, Silvio O Rizzoli, Volker Westphal, Reinhard Jahn, and Stefan W Hell. STED microscopy reveals that synaptotagmin remains clustered after synaptic vesicle exocytosis. Nature, 440(7086):935–939, 2006.

[35] Hari Shroff, Catherine G Galbraith, James A Galbraith, and Eric Betzig. Live-cell photoactivated localization microscopy of nanoscale adhesion dynamics. Nat. Methods, 5(5):417–423, 2008.

[36] Michael J Rust, Mark Bates, and Xiaowei Zhuang. Sub-diffraction-limit imaging by stochastic optical reconstruction microscopy (STORM). Nat. Methods, 3(10):793–796, 2006.

[37] John P Overington, Bissan Al-Lazikani, and Andrew L Hopkins. How many drug targets are there? Nat. Rev. Drug Discovery, 5(12):993–996, 2006.

[38] Kyoung-Duck Park, Dae-Chan Kim, Beom-Hoan O, Se-Geun Park, El-Hang Lee, and Seung Gol Lee. A new method of Q factor optimization by introducing two nodal wedges in a tuning-fork/fiber probe distance sensor. Rev. Sci. Instrum., 81(9):093702, 2010.

[39] Matthew Pelton. Modified spontaneous emission in nanophotonic structures. Nat. Photon., 9(7):427, 2015.

[40] Toshihide Takagahara and Kyozaburo Takeda. Theory of the quantum confinement effect on excitons in quantum dots of indirect-gap materials. Phys. Rev. B, 46(23):15578, 1992.

[41] Leo Kouwenhoven. Single-molecule transistors. Science, 275(5308):1896–1897, 1997.

[42] Wenjie Liang, Matthew P Shores, Marc Bockrath, Jeffrey R Long, and Hongkun Park. Kondo resonance in a single-molecule transistor. Nature, 417(6890):725, 2002.

[43] AK Geim and IV Grigorieva. Van der Waals heterostructures. Nature, 499(7459):419, 2013.

[44] Kostya S Novoselov, Andre K Geim, Sergei V Morozov, D Jiang, Y_ Zhang, Sergey V Dubonos, Irina V Grigorieva, and Alexandr A Firsov. Electric field effect in atomically thin carbon films. Science, 306(5696):666–669, 2004.

[45] Yuanbo Zhang, Yan-wen Tan, Horst L Stormer, and Philip Kim. Experimental observation of the quantum hall effect and Berry's phase in graphene. Nature, 438(7065):201–204, 2005.

[46] Alexander A Balandin, Suchismita Ghosh, Wenzhong Bao, Irene Calizo, Desalegne Teweldebrhan, Feng Miao, and Chun Ning Lau. Superior thermal conductivity of single-layer graphene. Nano Lett., 8(3):902–907, 2008.

[47] Mohammad A Rafiee, Javad Rafiee, Zhou Wang, Huaihe Song, Zhong-Zhen Yu, and Nikhil Koratkar. Enhanced mechanical properties of nanocomposites at low graphene content. ACS nano, 3(12):3884–3890, 2009.

[48] Andrea Splendiani, Liang Sun, Yuanbo Zhang, Tianshu Li, Jonghwan Kim, Chi-Yung Chim, Giulia Galli, and Feng Wang. Emerging photoluminescence in monolayer MoS_2. Nano Lett., 10(4):1271–1275, 2010.

[49] Kin Fai Mak, Changgu Lee, James Hone, Jie Shan, and Tony F Heinz. Atomically thin MoS_2: a new direct-gap semiconductor. Phys. Rev. Lett., 105(13):136805, 2010.

[50] Keun Soo Kim, Yue Zhao, Houk Jang, Sang Yoon Lee, Jong Min Kim, Kwang S Kim, Jong-Hyun Ahn, Philip Kim, Jae-Young Choi, and Byung Hee Hong. Large-scale pattern growth of graphene films for stretchable transparent electrodes. Nature, 457(7230):706, 2009.

[51] Max C Lemme, Tim J Echtermeyer, Matthias Baus, and Heinrich Kurz. A graphene field-effect device. IEEE Electron Device Lett., 28(4):282–284, 2007.

[52] Nan Liu, Zhonghuai Pan, Lei Fu, Chaohua Zhang, Boya Dai, and Zhongfan Liu. The origin of wrinkles on transferred graphene. Nano Res., 4(10):996–1004, 2011.

[53] Xuesong Li, Weiwei Cai, Jinho An, Seyoung Kim, Junghyo Nah, Dongxing Yang, Richard Piner, Aruna Velamakanni, Inhwa Jung, Emanuel Tutuc, Sanjay K. Banerjee, Luigi Colombo, and Rodney S. Ruoff. Large-area synthesis of high-quality and uniform graphene films on copper foils. Science, 324(5932):1312–1314, 2009.

[54] Francesco Bonaccorso, Z Sun, Ta Hasan, and AC Ferrari. Graphene photonics and optoelectronics. Nat. Photon., 4(9):611–622, 2010.

[55] Seung Jin Chae, Fethullah Güneş, Ki Kang Kim, Eun Sung Kim, Gang Hee Han, Soo Min Kim, Hyeon-Jin Shin, Seon-Mi Yoon, Jae-Young Choi, Min Ho Park, Cheol Woong Yang, Didier Pribat, and Young Hee Lee. Synthesis of large-area graphene layers on poly-nickel substrate by chemical vapor deposition: wrinkle formation. Adv. Mater., 21(22):2328–2333, 2009.

[56] Kwanpyo Kim, Zonghoon Lee, William Regan, C Kisielowski, MF Crommie, and A Zettl. Grain boundary mapping in polycrystalline graphene. ACS Nano, 5(3):2142–2146, 2011.

[57] Dinh Loc Duong, Gang Hee Han, Seung Mi Lee, Fethullah Gunes, Eun Sung Kim, Sung Tae Kim, Heetae Kim, Quang Huy Ta, Kang Pyo So, Seok Jun Yoon, Seung Jin Chae, Young Woo

Jo, Min Ho Park, Sang Hoon Chae, Seong Chu Lim, Jae Young Choi, and Young Hee Lee. Probing graphene grain boundaries with optical microscopy. Nature, 490(7419):235–239, 2012.

[58] Adam W Tsen, Lola Brown, Mark P Levendorf, Fereshte Ghahari, Pinshane Y Huang, Robin W Havener, Carlos S Ruiz-Vargas, David A Muller, Philip Kim, and Jiwoong Park. Tailoring electrical transport across grain boundaries in polycrystalline graphene. Science, 336(6085):1143–1146, 2012.

[59] Oleg V Yazyev and Steven G Louie. Electronic transport in polycrystalline graphene. Nat. Mater., 9(10):806–809, 2010.

[60] Qingkai Yu, Luis A Jauregui, Wei Wu, Robert Colby, Jifa Tian, Zhihua Su, Helin Cao, Zhihong Liu, Deepak Pandey, Dongguang Wei, Ting Fung Chung, Peng Peng, Nathan P. Guisinger, Eric A. Stach, Jiming Bao, Shin-Shem Pei, and Yong P. Chen. Control and characterization of individual grains and grain boundaries in graphene grown by chemical vapour deposition. Nat. Mater., 10(6):443–449, 2011.

[61] Inanc Meric, Melinda Y Han, Andrea F Young, Barbaros Ozyilmaz, Philip Kim, and Kenneth L Shepard. Current saturation in zero-bandgap, top-gated graphene field-effect transistors. Nat. Nanotech., 3(11):654–659, 2008.

[62] KS Novoselov. Nobel lecture: Graphene: Materials in the flatland. Rev. Mod. Phys., 83(3):837, 2011.

[63] ZY Zhu, YC Cheng, and Udo Schwingenschlögl. Giant spin-orbit-induced spin splitting in two-dimensional transition-metal dichalcogenide semiconductors. Phys. Rev. B, 84(15):153402, 2011.

[64] Kin Fai Mak, Keliang He, Jie Shan, and Tony F Heinz. Control of valley polarization in monolayer MoS_2 by optical helicity. Nat. Nanotech., 7(8):494–498, 2012.

[65] Leandro M Malard, Thonimar V Alencar, Ana Paula M Barboza, Kin Fai Mak, and Ana M de Paula. Observation of intense second harmonic generation from MoS_2 atomic crystals. Phys. Rev. B, 87(20):201401, 2013.

[66] Kyle L Seyler, John R Schaibley, Pu Gong, Pasqual Rivera, Aaron M Jones, Sanfeng Wu, Jiaqiang Yan, David G Mandrus, Wang Yao, and Xiaodong Xu. Electrical control of second-harmonic generation in a WSe_2 monolayer transistor. Nat. Nanotech., 10(5):407–411, 2015.

[67] Philippe K Chow, Robin B Jacobs-Gedrim, Jian Gao, Toh-Ming Lu, Bin Yu, Humberto Terrones, and Nikhil Koratkar. Defect-induced photoluminescence in monolayer semiconducting transition metal dichalcogenides. ACS Nano, 9(2):1520–1527, 2015.

[68] Arend M van der Zande, Pinshane Y Huang, Daniel A Chenet, Timothy C Berkelbach, YuMeng You, Gwan-Hyoung Lee, Tony F Heinz, David R Reichman, David A Muller, and James C Hone. Grains and grain boundaries in highly crystalline monolayer molybdenum disulphide. Nat. Mater., 12(6):554–561, 2013.

[69] Zheng Liu, Matin Amani, Sina Najmaei, Quan Xu, Xiaolong Zou, Wu Zhou, Ting Yu, Caiyu Qiu, A Glen Birdwell, Frank J Crowne, Robert Vajtai, Boris I Yakobson, Zhenhai Xia, Madan

Dubey, Pulickel M Ajayan, and Jun Lou. Strain and structure heterogeneity in MoS_2 atomic layers grown by chemical vapour deposition. Nat. Commun., 5:5246, 2014.

[70] Xiao-Xiao Zhang, Ting Cao, Zhengguang Lu, Yu-Chuan Lin, Fan Zhang, Ying Wang, Zhiqiang Li, James C Hone, Joshua A Robinson, Dmitry Smirnov, Steven G Louie, and Tony F Heinz. Magnetic brightening and control of dark excitons in monolayer WSe_2. preprint arXiv:1612.03558, Nat. Nanotech., 2017.

[71] You Zhou, Giovanni Scuri, Dominik S Wild, Alexander A High, Alan Dibos, Luis A Jauregui, Chi Shu, Kristiaan De Greve, Kateryna Pistunova, Andrew Joe, Takashi Taniguchi, Kenji Watanabe, Philip Kim, Mikhail D Lukin, and Hongkun Park. Probing dark excitons in atomically thin semiconductors via near-field coupling to surface plasmon polaritons. preprint arXiv:1701.05938, Nat. Nanotech., 2017.

[72] M Koperski, K Nogajewski, A Arora, V Cherkez, P Mallet, J-Y Veuillen, J Marcus, P Kossacki, and M Potemski. Single photon emitters in exfoliated WSe_2 structures. Nat. Nanotech., 10(6):503–506, 2015.

[73] Ajit Srivastava, Meinrad Sidler, Adrien V Allain, Dominik S Lembke, Andras Kis, and A Imamoğlu. Optically active quantum dots in monolayer WSe_2. Nat. Nanotech., 10(6):491–496, 2015.

[74] Nardeep Kumar, Sina Najmaei, Qiannan Cui, Frank Ceballos, Pulickel M Ajayan, Jun Lou, and Hui Zhao. Second harmonic microscopy of monolayer MoS_2. Phys. Rev. B, 87(16):161403, 2013.

[75] Xiaobo Yin, Ziliang Ye, Daniel A Chenet, Yu Ye, Kevin O'Brien, James C Hone, and Xiang Zhang. Edge nonlinear optics on a MoS_2 atomic monolayer. Science, 344(6183):488–490, 2014.

[76] Wei-Ting Hsu, Zi-Ang Zhao, Lain-Jong Li, Chang-Hsiao Chen, Ming-Hui Chiu, Pi-Shan Chang, Yi-Chia Chou, and Wen-Hao Chang. Second harmonic generation from artificially stacked transition metal dichalcogenide twisted bilayers. ACS Nano, 8(3):2951–2958, 2014.

[77] M Fiebig, D Fröhlich, Th Lottermoser, and M Maat. Probing of ferroelectric surface and bulk domains in $RMnO_3$ (R = Y, Ho) by second harmonic generation. Phys. Rev. B, 66(14):144102, 2002.

[78] William L Barnes, Alain Dereux, and Thomas W Ebbesen. Surface plasmon subwavelength optics. Nature, 424(6950):824, 2003.

[79] Justin A Gerber, Samuel Berweger, Brian T OCallahan, and Markus B Raschke. Phase-resolved surface plasmon interferometry of graphene. Phys. Rev. Lett., 113(5):055502, 2014.

[80] Jens Dorfmuller, Ralf Vogelgesang, Worawut Khunsin, Carsten Rockstuhl, Christoph Etrich, and Klaus Kern. Plasmonic nanowire antennas: experiment, simulation, and theory. Nano Lett., 10(9):3596–3603, 2010.

[81] W Rechberger, A Hohenau, A Leitner, JR Krenn, B Lamprecht, and FR Aussenegg. Optical properties of two interacting gold nanoparticles. Opt. Commun., 220(1):137–141, 2003.

[82] NW Ashcroft and D Stroud. Theory of the thermodynamics of simple liquid metals. Solid State Physics, 33:1–81, 1978.

[83] Lukas Novotny and Bert Hecht. Principles of nano-optics. Cambridge university press, 2012.

[84] David FP Pile and Dmitri K Gramotnev. Channel plasmon–polariton in a triangular groove on a metal surface. Opt. Lett., 29(10):1069–1071, 2004.

[85] B Steinberger, A Hohenau, H Ditlbacher, AL Stepanov, A Drezet, FR Aussenegg, A Leitner, and JR Krenn. Dielectric stripes on gold as surface plasmon waveguides. Appl. Phys. Lett., 88(9):094104, 2006.

[86] Ji Feng, Xiaofeng Qian, Cheng-Wei Huang, and Ju Li. Strain-engineered artificial atom as a broad-spectrum solar energy funnel. Nat. Photon., 6(12):866–872, 2012.

[87] Daisuke Inoue, Atsushi Miura, Tsuyoshi Nomura, Hisayoshi Fujikawa, Kazuo Sato, Naoki Ikeda, Daiju Tsuya, Yoshimasa Sugimoto, and Yasuo Koide. Polarization independent visible color filter comprising an aluminum film with surface-plasmon enhanced transmission through a subwavelength array of holes. Appl. Phys. Lett., 98(9):093113, 2011.

[88] C. F. Bohren and D. R. Huffmann. Absorption and Scattering of Light by Small Particles. Wiley, New York, 1998.

[89] Samuel Berweger. Plasmonic Antennas for Optical Nanocrystallography and Femtosecond Spatio-Temporal Control. University of Washington, 2011.

[90] Joanna M Atkin, Samuel Berweger, Andrew C Jones, and Markus B Raschke. Nano-optical imaging and spectroscopy of order, phases, and domains in complex solids. Adv. Phys., 61(6):745–842, 2012.

[91] J. D. Jackson. Classical Electrodynamics. Wiley, New York, 1998.

[92] E. H. Synge. A suggested method for extending microscopic resolution into the ultra-microscopic region. Phil. Mag., 6(356-362):1, 1928.

[93] MS Jeong, JY Kim, Y-W Kim, JO White, E-K Suh, C-H Hong, and HJ Lee. Spatially resolved photoluminescence in InGaN/GaN quantum wells by near-field scanning optical microscopy. Appl. Phys. Lett., 79(7):976–978, 2001.

[94] Shi-Li Quan, Hyun-Sik Lee, El-Hang Lee, Kyoung-Duck Park, Seung Gol Lee, and In-Joo Chin. Ultrafine PMMA(QDs)/PVDF core–shell fibers for nanophotonic applications. Microelectron. Eng., 87(5):1308–1311, 2010.

[95] Kyoung-Duck Park, Seung Gol Lee, Chaejeong Heo, Young Hee Lee, and Mun Seok Jeong. Sensitivity maximized near-field scanning optical microscope with dithering sample stage. Rev. Sci. Instrum., 83(9):093710, 2012.

[96] W Patrick Ambrose, Peter M Goodwin, John C Martin, and Richard A Keller. Alterations of single molecule fluorescence lifetimes in near-field optical microscopy. Science, 265(5170):364–368, 1994.

[97] Stefan A Maier, Pieter G Kik, Harry A Atwater, Sheffer Meltzer, Elad Harel, Bruce E Koel, and Ari AG Requicha. Local detection of electromagnetic energy transport below the diffraction limit in metal nanoparticle plasmon waveguides. Nat. Mater., 2(4):229, 2003.

[98] Kyoung-Duck Park, Hyun Jeong, Yong Hwan Kim, Sang-Youp Yim, Hong Seok Lee, Eun-Kyung Suh, and Mun Seok Jeong. Time-resolved ultraviolet near-field scanning optical microscope for characterizing photoluminescence lifetime of light-emitting devices. J. Nanosci. Nanotech., 13(3):1798–1801, 2013.

[99] Kyoung-Duck Park, Won-Soo Ji, Dae-Seo Park, Dae-Chan Kim, O Beom-Hoan, Se-Geun Park, El-Hang Lee, and Seung Gol Lee. Measuring near-field optical distributions emitted from chip surface of photonic crystal patterned light emitting diodes. In Photonics Europe, pages 69880P–69880P. International Society for Optics and Photonics, 2008.

[100] Doo Jae Park, Kyoung-Duck Park, Geun Chang Choi, Seung Gol Lee, Clare Chisu Byeon, Mun Seok Jeong, and Soo Bong Choi. A resonance tracking method for stable operation of a near-field scanning optical microscope in liquid environment. Curr. Appl. Phys., 14:S12–S16, 2014.

[101] Kyoung-Duck Park, Markus B Raschke, Min Jung Jang, Jung Hwa Kim, Beom-Hoan O, Se-Geun Park, El-Hang Lee, and Seung Gol Lee. Near-field imaging of cell membranes in liquid enabled by active scanning probe mechanical resonance control. J. Phys. Chem. C, 120(37):21138–21144, 2016.

[102] Kyoung-Duck Park, Doo Jae Park, Mun Seok Jeong, Geun Chang Choi, Seung Gol Lee, Clare Chisu Byeon, and Soo Bong Choi. Cancer cell imaging by stable wet near-field scanning optical microscope with resonance tracking method. J. Kor. Phys. Soc., 64(10):1500–1503, 2014.

[103] H. A. Bethe. Theory of diffraction by small holes. Phys. Rev., 66(7-8):163, October 1944.

[104] B. B. Akhremitchev, S. Pollack, and G. C. Walker. Apertureless scanning near-field infrared microscopy of a rough polymeric surface. Langmuir, 17:2774, 2001.

[105] Fritz Keilmann, Andreas Huber, and Rainer Hillenbrand. Nanoscale conductivity contrast by scattering-type near-field optical microscopy in the visible, infrared and thz domains. Journal of Infrared, Millimeter and Terahertz Waves, 30:1255–1268, 2009. 10.1007/s10762-009-9525-3.

[106] Antonello Nesci, René Dändliker, and Hans Peter Herzig. Quantitative amplitude and phase measurement by use of a heterodyne scanning near-field optical microscope. Opt. Lett., 26(4):208–210, 2001.

[107] Kyoung-Duck Park, Yong Hwan Kim, Jin-Ho Park, Jung Su Park, Hong Seok Lee, Sang-Youp Yim, Young Hee Lee, and Mun Seok Jeong. Ultraviolet tip-enhanced nanoscale raman imaging. J. Raman Spectrosc., 43(12):1931–1934, 2012.

[108] David A. Vanden Bout, Wai-Tak Yip, Dehong Hu, Dian-Kui Fu, Timothy M. Swager, and Paul F. Barbara. Discrete Intensity Jumps and Intramolecular Electronic Energy Transfer in the Spectroscopy of Single Conjugated Polymer Molecules. Science, 277(5329):1074–1077, August 1997.

[109] Yuxi Tian, Pedro Navarro, Boleslaw Kozankiewicz, and Michel Orrit. Spectral diffusion of single dibenzoterrylene molecules in 2,3-dimethylanthracene. ChemPhysChem, 13(15):3510–5, October 2012.

[110] H Sosa, E J Peterman, W E Moerner, and L S Goldstein. ADP-induced rocking of the kinesin motor domain revealed by single-molecule fluorescence polarization microscopy. Nat. Struct. Mol. Biol., 8(6):540–4, June 2001.

[111] Alexandros Pertsinidis, Yunxiang Zhang, and Steven Chu. Subnanometre single-molecule localization, registration and distance measurements. Nature, 466(7306):647–651, July 2010.

[112] Randall H Goldsmith and W E Moerner. Watching conformational- and photo-dynamics of single fluorescent proteins in solution. Nat. Chem., 2(3):179–86, March 2010.

[113] G. Sallen, A. Tribu, T. Aichele, R. André, L. Besombes, C. Bougerol, M. Richard, S. Tatarenko, K. Kheng, and J.-Ph. Poizat. Subnanosecond spectral diffusion measurement using photon correlation. Nat. Photonics, 4(10):696–699, July 2010.

[114] J Stadler, T Schmid, and R Zenobi. Nanoscale chemical imaging using top-illumination tip-enhanced Raman spectroscopy. Nano Lett., 10(11):4514–20, November 2010.

[115] Evelien M van Schrojenstein Lantman, Tanja Deckert-Gaudig, Arjan J G Mank, Volker Deckert, and Bert M Weckhuysen. Catalytic processes monitored at the nanoscale with tip-enhanced Raman spectroscopy. Nat. Nanotechnol., 7(9):583–6, September 2012.

[116] R Zhang, Y Zhang, Z C Dong, S Jiang, C Zhang, L G Chen, L Zhang, Y Liao, J Aizpurua, Y Luo, J L Yang, and J G Hou. Chemical mapping of a single molecule by plasmon-enhanced Raman scattering. Nature, 498(7452):82–6, June 2013.

[117] Jordan M Klingsporn, Nan Jiang, Eric A Pozzi, Matthew D Sonntag, Dhabih Chulhai, Tamar Seideman, Lasse Jensen, Mark C Hersam, and Richard P Van Duyne. Intramolecular insight into adsorbate-substrate interactions via low-temperature, ultrahigh-vacuum tip-enhanced Raman spectroscopy. J. Am. Chem. Soc., 136(10):3881–7, March 2014.

[118] Camille Artur, Eric C. Le Ru, and Pablo G. Etchegoin. Temperature Dependence of the Homogeneous Broadening of Resonant Raman Peaks Measured by Single-Molecule Surface-Enhanced Raman Spectroscopy. J. Phys. Chem. Lett., 2(23):3002–3005, December 2011.

[119] Catalin C Neacsu, G A Steudle, and Markus B Raschke. Plasmonic light scattering from nanoscopic metal tips. Appl. Phys. B, 80(3):295–300, 2005.

[120] Khaled Karrai and Robert D Grober. Piezoelectric tip-sample distance control for near field optical microscopes. Appl. Phys. Lett., 66(14):1842–1844, 1995.

[121] Vasily Kravtsov, Samuel Berweger, Joanna M Atkin, and Markus B Raschke. Control of plasmon emission and dynamics at the transition from classical to quantum coupling. Nano Lett., 14(9):5270–5275, 2014.

[122] Marcus Sackrow, Catrinel Stanciu, M Andreas Lieb, and Alfred J Meixner. ChemPhysChem, 9:316–20, 2008.

[123] Dai Zhang, Xiao Wang, Kai Braun, Hans-Joachim Egelhaaf, Monika Fleischer, Laura Hennemann, Holger Hintz, Catrinel Stanciu, Christoph J. Brabec, Dieter P. Kern, and Alfred J. Meixner. Parabolic mirror-assisted tip-enhanced spectroscopic imaging for non-transparent materials. J. Raman Spectrosc., 40(10):1371–1376, October 2009.

[124] Hyun Woo Kihm, Jineun Kim, Sukmo Koo, Jaesung Ahn, Kwangjun Ahn, Kwanggeol Lee, Namkyoo Park, and Dai-Sik Kim. Optical magnetic field mapping using a subwavelength aperture. Opt. Express, 21(5):5625–33, March 2013.

[125] Bruno Pettinger, Bin Ren, Gennaro Picardi, Rolf Schuster, and Gerhard Ertl. Nanoscale Probing of Adsorbed Species by Tip-Enhanced Raman Spectroscopy. Phys. Rev. Lett., 92(9):096101, March 2004.

[126] Steven Yampolsky, Dmitry A. Fishman, Shirshendu Dey, Eero Hulkko, Mayukh Banik, Eric O. Potma, and Vartkess A. Apkarian. Nat. Photon., 8:650–656, 2014.

[127] Pablo G Etchegoin and Eric C Le Ru. Resolving single molecules in surface-enhanced Raman scattering within the inhomogeneous broadening of Raman peaks. Anal. Chem., 82(7):2888–92, May 2010.

[128] A. G. Redfield. On the Theory of Relaxation Processes. IBM J. Res. Dev., 1(1):19–31, January 1957.

[129] C. Harris, R. Shelby, and P. Cornelius. Effects of Energy Exchange on Vibrational Dephasing Times in Raman Scattering. Phys. Rev. Lett., 38(24):1415–1419, June 1977.

[130] R. M. Shelby, C. B. Harris, and P. A. Cornelius. The origin of vibrational dephasing of polyatomic molecules in condensed phases. J. Chem. Phys., 70(1):34, July 1979.

[131] B. Persson and R. Ryberg. Brownian motion and vibrational phase relaxation at surfaces: CO on Ni(111). Phys. Rev. B, 32(6):3586–3596, September 1985.

[132] J. L. Skinner and D. Hsu. Pure dephasing of a two-level system. J. Phys. Chem., 90(21):4931–4938, October 1986.

[133] Michael Karavitis, Takayuki Kumada, Ilya U. Goldschleger, and V. Ara Apkarian. Vibrational dissipation and dephasing of I_2(v= 1-19) in solid Kr. Phys. Chem. Chem. Phys., 7(5):791, February 2005.

[134] Andreas C. Albrecht. On the Theory of Raman Intensities. J. Chem. Phys., 34(5):1476, August 1961.

[135] John R. Lombardi and Ronald L. Birke. A unified view of surface-enhanced raman scattering. Acc. Chem. Res., 42(6):734–742, 2009.

[136] Alberto Baiardi, Julien Bloino, and Vincenzo Barone. A general time-dependent route to Resonance-Raman spectroscopy including Franck-Condon, Herzberg-Teller and Duschinsky effects. J. Chem. Phys., 141(11):114108, September 2014.

[137] Mayukh Banik, Patrick Z El-Khoury, Amit Nag, Alejandro Rodriguez-Perez, Nekane Guarrotxena, Guillermo C Bazan, and Vartkess A Apkarian. Surface-enhanced Raman trajectories on a nano-dumbbell: transition from field to charge transfer plasmons as the spheres fuse. ACS nano, 6(11):10343–54, November 2012.

[138] Patrick Z. El-Khoury, Dehong Hu, and Wayne P. Hess. Junction plasmon-induced molecular reorientation. J. Phys. Chem. Lett., 4(20):3435–3439, 2013.

[139] M. Moskovits. Surface selection rules. J. Chem. Phys., 77(9):4408, November 1982.

[140] J.A. Creighton. Surface raman electromagnetic enhancement factors for molecules at the surface of small isolated metal spheres: The determination of adsorbate orientation from sers relative intensities. Surf. Sci., 124(1):209–219, January 1983.

[141] Peter Hildebrandt and Manfred Stockburger. Surface-enhanced resonance Raman spectroscopy of Rhodamine 6G adsorbed on colloidal silver. J. Phys. Chem., 88(24):5935–5944, November 1984.

[142] Alan Campion and Patanjali Kambhampati. Surface-enhanced Raman scattering. Chem. Soc. Rev., 27(4):241–250, 1998.

[143] Masatoshi Osawa, Naoki Matsuda, Katsumasa Yoshii, and Isamu Uchida. Charge transfer resonance raman process in surface-enhanced raman scattering from p-aminothiophenol adsorbed on silver: Herzberg-teller contribution. J. Phys. Chem., 98(48):12702–12707, 1994.

[144] Marc Chaigneau, Gennaro Picardi, and Razvigor Ossikovski. Molecular arrangement in self-assembled azobenzene-containing thiol monolayers at the individual domain level studied through polarized near-field Raman spectroscopy. Int. J. Mol. Sci., 12(2):1245–58, January 2011.

[145] Amy A. Moore, Michele L. Jacobson, Nadia Belabas, Kathy L. Rowlen, and David M. Jonas. 2d correlation analysis of the continuum in single molecule surface enhanced raman spectroscopy. J. Am. Chem. Soc., 127(20):7292–7293, 2005.

[146] Matthew. D. Sonntag, Dhabih Chulhai, Tamar Seideman, Lasse Jensen, and Richard P. Van Duyne. The origin of relative intensity fluctuations in single-molecule tip-enhanced raman spectroscopy. J. Am. Chem. Soc., 135(45):17187–17192, 2013.

[147] N V Surovtsev, V K Malinovsky, and E V Boldyreva. Raman study of low-frequency modes in three glycine polymorphs. J. Chem. Phys., 134(4):045102, January 2011.

[148] Yung Sam Kim and Robin M Hochstrasser. Applications of 2D IR spectroscopy to peptides, proteins, and hydrogen-bond dynamics. J. Phys. Chem. B, 113(24):8231–51, June 2009.

[149] Rossend Rey, Klaus B Mø ller, and James T Hynes. Ultrafast vibrational population dynamics of water and related systems: a theoretical perspective. Chem. Rev., 104(4):1915–28, April 2004.

[150] Kei Moritsugu, Osamu Miyashita, and Akinori Kidera. Temperature Dependence of Vibrational Energy Transfer in a Protein Molecule. J. Phys. Chem. B, 107(14):3309–3317, April 2003.

[151] Danijela Vojta and Goran Baranović. Intramolecular couplings and the secondary structure of CC stretching bands. Vib. Spectrosc, 52(2):178–187, March 2010.

[152] Qiuping Bian, S.K. Bose, and R.C. Shukla. Vibrational and thermodynamic properties of metals from a model embedded-atom potential. J. Phys. Chem. Solids, 69(1):168–181, January 2008.

[153] Valeriy M. Kasyanenko, Patrick Keiffer, and Igor V. Rubtsov. Intramolecular vibrational coupling contribution to temperature dependence of vibrational mode frequencies. J. Chem. Phys., 136(14), 2012.

[154] K. D. Rector and M. D. Fayer. Vibrational echoes: A new approach to condensed-matter vibrational spectroscopy. Int. Rev. Phys. Chem., 17(3):261–306, July 1998.

[155] Anneli Hoggard, Lin-Yung Wang, Lulu Ma, Ying Fang, Ge You, Jana Olson, Zheng Liu, Wei-Shun Chang, Pulickel M. Ajayan, and Stephan Link. Using the Plasmon Linewidth To Calculate the Time and Efficiency of Electron Transfer between Gold Nanorods and Graphene. ACS Nano, 7(12):11209–11217, December 2013.

[156] Jason K. Streit, Sergei M. Bachilo, Stephen R. Sanchez, Ching-Wei Lin, and R. Bruce Weisman. Variance Spectroscopy. J. Phys. Chem. Lett., 6(19):3976–3981, October 2015.

[157] T. Ha, T. Enderle, D. F. Ogletree, D. S. Chemla, P. R. Selvin, and S. Weiss. Probing the interaction between two single molecules: fluorescence resonance energy transfer between a single donor and a single acceptor. Proc. Natl. Acad. Sci., 93(13):6264–6268, June 1996.

[158] Samuel L Kleinman, Emilie Ringe, Nicholas Valley, Kristin L Wustholz, Eric Phillips, Karl A Scheidt, George C Schatz, and Richard P Van Duyne. Single-molecule surface-enhanced Raman spectroscopy of crystal violet isotopologues: theory and experiment. J. Am. Chem. Soc., 133(11):4115–22, March 2011.

[159] Jon A Dieringer, Robert B Lettan, Karl A Scheidt, and Richard P Van Duyne. A frequency domain existence proof of single-molecule surface-enhanced Raman spectroscopy. J. Am. Chem. Soc., 129(51):16249–56, December 2007.

[160] Matthew D. Sonntag, Jordan M. Klingsporn, Luis K. Garibay, John M. Roberts, Jon A. Dieringer, Tamar Seideman, Karl A. Scheidt, Lasse Jensen, George C. Schatz, and Richard P. Van Duyne. Single-Molecule Tip-Enhanced Raman Spectroscopy. J. Phys. Chem. C, 116(1):478–483, January 2012.

[161] Nicholas Tallarida, Laura Rios, Vartkess A Apkarian, and Joonhee Lee. Isomerization of One Molecule Observed through Tip-Enhanced Raman Spectroscopy. Nano lett., September 2015.

[162] Richard W Taylor, Felix Benz, Daniel O Sigle, Richard W Bowman, Peng Bao, Johannes S Roth, George R Heath, Stephen D Evans, and Jeremy J Baumberg. Watching individual molecules flex within lipid membranes using sers. Sci. Rep., 4:5940, 2014.

[163] Xiaoping Gao, John P Davies, and Michael J Weaver. Test of surface selection rules for surface-enhanced raman scattering: the orientation of adsorbed benzene and monosubstituted benzenes on gold. J. Phys. Chem., 94(17):6858–6864, 1990.

[164] Fatemeh Mirjani, Joseph M. Thijssen, and Mark A. Ratner. Probing Charge States in Molecular Junctions Using Raman Spectroscopy. J. Phys. Chem. C, 116(43):23120–23129, November 2012.

[165] William E Gifford. The gifford-mcmahon cycle. In Advances in Cryogenic Engineering, pages 152–159. Springer, 1966.

[166] Xiao-Xiao Zhang, Yumeng You, Shu Yang Frank Zhao, and Tony F Heinz. Experimental evidence for dark excitons in monolayer WSe_2. Phys. Rev. Lett., 115(25):257403, 2015.

[167] Chitraleema Chakraborty, Laura Kinnischtzke, Kenneth M Goodfellow, Ryan Beams, and A Nick Vamivakas. Voltage-controlled quantum light from an atomically thin semiconductor. Nat. Nanotech., 10(6):507–511, 2015.

[168] Yu-Ming He, Genevieve Clark, John R Schaibley, Yu He, Ming-Cheng Chen, Yu-Jia Wei, Xing Ding, Qiang Zhang, Wang Yao, Xiaodong Xu, Chao-Yang Lu, and Jian-Wei Pan. Single quantum emitters in monolayer semiconductors. Nat. Nanotech., 10(6):497–502, 2015.

[169] Carmen Palacios-Berraquero, Matteo Barbone, Dhiren M Kara, Xiaolong Chen, Ilya Goykhman, Duhee Yoon, Anna K Ott, Jan Beitner, Kenji Watanabe, Takashi Taniguchi, Andrea C Ferrari, and Mete Atature. Atomically thin quantum light-emitting diodes. Nat. Commun., 7, 2016.

[170] David J Nesbitt and Robert W Field. Vibrational energy flow in highly excited molecules: role of intramolecular vibrational redistribution. J. Phys. Chem., 100(31):12735–12756, 1996.

[171] Turgay Uzer and WH Miller. Theories of intramolecular vibrational energy transfer. Phys. Rep., 199(2):73–146, 1991.

[172] David M Leitner. Quantum ergodicity and energy flow in molecules. Adv. Phys., 64(4):445–517, 2015.

[173] Sander Woutersen and Huib J Bakker. Resonant intermolecular transfer of vibrational energy in liquid water. Nature, 402(6761):507–509, 1999.

[174] Fabian Dahms, Rene Costard, Erik TJ Nibbering, and Thomas Elsaesser. Ultrafast vibrational energy flow in water monomers in acetonitrile. Chem. Phys. Lett., 652:50–55, 2016.

[175] A Weigel and NP Ernsting. Excited stilbene: intramolecular vibrational redistribution and solvation studied by femtosecond stimulated raman spectroscopy. J. Phys. Chem. B, 114(23):7879–7893, 2010.

[176] C Ferrante, E Pontecorvo, G Cerullo, MH Vos, and T Scopigno. Direct observation of subpicosecond vibrational dynamics in photoexcited myoglobin. Nat. Chem., 2016.

[177] Vivek Tiwari, William K Peters, and David M Jonas. Electronic resonance with anticorrelated pigment vibrations drives photosynthetic energy transfer outside the adiabatic framework. Proc. Natl. Ac. Sci., 110(4):1203–1208, 2013.

[178] Trevor L Courtney, Zachary W Fox, Laura Estergreen, and Munira Khalil. Measuring coherently coupled intramolecular vibrational and charge-transfer dynamics with two-dimensional vibrational–electronic spectroscopy. J. Phys. Chem. Lett., 6(7):1286–1292, 2015.

[179] Wolfgang Freyer, Catalin C Neacsu, and Markus B Raschke. Absorption, luminescence, and raman spectroscopic properties of thin films of benzo-annelated metal-free porphyrazines. J. Luminescence, 128(4):661–672, 2008.

[180] Ralf Tonner, Phil Rosenow, and Peter Jakob. Molecular structure and vibrations of NTCDA monolayers on Ag (111) from density-functional theory and infrared absorption spectroscopy. Phys. Chem. Chem. Phys., 18(8):6316–6328, 2016.

[181] Sebastian Thussing and Peter Jakob. Structural and vibrational properties of CuPc/Ag (111) ultrathin films. J. Phys. Chem. C, 120(18):9904–9913, 2016.

[182] Rocco P Fornari, Juan Aragó, and Alessandro Troisi. Exciton dynamics in phthalocyanine molecular crystals. J. Phys. Chem. C, 120(15):7987–7996, 2016.

[183] Jakob G Woller, Jonas K Hannestad, and Bo Albinsson. Self-assembled nanoscale DNA–porphyrin complex for artificial light harvesting. J. Am. Chem. Soc., 135(7):2759–2768, 2013.

[184] Gita Sedghi, Víctor M García-Suárez, Louisa J Esdaile, Harry L Anderson, Colin J Lambert, Santiago Martín, Donald Bethell, Simon J Higgins, Martin Elliott, Neil Bennett, et al. Long-range electron tunnelling in oligo-porphyrin molecular wires. Nat. Nanotech., 6(8):517–523, 2011.

[185] Giovanni Bottari, Gema De La Torre, and Tomas Torres. Phthalocyanine-nanocarbon ensembles: from discrete molecular and supramolecular systems to hybrid nanomaterials. Acc. Chem. Res., 2015.

[186] KA Cochrane, A Schiffrin, TS Roussy, M Capsoni, and SA Burke. Pronounced polarization-induced energy level shifts at boundaries of organic semiconductor nanostructures. Nat. Commun., 6, 2015.

[187] Marc Smits, Avishek Ghosh, Jens Bredenbeck, Susumu Yamamoto, Michiel Müller, and Mischa Bonn. Ultrafast energy flow in model biological membranes. New J. Phys., 9(10):390, 2007.

[188] Nikolai Wintjes, Davide Bonifazi, Fuyong Cheng, Andreas Kiebele, Meike Stöhr, Thomas Jung, Hannes Spillmann, and François Diederich. A supramolecular multiposition rotary device. Angew. Chem., 119(22):4167–4170, 2007.

[189] XH Qiu, GV Nazin, and W Ho. Vibronic states in single molecule electron transport. Phys. Rev. Lett., 92(20):206102, 2004.

[190] H Yanagi, K Ikuta, H Mukai, and T Shibutani. STM-induced flip-flop switching of adsorbed subphthalocyanine molecular arrays. Nano Lett., 2(9):951–955, 2002.

[191] Su Ying Quek, Maria Kamenetska, Michael L Steigerwald, Hyoung Joon Choi, Steven G Louie, Mark S Hybertsen, JB Neaton, and Latha Venkataraman. Mechanically controlled binary conductance switching of a single-molecule junction. Nat. Nanotech., 4(4):230–234, 2009.

[192] Xiaoyin Xiao, Bingqian Xu, and Nongjian Tao. Changes in the conductance of single peptide molecules upon metal-ion binding. Angew. Chem., 43(45):6148–6152, 2004.

[193] NJ Tao. Electron transport in molecular junctions. Nat. Nanotech., 1(3):173–181, 2006.

[194] Brian Capozzi, Jianlong Xia, Olgun Adak, Emma J Dell, Zhen-Fei Liu, Jeffrey C Taylor, Jeffrey B Neaton, Luis M Campos, and Latha Venkataraman. Single-molecule diodes with high rectification ratios through environmental control. Nat. Nanotech., 10(6):522–527, 2015.

[195] Youngsang Kim, Hyunwook Song, Florian Strigl, Hans-Fridtjof Pernau, Takhee Lee, and Elke Scheer. Conductance and vibrational states of single-molecule junctions controlled by mechanical stretching and material variation. Phys. Rev. Lett., 106(19):196804, 2011.

[196] Takahito Ohshiro, Makusu Tsutsui, Kazumichi Yokota, Masayuki Furuhashi, Masateru Taniguchi, and Tomoji Kawai. Detection of post-translational modifications in single peptides using electron tunnelling currents. Nat. Nanotech., 9(10):835–840, 2014.

[197] Mickael L Perrin, Christopher JO Verzijl, Christian A Martin, Ahson J Shaikh, Rienk Eelkema, Jan H Van Esch, Jan M Van Ruitenbeek, Joseph M Thijssen, Herre SJ Van Der Zant, and Diana Dulić. Large tunable image-charge effects in single-molecule junctions. Nat. Nanotech., 8(4):282–287, 2013.

[198] Timothy A Su, Haixing Li, Michael L Steigerwald, Latha Venkataraman, and Colin Nuckolls. Stereoelectronic switching in single-molecule junctions. Nat. Chem., 7(3):215–220, 2015.

[199] Youngsang Kim, Aran Garcia-Lekue, Dmytro Sysoiev, Thomas Frederiksen, Ulrich Groth, and Elke Scheer. Charge transport in azobenzene-based single-molecule junctions. Phys. Rev. Lett., 109(22):226801, 2012.

[200] Latha Venkataraman, Jennifer E Klare, Colin Nuckolls, Mark S Hybertsen, and Michael L Steigerwald. Dependence of single-molecule junction conductance on molecular conformation. Nature, 442(7105):904–907, 2006.

[201] Zheng Liu, Song-Yuan Ding, Zhao-Bin Chen, Xiang Wang, Jing-Hua Tian, Jason R Anema, Xiao-Shun Zhou, De-Yin Wu, Bing-Wei Mao, Xin Xu, Bin Ren, and Zhong-Qun Tian. Revealing the molecular structure of single-molecule junctions in different conductance states by fishing-mode tip-enhanced raman spectroscopy. Nature communications, 2:305, 2011.

[202] Robert PJ Nieuwenhuizen, Keith A Lidke, Mark Bates, Daniela Leyton Puig, David Grünwald, Sjoerd Stallinga, and Bernd Rieger. Measuring image resolution in optical nanoscopy. Nat. Methods, 10(6):557–562, 2013.

[203] Seamus J Holden, Stephan Uphoff, and Achillefs N Kapanidis. Daostorm: An algorithm for high-density super-resolution microscopy. Nat. Methods, 8:279–280, 2011.

[204] Bonnie O Leung and Keng C Chou. Review of super-resolution fluorescence microscopy for biology. Appl. Spectrosc., 65(9):967–980, 2011.

[205] Markus B Raschke and Christoph Lienau. Apertureless near-field optical microscopy: Tip–sample coupling in elastic light scattering. Appl. Phys. Lett., 83(24):5089–5091, 2003.

[206] Vasily Kravtsov, Ronald Ulbricht, Joanna M Atkin, and Markus B Raschke. Plasmonic nanofocused four-wave mixing for femtosecond near-field imaging. Nat. Nanotech., 11(5):459–464, 2016.

[207] Celine Heu, Alexandre Berquand, Celine Elie-Caille, and Laurence Nicod. Glyphosate-induced stiffening of hacat keratinocytes, a peak force tapping study on living cells. J. Struct. Biol., 178(1):1–7, 2012.

[208] Lukas Novotny and Niek van Hulst. Antennas for light. Nat. Photon., 5(2):83–90, 2011.

[209] Xin Ting Zheng and Chang Ming Li. Single cell analysis at the nanoscale. Chem. Soc. Rev., 41(6):2061–2071, 2012.

[210] Marjolein Koopman, Alessandra Cambi, Bärbel I de Bakker, Ben Joosten, Carl G Figdor, Niek F van Hulst, and Maria F Garcia-Parajo. Near-field scanning optical microscopy in liquid for high resolution single molecule detection on dendritic cells. FEBS Lett., 573(1):6–10, 2004.

[211] Christiane Höppener and Lukas Novotny. Antenna-based optical imaging of single ca^{2+} transmembrane proteins in liquids. Nano Lett., 8(2):642–646, 2008.

[212] Thomas S van Zanten, Maria J Lopez-Bosque, and Maria F Garcia-Parajo. Imaging individual proteins and nanodomains on intact cell membranes with a probe-based optical antenna. Small, 6(2):270–275, 2010.

[213] Thomas Schmid, Boon-Siang Yeo, Grace Leong, Johannes Stadler, and Renato Zenobi. Performing tip-enhanced raman spectroscopy in liquids. J. Raman Spectrosc., 40(10):1392–1399, 2009.

[214] Zhi-Cong Zeng, Sheng-Chao Huang, De-Yin Wu, Ling-Yan Meng, Mao-Hua Li, Teng-Xiang Huang, Jin-Hui Zhong, Xiang Wang, Zhi-Lin Yang, and Bin Ren. Electrochemical tip-enhanced raman spectroscopy. J. Am. Chem. Soc., 137(37):11928–11931, 2015.

[215] Kyoung-Duck Park, Doo Jae Park, Seung Gol Lee, Geunchang Choi, Dai-Sik Kim, Clare Chisu Byeon, Soo Bong Choi, and Mun Seok Jeong. Operation of a wet near-field scanning optical microscope in stable zones by minimizing the resonance change of tuning forks. Nanotechnology, 25(7):075704, 2014.

[216] Jérôme Morville, Jinquan Liu, Andrea Callegari, and Majed Chergui. Q-factor optimization of a tuning-fork/fiber sensor for shear-force detection. Appl. Phys. Lett., 86(6):064103, 2005.

[217] Daniel J Inman and Ramesh Chandra Singh. Engineering Vibration, volume 3. Prentice Hall Upper Saddle River, 2001.

[218] Kyoung-Duck Park, Seung Gol Lee, and Mun Seok Jeong. Epidermal growth factor receptor imaging of a431 cancer cells using gold nanorods. J. Nanosci. Nanotechnol., 11(8):7053–7056, 2011.

[219] M Arif Hayat. Colloidal Gold: Principles, Methods, and Applications. Elsevier, 2012.

[220] Nastassja Lewinski, Vicki Colvin, and Rebekah Drezek. Cytotoxicity of nanoparticles. Small, 4(1):26–49, 2008.

[221] C Höppener, JP Siebrasse, R Peters, U Kubitscheck, and A Naber. High-resolution near-field optical imaging of single nuclear pore complexes under physiological conditions. Biophys. J., 88(5):3681–3688, 2005.

[222] Fawaz G Haj, Peter J Verveer, Anthony Squire, Benjamin G Neel, and Philippe IH Bastiaens. Imaging sites of receptor dephosphorylation by ptp1b on the surface of the endoplasmic reticulum. Science, 295(5560):1708–1711, 2002.

[223] Frederick R Maxfield and Daniel Wüstner. Intracellular cholesterol transport. J. Clin. Invest., 110(110 (7)):891–898, 2002.

[224] Birka Hein, Katrin I Willig, and Stefan W Hell. Stimulated emission depletion (STED) nanoscopy of a fluorescent protein-labeled organelle inside a living cell. Proc. Natl. Acad. Sci. USA, 105(38):14271–14276, 2008.

[225] WHJ Rensen, NF van Hulst, and SB Kämmer. Imaging soft samples in liquid with tuning fork based shear force microscopy. Appl. Phys. Lett., 77(10):1557–1559, 2000.

[226] Lynn F Lee, Richard D Schaller, Louis H Haber, and Richard J Saykally. High spatial resolution imaging with near-field scanning optical microscopy in liquids. Anal. Chem., 73(21):5015–5019, 2001.

[227] Doo Jae Park, Kyoung-Duck Park, Geun Chang Choi, Seung Gol Lee, Clare Chisu Byeon, Mun Seok Jeong, and Soo Bong Choi. A resonance tracking method for stable operation of a near-field scanning optical microscope in liquid environment. Curr. Appl. Phys., 14:S12–S16, 2014.

[228] M Koopman, BI De Bakker, MF Garcia-Parajo, and NF van Hulst. Shear force imaging of soft samples in liquid using a diving bell concept. Appl. Phys. Lett., 83(24):5083–5085, 2003.

[229] Carlo Manzo, Thomas S van Zanten, and Maria F Garcia-Parajo. Nanoscale fluorescence correlation spectroscopy on intact living cell membranes with nsom probes. Biophys. J., 100(2):L8–L10, 2011.

[230] Wei Bao, M Melli, N Caselli, F Riboli, DS Wiersma, M Staffaroni, H Choo, DF Ogletree, S Aloni, J Bokor, S Cabrini, F Intonti, M B Salmeron, E Yablonovitch, and P J Schuck. Mapping local charge recombination heterogeneity by multidimensional nanospectroscopic imaging. Science, 338(6112):1317–1321, 2012.

[231] Anatoli Ianoul, Donna D Grant, Yanouchka Rouleau, Mahmud Bani-Yaghoub, Linda J Johnston, and John Paul Pezacki. Imaging nanometer domains of β-adrenergic receptor complexes on the surface of cardiac myocytes. Nat. Chem. Biol., 1(4):196–202, 2005.

[232] Kelly-Ann D Walker, Claire Morgan, Shareen H Doak, and Peter R Dunstan. Quantum dots for multiplexed detection and characterisation of prostate cancer cells using a scanning near-field optical microscope. PloS One, 7(2):e31592, 2012.

[233] Abedelnasser Abulrob, Zhengfang Lu, Ewa Baumann, Dusan Vobornik, Rod Taylor, Danica Stanimirovic, and Linda J Johnston. Nanoscale imaging of epidermal growth factor receptor clustering effects of inhibitors. J. Biol. Chem., 285(5):3145–3156, 2010.

[234] Daniel C Gaffney, H Peter Soyer, and Fiona Simpson. The epidermal growth factor receptor in squamous cell carcinoma: An emerging drug target. Australas. J. Dermatol., 55(1):24–34, 2014.

[235] Emilia Galperin, Vladislav V Verkhusha, and Alexander Sorkin. Three-chromophore fret microscopy to analyze multiprotein interactions in living cells. Nat. Methods, 1(3):209–217, 2004.

[236] Bruce T Blakely, Fabio MV Rossi, Bonnie Tillotson, Michelle Palmer, Angeles Estelles, and Helen M Blau. Epidermal growth factor receptor dimerization monitored in live cells. Nat. Biotechnol., 18(2):218–222, 2000.

[237] Kyoung-Duck Park, Yong Hwan Kim, Jin-Ho Park, Jung Su Park, Hong Seok Lee, Sang-Youp Yim, Young Hee Lee, and Mun Seok Jeong. Ultraviolet tip-enhanced nanoscale raman imaging. J. Raman Spectrosc., 43(12):1931–1934, 2012.

[238] Noeul Park, Kyoung-Duck Park, Youngjoo Chung, and Mun Seok Jeong. Scanning absorption nanoscopy with supercontinuum light sources based on photonic crystal fiber. Rev. Sci. Instrum., 82(12):123102, 2011.

[239] Cecil Allen Parker. Photoluminescence of solutions. Elsevier Publishing Company, 1968.

[240] Sokrates T Pantelides. The electronic structure of impurities and other point defects in semiconductors. Rev. Mod. Phys., 50(4):797, 1978.

[241] Karl Leo, M Wegener, Jagdeep Shah, DS Chemla, EO Göbel, TC Damen, S Schmitt-Rink, and W Schäfer. Effects of coherent polarization interactions on time-resolved degenerate four-wave mixing. Phys. Rev. Lett., 65(11):1340, 1990.

[242] Fausto Rossi and Tilmann Kuhn. Theory of ultrafast phenomena in photoexcited semiconductors. Rev. Mod. Phys., 74(3):895, 2002.

[243] U Bockelmann. Exciton relaxation and radiative recombination in semiconductor quantum dots. Phys. Rev. B, 48(23):17637, 1993.

[244] J Frenkel. On the solid body model of heavy nuclei. Phys. Z. Soviet Union, 9:158, 1936.

[245] Gregory H Wannier. The structure of electronic excitation levels in insulating crystals. Phys. Rev., 52(3):191, 1937.

[246] NF Mott. Note on the contact between a metal and an insulator or semi-conductor. In Mathematical Proceedings of the Cambridge Philosophical Society, volume 34, pages 568–572. Cambridge University Press, 1938.

[247] N Baer, C Gies, J Wiersig, and F Jahnke. Luminescence of a semiconductor quantum dot system. Eur. Phys. J. B, 50(3):411–418, 2006.

[248] Andrew M Smith and Shuming Nie. Chemical analysis and cellular imaging with quantum dots. Analyst, 129(8):672–677, 2004.

[249] Alexander L Efros and David J Nesbitt. Origin and control of blinking in quantum dots. Nat. Nanotech., 11(8):661–671, 2016.

[250] Tomasz J Antosiewicz, S Peter Apell, and Timur Shegai. Plasmon–exciton interactions in a core–shell geometry: from enhanced absorption to strong coupling. Acs Photon., 1(5):454–463, 2014.

[251] Rohit Chikkaraddy, Bart de Nijs, Felix Benz, Steven J Barrow, Oren A Scherman, Edina Rosta, Angela Demetriadou, Peter Fox, Ortwin Hess, and Jeremy J Baumberg. Single-molecule strong coupling at room temperature in plasmonic nanocavities. Nature, 535(7610):127–130, 2016.

[252] Gülis Zengin, Martin Wersäll, Sara Nilsson, Tomasz J Antosiewicz, Mikael Käll, and Timur Shegai. Realizing strong light-matter interactions between single-nanoparticle plasmons and molecular excitons at ambient conditions. Phys. Rev. Lett., 114(15):157401, 2015.

[253] Kyoung-Duck Park, Markus B Raschke, Joanna M Atkin, Young Hee Lee, and Mun Seok Jeong. Probing bilayer grain boundaries in large-area graphene with tip-enhanced Raman spectroscopy. Adv. Mater., 29(7), 2017.

[254] Wei Yan, Wen-Yu He, Zhao-Dong Chu, Mengxi Liu, Lan Meng, Rui-Fen Dou, Yanfeng Zhang, Zhongfan Liu, Jia-Cai Nie, and Lin He. Strain and curvature induced evolution of electronic band structures in twisted graphene bilayer. Nat. Commun., 4:2159, 2013.

[255] Justin C Koepke, Joshua D Wood, David Estrada, Zhun-Yong Ong, Kevin T He, Eric Pop, and Joseph W Lyding. Atomic-scale evidence for potential barriers and strong carrier scattering at graphene grain boundaries: a scanning tunneling microscopy study. ACS Nano, 7(1):75–86, 2013.

[256] Pinshane Y Huang, Carlos S Ruiz-Vargas, Arend M van der Zande, William S Whitney, Mark P Levendorf, Joshua W Kevek, Shivank Garg, Jonathan S Alden, Caleb J Hustedt, Ye Zhu, Jiwoong Park, Paul L. McEuen, and David A. Muller. Grains and grain boundaries in single-layer graphene atomic patchwork quilts. Nature, 469(7330):389–392, 2011.

[257] Iskandar N Kholmanov, Carl W Magnuson, Ali E Aliev, Huifeng Li, Bin Zhang, Ji Won Suk, Li Li Zhang, Eric Peng, S Hossein Mousavi, Alexander B Khanikaev, Richard Piner, Gennady Shvets, and Rodney S. Ruoff. Improved electrical conductivity of graphene films integrated with metal nanowires. Nano Lett., 12(11):5679–5683, 2012.

[258] Gang Hee Han, Fethullah Gunes, Jung Jun Bae, Eun Sung Kim, Seung Jin Chae, Hyeon-Jin Shin, Jae-Young Choi, Didier Pribat, and Young Hee Lee. Influence of copper morphology in forming nucleation seeds for graphene growth. Nano Lett., 11(10):4144–4148, 2011.

[259] Peijie Wang, Duan Zhang, Lilin Li, Zhipeng Li, Lisheng Zhang, and Yan Fang. Reversible defect in graphene investigated by tip-enhanced Raman spectroscopy. Plasmonics, 7(3):555–561, 2012.

[260] Johannes Stadler, Thomas Schmid, and Renato Zenobi. Nanoscale chemical imaging of single-layer graphene. ACS Nano, 5(10):8442–8448, 2011.

[261] LM Malard, MA Pimenta, G Dresselhaus, and MS Dresselhaus. Raman spectroscopy in graphene. Phys. Rep., 473(5):51–87, 2009.

[262] Wenjuan Zhu, Tony Low, Vasili Perebeinos, Ageeth A Bol, Yu Zhu, Hugen Yan, Jerry Tersoff, and Phaedon Avouris. Structure and electronic transport in graphene wrinkles. Nano Lett., 12(7):3431–3436, 2012.

[263] Kiran M Subhedar, Indu Sharma, and Sanjay R Dhakate. Control of layer stacking in CVD graphene under quasi-static condition. Phys. Chem. Chem. Phys., 17(34):22304–22310, 2015.

[264] Sinisa Coh, Liang Z Tan, Steven G Louie, and Marvin L Cohen. Theory of the Raman spectrum of rotated double-layer graphene. Phys. Rev. B, 88(16):165431, 2013.

[265] Kwanpyo Kim, Sinisa Coh, Liang Z Tan, William Regan, Jong Min Yuk, Eric Chatterjee, MF Crommie, Marvin L Cohen, Steven G Louie, and A Zettl. Raman spectroscopy study of rotated double-layer graphene: misorientation-angle dependence of electronic structure. Phys. Rev. Lett., 108(24):246103, 2012.

[266] Yuming Chen, Lijuan Meng, Weiwei Zhao, Zheng Liang, Xing Wu, Haiyan Nan, Zhangting Wu, Shan Huang, Litao Sun, Jinlan Wang, and Zhenhua Ni. Raman mapping investigation of chemical vapor deposition-fabricated twisted bilayer graphene with irregular grains. Phys. Chem. Chem. Phys., 16(39):21682–21687, 2014.

[267] Robin W Havener, Houlong Zhuang, Lola Brown, Richard G Hennig, and Jiwoong Park. Angle-resolved Raman imaging of interlayer rotations and interactions in twisted bilayer graphene. Nano Lett., 12(6):3162–3167, 2012.

[268] Leonidas Tsetseris and Sokrates T Pantelides. Hydrogen uptake by graphene and nucleation of graphane. J. Mater. Sci., 47(21):7571–7579, 2012.

[269] Maria Losurdo, Maria Michela Giangregorio, Pio Capezzuto, and Giovanni Bruno. Graphene CVD growth on copper and nickel: role of hydrogen in kinetics and structure. Phys. Chem. Chem. Phys., 13(46):20836–20843, 2011.

[270] Ke Xu, Peigen Cao, and James R Heath. Scanning tunneling microscopy characterization of the electrical properties of wrinkles in exfoliated graphene monolayers. Nano Lett., 9(12):4446–4451, 2009.

[271] AC Ferrari, JC Meyer, V Scardaci, C Casiraghi, Michele Lazzeri, Francesco Mauri, S Piscanec, Da Jiang, KS Novoselov, S Roth, and AK Geim. Raman spectrum of graphene and graphene layers. Phys. Rev. Lett., 97(18):187401, 2006.

[272] Chenfang Lin, Yexin Feng, Yingdong Xiao, Michael Durr, Xiangqian Huang, Xiaozhi Xu, Ruguang Zhao, Enge Wang, Xin-Zheng Li, and Zonghai Hu. Direct observation of ordered configurations of hydrogen adatoms on graphene. Nano Lett., 15(2):903–908, 2015.

[273] Axel Eckmann, Alexandre Felten, Artem Mishchenko, Liam Britnell, Ralph Krupke, Kostya S Novoselov, and Cinzia Casiraghi. Probing the nature of defects in graphene by Raman spectroscopy. Nano Lett., 12(8):3925–3930, 2012.

[274] Kibum Kang, Saien Xie, Lujie Huang, Yimo Han, Pinshane Y Huang, Kin Fai Mak, Cheol-Joo Kim, David Muller, and Jiwoong Park. High-mobility three-atom-thick semiconducting films with wafer-scale homogeneity. Nature, 520(7549):656–660, 2015.

[275] Xu Cui, Gwan-Hyoung Lee, Young Duck Kim, Ghidewon Arefe, Pinshane Y Huang, Chul-Ho Lee, Daniel A Chenet, Xian Zhang, Lei Wang, Fan Ye, Filippo Pizzocchero, Bjarke S. Jessen, Kenji Watanabe, Takashi Taniguchi, David A. Muller, Tony Low, Philip Kim, and James Hone. Multi-terminal transport measurements of MoS_2 using a van der Waals heterostructure device platform. Nat. Nanotech., 10:534–540, 2015.

[276] Galan Moody, Chandriker Kavir Dass, Kai Hao, Chang-Hsiao Chen, Lain-Jong Li, Akshay Singh, Kha Tran, Genevieve Clark, Xiaodong Xu, Gunnar Berghäuser, Ermin Malic, Andreas Knorr, and Xiaoqin Li. Intrinsic homogeneous linewidth and broadening mechanisms of excitons in monolayer transition metal dichalcogenides. Nat. Commun., 6:8315, 2015.

[277] Xiaofeng Qian, Junwei Liu, Liang Fu, and Ju Li. Quantum spin hall effect in two-dimensional transition metal dichalcogenides. Science, 346(6215):1344–1347, 2014.

[278] FHL Koppens, T Mueller, Ph Avouris, AC Ferrari, MS Vitiello, and M Polini. Photodetectors based on graphene, other two-dimensional materials and hybrid systems. Nat. Nanotech., 9(10):780–793, 2014.

[279] Qing Hua Wang, Kourosh Kalantar-Zadeh, Andras Kis, Jonathan N Coleman, and Michael S Strano. Electronics and optoelectronics of two-dimensional transition metal dichalcogenides. Nat. Nanotech., 7(11):699–712, 2012.

[280] Agnieszka Kuc, Nourdine Zibouche, and Thomas Heine. Influence of quantum confinement on the electronic structure of the transition metal sulfide TS_2. Phys. Rev. B, 83(24):245213, 2011.

[281] Aaron M Jones, Hongyi Yu, Nirmal J Ghimire, Sanfeng Wu, Grant Aivazian, Jason S Ross, Bo Zhao, Jiaqiang Yan, David G Mandrus, Di Xiao, Wang Yao, and Xiaodong Xu. Optical generation of excitonic valley coherence in monolayer WSe_2. Nat. Nanotech., 8(9):634–638, 2013.

[282] Xiaodong Xu, Wang Yao, Di Xiao, and Tony F Heinz. Spin and pseudospins in layered transition metal dichalcogenides. Nat. Phys., 10(5):343–350, 2014.

[283] Jingxin Cheng, Tao Jiang, Qingqing Ji, Yu Zhang, Zhiming Li, Yuwei Shan, Yanfeng Zhang, Xingao Gong, Weitao Liu, and Shiwei Wu. Kinetic nature of grain boundary formation in as-grown MoS_2 monolayers. Adv. Mater., 27(27):4069–4074, 2015.

[284] Sina Najmaei, Zheng Liu, Wu Zhou, Xiaolong Zou, Gang Shi, Sidong Lei, Boris I Yakobson, Juan-Carlos Idrobo, Pulickel M Ajayan, and Jun Lou. Vapour phase growth and grain boundary structure of molybdenum disulphide atomic layers. Nat. Mater., 12(8):754–759, 2013.

[285] Yu Li Huang, Yifeng Chen, Wenjing Zhang, Su Ying Quek, Chang-Hsiao Chen, Lain-Jong Li, Wei-Ting Hsu, Wen-Hao Chang, Yu Jie Zheng, Wei Chen, and Andrew T. S. Wee. Bandgap tunability at single-layer molybdenum disulphide grain boundaries. Nat. Commun., 6:6298, 2015.

[286] Seki Park, Min Su Kim, Hyun Kim, Jubok Lee, Gang Hee Han, Jeil Jung, and Jeongyong Kim. Spectroscopic visualization of grain boundaries of monolayer molybdenum disulfide by stacking bilayers. ACS Nano, 9(11):11042–11048, 2015.

[287] Wei Bao, Nicholas J Borys, Changhyun Ko, Joonki Suh, Wen Fan, Andrew Thron, Yingjie Zhang, Alexander Buyanin, Jie Zhang, Stefano Cabrini, Paul D. Ashby, Alexander Weber-Bargioni, Sefaattin Tongay, Shaul Aloni, D. Frank Ogletree, Junqiao Wu, Miquel B. Salmeron, and P. James Schuck. Visualizing nanoscale excitonic relaxation properties of disordered edges and grain boundaries in monolayer molybdenum disulfide. Nat. Commun., 6:8993, 2015.

[288] Yongjun Lee, Seki Park, Hyun Kim, Gang Hee Han, Young Hee Lee, and Jeongyong Kim. Characterization of the structural defects in CVD-grown monolayered MoS_2 using near-field photoluminescence imaging. Nanoscale, 7(28):11909–11914, 2015.

[289] Genevieve Clark, Sanfeng Wu, Pasqual Rivera, Joseph Finney, Paul Nguyen, David H Cobden, and Xiaodong Xu. Vapor-transport growth of high optical quality WSe_2 monolayers. APL Mater., 2(10):101101, 2014.

[290] Shao-Yu Chen, Changxi Zheng, Michael S Fuhrer, and Jun Yan. Helicity-resolved Raman scattering of MoS_2, $MoSe_2$, WS_2, and WSe_2 atomic layers. Nano Lett., 15(4):2526–2532, 2015.

[291] Weijie Zhao, Zohreh Ghorannevis, Kiran Kumar Amara, Jing Ren Pang, Minglin Toh, Xin Zhang, Christian Kloc, Ping Heng Tan, and Goki Eda. Lattice dynamics in mono-and few-layer sheets of WS_2 and WSe_2. Nanoscale, 5(20):9677–9683, 2013.

[292] Yumeng You, Xiao-Xiao Zhang, Timothy C Berkelbach, Mark S Hybertsen, David R Reichman, and Tony F Heinz. Observation of biexcitons in monolayer WSe_2. Nat. Phys., 11:477–481, 2015.

[293] Jingzhi Shang, Xiaonan Shen, Chunxiao Cong, Namphung Peimyoo, Bingchen Cao, Mustafa Eginligil, and Ting Yu. Observation of excitonic fine structure in a 2D transition-metal dichalcogenide semiconductor. ACS Nano, 9(1):647–655, 2015.

[294] Min Su Kim, Seok Joon Yun, Yongjun Lee, Changwon Seo, Gang Hee Han, Ki Kang Kim, Young Hee Lee, and Jeongyong Kim. Biexciton emission from edges and grain boundaries of triangular ws2 monolayers. ACS Nano, 10(2):2399–2405, 2016.

[295] Sujay B Desai, Gyungseon Seol, Jeong Seuk Kang, Hui Fang, Corsin Battaglia, Rehan Kapadia, Joel W Ager, Jing Guo, and Ali Javey. Strain-induced indirect to direct bandgap transition in multilayer WSe_2. Nano Lett., 14(8):4592–4597, 2014.

[296] Frédéric Laquai, Young-Seo Park, Jang-Joo Kim, and Thomas Basché. Excitation energy transfer in organic materials: From fundamentals to optoelectronic devices. Macromol. Rapid Commun., 30(14):1203–1231, 2009.

[297] CR Kagan, CB Murray, M Nirmal, and MG Bawendi. Electronic energy transfer in CdSe quantum dot solids. Phys. Rev. Lett., 76(9):1517, 1996.

[298] Bilu Liu, Mohammad Fathi, Liang Chen, Ahmad Abbas, Yuqiang Ma, and Chongwu Zhou. Chemical vapor deposition growth of monolayer WSe_2 with tunable device characteristics and growth mechanism study. ACS Nano, 9:6119–6127, 2015.

[299] Chunxiao Cong, Jingzhi Shang, Xing Wu, Bingchen Cao, Namphung Peimyoo, Caiyu Qiu, Litao Sun, and Ting Yu. Synthesis and optical properties of large-area single-crystalline 2D semiconductor WS_2 monolayer from chemical vapor deposition. Adv. Opt. Mater., 2(2):131–136, 2014.

[300] Keliang He, Charles Poole, Kin Fai Mak, and Jie Shan. Experimental demonstration of continuous electronic structure tuning via strain in atomically thin MoS_2. Nano Lett., 13(6):2931–2936, 2013.

[301] Hiram J Conley, Bin Wang, Jed I Ziegler, Richard F Haglund Jr, Sokrates T Pantelides, and Kirill I Bolotin. Bandgap engineering of strained monolayer and bilayer MoS_2. Nano Lett., 13(8):3626–3630, 2013.

[302] Andres Castellanos-Gomez, Rafael Roldán, Emmanuele Cappelluti, Michele Buscema, Francisco Guinea, Herre SJ van der Zant, and Gary A Steele. Local strain engineering in atomically thin MoS_2. Nano Lett., 13(11):5361–5366, 2013.

[303] Kyoung-Duck Park, Tao Jiang, Genevieve Clark, Xiaodong Xu, and Markus B Raschke. Radiative control of dark excitons at room temperature by nano-optical antenna-tip induced Purcell effect. preprint arXiv:1706.09085, Nat. Nanotech., 2017.

[304] Keliang He, Nardeep Kumar, Liang Zhao, Zefang Wang, Kin Fai Mak, Hui Zhao, and Jie Shan. Tightly bound excitons in monolayer WSe_2. Phys. Rev. Lett., 113(2):026803, 2014.

[305] Kin Fai Mak and Jie Shan. Photonics and optoelectronics of 2D semiconductor transition metal dichalcogenides. Nat. Photon., 10(4):216–226, 2016.

[306] DN Basov, MM Fogler, and FJ García de Abajo. Polaritons in van der Waals materials. Science, 354(6309):aag1992, 2016.

[307] Qingjun Tong, Hongyi Yu, Qizhong Zhu, Yong Wang, Xiaodong Xu, and Wang Yao. Topological mosaics in moire superlattices of van der Waals heterobilayers. Nat. Phys., 13:356–362, 2017.

[308] Kai Hao, Galan Moody, Fengcheng Wu, Chandriker Kavir Dass, Lixiang Xu, Chang-Hsiao Chen, Liuyang Sun, Ming-Yang Li, Lain-Jong Li, Allan H MacDonald, and Xiaoqin Li. Direct measurement of exciton valley coherence in monolayer WSe_2. Nat. Phys., page Online Publication, 2016.

[309] Gui-Bin Liu, Wen-Yu Shan, Yugui Yao, Wang Yao, and Di Xiao. Three-band tight-binding model for monolayers of group-vib transition metal dichalcogenides. Phys. Rev. B, 88(8):085433, 2013.

[310] K Kośmider, Jhon W González, and Joaquín Fernández-Rossier. Large spin splitting in the conduction band of transition metal dichalcogenide monolayers. Phys. Rev. B, 88(24):245436, 2013.

[311] JP Echeverry, B Urbaszek, T Amand, X Marie, and IC Gerber. Splitting between bright and dark excitons in transition metal dichalcogenide monolayers. Phys. Rev. B, 93(12):121107, 2016.

[312] Ashish Arora, Maciej Koperski, Karol Nogajewski, Jacques Marcus, Clément Faugeras, and Marek Potemski. Excitonic resonances in thin films of WSe_2: from monolayer to bulk material. Nanoscale, 7(23):10421–10429, 2015.

[313] Maciej Koperski, Maciej R Molas, Ashish Arora, Karol Nogajewski, Artur O Slobodeniuk, Clement Faugeras, and Marek Potemski. Optical properties of atomically thin transition metal dichalcogenides: Observations and puzzles. Nanophotonics, pages https://doi.org/10.1515/nanoph–2016–0165, 2017.

[314] AO Slobodeniuk and DM Basko. Spin–flip processes and radiative decay of dark intravalley excitons in transition metal dichalcogenide monolayers. 2D Mater., 3(3):035009, 2016.

[315] MR Molas, Clement Faugeras, AO Slobodeniuk, Karol Nogajewski, Miroslav Bartos, DM Basko, and Marek Potemski. Brightening of dark excitons in monolayers of semiconducting transition metal dichalcogenides. 2D Mater., 4(2):021003, 2017.

[316] G Wang, C Robert, MM Glazov, F Cadiz, E Courtade, T Amand, D Lagarde, T Taniguchi, K Watanabe, B Urbaszek, and X Marie. In-plane propagation of light in transition metal dichalcogenide monolayers: Optical selection rules. Phys. Rev. Lett., 119(7):047401, 2017.

[317] Tomasz Smoleński, T Kazimierczuk, M Goryca, Piotr Wojnar, and Piotr Kossacki. Mechanism and dynamics of biexciton formation from a long-lived dark exciton in a CdTe quantum dot. Phys. Rev. B, 91(15):155430, 2015.

[318] E Poem, Y Kodriano, C Tradonsky, NH Lindner, BD Gerardot, PM Petroff, and D Gershoni. Accessing the dark exciton with light. Nat. Phys., 6(12):993–997, 2010.

[319] Monique Combescot, Odile Betbeder-Matibet, and Roland Combescot. Bose-Einstein condensation in semiconductors: The key role of dark excitons. Phys. Rev. Lett., 99(17):176403, 2007.

[320] Manoj Nirmal, David J Norris, Masaru Kuno, Moungi G Bawendi, Al L Efros, and M Rosen. Observation of the 'dark exciton' in CdSe quantum dots. Phys. Rev. Lett., 75(20):3728, 1995.

[321] Tomasz Smoleński, Tomasz Kazimierczuk, Mateusz Goryca, Tomasz Jakubczyk, P Wojnar, A Golnik, and P Kossacki. In-plane radiative recombination channel of a dark exciton in self-assembled quantum dots. Phys. Rev. B, 86(24):241305, 2012.

[322] B Lee, J Park, GH Han, HS Ee, CH Naylor, W Liu, AT Johnson, and R Agarwal. Fano resonance and spectrally modified photoluminescence enhancement in monolayer MoS_2 integrated with plasmonic nanoantenna array. Nano Lett., 15(5):3646–3653, 2015.

[323] Zhuo Wang, Zhaogang Dong, Yinghong Gu, Yung-Huang Chang, Lei Zhang, Lain-Jong Li, Weijie Zhao, Goki Eda, Wenjing Zhang, Gustavo Grinblat, Stefan A Maier, Joel K W Yang, Cheng-Wei Qiu, and Andrew T S Wee. Giant photoluminescence enhancement in tungsten-diselenide–gold plasmonic hybrid structures. Nat. Commun., 7:11283, 2016.

[324] Sergei Kühn, Ulf Håkanson, Lavinia Rogobete, and Vahid Sandoghdar. Enhancement of single-molecule fluorescence using a gold nanoparticle as an optical nanoantenna. Phys. Rev. Lett., 97(1):017402, 2006.

[325] Yu A Bychkov and Emmanuel I Rashba. Oscillatory effects and the magnetic susceptibility of carriers in inversion layers. J. Phys. C Solid State Phys., 17(33):6039, 1984.

[326] Héctor Ochoa and Rafael Roldán. Spin-orbit-mediated spin relaxation in monolayer MoS_2. Phys. Rev. B, 87(24):245421, 2013.

[327] Gleb M Akselrod, Christos Argyropoulos, Thang B Hoang, Cristian Ciracì, Chao Fang, Jiani Huang, David R Smith, and Maiken H Mikkelsen. Probing the mechanisms of large purcell enhancement in plasmonic nanoantennas. Nat. Photon., 8(11):835–840, 2014.

[328] Alec Rose, Thang B Hoang, Felicia McGuire, Jack J Mock, Cristian Ciracì, David R Smith, and Maiken H Mikkelsen. Control of radiative processes using tunable plasmonic nanopatch antennas. Nano Lett., 14(8):4797–4802, 2014.

[329] SA Crooker, T Barrick, JA Hollingsworth, and VI Klimov. Multiple temperature regimes of radiative decay in CdSe nanocrystal quantum dots: Intrinsic limits to the dark-exciton lifetime. Appl. Phys. Lett., 82(17):2793–2795, 2003.

[330] Yimin Kang, Sina Najmaei, Zheng Liu, Yanjun Bao, Yumin Wang, Xing Zhu, Naomi J Halas, Peter Nordlander, Pulickel M Ajayan, Jun Lou, and Zheyu Fang. Plasmonic hot electron induced structural phase transition in a MoS_2 monolayer. Adv. Mater., 26(37):6467–6471, 2014.

[331] Ziwei Li, Yingdong Xiao, Yongji Gong, Zongpeng Wang, Yimin Kang, Shuai Zu, Pulickel M Ajayan, Peter Nordlander, and Zheyu Fang. Active light control of the MoS_2 monolayer exciton binding energy. ACS Nano, 9(10):10158–10164, 2015.

[332] Evelien M van Schrojenstein Lantman, Tanja Deckert-Gaudig, Arjan JG Mank, Volker Deckert, and Bert M Weckhuysen. Catalytic processes monitored at the nanoscale with tip-enhanced raman spectroscopy. Nat. Nanotech., 7(9):583–586, 2012.

[333] Marie-Elena Kleemann, Rohit Chikkaraddy, Evgeny M Alexeev, Dean Kos, Cloudy Carnegie, Will Deacon, Alex de Casalis de Pury, Christoph Grosse, Bart de Nijs, Jan Mertens, Alexander I Tartakovskii, and Jeremy J Baumberg. Strong-coupling of WSe_2 in ultra-compact plasmonic nanocavities at room temperature. preprint arXiv:1704.02756, 2017.

[334] Chenhao Jin, Jonghwan Kim, Joonki Suh, Zhiwen Shi, Bin Chen, Xi Fan, Matthew Kam, Kenji Watanabe, Takashi Taniguchi, Sefaattin Tongay, Alex Zettl, Junqiao Wu, and Feng Wang. Interlayer electron-phonon coupling in WSe_2/hBN heterostructures. Nat. Phys., 13:127–131, 2017.

[335] Pasqual Rivera, Kyle L Seyler, Hongyi Yu, John R Schaibley, Jiaqiang Yan, David G Mandrus, Wang Yao, and Xiaodong Xu. Valley-polarized exciton dynamics in a 2D semiconductor heterostructure. Science, 351(6274):688–691, 2016.

[336] Philippe Grangier, Gerard Roger, and Alain Aspect. Experimental evidence for a photon anticorrelation effect on a beam splitter: a new light on single-photon interferences. Europhys. Lett., 1(4):173, 1986.

[337] David Press, Stephan Götzinger, Stephan Reitzenstein, Carolin Hofmann, Andreas Löffler, Martin Kamp, Alfred Forchel, and Yoshihisa Yamamoto. Photon antibunching from a single quantum-dot-microcavity system in the strong coupling regime. Phys. Rev. Lett., 98(11):117402, 2007.

[338] Valery Zwiller, Hans Blom, Per Jonsson, Nikolay Panev, Sören Jeppesen, Tedros Tsegaye, Edgard Goobar, Mats-Erik Pistol, Lars Samuelson, and Gunnar Björk. Single quantum dots emit single photons at a time: Antibunching experiments. Appl. Phys. Lett., 78(17):2476–2478, 2001.

[339] Charles Kittel. Introduction to solid state physics. Wiley, 2005.

[340] P Michler, A Kiraz, C Becher, WV Schoenfeld, PM Petroff, Lidong Zhang, E Hu, and A Imamoglu. A quantum dot single-photon turnstile device. science, 290(5500):2282–2285, 2000.

[341] Axel Kuhn, Markus Hennrich, and Gerhard Rempe. Deterministic single-photon source for distributed quantum networking. Phys. Rev. Lett., 89(6):067901, 2002.

[342] Fu-Guo Deng and Gui Lu Long. Bidirectional quantum key distribution protocol with practical faint laser pulses. Phys. Rev. A, 70(1):012311, 2004.

[343] Alessandro Zavatta, Silvia Viciani, and Marco Bellini. Quantum-to-classical transition with single-photon-added coherent states of light. science, 306(5696):660–662, 2004.

[344] Hidetoshi Katori, Tetsuya Ido, Yoshitomo Isoya, and Makoto Kuwata-Gonokami. Magneto-optical trapping and cooling of strontium atoms down to the photon recoil temperature. Phys. Rev. Lett., 82(6):1116, 1999.

[345] Peter Michler. Single semiconductor quantum dots. Springer, 2009.

[346] Philipp Tonndorf, Robert Schmidt, Robert Schneider, Johannes Kern, Michele Buscema, Gary A Steele, Andres Castellanos-Gomez, Herre SJ van der Zant, Steffen Michaelis de Vasconcellos, and Rudolf Bratschitsch. Single-photon emission from localized excitons in an atomically thin semiconductor. Optica, 2(4):347–352, 2015.

[347] Samuel Berweger, Catalin C Neacsu, Yuanbing Mao, Hongjun Zhou, Stanislaus S Wong, and Markus B Raschke. Optical nanocrystallography with tip-enhanced phonon Raman spectroscopy. Nat. Nanotech., 4(8):496–499, 2009.

[348] H Najafov, B Lee, Q Zhou, LC Feldman, Podzorov, and V. Observation of long-range exciton diffusion in highly ordered organic semiconductors. Nat. Mater., 9(11):938, 2010.

[349] E Anastassakis. Selection rules of Raman scattering by optical phonons in strained cubic crystals. J. Appl. Phys., 82(4):1582–1591, 1997.

[350] M Fiebig, D Fröhlich, K Kohn, Th Lottermoser, VV Pavlov, and RV Pisarev. Determination of the magnetic symmetry of hexagonal manganites by second harmonic generation. Phys. Rev. Lett., 84(24):5620, 2000.

[351] KG Lee, HW Kihm, JE Kihm, WJ Choi, H Kim, C Ropers, DJ Park, YC Yoon, SB Choi, DH Woo, J Kim, B Lee, QH Park, C Lienau, and DS Kim. Vector field microscopic imaging of light. Nat. Photon., 1(1):53–56, 2007.

[352] Robert L Olmon, Matthias Rang, Peter M Krenz, Brian A Lail, Laxmikant V Saraf, Glenn D Boreman, and Markus B Raschke. Determination of electric-field, magnetic-field, and electric-current distributions of infrared optical antennas: a near-field optical vector network analyzer. Phys. Rev. Lett., 105(16):167403, 2010.

[353] M Burresi, D Van Oosten, T Kampfrath, H Schoenmaker, R Heideman, A Leinse, and L Kuipers. Probing the magnetic field of light at optical frequencies. Science, 326(5952):550–553, 2009.

[354] HW Kihm, SM Koo, QH Kim, K Bao, JE Kihm, WS Bak, SH Eah, C Lienau, H Kim, P Nordlander, NJ Halas, NK Park, and Kim D-S. Bethe-hole polarization analyser for the magnetic vector of light. Nat. Commun., 2:451, 2011.

[355] Z Fei, AS Rodin, GO Andreev, W Bao, AS McLeod, M Wagner, LM Zhang, Z Zhao, M Thiemens, G Dominguez, MM Fogler, AH Castro Neto, CN Lau, F Keilmann, and DN Basov. Gate-tuning of graphene plasmons revealed by infrared nano-imaging. Nature, 487(7405):82, 2012.

[356] Jianing Chen, Michela Badioli, Pablo Alonso-gonzález, Sukosin Thongrattanasiri, Florian Huth, Johann Osmond, Marko Spasenović, Alba Centeno, Amaia Pesquera, Philippe Godignon, Amaia Zurutuza Elorza, Nicolas Camara, F. Javier Garca de Abajo, Rainer Hillenbrand, and Frank H. L. Koppens. Optical nano-imaging of gate-tunable graphene plasmons. Nature, 487(7405):77–81, 2012.

[357] AR Damodaran, JD Clarkson, Z Hong, H Liu, AK Yadav, CT Nelson, SL Hsu, MR McCarter, KD Park, V Kravtsov, A Farhan, Y Dong, Z Cai, H Zhou, P Aguado-Puente, P Garca-Fernndez, J iguez, J Junquera, A Scholl, MB Raschke, LQ Chen, DD Fong, R Ramesh, and LW Martin. Phase coexistence and electric-field control of toroidal order in oxide superlattices. Nat. Mater., 2017.

[358] Chad E Talley, Joseph B Jackson, Chris Oubre, Nathaniel K Grady, Christopher W Hollars, Stephen M Lane, Thomas R Huser, Peter Nordlander, and Naomi J Halas. Surface-enhanced Raman scattering from individual Au nanoparticles and nanoparticle dimer substrates. Nano Lett., 5(8):1569–1574, 2005.

[359] Alan Sanders, Richard W Bowman, Liwu Zhang, Vladimir Turek, Daniel O Sigle, Anna Lombardi, Lee Weller, and Jeremy J Baumberg. Understanding the plasmonics of nanostructured atomic force microscopy tips. Appl. Phys. Lett., 109(15):153110, 2016.

[360] Ioan Notingher and Alistair Elfick. Effect of sample and substrate electric properties on the electric field enhancement at the apex of SPM nanotips. J. Phys. Chem. B, 109(33):15699–15706, 2005.

[361] Wenzhuo Wu, Lei Wang, Yilei Li, Fan Zhang, Long Lin, Simiao Niu, Daniel Chenet, Xian Zhang, Yufeng Hao, Tony F Heinz, James Hone, and Zhong Lin Wang. Piezoelectricity of single-atomic-layer MoS_2 for energy conversion and piezotronics. Nature, 514(7523):470–474, 2014.

[362] Alexander Weber-Bargioni, Adam Schwartzberg, Matteo Cornaglia, Ariel Ismach, Jeffrey J Urban, YuanJie Pang, Reuven Gordon, Jeffrey Bokor, Miquel B Salmeron, D Frank Ogletree, Paul Ashby, Stefano Cabrini, and P James Schuck. Hyperspectral nanoscale imaging on dielectric substrates with coaxial optical antenna scan probes. Nano Lett., 11(3):1201–1207, 2011.

[363] Thiago L Vasconcelos, Bráulio S Archanjo, Benjamin Fragneaud, Bruno S Oliveira, Juha Riikonen, Changfeng Li, Douglas S Ribeiro, Cassiano Rabelo, Wagner N Rodrigues, Ado Jorio, Carlos A Achete, and Luiz Gustavo Canado. Tuning localized surface plasmon resonance in scanning near-field optical microscopy probes. ACS Nano, 9(6):6297–6304, 2015.

[364] Brenden A Magill, Kyoung-Duck Park, Yuan Zhou, Anuj Chopra, Deepam Maurya, Shashank Priya, Markus Raschke, Alexey Belyanin, Christopher J Stanton, and Giti A Khodaparast. Ultrafast anisotropic optical response and coherent acoustic phonon generation in polycrystalline $BaTiO_3$-$BiFeO_3$. Energy Harvesting and Systems, 3(3):229–236, 2016.

[365] Wilma Eerenstein, ND Mathur, and James F Scott. Multiferroic and magnetoelectric materials. Nature, 442(7104):759, 2006.

[366] T Zhao, A Scholl, F Zavaliche, K Lee, M Barry, A Doran, MP Cruz, YH Chu, C Ederer, NA Spaldin, RR Das, DM Kim, SH Baek, CB Eom, and R Ramesh. Electrical control of

antiferromagnetic domains in multiferroic $BiFeO_3$ films at room temperature. Nat. Mater., 5(10):823, 2006.

[367] Dhanvir Singh Rana, Iwao Kawayama, Krushna Mavani, Kouhei Takahashi, Hironaru Murakami, and Masayoshi Tonouchi. Understanding the nature of ultrafast polarization dynamics of ferroelectric memory in the multiferroic $BiFeO_3$. Adv. Mater., 21(28):2881–2885, 2009.

[368] SY Yang, LW Martin, SJ Byrnes, TE Conry, SR Basu, D Paran, L Reichertz, J Ihlefeld, C Adamo, A Melville, YH Chu, CH Yang, JL Musfeldt, DG Schlom, JW Ager, and R Ramesh. Photovoltaic effects in $BiFeO_3$. Appl. Phys. Lett., 95(6):062909, 2009.

[369] Ramaroorthy Ramesh and Nicola A Spaldin. Multiferroics: progress and prospects in thin films. Nat. Mater., 6(1):21–29, 2007.

[370] Claude Ederer and Nicola A Spaldin. Weak ferromagnetism and magnetoelectric coupling in bismuth ferrite. Phys. Rev. B, 71(6):060401, 2005.

[371] N Hur, S Park, PA Sharma, JS Ahn, S Guha, and SW Cheong. Electric polarization reversal and memory in a multiferroic material induced by magnetic fields. Nature, 429(6990):392, 2004.

[372] Jungho Ryu, Chang-Woo Baek, Yong-Seok Lee, Nam-Keun Oh, Guifang Han, Jong-Woo Kim, Byung-Dong Hahn, Jong-Jin Choi, Woon-Ha Yoon, Joon-Hwan Choi, Dong-Soo Park, and Dae-Yong Jeong. Enhancement of multiferroic properties in $BiFeO_3$–$Ba(Cu_{1/3}Nb_{2/3})O_3$: film fabricated by aerosol deposition. J. Am. Ceram. Soc., 94(2):355–358, 2011.

[373] Mariusz Lejman, Gwenaelle Vaudel, Ingrid C Infante, Pascale Gemeiner, Vitalyi E Gusev, Brahim Dkhil, and Pascal Ruello. Giant ultrafast photo-induced shear strain in ferroelectric $BiFeO_3$. Nat. Commun., 5:4301, 2014.

[374] LY Chen, JC Yang, CW Luo, CW Laing, KH Wu, J-Y Lin, TM Uen, JY Juang, YH Chu, and T Kobayashi. Ultrafast photoinduced mechanical strain in epitaxial $BiFeO_3$ thin films. Appl. Phys. Lett., 101(4):041902, 2012.

[375] P Rovillain, R De Sousa, Y t Gallais, A Sacuto, MA Méasson, D Colson, A Forget, M Bibes, A Barthélémy, and M Cazayous. Electric-field control of spin waves at room temperature in multiferroic $BiFeO_3$. Nat. Mater., 9:975, 2010.

[376] Tae-Jin Park, Georgia C Papaefthymiou, Arthur J Viescas, Yongjae Lee, Hongjun Zhou, and Stanislaus S Wong. Composition-dependent magnetic properties of $BiFeO_3$-$BaTiO_3$ solid solution nanostructures. Phys. Rev. B, 82(2):024431, 2010.

[377] Su-Chul Yang, Ashok Kumar, Valeri Petkov, and Shashank Priya. Room-temperature magnetoelectric coupling in single-phase $BiFeO_3$-$BiFeO_3$ system. J. Appl. Phys., 113(14):144101, 2013.

[378] MO Ramirez, A Kumar, SA Denev, NJ Podraza, XS Xu, RC Rai, YH Chu, J Seidel, LW Martin, S-Y Yang, E Saiz, JF Ihlefeld, S Lee, J Klug, SW Cheong, MJ Bedzyk, O Auciello, DG Schlom, R Ramesh, J Orenstein, JL Musfeldt, and V Gopalan. Magnon sidebands and spin-charge coupling in bismuth ferrite probed by nonlinear optical spectroscopy. Phys. Rev. B, 79(22):224106, 2009.

[379] AK Yadav, CT Nelson, SL Hsu, Z Hong, JD Clarkson, CM Schlepüetz, AR Damodaran, P Shafer, E Arenholz, LR Dedon, D Chen, A Vishwanath, AM Minor, LQ Chen, JF Scott, LW Martin, and Ramesh R. Observation of polar vortices in oxide superlattices. Nature, 530(7589):198, 2016.

[380] ED Mishina, NE Sherstyuk, TV Misyuraev, AS Sigov, AM Grishin, Th Rasing, and OA Aktsipetrov. Structural studies of epitaxial $PbTiO_3$ films by optical second harmonic generation. Thin Solid Films, 336(1):291–294, 1998.

[381] WJ Chen, Yue Zheng, Biao Wang, and JY Liu. Coexistence of toroidal and polar domains in ferroelectric systems: A strategy for switching ferroelectric vortex. J. Appl. Phys., 115(21):214106, 2014.

[382] S Prosandeev, I Ponomareva, I Kornev, I Naumov, and L Bellaiche. Controlling toroidal moment by means of an inhomogeneous static field: An ab initio study. Phys. Rev. Lett., 96(23):237601, 2006.

[383] Ivan Naumov and Huaxiang Fu. Vortex-to-polarization phase transformation path in ferroelectric $Pb(ZrTi)O_3$ nanoparticles. Phys. Rev. Lett., 98(7):077603, 2007.

[384] Y Nahas, S Prokhorenko, L Louis, Z Gui, Igor Kornev, and Laurent Bellaiche. Discovery of stable skyrmionic state in ferroelectric nanocomposites. Nat. Commun., 6, 2015.

[385] Kun Chen, Xi Wan, Jinxiu Wen, Weiguang Xie, Zhiwen Kang, Xiaoliang Zeng, Huanjun Chen, and Jian-Bin Xu. Electronic properties of MoS_2–WS_2 heterostructures synthesized with two-step lateral epitaxial strategy. ACS Nano, 9(10):9868–9876, 2015.

[386] Xidong Duan, Chen Wang, Jonathan C Shaw, Rui Cheng, Yu Chen, Honglai Li, Xueping Wu, Ying Tang, Qinling Zhang, Anlian Pan, et al. Lateral epitaxial growth of two-dimensional layered semiconductor heterojunctions. Nat. Nanotech., 9:1024–1030, 2014.